Quantum-Kinetic Modeling of Electron Release in Low-Energy Surface Collisions of Atoms and Molecules

Inauguraldissertation

zur

Erlangung des akademischen Grades eines

Doktors der Naturwissenschaften

der

Mathematisch-Naturwissenschaftlichen Fakultät

der

Ernst-Moritz-Arndt-Universität Greifswald

vorgelegt von

Johannes Marbach

geboren am 19. Juli 1984

in Eberswalde

Greifswald, 20. September 2012

Dekan:	Prof. Dr. Klaus Fesser
1. Gutachter:	PD Dr. Franz Xaver Bronold
2. Gutachter:	Prof. Dr. Thomas Pruschke
Tag der Promotion:	20.12.2012

Contents

List of Symbols and Abbreviations

Symbols

$\parallel$	Parallel orientation
$\perp$	Perpendicular orientation
$\vec{k}$, $\vec{k}'$, $\vec{k}_1$, $\vec{k}_2$	Electronic state within the surface
$\vec{q}$	Free continuum state moving along with the projectile

Surface Reaction Labels

an	Auger neutralization
dad	Direct Auger de-excitation
iad	Indirect Auger de-excitation
rc	Resonant capture (1^{st} step of two-step resonant de-excitation)
rn	Resonant neutralization
rr	Resonant release (2^{nd} step of two-step resonant de-excitation)

Other Abbreviations

CB	Conduction band
DBD	Dielectric barrier discharge
GSL	GNU Scientific Library
H.c.	Hermitian conjugate
LCAO	Linear combination of atomic orbitals
occ.	occupied
PDP	Plasma display panel
RCT	Resonant charge transfer
unocc.	unoccupied
VB	Valence band

Chapter 1

Preface

1.1 Introduction

Charge exchange processes during atom-surface or molecule-surface collisions have been the subject of intense scientific research during the last decades[108,141]. Clearly, this type of surface reactions is of fundamental interest. Technically, it represents a quantum-impurity problem where a finite many-body system with discrete quantum states couples to an extended system of continuum states essentially acting as a reservoir for electrons. Under appropriate conditions[52,94,120] such an arrangement for instance gives rise to the Kondo effect[51] originally found in metals containing magnetic impurities or to Coulomb blockades as discussed in the field of nanostructures[41].

Apart from being a particular realization of a quantum impurity problem, atom- and molecule-surface collisions are also of immense technological interest, mainly due to the associated secondary electron emission. The latter can be due to a variety of different surface reaction channels the presence of which is determined by the energetic structure of the projectile-surface system. The resulting electron yield is usually encapsulated in the secondary electron emission coefficient γ_e which denotes the average number of electrons released in an elementary surface reaction involving a single projectile and one or multiple reaction channels. Thus, the emission coefficient γ_e is specific to the surface material, the projectile and the particular collision processes under consideration.

To illustrate the particular technological importance of secondary electron emission in the wake of atom- and molecule-surface scattering, we consider a few examples. For one thing, emission spectra of secondary electrons generated during the surface de-excitation of metastable atoms are used in surface-sensitive electron spectroscopy experiments[47,67,119,140]. Moreover, secondary electron emission plays an important role in a number of industrial applications. Among the latter are for instance atmospheric pressure dielectric barrier discharges, commonly known as DBDs. This type of discharge is used in various technological processes like polymer surface treatment, thin film coating, sterilization, gas flow control and ozone production[40,92]. For all of these applications the discharge's stability and homogeneity are vital to a steady and successful performance. Secondary electron emission from the electrodes increases the DBD's self-sustain and is, thus, crucial to the discharge's operation mode. In particular, there is experimental evidence that the stability of DBDs is controlled by secondary electron emission from plasma boundaries for in-

stance due to impacting metastable species[15,91]. In DBDs the latter process is one of the main wall-based secondary electron emission channels which together with wall recombination and various volume-based charge production and destruction channels governs the overall charge balance in the plasma[79]. Hence, controlling the yield with which secondary electrons are produced is of great practical interest. This generally applies to bounded low-temperature plasmas and even more so to microdischarges[10] where the continuing miniaturization steadily increases the influence of charge-transferring surface reactions on the properties of the discharge.

Another technological application which is strongly influenced by secondary electron emission from surfaces are plasma display panels, also known as PDPs. These devices are commonly found in modern-day large size TV monitors. PDPs are usually based on AC driven high pressure microdischarges[107] in noble gas mixtures[9] and often utilize electrodes coated with Al_2O_3 or MgO[132]. The panel's firing voltage, that is the voltage required for discharging, is directly influenced by secondary electron emission from the dielectric electrodes[132], for instance due to impacting metastable species present in the discharge.

Focusing on DBDs and PDPs we clearly see that the operativeness of these applications heavily depends on the yield of secondary electrons which, as mentioned before, can be condensed into the emission coefficient γ_e. The latter either has to be measured experimentally or calculated from first principles and is an important input parameter for numerical simulations. For the particular case of DBDs these investigations are inevitable[15,40] since although this type of discharge has been studied for more than 20 years, its basic mechanisms are still not entirely understood[92]. Furthermore, for PDPs a numerical analysis of the employed materials, the overall discharge geometry and the operation mode can help to improve the performance of the discharge[107].

The demand for reliable γ_e values for use in numerical simulations of DBDs, PDPs and related gas discharges contrasts with the very sparse and often uncertain available reference data. In many cases crude rules of thumb have to be used[109]. Moreover, the database is especially sparse for secondary electron emission due to molecular projectiles. With the present work we aim to contribute to the filling of this gap. Our objective is, however, not the mere production of reference data but rather the setup of a flexible and easy-to-use model that allows for a convenient calculation of the emission coefficient and related quantities for a wide range of projectile-surface systems. In particular, we focus on atomic and especially diatomic molecular species impacting on a metallic or dielectric surface. In such a surface collision process generally both the target and the projectile are composite objects. Hence, usually a great variety of reaction channels is conceivable making the investigation of this scattering process a challenging task, particularly for molecules. However, not all of the theoretically allowed transitions are equally efficient. Consequently, we restrict our investigations to the most dominant reaction channels having a direct or indirect impact on the secondary electron yield.

One of these channels is the surface de-excitation of metastables. For atomic projectiles this process has been studied exhaustively in the past[13,25,58,86,90,103,115,119] and, thus, will not be considered in the present work. For molecular species, on the other hand, an in-depth understanding of the dominating de-excitation channels is still missing. Therefore, we will concentrate on the de-excitation of diatomic molecules using the example of the dominant metastable state of the nitrogen mol-

ecule, $N_2(^3\Sigma_u^+)$. This case is especially interesting because as a result of resonant electron capture $N_2(^3\Sigma_u^+)$ can form the negative ion shape resonance $N_2^-(^2\Pi_g)$ which itself can decay into the ground state $N_2(^1\Sigma_g^+)$ by resonantly emitting an electron[127]. Thus, de-excitation of $N_2(^3\Sigma_u^+)$ is possible via a two-step resonant charge transfer (RCT) reaction. In addition, $N_2(^3\Sigma_u^+)$ can also de-excite indirectly in an Auger transition[127].

Both of these reactions have been investigated experimentally by Stracke et al.[127] for a tungsten surface. The latter authors concluded that out of the two competing processes the resonant reaction should be more efficient as it is a combination of two single-electron charge transfer transitions whereas the Auger channel represents a less probable two-electron transition. Using thermal molecules Stracke et al.[127] measured the energy spectrum of the released electrons and estimated the overall secondary electron emission coefficient γ_e to lie between 10^{-3} and 10^{-2}. This experimental estimate for γ_e does, however, not discriminate between the two de-excitation channels but rather includes both of them. Indeed, Stracke et al.[127] mention that in the emission spectrum they observe a weak signal due to Auger de-excitation giving rise to an isolated emission coefficient of about 10^{-4} to 10^{-3}.

In a subsequent theoretical work Lorente et al.[82] investigated the de-excitation of $N_2(^3\Sigma_u^+)$ molecules on an aluminum surface based on the assumption that the resonant channel is the dominant one. The resonance-driven secondary electron emission coefficient resulting from their calculated electron emission spectrum amounts to approximately 10^{-1} which is one order of magnitude larger than the value Stracke et al.[127] give for tungsten.

While the works of Stracke and Lorente[82,127] mainly focused on the RCT mechanism, for a different surface material Auger and resonant de-excitation might be eye-to-eye competitors. Moreover, in general the surface's band structure may permit either none, one or both of the channels to operate at the same time, thus, allowing for a wide range of coupling effects. A detailed analysis of these features is, however, still lacking for the $N_2(^3\Sigma_u^+)$ molecule as former studies concerning the interaction of resonant and Auger channels in surface collisions were mainly limited to atomic projectiles[70,83,104,125,145]. In particular, for the case of $Li(2p)$ atoms de-exciting on a metallic surface an investigation of the coupling between tunneling and Auger processes has been conducted by Onufriev and Marston[102]. Using a sophisticated many-body theoretical description of the scattering process they concluded that depending on the model parameters the two de-excitation channels interfere either constructively or destructively. Further studies were carried out by other authors. Starting with the work of Vicente Alvarez et al.[131] a detailed theoretical analysis of the interference of Auger and resonant tunneling processes has been given by Goldberg and coworkers[33,39,134]. Their results for H^+ and He^+ indicate that the Auger channel is only active close to the surface whereas the resonant channel is already efficient at rather large projectile-surface distances. Hence, when both channels are coupled together the dynamics of the system is controlled by the resonant channel since it destroys the initial species before the Auger channel can become operative. The latter is, therefore, strongly suppressed in the coupled system albeit the individual efficiencies of the two channels are comparable.

With this work we aim to provide a fundamental investigation of the coupling between resonant and Auger de-excitation of $N_2(^3\Sigma_u^+)$ with an eye on the secondary electron yield. As our interest in these surface processes primarily stems from their

relevance for bounded low-temperature gas discharges, we will focus on the regime of low projectile energies and develop an effective model of the projectile-surface interaction. Stripping some of the microscopic details, the model we propose concentrates on the most important degrees of freedom and enables us to describe the system by only a small number of parameters which are easily accessible through experiments or theoretical calculations. Thus, to some extent our description possesses universality since it can easily be applied to different projectile-surface combinations by adjusting the parameters.

In particular, our model is centered about a square potential well approximation of the solid surface and a semi-empirical two-level representation of the metastable molecule. The latter is based on an LCAO approach and consists of an initially empty ground state level and an initially occupied excited level. Furthermore, molecular continuum states are described by two-center Coulomb waves.

Within the overall system of solid and projectile states we then consider two active electrons, one of them residing in a specific energy band of the surface and the other being located in the excited level of the molecular system. The associated Hamiltonian is obtained from a generalization of an approach due to Gadzuk[30] by considering the interplay of the various real and image charges. This Hamiltonian is, however, not capable of describing the combination of both de-excitation channels due to two reasons. Firstly, it does not account for the conditional coupling between the two subreactions of the resonant channel[1]. Secondly, our two-level approximation of the molecule disregards a number of passive electrons which can introduce additional intra-molecular Coulomb correlations leading to a displacement of the active energy levels.

A way to overcome these problems would be to set up a more general projectile Hamiltonian, including active and spectator electrons and their mutual Coulomb interactions. However, treating these intra-molecular Coulomb correlations explicitly is extremely demanding. It embraces a full quantum-chemical description of the approaching molecule which cannot easily be adapted from one projectile to another. Retaining this adaptability is, however, an important criterion for us in view of the application of our model to bounded low-temperature plasmas. Therefore, we stay within the limits of our semi-empirical two-level system and introduce a set of projection operators together with two auxiliary bosonic levels. The projection operators allow us to assign different parameterizations to the molecular two-level system, depending on its occupancy. Moreover, they can be used to assure that the positive ion state $N_2^+(^2\Pi_u)$ never occurs in the dynamical evolution of the system which automatically generates the conditional coupling of the RCT subreactions. In addition, the auxiliary boson states enable us to mimic the intra-molecular Coulomb correlations which need to kick in to ensure resonance in the two tunneling processes of the RCT de-excitation reaction. As a result, we can formulate a Hamiltonian containing both de-excitation channels without explicitly considering intra-molecular Coulomb interactions.

We then express the projection operators in terms of boson- and fermion-like pseudo-particle operators representing the individual states of the nitrogen molecule. The strength and flexibility of the pseudo-particle or slave field approach, originally developed by Coleman[22] in the context of the infinite-U Anderson model, has been demonstrated many times for Anderson- and Anderson-Newns-type Hamil-

[1] The second subreaction can only launch after the first has completed.

tonians[3,26,76,120,139]. Here we apply this method to a generalized Anderson-Newns model describing the coupling of different molecular configurations to a solid. In particular, our Hamiltonian is of the type but not identical to the one introduced by Marston and coworkers[90,102].

Building upon the original and the slave-particle Hamiltonian, we subsequently simulate the kinetics of electrons within our effective model by employing the non-equilibrium[2] Green function technique[12,23,69,110] in a quantum-kinetic calculation. Admittedly, a description of surface collisions with Green functions[26,38,86,87,120,131] is mathematically more demanding than using the widespread rate equation approach[13,18,44,103,115,143]. The Green function formalism is, however, more flexible in handling the non-adiabaticity of the projectile's motion[86,87], the Coulomb correlations on the projectile[26,38,120] and the collective electronic excitations of the surface[131]. Moreover, a theoretical description based on Green functions can easily embrace level shifts and broadenings due to image interactions as well as molecular vibrations.

In particular, for the isolated reactions of Auger de-excitation, resonant electron capture and resonant electron emission our quantum-kinetic calculation follows along the lines of Makoshi and coworkers[86,87,95,143]. The latter authors employed the Keldysh formulation[69] of the non-equilibrium Green function technique to calculate the secondary electron emission coefficient and related quantities within the trajectory approximation[143]. The analysis presented in this work, however, goes beyond the studies of Makoshi et al. since we don't restrict ourselves to time-local self-energies and, thus, to the wide-band approximation. Instead we analytically solve the Dyson equations and replace the exact solution by an approximate exponential form which still accounts for the nonlocality of the self-energies. In addition, our approach is not restricted to phenomenological matrix elements as we work with the full expressions and merely exploit the locality of the bound molecular states and the large distance of the molecule's turning point from the surface.

In order to combine the isolated reactions within our slave-particle model, we then follow the works of Langreth et al.[76,120] and derive a system of quantum-kinetic equations for the pseudo-particle propagators. Using the semi-classical approximation we reduce this system to a set of rate equations for the occupancies of the molecular pseudo-particle states which represent the probabilities of finding the different molecular states in the course of the collision. The resulting rate equation system is capable of describing the de-excitation of $N_2(^3\Sigma_u^+)$ in situations where the resonant and the Auger channel are active simultaneously and relies on quantum-kinetic transition rates.

Finally, as a proof of concept we will generalize our effective model of the projectile-surface system to the neutralization of positive ions. Similar to the de-excitation of $N_2(^3\Sigma_u^+)$ the neutralization can proceed via a resonant or an Auger channel. Here, however, the resonant reaction is a one-step process which neutralizes the projectile without generating secondary electrons. Consequently, only the Auger neutralization process can contribute directly to the emission coefficient γ_e. When both neutralization channels are active at the same time, the resonant reaction can, however, have an indirect effect on the secondary electron yield by neutralizing the incoming projectile before the Auger channel can get operative.

[2]The non-equilibrium character of our system is introduced by the motion of the projectile which results in time-dependent interaction potentials.

By analogy to the previously discussed de-excitation reactions former theoretical studies of surface neutralization processes were primarily concerned with atomic projectiles[18,32,43–45,59,81,101,122,129]. Moreover, most investigations focused on metallic surfaces and the regime of high kinetic energies (keV and above). For the case of low projectile energies an extensive analysis of resonant and Auger neutralization on metallic surfaces was conducted by Heiland and coworkers for atomic[50,124,125] as well as molecular[49,55,56] projectiles using a rate equation approach. Their results for H^+ and H_2^+ indicate that for a realistic description of the neutralization process both the resonant and the Auger channel have to be considered provided that they are operative simultaneously.

In view of gas discharges the aforementioned common restriction to high energy projectiles might appear justified since in front of a charged surface, like for instance an electrode inside a DBD, an ion can pick up significant amounts of kinetic energy. However, inside a plasma the ion also collides with other particles and, hence, possesses a mean free path which limits its maximum kinetic energy. Thus, depending on the discharge parameters the case of low kinetic energies might be important as well. With an eye on bounded low-temperature plasmas we will, therefore, focus on the low energy situation in the present work and perform a quantum-kinetic investigation of the interaction of resonant and Auger neutralization for dielectric surfaces. Here the amount of available emission coefficients is particularly small.

Generalizing our effective treatment of the de-excitation reactions, the projectile enters our neutralization model merely with a single localized level which for $N_2^+(^2\Pi_u)$ corresponds to the ground state of our previously discussed two-level system. As a result, it is particularly easy to consider different projectiles since one only has to exchange a single wave function in the neutralization matrix elements. In addition to $N_2^+(^2\Pi_u)$ we will, therefore, also investigate the neutralization of the atomic ions $He^+(^2S_{1/2})$ and $Ar^+(^2P_{3/2})$.

Finally, we stress that the effective nature of our model bolsters the ease of its adaption to different material combinations and surface reaction channels emphasizing once more its partial universality. In order to demonstrate the particular versatility of our description we will present numerical results for several different metallic and dielectric surface materials including aluminum, tungsten, Al_2O_3, CaO, Diamond, MgO and SiO_2. For this purpose we employ a numerical scheme based on a combination of tabulation, interpolation and Monte-Carlo integration techniques which allows us to efficiently evaluate the final semi-classical equations emerging from our quantum-kinetic treatment.

We close this introductory section by briefly sketching the structure of the remainder of this work. In the next sections of this chapter we will further discuss the particular surface reaction channels under consideration (see Sec. 1.2) and introduce our method of calculation, the non-equilibrium Green function technique (see Sec. 1.3). In Chapter 2 we will then explicitly present our effective model of the projectile-surface system and discuss the involved approximations. Afterwards, Chapter 3 will guide the reader through a quantum-kinetic calculation with respect to the various surface reactions. In the following we will concretize the matrix elements and present numerical results for the de-excitation and neutralization channels in Chapters 4 and 5, respectively. Finally, we will sum up the main results of this work and discuss possible further targets of investigation in Chapter 6. In the appendices we will then list the explicit values of the material parameters (see

Appendix A) as well as the particular form of the Langreth-Wilkins rules (see Appendix B) that were employed in this work. Moreover, we will discuss the nested double integral series emerging from our iterative solution of the Dyson equations in Appendix C and explicitly evaluate the lateral Fourier transforms needed for the calculation of the Auger neutralization matrix element in Appendix D. Finally, Appendix E briefly sketches the basics of our numerical scheme.

1.2 Surface Reaction Channels

In the following we will discuss the particular de-excitation and neutralization reactions introduced in Sec. 1.1 in a more detailed way.

1.2.1 De-Excitation of Metastable Species

As stated earlier, in this work we will study the surface de-excitation of metastables using the example of the dominant metastable state of the nitrogen molecule, $N_2(^3\Sigma_u^+)$. The different de-excitation channels are best understood in terms of the aforementioned two-level approximation of the nitrogen molecule which consists of a ground state level and an excited level[3]. In the metastable state $N_2(^3\Sigma_u^+)$ the ground state level is empty whereas the excited level carries a single electron. Being located in front of an occupied energy band of a solid surface the metastable molecule can then resonantly capture an electron into the empty ground state level and form the negative ion shape resonance $N_2^-(^2\Pi_g)$. The latter has a lifetime of 1.6 fs[24] and naturally decays into the ground state molecule $N_2(^1\Sigma_g^+)$ by resonantly emitting the electron from the excited level. This process is sometimes also referred to as auto-decay. In addition to the natural decay, in front of a surface the resonant emission of the excited electron can also be triggered by the molecule-surface interaction potential. Note that in both cases the electron emission proceeds into a molecular continuum state that means a free electron state moving along with the projectile. In total this two-step RCT reaction can be written in the schematic form

$$N_2(^3\Sigma_u^+) + e^-_{\vec{k}} \xrightarrow{\text{resonant capture}} N_2^-(^2\Pi_g) \xrightarrow[\text{natural/surface-induced}]{\text{resonant emission}} N_2(^1\Sigma_g^+) + e^-_{\vec{q}}\ . \quad (1.1)$$

Here $e^-_{\vec{k}}$ represents an electron inside the surface and $e^-_{\vec{q}}$ denotes an electron in a molecular continuum state. For the particular case of a diamond surface a visual representation of Eq. (1.1) can be found in the left-hand panel of Fig. 1.1.

In addition to the resonant channel, $N_2(^3\Sigma_u^+)$ can also de-excite indirectly via the Auger reaction

$$N_2(^3\Sigma_u^+) + e^-_{\vec{k}} \xrightarrow{\text{Auger transition}} N_2(^1\Sigma_g^+) + e^-_{\vec{q}}\ , \quad (1.2)$$

which is also known as Penning de-excitation. Here the metastable molecule captures an electron from the surface into its empty ground state level and simultaneously releases the electron from the excited level into a molecular continuum state. The de-excitation, thus, proceeds in an indirect way (see right-hand panel of Fig. 1.1). In a direct de-excitation, on the other hand, the electron from the excited molecular level straightly falls down into the ground state level thereby exciting a surface electron

[3] Details of this representation will be given in Sec. 2.2.3.

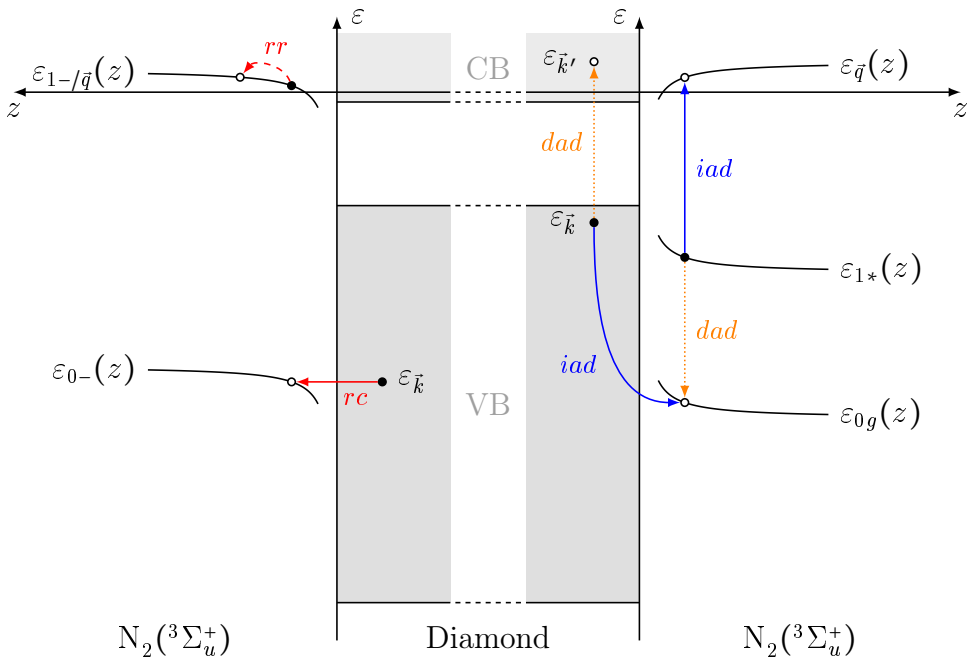

Figure 1.1: Schematic illustration of the different de-excitation channels of $N_2(^3\Sigma_u^+)$ on a diamond surface. Occupied electronic states are indicated by • while empty states are marked with ∘. Furthermore, the drawing is to scale in terms of energy units and VB and CB denote the valence and conduction band, respectively. The left panel depicts the RCT reaction (1.1) embracing the subprocesses of resonant capture (*rc*) and resonant release (*rr*) of an electron. The latter transition is drawn with a dashed line because the electron emission actually occurs at the same z-position and, hence, at the same energy. Consequently, the emitted electron will only reach the shown location over time. Furthermore, the right panel shows the reactions of indirect Auger de-excitation (*iad*) and direct Auger de-excitation (*dad*), Eqs. (1.2) and (1.3). The direct Auger transition is drawn with a dotted line as it is spin-blocked for the $N_2(^3\Sigma_u^+)$-state. Note that the projectile levels' energies and image shifts are determined in terms of the removal of an electron and, hence, depend on the molecular state formed through the transitions (see Table A.3 and Sec. 2.2.4). For clearness in the above figure the level energies ε_0 and ε_1, thus, carry additional subscripts g, $*$ and $-$ denoting the respective level's energy in the molecular ground state $N_2(^1\Sigma_g^+)$, the metastable molecule $N_2(^3\Sigma_u^+)$ and the negative ion $N_2^-(^2\Pi_g)$.

from an occupied band state $\vec{k}$ into an empty band state $\vec{k}'$. This complementary transition is also depicted in the right-hand panel of Fig. 1.1 and can be expressed schematically as

$$N_2(^3\Sigma_u^+) + e^-_{\vec{k}} \xrightarrow{\text{Auger transition}} N_2(^1\Sigma_g^+) + e^-_{\vec{k}'} \,. \tag{1.3}$$

Depending on the surface's band structure the excited state $\vec{k}'$ may lie above the vacuum level. An electron in such a state could, thus, tunnel through the surface barrier and contribute to the experimentally observable secondary electron yield. However, for the particular case of $N_2(^3\Sigma_u^+)$ a direct de-excitation is spin-blocked by the electronic configuration rendering the Auger transition (1.3) impossible. For different metastable states of the nitrogen molecule, on the other hand, the direct channel might be allowed and, hence, could account for an important contribution to the emission coefficient γ_e. Therefore, we will, nevertheless, consider Eq. (1.3) in our quantum-kinetic treatment. Since in the present work we exclusively concentrate

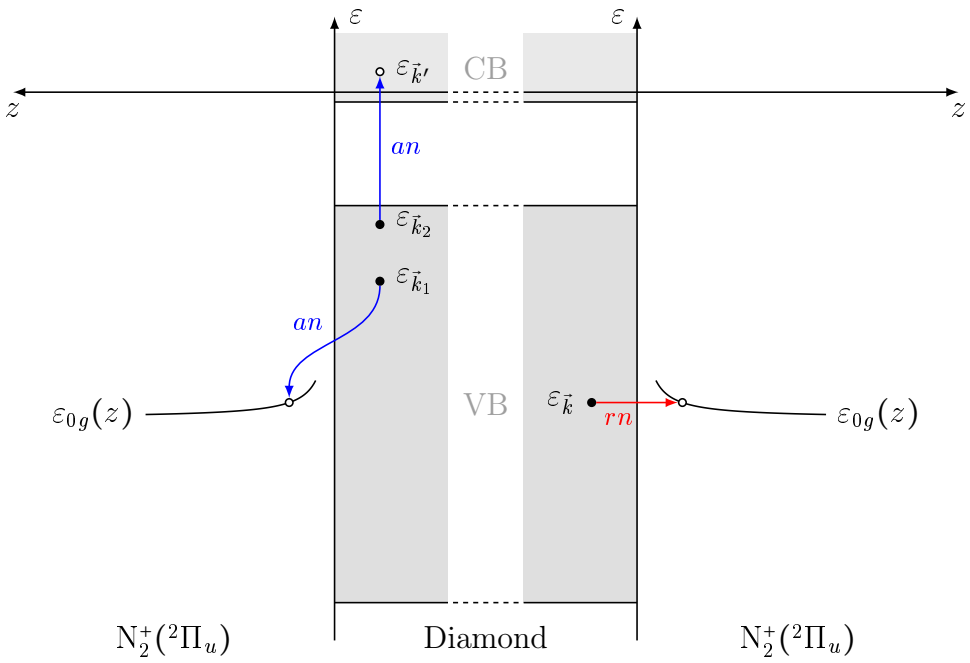

Figure 1.2: Schematic representation of the Auger and resonant neutralization channels for the special case of $N_2^+(^2\Pi_u)$ on a diamond surface. The figure is to scale in terms of energy units. The left panel shows the Auger neutralization (an) reaction (1.4) whereas the right panel depicts the resonant neutralization (rn) channel (1.5). As the neutralization ends up in the molecular ground state $N_2(^1\Sigma_g^+)$, the projectile level's energy is ε_{0g} in both reaction channels (see also the caption of Fig. 1.1).

on the dominant metastable state $N_2(^3\Sigma_u^+)$, we will, however, neither concretize the matrix element nor present numerical results for this reaction channel. Even so, the outcome of our quantum-kinetic calculation will be beneficial to future theoretical studies concerned with different metastable species.

1.2.2 Neutralization of Positive Ions

Within the bounds of our effective model the surface neutralization of a singly charged positive ions can be described by considering only one initially empty projectile level. For the special case of $N_2^+(^2\Pi_u)$ the latter corresponds to the ground state level of our molecular two-level system. For simplicity we will, therefore, refer to this level as the ground state level regardless of the particular projectile in question.

In the following we will consider a general positive ion A^+. In front of a surface such a particle can be neutralized by capturing an electron from an occupied energy band of the surface into its empty ground state level. As noted earlier, this can be achieved by two different reaction channels.

First there is the possibility of Auger neutralization involving two surface electrons populating the states $\vec{k}_1$ and $\vec{k}_2$, respectively. In the Auger transition one of these electrons fills the ion's empty ground state level while the other is excited into a previously unoccupied band state $\vec{k}'$ (see left-hand panel of Fig. 1.2). We may, thus, describe this reaction by

$$A^+ + e^-_{\vec{k}_1} + e^-_{\vec{k}_2} \xrightarrow{\text{Auger transition}} A + e^-_{\vec{k}'} \,. \tag{1.4}$$

Similar to the direct Auger de-excitation reaction (1.3) the excited electron $e^-_{\vec{k}'}$ may reside in a state with positive energy. Thus, under certain conditions it can breach through the surface barrier whereupon it is detectable as a secondary electron by diagnostic tools.

In addition to the Auger channel (1.4) a positive ion A^+ can also be neutralized by resonantly capturing a surface electron into its empty ground state level. This reaction can be expressed as

$$A^+ + e^-_{\vec{k}} \xrightarrow{\text{resonant capture}} A\,, \tag{1.5}$$

and is depicted in the right-hand panel of Fig. 1.2. Even though the transition (1.5) does not generate secondary electrons, it can still have an immense effect on the emission coefficient γ_e. In particular, when both neutralization channels are active at the same time, a very efficient resonant reaction (1.5) can cause the incoming projectile to be completely neutralized before the Auger channel (1.4) can kick in. For a realistic theoretical treatment it is, thus, necessary to consider both neutralization channels although the resonant reaction does not generate secondary electrons.

Note that for the particular case of $N_2^+(^2\Pi_u)$ in terms of the molecular ground state level the transition (1.5) is equivalent to the first step of (1.1). It does, however, lead to a different state of the nitrogen molecule and, hence, the energy of the ground state level ε_0 and its image shift are different from the situation described by (1.1) (see also Figs. 1.1 and 1.2). This point will become more clear in our discussion of the projectile states in Sec. 2.2.

Finally, as stated earlier, within this work we will analyze the interplay of resonant and Auger neutralization for the positive ions of helium, argon and the nitrogen molecule. Hence, in the reactions (1.4) and (1.5) the ion A^+ corresponds to either one of $He^+(^2S_{1/2})$, $Ar^+(^2P_{3/2})$ and $N_2^+(^2\Pi_u)$ while the neutral species A equals the respective ground state $He(^1S_0)$, $Ar(^1S_0)$ or $N_2(^1\Sigma_g^+)$.

1.3 Non-Equilibrium Green Functions

In the surface reactions considered in this work the projectile constantly moves with respect to the surface. As a result, the projectile-surface interaction is time dependent and we are faced with a non-equilibrium problem. In order to treat these situations dynamically we will employ the non-equilibrium Green function formalism. The latter represents a quantum-kinetic generalization of the ordinary Green function method to systems out of equilibrium. The technique is particularly flexible and has been employed successfully in various contexts. Among them are transport phenomena in metals[27,60,69], non-equilibrium superconductivity[6,54] and Fermi liquids[2,80]. More recently it has also been used to simulate quantum dots[3,139] as well as charge transfer during atom- and ion-surface collisions[34,38,76,86,131,143].

The non-equilibrium Green function technique comes in two different formulations which have been developed in parallel by Keldysh[69] and Kadanoff and Baym[65], respectively. In the following we give a brief description of the technique's general idea and the two formulations. The main purpose of this section is to fix our notation for the quantum-kinetic calculations of Chapter 3. For a comprehensive overview of the formalism we refer the reader to Refs. [23, 48, 80, 110] for further details.

1.3.1 General Idea

Consider a system described by the Hamiltonian

$$\hat{H}(t) = \hat{H}_0 + \hat{H}_1(t) \,, \tag{1.6}$$

where $\hat{H}_0$ represents the non-interacting system and $\hat{H}_1(t)$ denotes a time-dependent perturbation. We assume the perturbation to be adiabatically switched on and off at times $-t_0$ and $+t_0$, respectively, and initially let $t_0 \to \infty$ (see Ref. [48]). The non-interacting Hamiltonian $\hat{H}_0$ may possess a simple, meaning diagonalizable, time dependence as well. The operator does, however, not vanish as t approaches $\pm t_0$. For the sake of clearness we, therefore, suppress this time dependence in our notation.

Due to the adiabatic time dependence of the perturbation Hamiltonian $\hat{H}_1$, Eq. (1.6) represents a non-equilibrium system. We will now show how the ordinary Green function technique can be generalized to such a situation. To do so, we first consider the expectation value of an arbitrary one-particle operator $\hat{O}$ given by

$$\left\langle \hat{O}^{(h)}(t) \right\rangle = \left\langle \Phi^{(h)} \middle| \hat{U}(-\infty, t)\, \hat{O}^{(i)}(t)\, \hat{U}(t, -\infty) \middle| \Phi^{(h)} \right\rangle , \tag{1.7}$$

where the superscripts (h) and (i) denote the Heisenberg representation and the interaction representation, respectively (see for instance Ref. [35]). Moreover, Φ is an arbitrary state of the system and $\hat{U}(t_1, t_2)$ represents the interaction picture time evolution operator defined by[23]

$$\hat{U}(t_1, t_2) = \left[\Theta(t_1 - t_2)\, \hat{T}_c + \Theta(t_2 - t_1)\, \hat{T}_a \right] e^{-\frac{i}{\hbar} \int_{t_2}^{t_1} \mathrm{d}t'\, \hat{H}_1^{(i)}(t')} \,, \tag{1.8}$$

with $\hat{T}_c$ and $\hat{T}_a$ labeling the real time chronological and anti-chronological time-ordering operator, respectively, and $\hbar$ identifying Planck's Constant h divided by 2π. In equilibrium theory one now rewrites the time evolution operators of (1.7) in the form

$$\hat{U}(-\infty, t) = \hat{U}(-\infty, \infty)\, \hat{U}(\infty, t) \,, \tag{1.9}$$

and utilizes the fact that the system's final state is equal to the initial state multiplied by a phase factor (see for instance Ref. [74]). Here, however, we cannot follow this track since in general for a non-equilibrium system the final state of the system is fundamentally distinct from its initial state. Therefore, we need to formulate the evolution of the system with reference to its initial state only and avoid any reference to asymptotically large times[48]. For this purpose we first insert (1.8) into (1.7) and obtain

$$\left\langle \hat{O}^{(h)}(t) \right\rangle = \left\langle \Phi^{(h)} \middle| \hat{T}_a \left[e^{-\frac{i}{\hbar} \int_t^{-\infty} \mathrm{d}t'\, \hat{H}_1^{(i)}(t')} \right] \hat{O}^{(i)}(t)\, \hat{T}_c \left[e^{-\frac{i}{\hbar} \int_{-\infty}^{t} \mathrm{d}t'\, \hat{H}_1^{(i)}(t')} \right] \middle| \Phi^{(h)} \right\rangle . \tag{1.10}$$

In order to join the exponentials to the left and right of $\hat{O}^{(i)}(t)$, we now imagine the time to run on a contour $\mathcal{C}$ in the complex plane starting at $-\infty$, passing through some maximum time τ and returning to $-\infty$ (see Fig. 1.3). We then introduce a contour time-ordering operator $\hat{T}_\mathcal{C}$ that is equal to $\hat{T}_c$ on the increasing branch and equal to $\hat{T}_a$ on the decreasing branch. As a result, we can rewrite (1.10) as

$$\left\langle \hat{O}^{(h)}(t) \right\rangle = \left\langle \Phi^{(h)} \middle| \hat{T}_\mathcal{C} \left[e^{-\frac{i}{\hbar} \int_\mathcal{C} \mathrm{d}t'\, \hat{H}_1^{(i)}(t')} \hat{O}^{(i)}(t) \right] \middle| \Phi^{(h)} \right\rangle , \tag{1.11}$$

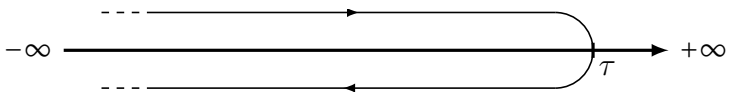

Figure 1.3: Contour $\mathcal{C}$ in the imaginary time plane running from $-\infty$ to a maximum time τ and back to $-\infty$. The value of τ should exceed the largest physical time under consideration and usually one lets $\tau \to \infty$.

where $\int_{\mathcal{C}}$ denotes the integral over the contour. Due to the introduction of the complex time path $\mathcal{C}$, the expectation value (1.11) is now in suitable form for diagrammatic expansion using Feynman diagrams. Note that the shape of the contour $\mathcal{C}$ is not limited to the special case depicted in Fig. 1.3 as it may be deformed in an arbitrary manner. Moreover, the maximum time value τ has no physical meaning beyond the fact that it exceeds the largest physical time under consideration. Consequently, one usually lets $\tau \to \infty$.

We now proceed with the generalization of the Green function onto the contour. The one-particle contour-ordered Green function $G_{\alpha\beta}(t,t')$ describes the propagation from a state β at time t' to a state α at time t and is defined as

$$iG_{\alpha\beta}(t,t') = \left\langle \hat{T}_{\mathcal{C}} \left[\hat{\Psi}_{\alpha}^{(h)}(t)\, \hat{\Psi}_{\beta}^{\dagger(h)}(t') \right] \right\rangle , \tag{1.12}$$

with $\hat{\Psi}$ denoting the usual fermionic or bosonic field operator. When the system's initial state is uncorrelated[4], Eq. (1.12) can be straightforwardly expanded into a perturbation series by employing (1.11) and Wick's theorem[110]. The procedure is analogous to the equilibrium case except that here one has to integrate over the complex time contour $\mathcal{C}$ rather than over inverse temperatures.

Moreover, as in equilibrium theory, the details of the perturbation expansion can be encapsulated in a Dyson equation. The latter contains the self-energy Σ which may be calculated to an arbitrary order by diagrammatic techniques. To shorten our representation of the Dyson equation, we introduce the compact notation

$$\left\{ A_{\alpha\gamma} * B_{\gamma\beta} \right\}_{\mathcal{C}}(t,t') = \sum_{\gamma} \int_{\mathcal{C}} \mathrm{d}t_1 \; A_{\alpha\gamma}(t,t_1)\, B_{\gamma\beta}(t_1,t') , \tag{1.13}$$

which can be extended to a product of three quantities straightforwardly. Note that within (1.13) the sum over γ is only to be taken if $\alpha \neq \gamma \neq \beta$. Making use of (1.13) we can express the contour Dyson equation either in integral form[80]

$$G_{\alpha\beta}(t,t') = G^{(0)}_{\alpha\beta}(t,t') + \left\{ G^{(0)}_{\alpha\gamma} * \Sigma_{\gamma\delta} * G_{\delta\beta} \right\}_{\mathcal{C}}(t,t') , \tag{1.14}$$

or in differential form[80]

$$\left[i\frac{\partial}{\partial t} - \frac{\varepsilon_{\alpha}(t)}{\hbar} \right] G_{\alpha\beta}(t,t') = \delta(t-t') + \left\{ \Sigma_{\alpha\gamma} * G_{\gamma\beta} \right\}_{\mathcal{C}}(t,t') . \tag{1.15}$$

Here ε_{α} denotes the energy of the state α and $G^{(0)}$ represents the unperturbed Green function which is determined by $\hat{H}_0$ only. Equations (1.14) and (1.15) may also be written in their adjoint forms[80]

$$G_{\alpha\beta}(t,t') = G^{(0)}_{\alpha\beta}(t,t') + \left\{ G_{\alpha\gamma} * \Sigma_{\gamma\delta} * G^{(0)}_{\delta\beta} \right\}_{\mathcal{C}}(t,t') , \tag{1.16}$$

[4] For the treatment of a correlated initial state see Ref. [110] and references therein.

and

$$\left[-i\frac{\partial}{\partial t'} - \frac{\varepsilon_\beta(t')}{\hbar}\right] G_{\alpha\beta}(t,t') = \delta(t-t') + \left\{G_{\alpha\gamma} * \Sigma_{\gamma\beta}\right\}_{\mathcal{C}}(t,t') \,. \tag{1.17}$$

For a further analytical or numerical treatment of these equations the contained contour integrations now need to be broken down onto the real axis. This step is sometimes also referred to as analytic continuation. The two different formulations of the theory, which we will present in the following sections, utilize different approaches to cope with this situation.

1.3.2 Keldysh Formulation

In the formulation due to Keldysh[69] the complex time contour is divided into an increasing branch labeled + and a decreasing branch labeled −. Depending on the position of its time arguments on either one of these branches the Green function (1.12) can, thus, be decomposed into the four analytical pieces

$$iG^{++}_{\alpha\beta}(t,t') = \left\langle \hat{T}_c \left[\hat{\Psi}^{(h)}_\alpha(t)\, \hat{\Psi}^{\dagger(h)}_\beta(t')\right]\right\rangle , \tag{1.18a}$$

$$iG^{+-}_{\alpha\beta}(t,t') = \mp\left\langle \hat{\Psi}^{\dagger(h)}_\beta(t')\, \hat{\Psi}^{(h)}_\alpha(t)\right\rangle , \tag{1.18b}$$

$$iG^{-+}_{\alpha\beta}(t,t') = \left\langle \hat{\Psi}^{(h)}_\alpha(t)\, \hat{\Psi}^{\dagger(h)}_\beta(t')\right\rangle , \tag{1.18c}$$

$$iG^{--}_{\alpha\beta}(t,t') = \left\langle \hat{T}_a \left[\hat{\Psi}^{(h)}_\alpha(t)\, \hat{\Psi}^{\dagger(h)}_\beta(t')\right]\right\rangle , \tag{1.18d}$$

where the upper sign holds for fermions and the lower one for bosons. Obviously, the analytical parts of the Green function are linearly dependent as the relation

$$G^{++}_{\alpha\beta}(t,t') + G^{--}_{\alpha\beta}(t,t') = G^{+-}_{\alpha\beta}(t,t') + G^{-+}_{\alpha\beta}(t,t') \,, \tag{1.19}$$

follows directly from the definition of the ++, +−, −+ and −− components of $G_{\alpha\beta}$. Furthermore, the decomposition (1.18) can also be expressed in matrix notation,

$$G_{\alpha\beta}(t,t') = \begin{pmatrix} G^{++}_{\alpha\beta}(t,t') & G^{+-}_{\alpha\beta}(t,t') \\ G^{-+}_{\alpha\beta}(t,t') & G^{--}_{\alpha\beta}(t,t') \end{pmatrix} . \tag{1.20}$$

Since the self-energy Σ is defined on the contour as well, it possesses an analogous matrix representation,

$$\Sigma_{\alpha\beta}(t,t') = \begin{pmatrix} \Sigma^{++}_{\alpha\beta}(t,t') & \Sigma^{+-}_{\alpha\beta}(t,t') \\ \Sigma^{-+}_{\alpha\beta}(t,t') & \Sigma^{--}_{\alpha\beta}(t,t') \end{pmatrix} . \tag{1.21}$$

Consequently, the Dyson equation turns into a matrix equation which yields equations of motion for the analytical pieces of the Green function upon expansion of the matrix products. Moreover, the rules for the diagrammatic calculation of the self-energy components (1.21) are equivalent to the equilibrium case except that one has to handle the + and − signs at the ends of each line. For details we refer the reader to Ref. [80].

Employing (1.19) together with the matrix Dyson equation one finds the identity[80]

$$\Sigma^{++}_{\alpha\beta}(t,t') + \Sigma^{--}_{\alpha\beta}(t,t') = -\Sigma^{+-}_{\alpha\beta}(t,t') - \Sigma^{-+}_{\alpha\beta}(t,t') \,. \tag{1.22}$$

Thus, the analytical pieces of the self-energy are linearly dependent as well. This fact can be exploited in order to simplify the structure of the matrix Dyson equation. Employing the unitary transformation

$$U = \frac{1}{\sqrt{2}} \begin{pmatrix} 1 & -1 \\ 1 & 1 \end{pmatrix} , \tag{1.23}$$

we obtain the transformed expressions

$$U\, G_{\alpha\beta}\, U^\dagger = \begin{pmatrix} 0 & G^A_{\alpha\beta} \\ G^R_{\alpha\beta} & G^K_{\alpha\beta} \end{pmatrix} , \quad U\, \Sigma_{\alpha\beta}\, U^\dagger = \begin{pmatrix} \Sigma^K_{\alpha\beta} & \Sigma^R_{\alpha\beta} \\ \Sigma^A_{\alpha\beta} & 0 \end{pmatrix} . \tag{1.24}$$

Here the superscripts A, R and K denote the advanced, retarded and Keldysh part of the corresponding quantity, respectively. The individual components of (1.24) are given by

$$G^A_{\alpha\beta}(t,t') = G^{++}_{\alpha\beta}(t,t') - G^{-+}_{\alpha\beta}(t,t') = G^{+-}_{\alpha\beta}(t,t') - G^{--}_{\alpha\beta}(t,t') , \tag{1.25a}$$
$$G^R_{\alpha\beta}(t,t') = G^{++}_{\alpha\beta}(t,t') - G^{+-}_{\alpha\beta}(t,t') = G^{-+}_{\alpha\beta}(t,t') - G^{--}_{\alpha\beta}(t,t') , \tag{1.25b}$$
$$G^K_{\alpha\beta}(t,t') = G^{++}_{\alpha\beta}(t,t') + G^{--}_{\alpha\beta}(t,t') = G^{+-}_{\alpha\beta}(t,t') + G^{-+}_{\alpha\beta}(t,t') , \tag{1.25c}$$

and

$$\Sigma^A_{\alpha\beta}(t,t') = \Sigma^{++}_{\alpha\beta}(t,t') + \Sigma^{-+}_{\alpha\beta}(t,t') = -\Sigma^{--}_{\alpha\beta}(t,t') - \Sigma^{+-}_{\alpha\beta}(t,t') , \tag{1.26a}$$
$$\Sigma^R_{\alpha\beta}(t,t') = \Sigma^{++}_{\alpha\beta}(t,t') + \Sigma^{+-}_{\alpha\beta}(t,t') = -\Sigma^{--}_{\alpha\beta}(t,t') - \Sigma^{-+}_{\alpha\beta}(t,t') , \tag{1.26b}$$
$$\Sigma^K_{\alpha\beta}(t,t') = \Sigma^{++}_{\alpha\beta}(t,t') + \Sigma^{--}_{\alpha\beta}(t,t') = -\Sigma^{+-}_{\alpha\beta}(t,t') - \Sigma^{-+}_{\alpha\beta}(t,t') . \tag{1.26c}$$

Note that the retarded and advanced parts of the Green function fulfill the relation[80]

$$G^A_{\alpha\beta}(t,t') = \left[G^R_{\beta\alpha}(t',t)\right]^* , \tag{1.27}$$

which follows from the combination of their definitions (1.25a) and (1.25b) with the explicit form of the analytical pieces (1.18).

We now employ the transformation (1.23) within the integral form of the Dyson equation (1.14) and obtain the following equations of motion

$$G^{A/R}_{\alpha\beta}(t,t') = G^{A/R(0)}_{\alpha\beta}(t,t') + \left\{G^{A/R(0)}_{\alpha\gamma} * \Sigma^{A/R}_{\gamma\delta} * G^{A/R}_{\delta\beta}\right\}(t,t') , \tag{1.28a}$$

$$\begin{aligned} G^K_{\alpha\beta}(t,t') = {} & G^{K(0)}_{\alpha\beta}(t,t') + \left\{G^{K(0)}_{\alpha\gamma} * \Sigma^A_{\gamma\delta} * G^A_{\delta\beta}\right\}(t,t') \\ & + \left\{G^{R(0)}_{\alpha\gamma} * \left[\Sigma^K_{\gamma\delta} * G^A_{\delta\beta} + \Sigma^R_{\gamma\delta} * G^K_{\delta\beta}\right]\right\}(t,t') . \end{aligned} \tag{1.28b}$$

Here we have used the compact notation

$$\left\{A_{\alpha\gamma} * B_{\gamma\beta}\right\}(t,t') = \sum_\gamma \int_{-\infty}^{\infty} \mathrm{d}t_1\, A_{\alpha\gamma}(t,t_1)\, B_{\gamma\beta}(t_1,t') , \tag{1.29}$$

where in contrast to (1.13) the time integration runs over the real axis only. Note that in (1.29), as before, the sum over γ is only needed when $\alpha \neq \gamma \neq \beta$.

The Keldysh component of the Dyson equation (1.28b) can be solved iteratively to give the important relation[12]

$$\begin{aligned} G^K_{\alpha\beta}(t,t') = &\left\{\left[\delta_{\alpha\gamma} + G^R_{\alpha\delta} * \Sigma^R_{\delta\gamma}\right] * G^{K(0)}_{\gamma\xi} * \left[\Sigma^A_{\xi\nu} * G^A_{\nu\beta} + \delta_{\xi\beta}\right]\right\}(t,t') \\ &+ \left\{G^R_{\alpha\delta} * \Sigma^K_{\delta\gamma} * G^A_{\gamma\beta}\right\}(t,t') \,. \end{aligned} \tag{1.30}$$

Thus, once the advanced and retarded parts of the Green function are known the Keldysh part can be computed directly from Eq. (1.30). The diagonal component $G^K_{\alpha\alpha}$ then yields the occupation of a state α at arbitrary times,

$$n_\alpha(t) = \frac{1}{2}\left[1 - iG^K_{\alpha\alpha}(t,t)\right] . \tag{1.31}$$

Finally, we consider the Green functions of an interaction-free Hamiltonian with a diagonalizable time dependence,

$$\hat{H}_0(t) = \sum_\alpha \varepsilon_\alpha(t)\, c^\dagger_\alpha\, c_\alpha \,. \tag{1.32}$$

Within our effective model subsystems of the general form (1.32) will act as the non-interacting part of the Hamiltonian. The associated Green functions, thus, represent the unperturbed propagators of our system and, hence, the starting point of our quantum-kinetic calculations (see Chapter 3). Employing Heisenberg's equation it is straightforward to calculate the time evolution of c_α and $c^\dagger_\alpha$ under (1.32). Making use of the general definitions (1.18) we find

$$iG^{++(0)}_{\alpha\beta}(t,t') = \left[\Theta(t-t') \mp n_\alpha(-\infty)\right] e^{-\frac{i}{\hbar}\int_{t'}^{t} \mathrm{d}t_1\, \varepsilon_\alpha(t_1)}\, \delta_{\alpha\beta} \,, \tag{1.33a}$$

$$iG^{+-(0)}_{\alpha\beta}(t,t') = \mp n_\alpha(-\infty)\, e^{-\frac{i}{\hbar}\int_{t'}^{t} \mathrm{d}t_1\, \varepsilon_\alpha(t_1)}\, \delta_{\alpha\beta} \,, \tag{1.33b}$$

$$iG^{-+(0)}_{\alpha\beta}(t,t') = \left[1 \mp n_\alpha(-\infty)\right] e^{-\frac{i}{\hbar}\int_{t'}^{t} \mathrm{d}t_1\, \varepsilon_\alpha(t_1)}\, \delta_{\alpha\beta} \,, \tag{1.33c}$$

$$iG^{--(0)}_{\alpha\beta}(t,t') = \left[\Theta(t'-t) \mp n_\alpha(-\infty)\right] e^{-\frac{i}{\hbar}\int_{t'}^{t} \mathrm{d}t_1\, \varepsilon_\alpha(t_1)}\, \delta_{\alpha\beta} \,, \tag{1.33d}$$

where, like before, the upper sign applies to fermionic particles and the lower one to bosonic particles. The transformed Green function components can be calculated by inserting (1.33) into (1.25) and read

$$G^{A(0)}_{\alpha\beta}(t,t') = i\Theta(t'-t)\, e^{-\frac{i}{\hbar}\int_{t'}^{t} \mathrm{d}t_1\, \varepsilon_\alpha(t_1)}\, \delta_{\alpha\beta} \,, \tag{1.34a}$$

$$G^{R(0)}_{\alpha\beta}(t,t') = -i\Theta(t-t')\, e^{-\frac{i}{\hbar}\int_{t'}^{t} \mathrm{d}t_1\, \varepsilon_\alpha(t_1)}\, \delta_{\alpha\beta} \,, \tag{1.34b}$$

$$G^{K(0)}_{\alpha\beta}(t,t') = -i\left[1 \mp 2n_\alpha(-\infty)\right] e^{-\frac{i}{\hbar}\int_{t'}^{t} \mathrm{d}t_1\, \varepsilon_\alpha(t_1)}\, \delta_{\alpha\beta} \,. \tag{1.34c}$$

Combining the expressions for $G^{A(0)}_{\alpha\beta}$, $G^{R(0)}_{\alpha\beta}$ and $G^{K(0)}_{\alpha\beta}$ we find the relation

$$G^{K(0)}_{\alpha\beta}(t,t') = -i\left[1 \mp 2n_\alpha(-\infty)\right] G^{R(0)}_{\alpha\beta}(t,-\infty)\, G^{A(0)}_{\alpha\beta}(-\infty,t') \,, \tag{1.35}$$

which after insertion into (1.30) and utilization of the advanced and retarded Dyson equations (see Eq. (1.28a)) yields

$$\begin{aligned} G^K_{\alpha\beta}(t,t') = &-i\sum_\gamma \left[1 \mp 2n_\gamma(-\infty)\right] G^R_{\alpha\gamma}(t,-\infty)\, G^A_{\gamma\beta}(-\infty,t') \\ &+ \left\{G^R_{\alpha\delta} * \Sigma^K_{\delta\gamma} * G^A_{\gamma\beta}\right\}(t,t') \,. \end{aligned} \tag{1.36}$$

Equation (1.36) is an important simplification of the more general form (1.30) and holds for any Hamiltonian with a non-interacting part in the structure of (1.32).

1.3.3 Kadanoff-Baym Formulation

Here we will present the Kadanoff-Baym variant of the non-equilibrium Green function technique in the form due to Langreth[75]. In this formulation contour-ordered quantities are split into analytical pieces according to the order of their time arguments along the contour. In particular, the Green function (1.12) is decomposed into

$$iG_{\alpha\beta}(t,t') = \Theta_{\mathcal{C}}(t-t')\,G^{>}_{\alpha\beta}(t,t') \mp \Theta_{\mathcal{C}}(t'-t)\,G^{<}_{\alpha\beta}(t,t')\;, \tag{1.37}$$

where $\Theta_{\mathcal{C}}$ is the contour step function and, as before, the upper sign holds for fermions and the lower one for bosons. Utilizing the definition (1.12) we obtain the explicit form of the analytical pieces $G^{>}_{\alpha\beta}$ and $G^{<}_{\alpha\beta}$,

$$G^{>}_{\alpha\beta}(t,t') = \left\langle \hat{\Psi}^{(h)}_{\alpha}(t)\,\hat{\Psi}^{\dagger(h)}_{\beta}(t') \right\rangle , \tag{1.38a}$$

$$G^{<}_{\alpha\beta}(t,t') = \left\langle \hat{\Psi}^{\dagger(h)}_{\beta}(t')\,\hat{\Psi}^{(h)}_{\alpha}(t) \right\rangle . \tag{1.38b}$$

Inspecting Eq. (1.38b) we find that within the Kadanoff-Baym formulation the occupation of a state α at time t can be calculated from

$$n_{\alpha}(t) = G^{<}_{\alpha\alpha}(t,t)\;. \tag{1.39}$$

Furthermore, the associated advanced and retarded Green functions are given by

$$iG^{A}_{\alpha\beta}(t,t') = -\Theta(t'-t)\left[G^{>}_{\alpha\beta}(t,t') \pm G^{<}_{\alpha\beta}(t,t')\right], \tag{1.40a}$$

$$iG^{R}_{\alpha\beta}(t,t') = \Theta(t-t')\left[G^{>}_{\alpha\beta}(t,t') \pm G^{<}_{\alpha\beta}(t,t')\right]. \tag{1.40b}$$

Moreover, the self-energy Σ possesses an analogous decomposition,

$$i\Sigma_{\alpha\beta}(t,t') = \Theta_{\mathcal{C}}(t-t')\,\Sigma^{>}_{\alpha\beta}(t,t') \mp \Theta_{\mathcal{C}}(t'-t)\,\Sigma^{<}_{\alpha\beta}(t,t')\;, \tag{1.41}$$

which results in the advanced and retarded components

$$i\Sigma^{A}_{\alpha\beta}(t,t') = -\Theta(t'-t)\left[\Sigma^{>}_{\alpha\beta}(t,t') \pm \Sigma^{<}_{\alpha\beta}(t,t')\right], \tag{1.42a}$$

$$i\Sigma^{R}_{\alpha\beta}(t,t') = \Theta(t-t')\left[\Sigma^{>}_{\alpha\beta}(t,t') \pm \Sigma^{<}_{\alpha\beta}(t,t')\right]. \tag{1.42b}$$

The analytical pieces of the self-energy can be calculated by employing the ordinary diagrammatic expansion technique and afterwards projecting the result onto the real axis by means of the Langreth-Wilkins rules (see Appendix B). The latter rules can also be used for the analytic continuation of the contour Dyson equation. In particular, we obtain the differential Dyson equations

$$\left[i\frac{\partial}{\partial t} - \frac{\varepsilon_{\alpha}(t)}{\hbar}\right] G^{>}_{\alpha\beta}(t,t') = \left\{\Sigma^{R}_{\alpha\gamma} * G^{>}_{\gamma\delta} + \Sigma^{>}_{\alpha\gamma} * G^{A}_{\gamma\delta}\right\}(t,t')\;, \tag{1.43a}$$

$$\left[i\frac{\partial}{\partial t} - \frac{\varepsilon_{\alpha}(t)}{\hbar}\right] G^{<}_{\alpha\beta}(t,t') = \left\{\Sigma^{R}_{\alpha\gamma} * G^{<}_{\gamma\delta} + \Sigma^{<}_{\alpha\gamma} * G^{A}_{\gamma\delta}\right\}(t,t')\;, \tag{1.43b}$$

$$\left[i\frac{\partial}{\partial t} - \frac{\varepsilon_{\alpha}(t)}{\hbar}\right] G^{A/R}_{\alpha\beta}(t,t') = \delta(t-t') + \left\{\Sigma^{A/R}_{\alpha\gamma} * G^{A/R}_{\gamma\delta}\right\}(t,t')\;, \tag{1.43c}$$

and their adjoint versions

$$\left[-i\frac{\partial}{\partial t'}-\frac{\varepsilon_\beta(t')}{\hbar}\right]G^{>}_{\alpha\beta}(t,t')=\left\{G^{R}_{\alpha\gamma}*\Sigma^{>}_{\gamma\delta}+G^{>}_{\alpha\gamma}*\Sigma^{A}_{\gamma\delta}\right\}(t,t')\,, \tag{1.44a}$$

$$\left[-i\frac{\partial}{\partial t'}-\frac{\varepsilon_\beta(t')}{\hbar}\right]G^{<}_{\alpha\beta}(t,t')=\left\{G^{R}_{\alpha\gamma}*\Sigma^{<}_{\gamma\delta}+G^{<}_{\alpha\gamma}*\Sigma^{A}_{\gamma\delta}\right\}(t,t')\,, \tag{1.44b}$$

$$\left[-i\frac{\partial}{\partial t'}-\frac{\varepsilon_\beta(t')}{\hbar}\right]G^{A/R}_{\alpha\beta}(t,t')=\delta(t-t')+\left\{G^{A/R}_{\alpha\gamma}*\Sigma^{A/R}_{\gamma\delta}\right\}(t,t')\,. \tag{1.44c}$$

We stress that the advanced and retarded Green function are identical in both formulations. Consequently, the Dyson equations (1.43c) and (1.44c) are nothing but the differential form of (1.28a) and the corresponding adjoint equation.

Finally, we again consider the Green functions associated with an interaction-free Hamiltonian of the general form (1.32). Making use of Heisenberg's equation and the definitions (1.38) we obtain

$$G^{>(0)}_{\alpha\beta}(t,t')=\left[1\mp n_\alpha(-\infty)\right]e^{-\frac{i}{\hbar}\int_{t'}^{t}\mathrm{d}t_1\,\varepsilon_\alpha(t_1)}\,\delta_{\alpha\beta}\,, \tag{1.45a}$$

$$G^{<(0)}_{\alpha\beta}(t,t')=n_\alpha(-\infty)\,e^{-\frac{i}{\hbar}\int_{t'}^{t}\mathrm{d}t_1\,\varepsilon_\alpha(t_1)}\,\delta_{\alpha\beta}\,, \tag{1.45b}$$

where once more the upper sign pertains to fermions and the lower one to bosons. The associated advanced and retarded function can be calculated from the combination of (1.45) and (1.40) which yields the expressions (1.34a) and (1.34b), respectively.

Chapter 2

Effective Model

The present chapter embraces the foundations of our effective model of the projectile-surface system. As noted earlier our description makes a distinction between two different types of electronic states. Electrons in the bulk of the solid, on the one hand, are modeled as an interaction-free electron gas inside a square potential well the boundaries of which are determined by the surface material's band structure. Projectile electronic states, on the other hand, are divided into bound and continuum states possessing negative and positive energies, respectively. Bound states are described by means of a hydrogen-like model with effective nucleus charge that, for the case of N_2, is combined with an LCAO approach. Furthermore, projectile continuum states, which in view of the surface reactions studied in this work have only to be considered for the nitrogen molecule, are approximated by two-center Coulomb waves satisfying the correct asymptotic boundary condition. The particular nature of electronic states in the surface and on the projectile will be discussed explicitly in Secs. 2.1 and 2.2, respectively.

Another integral part of our model is the projectile trajectory which we supply externally in consistence with the usual trajectory approximation (see Sec. 2.3). The associated turning point is calculated from a Morse-type approximation to the surface potential with material-specific parameters.

Building upon the aforementioned electronic states and the trajectory approximation we then consider two active electrons within the system and derive a Hamiltonian by analyzing the interplay of the various real and image charges in Sec. 2.4. Here the projectile's motion enters our description as a parametric time dependence of the interaction potentials and projectile level displacements. Section 2.5 subsequently explains how the Hamiltonian can be extended to account for Coulomb correlations on the projectile by means of a projection operator approach and two auxiliary bosonic levels.

Finally, in Sec. 2.6 we introduce a set of surface transmission functions. These functions cut off emitted electrons that are unable to breach through the surface barrier and can, thus, be used to extract the amount of experimentally observable secondary electrons from our theory.

The key strength of our model is its ease of adaption to different material combinations following from its small number of parameters. Most of these parameters pertain to the electronic structure of either the surface material or the projectile. An overview of the size of the parameter space and the particular values used in this work can be found in Appendix A.

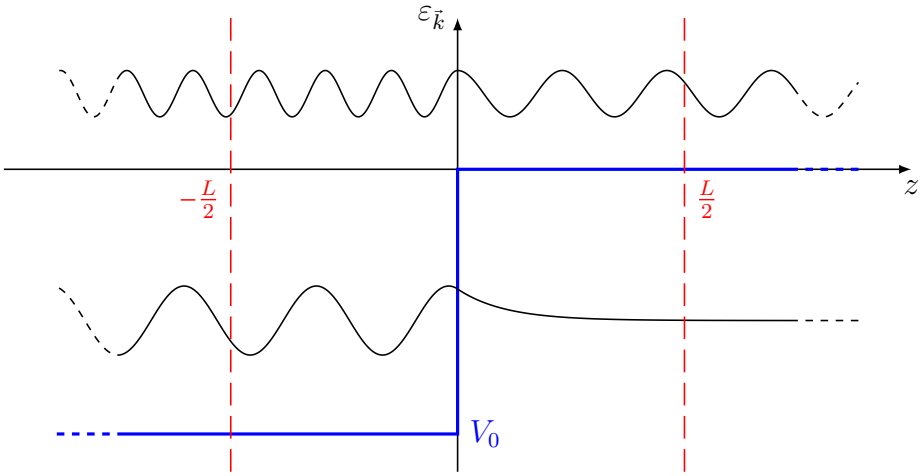

Figure 2.1: Square potential well model used for the calculation of the solid's wave functions. The vertical axis represents the energy scale while the horizontal axis denotes the distance from the surface edge. On the solid side the well has a depth of V_0 whereas outside the surface the potential vanishes. The dashed red lines mark the limits of the box normalization volume $[-L/2, L/2]^3$ on the z-axis. Also indicated here is the schematic form of the wave function for a bound and an internally excited electron.

2.1 Solid Surface

We assume the solid surface to be planar, ideal, uncharged and to stretch over the entire half space $z < 0$. In order to calculate the wave functions of bound or excited electrons within the surface, we employ a square potential well model, sometimes also referred to as the Sommerfeld model[30,58]. The latter has been used successfully in the context of atom-surface collisions by a number of authors[99,111,115,138] and is depicted schematically in Fig. 2.1. In particular, the well has a depth of V_0 within the surface and vanishes on the outside,

$$V(z) = \Theta(-z)V_0 \; . \tag{2.1}$$

The constant potential V_0 prevailing inside the solid may be identified with the lower edge of the respective energy band in question. The associated upper band edge is then realized by restricting the maximum energy of electrons inside the well. For a situation with more than one active energy band a description of this type can be employed separately for each band. We emphasize that this kind of treatment is an effective one since the many-particle details of the solid are encapsulated in the band edges which may be obtained from an ab initio calculation.

The wave functions of the square potential well model $\Psi_{\vec{k}}$ can be derived straightforwardly by solving the Schrödinger equation in the left and right half spaces. After matching the wave functions and their derivatives at the origin we find

$$\Psi_{\vec{k}}(\vec{r}) = N_L \, e^{ik_x x} \, e^{ik_y y} \, \Psi_{k_z}(z) \; , \tag{2.2}$$

with

$$\Psi_{k_z}(z) = \Theta(-z) \left[e^{ik_z z} + R_{k_z} \, e^{-ik_z z} \right] + \Theta(z) \, T_{k_z} \, e^{i\bar{k}_z z} \; . \tag{2.3}$$

Here N_L is a normalization constant while R_{k_z} and T_{k_z} denote the reflection and transmission coefficients given by

$$R_{k_z} = \frac{k_z - \bar{k}_z}{k_z + \bar{k}_z} \; , \qquad T_{k_z} = \frac{2k_z}{k_z + \bar{k}_z} \; . \tag{2.4}$$

Furthermore the scattered wave number $\bar{k}_z$ can be calculated from k_z via

$$\bar{k}_z = \sqrt{k_z^2 + \frac{2m_e V_0}{\hbar^2}} \,, \tag{2.5}$$

where m_e is the electronic mass.

The overall energy $\varepsilon_{\vec{k}}$ associated with the wave function (2.2) amounts to

$$\varepsilon_{\vec{k}} = \frac{\hbar^2 k^2}{2m_e} + V_0 = \underbrace{\frac{\hbar^2 k_x^2}{2m_e}}_{\varepsilon_{k_x}} + \underbrace{\frac{\hbar^2 k_y^2}{2m_e}}_{\varepsilon_{k_y}} + \underbrace{\frac{\hbar^2 k_z^2}{2m_e} + V_0}_{\varepsilon_{k_z}} \,. \tag{2.6}$$

Its vertical component ε_{k_z} determines the nature of the wave function. In particular, for the case $\varepsilon_{k_z} > 0$ the electron resides in an internally excited state. Here $\bar{k}_z$ is a real quantity and, consequently, the wave function $\Psi_{\vec{k}}$ is oscillatory on both sides of the surface edge (see upper wave function in Fig. 2.1). If, on the other hand, $\varepsilon_{k_z} < 0$, then the electron is bound in the z direction. In this case $\bar{k}_z$ is purely imaginary and we may write

$$\bar{k}_z = i\sqrt{-k_z^2 - \frac{2m_e V_0}{\hbar^2}} = i\kappa_{k_z} \,, \tag{2.7}$$

where κ_{k_z} is real. As a result, the vertical part of the wave function (2.3) turns into

$$\Psi_{k_z}(z) = \Theta(-z)\left[e^{ik_z z} + R_{k_z}\, e^{-ik_z z}\right] + \Theta(z)\, T_{k_z}\, e^{-\kappa_{k_z} z} \,. \tag{2.8}$$

As wee see, here $\Psi_{\vec{k}}$ is oscillatory within the surface and decreases exponentially on the outside (see lower wave function in Fig. 2.1). Moreover, the otherwise real-valued reflection and transmission coefficients (2.4) become complex quantities,

$$R_{k_z} = \frac{k_z - i\kappa_{k_z}}{k_z + i\kappa_{k_z}} \,, \quad T_{k_z} = \frac{2k_z}{k_z + i\kappa_{k_z}} \,. \tag{2.9}$$

Finally, we need to determine the normalization constant N_L. Since the wave function (2.2) is completely delocalized, it cannot be normalized in a strict sense. We can, however, normalize $\Psi_{\vec{k}}$ over a finite volume $[-L/2, L/2]^3$ and let $L \to \infty$ at the end of our calculation. This procedure is also referred to as box normalization (see for instance Ref. [93]) and is usually combined with periodic boundary conditions. In particular, we require that

$$\Psi_{\vec{k}}(x,y,z) \stackrel{!}{=} \Psi_{\vec{k}}(x \pm L, y, z) \,, \tag{2.10a}$$

$$\Psi_{\vec{k}}(x,y,z) \stackrel{!}{=} \Psi_{\vec{k}}(x, y \pm L, z) \,, \tag{2.10b}$$

$$\Psi_{\vec{k}}(x,y,z) \stackrel{!}{=} \begin{cases} \Psi_{\vec{k}}\left(x,y,z-\frac{L}{2}\right) & \text{for } z \le 0 \,, \\ \Psi_{\vec{k}}\left(x,y,z+\frac{L}{2}\right) & \text{for } z \ge 0 \text{ and } \varepsilon_{k_z} > 0 \,, \end{cases} \tag{2.10c}$$

which leads to a discretization of the $\vec{k}$-states with the spacings

$$\Delta k_x = \Delta k_y = \frac{2\pi}{L} \,, \quad \Delta k_z = \frac{4\pi}{L} \,. \tag{2.11}$$

Note that this discretization is an artifact of the seemingly peculiar periodicity requirements (2.10). When we let $L \to \infty$, the constraints (2.10), however, become

irrelevant. Consequently, the discretization disappears and $\vec{k}$ becomes continuous again. For a finite L we can now evaluate the normalization integral by leveraging (2.10) which yields

$$N_L = \frac{1}{L^{\frac{3}{2}}} , \tag{2.12}$$

where only the fastest growing power of L has been retained[1].

As we will see in the following chapters, the box normalization length L contained in (2.12) is canceled at the end of our calculation. In particular, the wave function (2.2) always appears as part of a matrix element, assigning to the latter an (at this point) discrete $\vec{k}$-dependency and a factor of N_L. We then have to sum the squared matrix element over all possible discrete $\vec{k}$-states. When we now let $L \to \infty$, the sum turns into an integral and we obtain

$$N_L^2 \sum_{\vec{k}} \cdots = \underbrace{\frac{N_L^2}{(\Delta k)^3}}_{\frac{1}{16\pi^3}} \sum_{\vec{k}} (\Delta k)^3 \ldots \xrightarrow{L\to\infty} \frac{1}{16\pi^3} \int \mathrm{d}\vec{k} \ \ldots , \tag{2.13}$$

where $(\Delta k)^3 = \Delta k_x \, \Delta k_y \, \Delta k_z$. As we see, the box parameter L is lifted completely and, hence, our calculation is consistent.

Finally, we admit that the square potential well model presented in this section neglects any image charge forces acting on electrons outside the surface. To account for the latter we could instead employ the truncated classical image potential

$$V_i(z) = \Theta(z_c - z) V_0 - \Theta(z - z_c) \, Q_\varepsilon \frac{e_0^2}{16\pi\varepsilon_0} \frac{1}{z - z_i} , \tag{2.14}$$

where e_0 is the elementary charge, ε_0 denotes the vacuum permittivity, z_i specifies the position of the image plane and z_c marks the intersection point of the constant bulk potential V_0 and the classical image potential,

$$z_c = z_i - \frac{e_0^2}{16\pi\varepsilon_0} \frac{1}{V_0} . \tag{2.15}$$

Moreover, Q_ε represents the factor

$$Q_\varepsilon = \begin{cases} \frac{\varepsilon_r^b + 1}{\varepsilon_r^b - 1} & \text{for a dielectric surface} , \\ 1 & \text{for a metallic surface} , \end{cases} \tag{2.16}$$

with ε_r^b labeling the static dielectric constant of the solid's bulk.

An even more sophisticated model could be constructed by employing the Jones-Jennings-Jepsen potential[63], often referred to as the Jennings potential,

$$V_j(z) = \begin{cases} Q_\varepsilon \frac{e_0^2}{16\pi\varepsilon_0} \frac{e^{-\lambda(z - z_i)} - 1}{z - z_i} & \text{for } z > z_i , \\ \frac{V_0}{A e^{B(z - z_i)} + 1} & \text{for } z < z_i . \end{cases} \tag{2.17}$$

Here λ is a material specific parameter while the constants A and B are determined by the continuity condition for $V(z)$ and its derivative at z_i,

$$A = -\frac{16\pi\varepsilon_0}{e_0^2} \frac{V_0}{\lambda} - 1 , \quad B = -\frac{16\pi\varepsilon_0}{e_0^2} \frac{V_0}{2A} . \tag{2.18}$$

[1] Slower growing powers become irrelevant as we let $L \to \infty$.

While offering a more realistic description, the potentials (2.14) and (2.17) involve a couple of issues. For one thing, both of them are only suitable for cases where $V_0 < 0$. Furthermore, the wave functions of electrons moving in these potentials are certainly more complicated than the wave functions of the square potential well (2.1). In fact, the wave functions associated with the truncated image potential (2.14) involve confluent hypergeometric functions outside the surface[84]. For the Jennings potential (2.17) the situation is even more involved. For $z < z_i$ the wave functions can be represented by a combination of general hypergeometric functions while for $z > z_i$ only a numerical solution seems to be possible[137]. The complexity of these wave functions is a significant issue as it almost completely denies any analytical manipulation of the matrix elements occurring in our further calculation. Moreover, the Jennings potential (2.17) relies on an additional material specific parameter λ which may not be available for arbitrary surface substances. Due to these reasons we won't consider the potentials (2.14) and (2.17) for the description of electronic states within the surface. Note, however, that we will employ the truncated classical image potential (2.14) when considering bound and continuum projectile levels in front of the surface.

2.2 Projectile States

We now turn our attention to the electronic states on the projectile. Here again our treatment carries an effective character to the extent that we are considering only those electrons which are active in the surface reactions studied in this work. The remaining passive electrons on the projectile are not included explicitly in our model. Rather we assume them to generate an effective nucleus charge number which is then used in the calculation of the active electrons' wave functions. As a result, we are able to reduce the description of the projectile to a small number of material parameters (see Appendix A).

Admittedly, such a treatment is most suitable for alkali atoms and noble gas metastables. Here, however, we assume the approach to be valid for other species as well. As we will see in Secs. 4.1 and 5.1, this allows us to retain the full time and single-particle quantum number dependence of the matrix elements. Thus, our analysis goes clearly beyond a number of previous studies[4,14,38,86,104].

2.2.1 Hydrogen-Like Model

For the projectile materials under consideration we construct the wave functions of bound states from a hydrogen-like model with an effective nucleus charge number Z_{eff}. In such a model the solutions of the Schrödinger equation for negative energies and a set of quantum numbers n, l and m are most conveniently expressed in spherical coordinates (r, ϑ, φ) and read[118]

$$\Psi_{nlm}(r, \vartheta, \varphi) = R_{nl}(r)\, Y_{lm}(\vartheta, \varphi) \,, \tag{2.19}$$

with

$$R_{nl}(r) = -\sqrt{\frac{(n-l-1)!\,(2\kappa_n)^3}{2n\big[(n+l)!\big]^3}}\,(2\kappa_n r)^l\, e^{-\kappa_n r}\, L_{n+l}^{2l+1}(2\kappa_n r) \,, \tag{2.20}$$

and

$$Y_{lm}(\vartheta,\varphi) = (-1)^{\frac{m+|m|}{2}} \sqrt{\frac{2l+1}{4\pi}\frac{(l-|m|)!}{(l+|m|)!}}\, e^{im\varphi} P_{l|m|}\big(\cos(\vartheta)\big)\,. \tag{2.21}$$

Here L_r^s denotes the associated Laguerre polynomial,

$$L_r^s(x) = \frac{\mathrm{d}^s}{\mathrm{d}x^s}\left(e^x \frac{\mathrm{d}^r}{\mathrm{d}x^r}\big[e^{-x}x^r\big]\right), \tag{2.22}$$

and P_{lm} represents the associated Legendre function,

$$P_{lm}\big(\cos(\vartheta)\big) = \frac{(-1)^l}{2^l\, l!}\sin^m(\vartheta)\frac{\mathrm{d}^{l+m}}{\mathrm{d}\big(\cos^{l+m}(\vartheta)\big)}\big[\sin^{2l}(\vartheta)\big]\,. \tag{2.23}$$

The effective nucleus charge Z_{eff} enters the wave function (2.19) via the constant κ_n given through

$$\kappa_n = \frac{Z_{\mathrm{eff}}}{n\, a_B}\,, \tag{2.24}$$

where a_B is the Bohr radius.

2.2.2 Positive Ions of Helium and Argon

As stated earlier, we describe the neutralization of singly charged positive ions using only a lone unoccupied projectile level. In the following we will present the associated wave functions emerging from the hydrogen-like model introduced in Sec. 2.2.1 for $\mathrm{He}^+(^2S_{1/2})$ and $\mathrm{Ar}^+(^2P_{3/2})$. In consistence with our treatment of the nitrogen molecule in a forthcoming passage (see Sec. 2.2.3) we will label these wave functions with $\Psi_0^{(\mathrm{He})}$ and $\Psi_0^{(\mathrm{Ar})}$, respectively. Here the subscript 0 is a tribute to the fact that for the $\mathrm{N}_2^+(^2\Pi_u)$ ion the active projectile level corresponds to the ground state level of our two-level approximation to the nitrogen molecule.

We start our considerations with the positive ion of helium. In the surface neutralization of $\mathrm{He}^+(^2S_{1/2})$ the neutralizing electron is captured into the empty portion of the $1s$ orbital. Consequently, we are interested in the wave function Ψ_{100} with an effective nucleus charge generated by the shielding due to the second electron in the same shell. Employing (2.19) we obtain

$$\Psi_0^{(\mathrm{He})}(r,\vartheta,\varphi) = \Psi_{100}(r,\vartheta,\varphi) = \frac{(\kappa_{\mathrm{He}})^{\frac{3}{2}}}{\sqrt{\pi}}\, e^{-\kappa_{\mathrm{He}} r}\,, \tag{2.25}$$

which may also be written in cylindrical coordinates[2], denoted (R,φ,z), leading to

$$\Psi_0^{(\mathrm{He})}(R,\varphi,z) = \frac{(\kappa_{\mathrm{He}})^{\frac{3}{2}}}{\sqrt{\pi}}\, e^{-\kappa_{\mathrm{He}}\sqrt{R^2+z^2}}\,. \tag{2.26}$$

Here κ_{He} is given by

$$\kappa_{\mathrm{He}} = \frac{Z_{\mathrm{eff}}}{a_B}\,, \tag{2.27}$$

[2]The cylindrical form of the projectile wave functions will be needed for the calculation of lateral Fourier transforms in Appendix D

and involves the effective nucleus charge number $Z_{\text{eff}} = 1.7$ which can be derived by means of Slater's rules for the determination of atomic shielding constants[123].

We now proceed with the $Ar^+(^2P_{3/2})$ ion. Employing Hund's rules (see for instance Ref. [29]) we find that here the neutralizing electron fills the $m = -1$ portion of the $3p$-orbital. Hence, we are seeking the wave function Ψ_{31-1}. Utilization of (2.19) yields

$$\Psi_0^{(\text{Ar})}(r,\vartheta,\varphi) = \Psi_{31-1}(r,\vartheta,\varphi) = \frac{2(\kappa_{\text{Ar}})^{\frac{5}{2}}}{\sqrt{3\pi}}\, r\left(1-\frac{\kappa_{\text{Ar}}}{2}r\right)e^{-\kappa_{\text{Ar}}r}\,\sin(\vartheta)\,e^{-i\varphi}\,, \tag{2.28}$$

which can as well be expressed in cylindrical coordinates,

$$\Psi_0^{(\text{Ar})}(R,\varphi,z) = \frac{2(\kappa_{\text{Ar}})^{\frac{5}{2}}}{\sqrt{3\pi}}R\left(1-\frac{\kappa_{\text{Ar}}}{2}\sqrt{R^2+z^2}\right)e^{-\kappa_{\text{Ar}}\sqrt{R^2+z^2}}\,e^{-i\varphi}\,. \tag{2.29}$$

The constant κ_{Ar} is defined as

$$\kappa_{\text{Ar}} = \frac{Z_{\text{eff}}}{3a_B}\,, \tag{2.30}$$

with an effective charge number $Z_{\text{eff}} = 6.75$ that can again be found by usage of Slater's rules[123].

2.2.3 Molecular Nitrogen

The set of surface reactions studied in this work involves transitions between four different states of the nitrogen molecule (see Sec. 1.2). In the two-step resonant de-excitation channel (1.1), for one thing, a metastable $N_2(^3\Sigma_u^+)$ molecule de-excites into the ground state $N_2(^1\Sigma_g^+)$ via the intermediate negative ion shape resonance $N_2^-(^2\Pi_g)$. The Auger de-excitation reactions (1.2) and (1.3), for another thing, consist of a one-step transition between the metastable $N_2(^3\Sigma_u^+)$ state and the ground state $N_2(^1\Sigma_g^+)$. Finally, the Auger and resonant neutralization channels (1.4) and (1.5) represent a conversion between the positive ion $N_2^+(^2\Pi_u)$ and the ground state $N_2(^1\Sigma_g^+)$. Consequently, our theoretical treatment has to embrace all of these molecular states. In addition, our model also has to account for molecular continuum states for electrons emitted from $N_2^-(^2\Pi_g)$ and $N_2(^3\Sigma_u^+)$ due to the resonant and the indirect Auger de-excitation reactions (1.1) and (1.2). Our approach to handle all of these states will be explained in the following.

We first focus on the description of bound molecular electrons. In order to obtain their wave functions, we employ the technique of linear combination of atomic orbitals (LCAO) an outline of which may be found for instance in Ref. [8]. The resulting molecular orbitals and their generating atomic nitrogen orbitals are depicted in Fig. 2.2 for the molecular ground state $N_2(^1\Sigma_g^+)$. The electronic configurations of the three remaining molecular states, $N_2^+(^2\Pi_u)$, $N_2(^3\Sigma_u^+)$ and $N_2^-(^2\Pi_g)$, differ from the ground state only in the occupation of the $2p\pi_u$ and $2p\pi_g^*$ orbitals, as shown in Fig. 2.3. Also indicated in the latter figure are those electronic states which actively participate in transitions between the four different molecular configurations. As wee see, only two out of the eight different electronic orbitals have to be changed in occupancy in order to switch between $N_2^+(^2\Pi_u)$, $N_2(^1\Sigma_g^+)$, $N_2(^3\Sigma_u^+)$ and $N_2^-(^2\Pi_g)$. Since the surface processes considered in this work constitute direct transitions between either two of these molecular states, we can treat the non-participating orbitals as

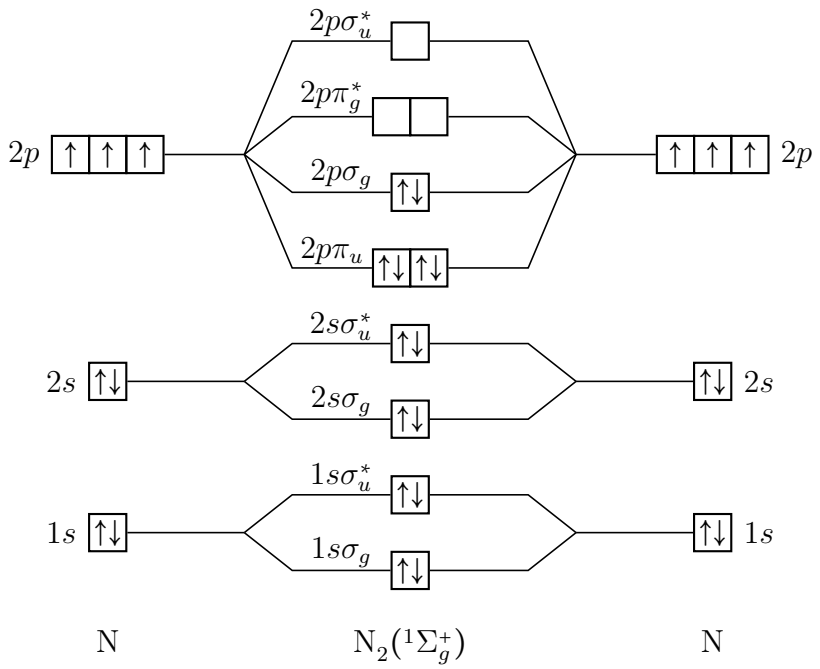

Figure 2.2: Molecular orbitals of N_2 as constructed from atomic nitrogen orbitals by means of the LCAO technique. Within the LCAO framework various different notation conventions for the designation of molecular orbitals have been established. In the above figure we employed a mixture of the styles used in Refs. [8] and [46]. Moreover, as usual, electrons with spin $\pm\frac{1}{2}$ are indicated by $\uparrow$ and $\downarrow$, respectively. Note that the σ-orbitals correspond to a magnetic quantum number of $m = 0$ whereas the π-orbitals are twofold degenerate in m involving $m = \pm 1$. Furthermore, the depicted occupation of the molecular orbitals represents the ground state $N_2(^1\Sigma_g^+)$.

passive spectators and focus exclusively on the active electronic states. As a result, the molecule reduces to a two-level system consisting of a ground state level "0" and an excited level "1" with energies ε_0 and ε_1. These levels mimic the active portions of the $2p\pi_u$ and $2p\pi_g^*$ orbitals (marked in red in Fig. 2.3) and can each carry exactly one electron. Hence, four different electronic configurations are possible each of them corresponding to one of the four different molecular states of the nitrogen molecule (see Fig. 2.4).

Note that the two-level system's parametrization, that means the value of the energies ε_0 and ε_1, depends on its occupation and, thus, on the particular molecular state (see Table A.3). For clearness we, therefore, attach an additional index $+$, g, $*$ or $-$ to these energies which denotes the value in the positive ion $N_2^+(^2\Pi_u)$, the ground state $N_2(^1\Sigma_g^+)$, the metastable state $N_2(^3\Sigma_u^+)$ and the negative ion $N_2^-(^2\Pi_g)$, respectively (see also Fig. 2.4). In our later analysis, however, only the energies of the occupied levels ε_{0g}, ε_{1*}, ε_{0-} and ε_{1-} will matter[3].

In addition, as seen from Fig. 2.3, the magnetic quantum numbers of the active orbitals are equal. Hence, the entire molecular two-level system possesses a single magnetic quantum number $m = \pm 1$ which enters our calculation as an initial parameter.

Exploiting the connection between our two-level system and the LCAO repre-

[3]Note that in our analysis of the positive ions $He^+(^2S_{1/2})$ and $Ar^+(^2P_{3/2})$ we will, for obvious reasons, label the active level's energy with ε_{0g} as well.

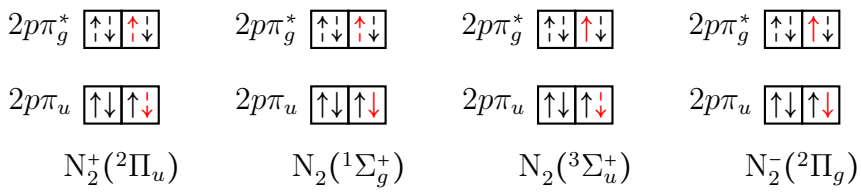

Figure 2.3: Occupation of the $2p\pi_u$ and $2p\pi_g^*$ orbitals in the different molecular states of nitrogen. Empty electronic states are indicated by the dashed arrows $\uparrow$ and $\downarrow$, respectively. Furthermore, electronic orbitals whose occupation has to be changed in order to switch between the depicted states of the molecule have been marked in red. Note that for the negative ion the depicted configuration is not the only possible arrangement. It does, however, emerge when an electron is attached to the metastable state which is the process under consideration in this work (see Eq. (1.1)).

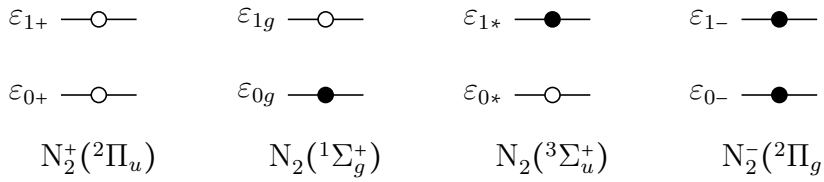

Figure 2.4: Effective two-level system and its relation to the different states of the nitrogen molecule. Occupied states are indicated by • whereas empty states are marked with ∘. Furthermore, ε_0 and ε_1 denote the energies of the levels 0 and 1 and the indices $+$, g, $*$ and $-$ characterize the respective molecular state.

sentation of the nitrogen molecule we can now calculate the wave functions of the ground state level $\Psi_{0m}^{(N_2)}$ and the excited level $\Psi_{1m}^{(N_2)}$ from the following combination of $2p$ atomic nitrogen wave functions

$$\Psi_{\nu m}^{(N_2)}(\vec{r}) = \frac{1}{\sqrt{N_\nu}}\left[\Psi_{21m}\left(\vec{r}+\frac{\varrho}{2}\right) + (-1)^\nu\,\Psi_{21m}\left(\vec{r}-\frac{\varrho}{2}\right)\right], \quad \nu = 0,1\,. \tag{2.31}$$

Here ν labels the respective level, ϱ denotes the bond length of the nitrogen molecule (see Appendix A) and N_ν represents a normalization constant. Employing (2.19) we then find the explicit form of the wave functions $\Psi_{\nu m}^{(N_2)}$ in Cartesian coordinates,

$$\begin{aligned}\Psi_{\nu m}^{(N_2)}(x,y,z) = -m\,\frac{(\kappa_{N_2})^{\frac{5}{2}}}{\sqrt{2\pi N_\nu}}\,(x+imy)\\ \times\left[e^{-\kappa_{N_2}\sqrt{x^2+y^2+\left(z+\frac{\varrho}{2}\right)^2}} + (-1)^\nu e^{-\kappa_{N_2}\sqrt{x^2+y^2+\left(z-\frac{\varrho}{2}\right)^2}}\right],\end{aligned} \tag{2.32}$$

which may also be expressed in cylindrical coordinates,

$$\begin{aligned}\Psi_{\nu m}^{(N_2)}(R,\varphi,z) = -m\,\frac{(\kappa_{N_2})^{\frac{5}{2}}}{\sqrt{2\pi N_\nu}}\,R\,e^{im\varphi}\\ \times\left[e^{-\kappa_{N_2}\sqrt{R^2+\left(z+\frac{\varrho}{2}\right)^2}} + (-1)^\nu e^{-\kappa_{N_2}\sqrt{R^2+\left(z-\frac{\varrho}{2}\right)^2}}\right].\end{aligned} \tag{2.33}$$

The constant κ_{N_2} appearing in (2.32) and (2.33) is given by

$$\kappa_{N_2} = \frac{Z_{\text{eff}}}{2a_B}\,, \tag{2.34}$$

and contains the effective nucleus charge number $Z_{\text{eff}} = 4$ which we have determined by fitting our hydrogen-like atomic nitrogen wave functions to the Roothaan-Hartree-Fock calculations of Clementi and Roetti[21].

Finally, the explicit values of the normalization constants N_ν can be calculated from the normalization integrals of the wave functions (2.31). In particular, we obtain

$$N_\nu = 2 + 2\,(\kappa_{\mathrm{N}_2})^5(-1)^\nu \int_0^\infty \mathrm{d}R \int_{-\infty}^\infty \mathrm{d}z\; R^3\, e^{-\kappa_{\mathrm{N}_2}\sqrt{R^2+\left(z+\frac{\varrho}{2}\right)^2}}\, e^{-\kappa_{\mathrm{N}_2}\sqrt{R^2+\left(z-\frac{\varrho}{2}\right)^2}}\,, \tag{2.35}$$

which needs to be evaluated numerically. Employing the parameters of Appendix A, a Monte Carlo integration of (2.35) yields

$$N_\nu = 2 + (-1)^\nu \cdot 0.53417540831\,, \tag{2.36}$$

with an error estimate of about 10^{-12}.

Having discussed our treatment of bound molecular states, we now turn to the continuum states which represent free states moving along with the molecule. These states are populated by electron emission from $\mathrm{N}_2^-(^2\Pi_g)$ and $\mathrm{N}_2(^3\Sigma_u^+)$ in the resonant and indirect Auger de-excitation channels (1.1) and (1.2), respectively. Generally the wave function of the emitted electron should carry the two-center character of the nitrogen molecule. This is especially true in the Auger reaction (1.2) since here the electron leaves a temporary positive charge behind. In this particular situation a description using plane waves would be utterly inappropriate as the latter reflect neither the two-center structure nor the temporary attractive charge. Instead we approximate the emitted electron's wave function by means of a two-center Coulomb wave. This special type of wave functions is based on a Pluvinage-like treatment[105] of the Schrödinger equation for an unbound electron moving in the field of two fixed centers. It was first introduced by Joulakian et al.[64] and has since been used successfully in the modeling of electron-impact ionization and photo-ionization of H_2 and H_2^+ molecules[135,136,144].

In particular, the two-center continuum wave function of an electron with the wave vector $\vec{q}$ moving in the field of two nuclear charges $Z_1\,e_0$ and $Z_2\,e_0$ reads[136]

$$\Psi_{\vec{q}}^{(\mathrm{N}_2)}(\vec{r}) = \frac{e^{i\vec{q}\cdot\vec{r}}}{(2\pi)^{\frac{3}{2}}}\, N_{Z_1}(q)\, C_{Z_1}(\vec{q},\vec{r}_1)\, N_{Z_2}(q)\, C_{Z_2}(\vec{q},\vec{r}_2)\,. \tag{2.37}$$

Here q stands for the absolute value of $\vec{q}$ and the vectors $\vec{r}_{1/2}$ represent the position vectors of the electron as seen from the two nuclear centers. Moreover, the functions $C_{Z_{1/2}}$ are defined by

$$C_Z(\vec{q},\vec{r}) = M\big(-i\delta, 1, -i[qr + \vec{q}\cdot\vec{r}]\big)\,, \tag{2.38}$$

where δ is shorthand for $Z/(q\,a_B)$ and M denotes the confluent hypergeometric function of the first kind. Finally, the normalization constants $N_{Z_{1/2}}$ can be calculated analytically and amount to

$$N_Z(q) = e^{\frac{\pi}{2}\delta}\,\Gamma(1+i\delta)\,, \tag{2.39}$$

with Γ representing the usual gamma function. Note that (2.39) is derived from a delta-function normalization condition. Hence, we can treat the $\vec{q}$-states as a true

continuum and don't have to introduce an artificial discretization like we did for the $\vec{k}$-states in Sec. 2.1. For the sake of visual consistency we will, however, still treat the $\vec{q}$-continuum as a discrete set on the level of the Hamiltonian. Consequently, the self-energies of our quantum-kinetic calculation (see Chapter 3) will involve discrete sums over $\vec{q}$. This fits in nicely with our notation for continuum states within the surface and is not an issue as long as we remember that any sum over $\vec{q}$-states can be replaced by an integral,

$$\sum_{\vec{q}} \ldots \longleftrightarrow \int \mathrm{d}\vec{q} \ \ldots \ . \tag{2.40}$$

We will now explicitly discuss the use of the two-center Coulomb wave (2.37) for the description of the emitted electron in the de-excitation channels (1.1) and (1.2). During the indirect Auger de-excitation reaction (1.2), in particular, the released electron departs from a neutral molecule. Consequently, a single positive charge is left behind. The latter is temporary since at the same time the molecule emits the electron from the excited level it captures a surface electron into its ground state level. Even so, the temporary charge will affect the emitted electron's wave function in the moment of emission. Therefore, as proposed in Ref. [135], we account for the partial screening of the nuclei by the passive electrons and choose $Z_1 = Z_2 = Z_C$ with $Z_C = \frac{1}{2}$.

In the resonant de-excitation channel (1.1), on the other hand, the departing electron leaves a neutral molecule behind. As a result, the residual charge numbers Z_1 and Z_2 vanish. In this case the two-center Coulomb wave (2.37) reduces to the plane wave

$$\Psi_{\vec{q}}^{(\mathrm{N}_2)}(\vec{r}) = \frac{e^{i\vec{q}\cdot\vec{r}}}{(2\pi)^{\frac{3}{2}}} \ . \tag{2.41}$$

We stress that here a plane wave description is appropriate since beyond a certain distance the emitted electron should not feel any nuclear charge. We will, however, only use the wave function (2.41) in the description of the surface-induced electron emission from $\mathrm{N}_2^-(^2\Pi_g)$. For the electron release due to the natural decay of $\mathrm{N}_2^-(^2\Pi_g)$, on the other hand, a corresponding matrix element cannot easily be constructed within the limits of our effective model. Therefore, we will manually incorporate the natural decay into the semi-classical rate equation system derived in Sec. 3.3. This requires knowledge of the natural decay rate and the associated line shape both of which will be discussed in the following.

First of all, the rate of natural decay Γ_n can be obtained from the negative ion's mean natural lifetime $\tau_n = 1.6\,\mathrm{fs}$[24] which implies that $\Gamma_n = \tau_n^{-1} = 0.625\,\mathrm{fs}^{-1}$. In addition, for the line shape of the auto-decay reaction Lorente et al.[82] have proposed the usage of a Lorentzian function, also known as Breit-Wigner distribution. In accordance with this approach we introduce the spectral decay rate $\varrho_n(\varepsilon_{\vec{q}}^{\infty})$ through

$$\varrho_n(\varepsilon_{\vec{q}}^{\infty}) = \frac{\delta_n}{2\pi\tau_n} \frac{1}{(\varepsilon_{\vec{q}}^{\infty} - \varepsilon_{1-}^{\infty})^2 + \frac{\delta_n^2}{4}} \ . \tag{2.42}$$

Here $\varepsilon_{\vec{q}}^{\infty}$ and $\varepsilon_{1-}^{\infty}$ denote the energies of a molecular continuum state $\vec{q}$ and the excited molecular level of $\mathrm{N}_2^-(^2\Pi_g)$ at an infinite distance from the surface. As we will see in Sec. 2.2.4, the image shifts of these states cancel exactly and, hence, do not enter ϱ_n.

Moreover, in (2.42) δ_n is the line's full width at half maximum and can be estimated using Heisenberg's uncertainty relation

$$\delta_n \gtrsim \frac{h}{\tau_n} \,. \tag{2.43}$$

The natural decay rate Γ_n then relates to ϱ_n via

$$\Gamma_n = \int_{-\infty}^{\infty} \mathrm{d}\varepsilon_{\bar{q}}^{\infty}\ \varrho_n(\varepsilon_{\bar{q}}^{\infty}) = \frac{1}{\tau_n} = 0.625\,\mathrm{fs}^{-1} \,. \tag{2.44}$$

Note that in order to account for the possible trapping of emitted electrons in the image potential in front of the surface, the line shape (2.42) needs to be multiplied by a surface transmission function. As will be explained in Sec. 2.6, this turns the decay rate's spectrum and with it the decay rate itself into time-dependent quantities.

2.2.4 Image Shift of Projectile Levels

After our investigation of the projectile wave functions in the previous sections we now turn to the variation of the associated energy levels during the surface reactions. In general, when an atomic or molecular particle approaches a metallic or dielectric surface its electronic levels are displaced due to image interactions between charges on the projectile and in the surface. Thus, in the scattering processes considered here the energies of projectile electrons exhibit a z-dependence which by way of the projectile trajectory turns into a time dependence.

For the projectile's continuum states, in particular, the energy variation is trivial since these states represent free electrons. Hence, their overall energy $\varepsilon_{\bar{q}}(z)$ obviously follows the image potential which here and in the following we approximate by the truncated classical form $V_i(z)$ given by (2.14). As a result we find

$$\varepsilon_{\bar{q}}(z) = \varepsilon_{\bar{q}}^{\infty} + V_i(z) \,. \tag{2.45}$$

For bound projectile electrons, on the other hand, things are a little more involved. In Sec. 2.4 we will see how these level shifts could be calculated from a matrix element involving electronic as well as nuclear image charges. However, since in this work we are considering the case of low kinetic energies, there is a more easy way of obtaining the level shifts. For this purpose we consider an occupied energy level ε_n of a neutral or singly charged projectile located at a distance z from the surface. Following the ideas of Newns et al.[101] we can estimate the level's effective ionization energy $\varepsilon_n(z)$ by considering the overall projectile energy change under three virtual operations.

1. **Move the projectile from the position z to infinity.**
   For neutral projectiles no energy change is associated with this step. When, on the other hand, the projectile carries a single charge, its overall energy at the position z from the surface is lowered by the value of the image potential at this location. Since the latter vanishes at infinity, the relocation causes the overall projectile energy to change by $-V_i(z)$.

2. **Ionize the bound electron to the vacuum level.**
   Since the projectile is infinitely far away from the surface, the level is at its unperturbed value ε_n^{∞}. Consequently, the ionization results in an overall projectile energy change of $-\varepsilon_n^{\infty}$.

3. **Bring the resulting projectile back to the initial position z.**
   This step introduces an energy change of $V_i(z)$ when the ionized projectile carries a single charge. If, however, the ionization led to a neutral projectile, no change of energy is connected with this step.

The value of ε_n at the position z is then given by the negative of the sum of these energy changes. Adding up the effects for an occupied level of a singly charged negative ion we obtain

$$\varepsilon_n(z) = -\Big[\underbrace{-V_i(z)}_{\text{Relocation to infinity}} + \overbrace{\left(-\varepsilon_n^\infty\right)}^{\text{Ionization at infinity}} + \underbrace{0}_{\text{Relocation to } z}\Big] = \varepsilon_n^\infty + V_i(z)\ . \tag{2.46}$$

Thus, the level ε_n shifts downwards upon approaching the surface. On the contrary, for a neutral projectile we find

$$\varepsilon_n(z) = -\Big[\underbrace{0}_{\text{Relocation to infinity}} + \overbrace{\left(-\varepsilon_n^\infty\right)}^{\text{Ionization at infinity}} + \underbrace{V_i(z)}_{\text{Relocation to } z}\Big] = \varepsilon_n^\infty - V_i(z)\ . \tag{2.47}$$

Consequently, the level moves upwards as the projectile gets closer to the surface.

We stress that the procedure presented here is independent of the specific projectile level. Thus, we conclude that upon approaching the surface all of the ionization levels of a negative ion like $N_2^-(^2\Pi_g)$ shift downwards due to (2.46). Similarly, according to (2.47) for neutral projectiles like $He(^1S_0)$, $Ar(^1S_0)$ and $N_2(^1\Sigma_g^+)$ each and any of the ionization levels are shifted upwards as the projectile approaches the surface. In terms of the previously introduced projectile energies ε_{0g}, ε_{1*}, ε_{0-} and ε_{1-} we, thus, find

$$\begin{aligned} \varepsilon_{0g}(z) &= \varepsilon_{0g}^\infty - V_i(z)\ , \quad \varepsilon_{1*}(z) = \varepsilon_{1*}^\infty - V_i(z)\ , \\ \varepsilon_{0-}(z) &= \varepsilon_{0-}^\infty + V_i(z)\ , \quad \varepsilon_{1-}(z) = \varepsilon_{1-}^\infty + V_i(z)\ . \end{aligned} \tag{2.48}$$

Finally, the reader may note that the shift of the ionization energies does not correspond to an actual energy change of the projectile. The ionization levels are defined solely in terms of the removal of an electron from the molecule and, hence, do not imply an energy change for a bound electron.

2.3 Projectile Trajectory

In the theoretical description of charge exchange during surface collisions of atomic and molecular projectiles one usually employs the trajectory approximation (see for instance Refs. [13, 56, 90, 143]). In particular, this means that the projectile motion is decoupled from the dynamics of the system and one supplies its trajectory externally. This approach completely ignores any feedback between the electronic degrees of freedom and the projectile motion[90]. Consequently, it is an adequate approximation only if the projectile mass is much larger than the electronic mass[13]. Hence, the trajectory approximation would for instance not be suitable to describe the scattering of a single electron from a surface. For the case of atomic and molecular projectiles, however, the overall projectile mass is in general at least three orders

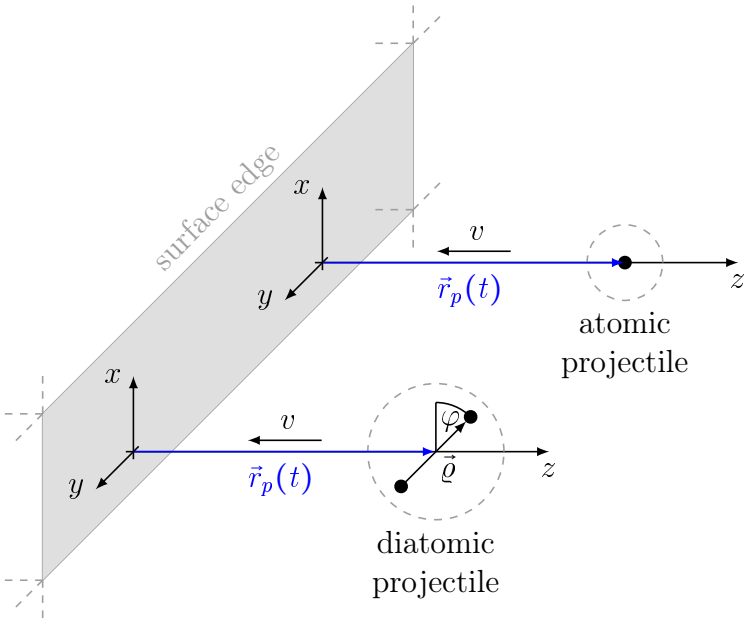

Figure 2.5: Schematic illustration of the collision geometry for atomic and diatomic projectiles. Here $\vec{r}_p$ denotes the projectile's center of mass and v represents its velocity. Moreover, for the diatomic case ϱ denotes the molecule's bond length and φ is the angle between the z-axis of the molecular reference frame and the surface. Note that the corresponding angle for atomic particles is not shown in order not to overload the drawing. In addition, the orientation of the projectile reference frame can be expected to play a minor part for mononuclear particles.

of magnitude larger than the mass of an electron. Therefore, the trajectory approximation is valid in these cases and will, thus, be employed in this work. In the following we will describe our particular choice for the projectile trajectory.

For simplicity we assume a classical trajectory. The projectile may start its motion at $t = -\infty$ and reach the turning point of its trajectory at $t = 0$. Moreover, it may approach the surface under normal incidence and with constant velocity v. Upon reaching the turning point z_0 the projectile then bounces off the surface and its motion is reversed instantly. Under these conditions the trajectory of the projectile's center of mass $\vec{r}_p$ can be described by

$$\vec{r}_p(t) = z_p(t)\,\vec{e}_z = \left(v\,|t| + z_0\right)\vec{e}_z \;, \tag{2.49}$$

where $\vec{e}_z$ is the unit vector in z direction.

In addition to this translative motion we also have to consider the orientation of the projectile axis, constituting the z-axis of the projectile's reference frame, with respect to the surface. In particular, it is sufficient to only consider rotations of the projectile about one specific< axis in the x-y-plane due to the translational symmetry of the solid surface in this plane. Here, without loss of generality, we choose the y-axis. Moreover, to simplify our analysis we assume the projectile axis to stay fixed throughout the scattering process, thus, neglecting any rotational excitations of the projectile. Hence, we can encapsulate the projectile orientation in the angle φ which measures the constant rotation of the projectile axis around the laboratory y-axis. The consequential overall geometry of the surface collision process is shown in Fig. 2.5.

Let us now turn to the turning point z_0. Since the center of mass trajectory is classical, z_0 can be determined by considering the motion of the projectile in the projectile-surface interaction potential V_{ps} for a given initial kinetic energy ε_{kin}. The latter relates to the projectile velocity v via

$$\varepsilon_{\text{kin}} = \frac{M_p}{2} v^2 \,, \tag{2.50}$$

where M_p is the projectile mass (see Appendix A). In particular, assuming the projectile's total energy to stay fixed during the scattering process[4] the turning point can be obtained by solving

$$V_{ps}(z_0) \stackrel{!}{=} \varepsilon_{\text{kin}} \,, \tag{2.51}$$

for z_0. This requires us first to concretize the projectile-surface interaction potential V_{ps}. In the range of low kinetic energies ($\varepsilon_{\text{kin}} \leq 1\text{eV}$) the latter is usually approximated by the Morse-type potential[13]

$$V_{ps}(z) = d\left[1 - e^{-a(z-z_e)}\right]^2 - d \,, \tag{2.52}$$

with material parameters d, a and z_e (see Appendix A). In general, these parameters are specific to both the projectile and the surface material. However, at least for nitrogen colliding with metallic surfaces it is claimed that the respective values are not very specific to the surface material[68]. For simplicity we, thus, assume that the parameters of (2.52) are only specific to the projectile material. Hence, the values listed in Appendix A are valid for arbitrary metallic and dielectric surfaces. We stress that this approximation is necessary due to a lack of consistent data for projectile turning points on different surface materials. However, this does not restrict the universality of our model since the turning only enters our calculations as a parameter and may, thus, be exchanged at any time.

Employing the Morse potential (2.52) we can now explicitly solve (2.51) for the turning point which yields

$$z_0 = z_e - \frac{1}{a} \ln\left(1 + \sqrt{1 + \frac{\varepsilon_{\text{kin}}}{d}}\right) \,. \tag{2.53}$$

Figure 2.6 shows the variation of z_0 over ε_{kin} as calculated from for the three different projectile materials considered in this work. As we see, for N_2 the turning point remains practically constant within the depicted range of kinetic energies. For He and Ar, on the other hand, the values of z_0 decrease significantly as the projectile's kinetic energy rises. In total, with values ranging significantly above $3\,a_B$ for kinetic energies below 0.1 eV, the turning point seems to be rather large for all of the three projectile substances.

Note that in addition to the z_0-values emerging from (2.53), for the neutralization of $He^+(^2S_{1/2})$ we will also consider the turning point $z_0 = 1.2 \cdot 10^{-10}\,\text{m} \approx 2.27\,a_B$ proposed by Modinos and Easa[96] for $\varepsilon_{\text{kin}} = 50\,\text{meV}$. This value significantly deviates from the turning point $z_0 \approx 3.6\,a_B$ calculated from the Morse potential (2.52) using

[4] Note that the effect of surface reactions proceeding at the expense of the projectile's kinetic energy can be neglected since here we focus on the case of slow projectiles ($\varepsilon_{\text{kin}} \leq 1\text{eV}$). Hence, the projectile's kinetic energy is significantly smaller than the energies of electrons involved in the surface reactions studied in this work.

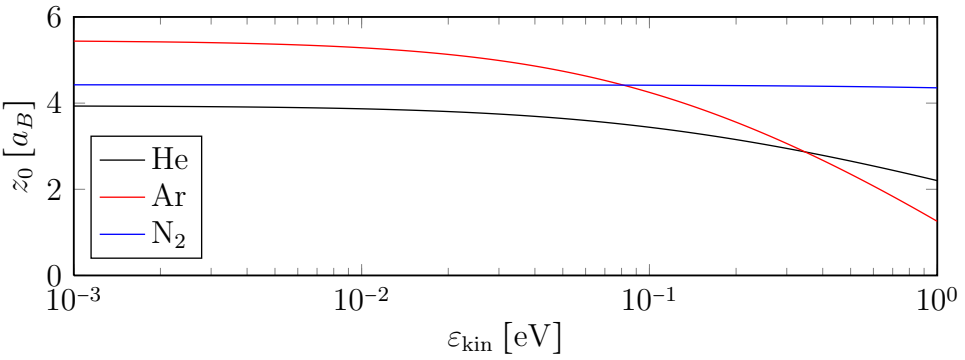

Figure 2.6: Variation of the turning point z_0 with the projectile's kinetic energy $\varepsilon_{\mathrm{kin}}$ for He, Ar and N_2. The values of z_0 were calculated from the Morse potential (2.52) by means of (2.53) using the parameters listed in Appendix A.

the parameters of Bonini et al.[13] for the metastable state of helium at the same kinetic energy (see Fig. 2.6). As will be shown in Chapter 5, this discrepancy in the turning point leads to a significant difference in the efficiency of the neutralization process.

Finally, we stress that the trajectory (2.49) is particularly handy and allows for an analytical evaluation of some of the time integrals occurring in our quantum-kinetic calculation (see for instance Sec. 4.1.2). Moreover, as we will see in Sec. 2.4, the trajectory only enters the Hamiltonian as a parameter determining the time dependence of the matrix elements. Thus, at the cost of sacrificing numerical performance our model allows for the inclusion of a more realistic, and hence more complicated, trajectory as well. This feature is a direct consequence of the trajectory approximation.

2.4 Hamiltonian

As pointed out earlier, we aim at constructing an effective model of the surface reactions discussed in Sec. 1.2. One important step towards achieving this objective was discussed in Sec. 2.3. Here we showed how the projectile's motion can be approximated by an externally supplied trajectory. This so called trajectory approximation allows us to separate the dynamics of the projectile nuclei from the rest of the system. As a result, the nuclei coordinates only enter the Hamiltonian parametrically and we can omit any interaction terms operating exclusively on the projectile's cores. Furthermore, instead of considering the full many-electron Hamiltonian we will restrict our analysis to those electrons which are actively participating in the charge transfer reactions we are studying. Since there are at most two electrons engaging in these reactions, we only consider two active electrons in our model. All of the remaining passive electrons are assumed to act as frozen spectators generating effective interaction potentials for the active electrons. As we saw in Secs. 2.1 and 2.2, on the solid side this leads to an effective bulk potential describing the solid's energy bands while on the projectile side this results in effective nucleus charges.

We will now outline the general procedure for deriving the Hamiltonian from the aforementioned assumptions. For the case of an atomic projectile a similar analysis has been presented by Gadzuk[30]. Here we adapt this approach to the case of a general multi-core projectile.

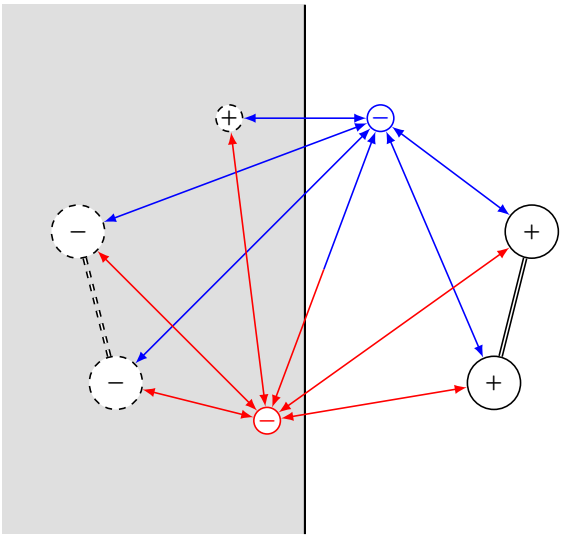

Figure 2.7: Exemplary distribution of actual (solid circles) and image (dashed circles) charges for a neutral diatomic molecule in front of a metallic or dielectric surface. The solid is located on the left-hand side and positive and negative charges have been marked with + and −, respectively. In the depicted situation the blue electron belongs to the projectile and resides outside the surface while the red electron occupies a band state inside the solid. The latter electron does, thus, not generate an image charge by itself. On the projectile side the positive nucleus charges result from the screening of the actual core charges by the passive electrons on the projectile. The relevant interactions between the electrons and the various real and image charges are marked with arrow lines.

In particular, to obtain the Hamiltonian we need to consider the interplay of the various real and image charges within the system. As shown by Gadzuk[30], we can, however, neglect interactions between image charges inside the surface. His argument is that these correlations should serve to shift the band states as a result of the external charges. Since the band represents a continuum of states all of these are shifted and, consequently, in case of an occupied band the resulting energy shift for a single state is negligible. Moreover, we also omit any forces acting on the projectile's nuclei as the nucleus motion has already been fixed by the trajectory approximation. Altogether, we, thus, only have to consider interactions pertaining to the two involved real electrons, as shown in Fig. 2.7 for the exemplary situation of a diatomic projectile. For the general case of a projectile with n_p nuclear centers the total Hamiltonian in position space representation reads (see also Ref. [58])

$$\hat{H}(\vec{r}_1, \vec{r}_2, t) = \sum_{\nu=1}^{2} \left[\hat{T}(\vec{r}_\nu) + \hat{H}_s(\vec{r}_\nu) + \hat{H}_p(\vec{r}_\nu, t) + \hat{H}_i(\vec{r}_\nu, t) \right] + \hat{H}_{ee}(\vec{r}_1, \vec{r}_2) \; . \tag{2.54}$$

Here $\hat{T}$ is the operator of kinetic energy,

$$\hat{T}(\vec{r}) = -\frac{\hbar^2}{2m_e} \nabla_{\vec{r}} \; , \tag{2.55}$$

and $\hat{H}_s(\vec{r}_\nu)$ contains the constant bulk potential within the solid,

$$\hat{H}_s(\vec{r}) = \Theta(-z)\, V_0 \; . \tag{2.56}$$

Moreover, $\hat{H}_p$ embraces the Coulomb interactions between the electrons and the projectile's nuclei,

$$\hat{H}_p(\vec{r},t) = -\sum_{j=1}^{n_p} \hat{V}_C^{Z_j}\left(\vec{r} - \vec{r}_{p_j}(t)\right) , \tag{2.57}$$

while $\hat{H}_i$ accounts for the electronic self-image interaction as well as the Coulomb interactions between the electrons and the images of the projectile's core charges,

$$\hat{H}_i(\vec{r},t) = \hat{V}_i(\vec{r}) + \sum_{j=1}^{n_p} \hat{V}_C^{Z_j}\left(\vec{r} - \vec{r}\,'_{p_j}(t)\right) . \tag{2.58}$$

Here and in the following a primed position vector $\vec{r}\,'$ marks the location of an image charge associated with a real charge at the position $\vec{r}$,

$$\vec{r}\,' = \vec{r} - 2\left(\vec{r}\cdot\vec{e}_z\right)\vec{e}_z , \tag{2.59}$$

and $\hat{V}_C^Z$ denotes the screened Coulomb potential of an electron in the field of Z-fold negative charge,

$$\hat{V}_C^Z(\vec{r}) = \frac{Ze_0^2}{4\pi\varepsilon_0\varepsilon_r(\vec{r})}\frac{e^{-\kappa(\vec{r})|\vec{r}|}}{|\vec{r}|} . \tag{2.60}$$

In (2.60) ε_r and κ label the static dielectric and screening constant both of which may depend on the positions of the interacting particles. Furthermore, in (2.58) the expression $\hat{V}_i$ represents the truncated classical self-image potential (2.14). Finally, the last term of (2.54), $\hat{H}_{ee}$, consists of the mutual Coulomb interactions between the two electrons and their images,

$$\hat{H}_{ee}(\vec{r}_1,\vec{r}_2) = \hat{V}_C(\vec{r}_1 - \vec{r}_2) - \hat{V}_C(\vec{r}_1 - \vec{r}\,'_2) - \hat{V}_C(\vec{r}\,'_1 - \vec{r}_2) , \tag{2.61}$$

where $\hat{V}_C$ is shorthand for $\hat{V}_C^1$ and the interaction between the images themselves has been neglected in accordance with Gadzuk's[30] aforementioned argument.

As pointed out earlier, the usage of the truncated classical self-image potential (2.14) is an approximation since in reality the image potential will gradually blend into the constant bulk potential. A better description would be given by the aforementioned Jones-Jennings-Jepsen potential[63] (see Eq. (2.17)). However, as noted at the end of Sec. 2.1, the latter potential involves additional material specific parameters and is not easily handled in an analytical or numerical treatment. Moreover, Kürpick and Thumm[72] have investigated various surface potential models and their influence on the matrix elements occurring in the interaction of hydrogenic levels with a metallic surface. Their results indicate that the truncated image potential is a reasonable approximation although the Jones-Jennings-Jepsen potential[63] yields better results in certain situations. Therefore, we stick with the truncated image potential (2.14) at this point. Note that for the dielectric surface materials considered in this work reliable values for the position of the image plane z_i were note available. We, therefore, assumed $z_i = 0$ for these situations.

In order to prepare the Hamiltonian (2.54) for a quantum-kinetic treatment, we now switch to the second quantization representation. For this purpose we assume that a basis of the Hilbert space can be formed by combining the states within the isolated solid $|\vec{k}\rangle$ and the bound and continuum states of the isolated projectile $|n\rangle$ into a set. Such a set represents a basis only when it fulfills the usual conditions of completeness and orthogonality. The former is not a problem as any arbitrary

state of the combined system may be constructed by a linear combination of $|\vec{k}\rangle$- and $|n\rangle$-states (see also Ref. [31]). The orthogonality condition, on the other hand, is in general not fulfilled exactly since the scalar product $\langle\vec{k}|n\rangle$ is non-vanishing in most cases. One might, however, argue that when the projectile's turning point is far enough outside the surface, the overlap of solid and projectile wave function is negligible and, hence, they may be considered orthogonal. This is also true if $\vec{k}$ and n pertain to continuum states as the asymptotic form of the projectile's continuum wave functions is a plane wave.

On the other hand, if the projectile's turning point is close enough to the surface the orthogonality approximation breaks down. In such situations orthogonality could for instance be enforced by subtracting the non-orthogonal component from the solid's states (see Ref. [18]),

$$|\vec{k}\rangle = |\vec{k}_0\rangle - \sum_n \langle n|\vec{k}_0\rangle |n\rangle \,. \tag{2.62}$$

Here $|\vec{k}_0\rangle$ denotes a state of the unperturbed surface and $|\vec{k}\rangle$ is an orthogonalized surface state. Since in this work we are considering the case of low kinetic energies resulting in a distant turning point (see Fig. 2.6), we can, however, safely stick with the orthogonality assumption.

We now calculate the second quantized version of (2.54) by employing the usual rules for one- and two-particle operators (see for instance Ref. [117]). We start with the one-particle terms which we collect in a quantity $\hat{H}_1$,

$$\hat{H}_1 = \sum_{b_1,b_2} \langle b_1|\, \hat{T} + \hat{H}_s + \hat{H}_p + \hat{H}_i\, |b_2\rangle\, c^\dagger_{b_1} c_{b_2} \,. \tag{2.63}$$

Here b_1 and b_2 run over all the states within the set $\{|\vec{k}\rangle, |n\rangle\}$. Making use of the Schrödinger equations of the isolated surface and projectile systems,

$$\left(\hat{T} + \hat{H}_s\right)|\vec{k}\rangle = \varepsilon_{\vec{k}}\, |\vec{k}\rangle \,, \tag{2.64a}$$

$$\left(\hat{T} + \hat{H}_p\right)|n\rangle = \varepsilon^\infty_n\, |n\rangle \,, \tag{2.64b}$$

Equation (2.63) turns into

$$\begin{aligned}\hat{H}_1 = &\sum_{\vec{k}} \varepsilon_{\vec{k}}\, c^\dagger_{\vec{k}}\, c_{\vec{k}} + \sum_n \varepsilon^\infty_n\, c^\dagger_n\, c_n + \sum_{n,n'} \langle n|\, \hat{H}_s + \hat{H}_i\, |n'\rangle\, c^\dagger_n\, c_{n'} \\ &+ \sum_{\vec{k},n} \left[\langle\vec{k}|\, \hat{T} + \hat{H}_s + \hat{H}_i + \hat{H}_p\, |n\rangle\, c^\dagger_{\vec{k}} c_n + \text{H.c.}\right] ,\end{aligned} \tag{2.65}$$

where we have neglected internal couplings between states inside the solid surface due to the aforementioned argument of Gadzuk[30]. In Eq. (2.65) the diagonal terms $\sum_{\vec{k}} \varepsilon_{\vec{k}}\, c^\dagger_{\vec{k}}\, c_{\vec{k}}$ and $\sum_n \varepsilon^\infty_n\, c^\dagger_n\, c_n$ describe unperturbed states within the solid and on the projectile, respectively. Moreover, the diagonal components of the matrix element $\langle n|\, \hat{H}_s + \hat{H}_i\, |n'\rangle$ represent the image shifts of projectile states in front of the surface. Hence, the effective energy of a projectile level n amounts to

$$\varepsilon_n(t) = \varepsilon^\infty_n + \langle n|\, \hat{H}_s + \hat{H}_i\, |n\rangle \,. \tag{2.66}$$

Here the time dependence of ε_n stems from the motion of the projectile with respect to the surface which results in time-dependent projectile wave functions. Note that

while we could use (2.66) to calculate the variation of the projectile levels along the trajectory, in this work we will rather employ the procedure introduced in Sec. 2.2.4 as it offers an easy-to-use approximate approach that is valid due to the distant turning point of the projectile. In total the diagonal component of $\hat{H}_1$ reads

$$\sum_{\vec{k}} \varepsilon_{\vec{k}}\, c_{\vec{k}}^{\dagger}\, c_{\vec{k}} + \varepsilon_0(t)\, c_0^{\dagger}\, c_0 + \varepsilon_1(t)\, c_1^{\dagger}\, c_1 + \sum_{\vec{q}} \varepsilon_{\vec{q}}(t)\, c_{\vec{q}}^{\dagger}\, c_{\vec{q}}\,, \tag{2.67}$$

where we have split up the projectile states n into the bound states 0 and 1, pertaining to our two-level system, and the continuum states $\vec{q}$.

We now consider the non-diagonal components of $\langle n|\, \hat{H}_s + \hat{H}_i\, |n'\rangle$. These terms describe the resonant tunneling between two different projectile states. Due to the strong effect of energy conservation, such a transition is only efficient when the two levels are degenerate. For the surface reactions under consideration in the present work this is only the case for the second step of the two-step resonant de-excitation of $N_2(^3\Sigma_u^+)$ consisting of the decay of the $N_2^-(^2\Pi_g)$ ion (see Eq. (1.1)). Here an electron resonantly tunnels between the excited state of our molecular two-level system $|1\rangle$ and a projectile continuum state $|\vec{q}\rangle$. Consequently, in any other case this interaction term can be neglected and we only retain

$$\sum_{\vec{q}} \Big[\underbrace{\langle \vec{q}|\, \hat{H}_s + \hat{H}_i\, |1\rangle}_{V_{\vec{q}}(t)}\, c_{\vec{q}}^{\dagger}\, c_1 + \text{H.c.} \Big]\,, \tag{2.68}$$

where the time dependence of the tunneling matrix element $V_{\vec{q}}(t)$ again is a consequence of the projectile motion. Note that (2.68) only describes the electron emission due to the surface-induced decay of $N_2^-(^2\Pi_g)$ since clearly the matrix element $V_{\vec{q}}$ merely involves interactions introduced by the presence of the surface but not the internal correlations of the negative ion. In principle the natural decay of $N_2^-(^2\Pi_g)$ could be described by an analogous term with a different matrix element. However, as mentioned in Sec. 2.2.3, we will not follow this track here as a corresponding matrix element cannot easily be derived within the limits of our effective model. Instead the natural decay reaction will be manually incorporated into our description in Sec. 3.3.

Further inspection of (2.65) draws our attention to the hybridization term between $|\vec{k}\rangle$- and $|n\rangle$-states which represents the resonant tunneling of electrons between the surface and the projectile. This expression can describe the resonant electron capture subreaction of the two-step resonant de-excitation of $N_2(^3\Sigma_u^+)$ (see Eq. (1.1)) as well as the resonant neutralization of a positive ion (see Eq. (1.5)). The associated matrix element $\langle \vec{k}|\, \hat{T} + \hat{H}_s + \hat{H}_i + \hat{H}_p\, |n\rangle$ can be further simplified by employing the orthogonality assumption of solid and projectile states together with either (2.64a) or (2.64b). This results in two different tunneling matrix elements involving either $\hat{H}_p$ and $\hat{H}_i$ or $\hat{H}_s$ and $\hat{H}_i$. As outlined in Ref. [31], the former one is preferable because it properly accounts for the orthogonality requirements within the limits of our approximation. Moreover, since we are only interested in the resonant electron tunneling between the projectile's ground state level $|0\rangle$ and surface states $|\vec{k}\rangle$, we strip out the remaining transitions keeping only the term

$$\sum_{\vec{k}} \Big[\underbrace{\langle \vec{k}|\, \hat{H}_p + \hat{H}_i\, |0\rangle}_{V_{\vec{k}}(t)}\, c_{\vec{k}}^{\dagger} c_0 + \text{H.c.} \Big]\,. \tag{2.69}$$

Here $V_{\vec{k}}(t)$ is the matrix element connected with the electron capture subreaction of the resonant de-excitation channel (1.1) and the resonant neutralization channel (1.5). Its time dependence once more follows from the motion of the projectile.

We now proceed with the two-particle term which we encapsulate in the operator $\hat{H}_{12}$,

$$\hat{H}_{12} = \sum_{b_1,b_2,b_3,b_4} \left\langle b_1\, b_2 \right| \hat{H}_{ee} \left| b_3\, b_4 \right\rangle c^\dagger_{b_1} c^\dagger_{b_2} c_{b_4} c_{b_3} \ . \tag{2.70}$$

Here the b_i-states ($i = 1, \ldots, 4$) again run over the entire set $\{|\vec{k}\rangle, |n\rangle\}$. Expansion of the series in (2.70) results in a vast number of terms most of which are not meaningful to us because either the transitions are energetically blocked or they are not relevant for the surface reactions we are interested in. Consequently, we only extract those expressions that describe the specific two-particle Auger transitions studied in this work (see Sec. 1.2). In particular, these are the direct Auger de-excitation term (see Eq. (1.3)),

$$\sum_{\vec{k},\vec{k}'} \Big[\underbrace{\left\langle 0\, \vec{k}' \right| \hat{H}_{ee} \left| 1\, \vec{k} \right\rangle}_{V_{\vec{k}\vec{k}'}(t)} c^\dagger_0 c_1 c^\dagger_{\vec{k}'} c_{\vec{k}} + \text{H.c.} \Big] , \tag{2.71}$$

the indirect Auger de-excitation term (see Eq. (1.2)),

$$\sum_{\vec{k},\vec{q}} \Big[\underbrace{\left\langle 0\, \vec{q} \right| \hat{H}_{ee} \left| \vec{k}\, 1 \right\rangle}_{V_{\vec{k}\vec{q}}(t)} c^\dagger_0 c_{\vec{k}} c^\dagger_{\vec{q}} c_1 + \text{H.c.} \Big] , \tag{2.72}$$

and the Auger neutralization term (see Eq. (1.4)),

$$\sum_{\vec{k}_1,\vec{k}_2,\vec{k}'} \Big[\underbrace{\left\langle 0\, \vec{k}' \right| \hat{H}_{ee} \left| \vec{k}_1\, \vec{k}_2 \right\rangle}_{V_{\vec{k}_1\vec{k}_2\vec{k}'}(t)} c^\dagger_0 c_{\vec{k}_1} c^\dagger_{\vec{k}'} c_{\vec{k}_2} + \text{H.c.} \Big] . \tag{2.73}$$

Here $V_{\vec{k}\vec{k}'}(t)$, $V_{\vec{k}\vec{q}}(t)$ and $V_{\vec{k}_1\vec{k}_2\vec{k}'}(t)$ are the associated Auger matrix elements. Since all of these involve states on the projectile and in the surface, they vary in time as the projectile moves along its trajectory.

The full Hamiltonian can now be obtained by adding the one- and two-particle operators $\hat{H}_1$ and $\hat{H}_{12}$. In particular, this involves the diagonal component (2.67), the hybridization terms (2.68) and (2.69) as well as the Auger terms (2.71), (2.72) and (2.73). The resulting Hamiltonian is of the generalized Anderson-Newns type[90] and can be used to analyze the Auger de-excitation reactions (1.2) and (1.3) as well as the Auger and resonant neutralization channels (1.4) and (1.5). It is, however, not capable of describing the two-step resonant de-excitation reaction (1.1) and its interaction with the Auger de-excitation channels (1.2) and (1.3) due to two reasons. For one thing, the Hamiltonian does not involve couplings between the subprocesses of (1.1), the resonant electron capture and the resonant electron emission, since these transitions involve different projectile levels (see Eqs. (2.68) and (2.69)). Hence, there is no way to restrict the electron emission from one level to only proceed after an electron has been captured into the other. For another thing, the Hamiltonian completely neglects Coulomb correlations between the active and passive electrons on the projectile. Inclusion of this effect is, however, required to describe the different parametrizations of the projectile level energies and to account for the energy that is picked up or released by the passive electrons during the resonant reaction (1.1).

These issues render the Hamiltonian inappropriate for the description of the resonant de-excitation channel (1.1) and its coupling to the Auger reactions (1.2) and (1.3) and call for a manual extension of our model. In the following section we will explain how this can be achieved by means of a projection operator approach leading to a pseudo-particle representation.

2.5 Pseudo-Particle Representation

We will now focus on the description of the de-excitation reactions (1.1), (1.2) and (1.3) building upon the Hamiltonian derived in the previous section. As explained earlier, the projectile level energies ε_0 and ε_1 depend on the particular occupation of the projectile levels n_0 and n_1 (see Sec. 2.2.3). The same also applies to the surface reactions themselves. The electron capture subreaction of (1.1) and its reverse, on the one hand, should only act on the configurations $(n_0, n_1) = (0, 1)$ and $(n_0, n_1) = (1, 1)$ representing the metastable state $N_2(^3\Sigma_u^+)$ and the negative ion $N_2^-(^2\Pi_g)$, respectively. On the other hand, the electron emission subchannel of (1.1) and the associated opposite reaction should only be effective for the situations $(n_0, n_1) = (1, 1)$ and $(n_0, n_1) = (1, 0)$ corresponding to the negative ion $N_2^-(^2\Pi_g)$ and the ground state $N_2(^1\Sigma_g^+)$, respectively. Finally, the Auger de-excitation channels (1.2) and (1.3) and their inverse reactions should only be active for the occupations $(n_0, n_1) = (0, 1)$ and $(n_0, n_1) = (1, 0)$ which stand for the metastable molecule $N_2(^3\Sigma_u^+)$ and the ground state $N_2(^1\Sigma_g^+)$, respectively.

Since this occupation dependence is obviously not contained in the Hamiltonian derived in Sec. 2.4, it needs to be incorporated manually. For this purpose we utilize the operators

$$P_{n_0 n_1} = |n_0 n_1\rangle\langle n_0 n_1| \,, \tag{2.74}$$

projecting onto the different configurations (n_0, n_1). In addition, we introduce two auxiliary bosonic levels $b_0^{(\dagger)}$ and $b_1^{(\dagger)}$ with energies ω_0 and ω_1. These levels shall engage in the subreactions of the two-step resonant de-excitation channel (1.1) and mimic the intra-molecular Coulomb correlations. For this purpose the explicit values of the energies ω_0 and ω_1 need to be fixed. This will be done later on in this section after the pseudo-particle representation has been derived.

Introducing the projection operators (2.74) and the auxiliary bosonic levels our extended Hamiltonian reads

$$\begin{aligned}
\hat{H}(t) = &\sum_{n_0,n_1} P_{n_0 n_1}\Big[\varepsilon_0^{(n_0 n_1)}(t)\, c_0^\dagger c_0 + \varepsilon_1^{(n_0 n_1)}(t)\, c_1^\dagger c_1\Big] \\
&+ \sum_{\vec{k}} \varepsilon_{\vec{k}}\, c_{\vec{k}}^\dagger c_{\vec{k}} + \sum_{\vec{q}} \varepsilon_{\vec{q}}(t)\, c_{\vec{q}}^\dagger c_{\vec{q}} + \omega_0\, b_0^\dagger b_0 + \omega_1\, b_1^\dagger b_1 \\
&+ \sum_{\vec{k}} \Big[(P_{01} + P_{11}) V_{\vec{k}}(t)\, c_{\vec{k}}^\dagger\, b_0^\dagger\, c_0 + \text{H.c.}\Big] \\
&+ \sum_{\vec{q}} \Big[(P_{10} + P_{11}) V_{\vec{q}}(t)\, c_{\vec{q}}^\dagger\, b_1^\dagger\, c_1 + \text{H.c.}\Big] \\
&+ \sum_{\vec{k},\vec{k}'} \Big[(P_{10} + P_{01}) V_{\vec{k}\vec{k}'}(t)\, c_0^\dagger\, c_1\, c_{\vec{k}'}^\dagger\, c_{\vec{k}} + \text{H.c.}\Big] \\
&+ \sum_{\vec{k},\vec{q}} \Big[(P_{10} + P_{01}) V_{\vec{k}\vec{q}}(t)\, c_0^\dagger\, c_{\vec{k}}\, c_{\vec{q}}^\dagger\, c_1 + \text{H.c.}\Big] \,.
\end{aligned} \tag{2.75}$$

Here the projected projectile energies are given by

$$\begin{aligned} P_{10}\,\varepsilon_0^{(n_1n_2)} &= \varepsilon_0^{(10)} = \varepsilon_{0g}\ , \qquad P_{01}\,\varepsilon_1^{(n_1n_2)} = \varepsilon_1^{(01)} = \varepsilon_{1*}\ , \\ P_{11}\,\varepsilon_0^{(n_1n_2)} &= \varepsilon_0^{(11)} = \varepsilon_{0-}\ , \qquad P_{11}\,\varepsilon_1^{(n_1n_2)} = \varepsilon_1^{(11)} = \varepsilon_{1-}\ , \end{aligned} \tag{2.76}$$

with the subscripts g, $*$ and $-$ denoting the respective energy value in the ground state molecule $N_2(^1\Sigma_g^+)$, the metastable state $N_2(^3\Sigma_u^+)$ and the negative ion $N_2^-(^2\Pi_g)$, respectively (see also Fig. 2.4). Note that we don't have to specify the remaining energies as these will drop out in the course of the pseudo-particle representation that will be introduced in the following.

As we see, the projection operators (2.74) permit us to describe the transitions (1.1), (1.2) and (1.3) by a single Hamiltonian. Depending on the process and, thus, the occupancy of the molecular levels, different matrix elements can be assigned to the Hamiltonian. Moreover, the projectors also guarantee that the occupancies of the two molecular levels never vanishes simultaneously. Thus, the $N_2^+(^2\Pi_u)$-state is never realized and the conditional coupling between the two subreactions of the resonant de-excitation channel (1.1) is contained automatically.

However, a significant drawback of the projection operators is that they are not suitable for a diagrammatic treatment which would offer a flexible and powerful way to obtain quantum-kinetic equations. In order to work around this situation, we now employ a pseudo-particle approach allowing us to rewrite the Hamiltonian (2.75) in terms of slave fields[3,22,26,76,120,139]. The starting point for this procedure is the completeness condition,

$$|00\rangle\langle 00| + |10\rangle\langle 10| + |01\rangle\langle 01| + |11\rangle\langle 11| = 1\ , \tag{2.77}$$

which expresses the fact that the molecule can exhibit exactly one of the configurations depicted in Fig. 2.4 at the same time. We then introduce pseudo-particle operators $c_+^\dagger$, $c_g^\dagger$, $c_*^\dagger$ and $c_-^\dagger$ which create the positive ion $N_2^+(^2\Pi_u)$, the ground state molecule $N_2(^1\Sigma_g^+)$, the metastable molecule $N_2(^3\Sigma_u^+)$ and the negative ion $N_2^-(^2\Pi_g)$ from an abstract vacuum state $|\mathrm{vac}\rangle$,

$$\begin{aligned} |00\rangle &= c_+^\dagger|\mathrm{vac}\rangle\ , \quad |10\rangle = c_g^\dagger||\mathrm{vac}\rangle\ , \\ |01\rangle &= c_*^\dagger|\mathrm{vac}\rangle\ , \quad |11\rangle = c_-^\dagger||\mathrm{vac}\rangle\ . \end{aligned} \tag{2.78}$$

As a result, the completeness condition (2.77) can be rewritten in the form

$$c_+^\dagger c_+ + c_g^\dagger c_g + c_*^\dagger c_* + c_-^\dagger c_- = 1\ . \tag{2.79}$$

Moreover, by employing (2.77) and (2.78) the operators $c_{0/1}^{(\dagger)}$ creating and destroying an electron in the two states of our molecular two-level system can be expressed as

$$c_0 = c_0 * 1 = |00\rangle\langle 10| - |01\rangle\langle 11| = c_+^\dagger c_g - c_*^\dagger c_-\ , \tag{2.80a}$$

$$c_0^\dagger = c_0^\dagger * 1 = |10\rangle\langle 00| - |11\rangle\langle 01| = c_g^\dagger c_+ - c_-^\dagger c_*\ , \tag{2.80b}$$

$$c_1 = c_1 * 1 = |00\rangle\langle 01| + |10\rangle\langle 11| = c_+^\dagger c_* + c_g^\dagger c_-\ , \tag{2.80c}$$

$$c_1^\dagger = c_1^\dagger * 1 = |01\rangle\langle 00| + |11\rangle\langle 10| = c_*^\dagger c_+ + c_-^\dagger c_g\ . \tag{2.80d}$$

Note that here we have defined $c_0\,|11\rangle = -|01\rangle$ and $c_0^\dagger\,|01\rangle = -|11\rangle$ in order to satisfy the anticommutation relations of the $c_{0/1}^{(\dagger)}$ (see also Ref. [17]). The relations (2.80)

then reproduce the completeness condition (2.79) when either the $c_{g/*}$ are bosonic and the $c_{-/+}$ are fermionic or the $c_{g/*}$ are fermionic and the $c_{-/+}$ are bosonic. Without loss of generality we choose c_g and c_* to be bosonic and declare the labeling conventions

$$c_g^{(\dagger)} \longrightarrow b_g^{(\dagger)} , \quad c_*^{(\dagger)} \longrightarrow b_*^{(\dagger)} , \quad c_+^{(\dagger)} \longrightarrow f_+^{(\dagger)} , \quad c_-^{(\dagger)} \longrightarrow f_-^{(\dagger)} . \tag{2.81}$$

Consequently, the constraint (2.79) takes the form

$$Q = b_g^\dagger b_g + b_*^\dagger b_* + f_-^\dagger f_- + f_+^\dagger f_+ = 1 , \tag{2.82}$$

where we have introduced the usual pseudo-particle number operator Q.

Formally, the auxiliary fermion and boson operators $f_{-/+}$ and $b_{*/g}$ represent pseudo-particle operators creating and annihilating molecular configurations. The constraint (2.82) ensures that at any time only one of the four possible molecular configurations is present in the system. The occupancy of a molecular pseudo-particle state is, thus, at most unity. Hence, it represents the probability with which the respective molecular configuration appears in the course of the scattering event.

We now construct the pseudo-particle representation of the Hamiltonian by inserting the decomposition (2.80) into (2.75), making the identifications (2.81) and collecting only terms which are in accordance with (2.82). The result reads

$$\begin{aligned}
\hat{H}(t) = {} & \varepsilon_g(t)\, b_g^\dagger b_g + \varepsilon_*(t)\, b_*^\dagger b_* + \varepsilon_-(t)\, f_-^\dagger f_- \\
& + \sum_{\vec{k}} \varepsilon_{\vec{k}}\, c_{\vec{k}}^\dagger c_{\vec{k}} + \sum_{\vec{q}} \varepsilon_{\vec{q}}(t)\, c_{\vec{q}}^\dagger c_{\vec{q}} + \omega_0\, b_0^\dagger b_0 + \omega_1\, b_1^\dagger b_1 \\
& - \sum_{\vec{k}} \Big[V_{\vec{k}}(t)\, c_{\vec{k}}^\dagger\, b_0^\dagger\, b_*^\dagger\, f_- + \text{H.c.} \Big] + \sum_{\vec{q}} \Big[V_{\vec{q}}(t)\, c_{\vec{q}}^\dagger\, b_1^\dagger\, b_g^\dagger\, f_- + \text{H.c.} \Big] \\
& + \sum_{\vec{k},\vec{k}'} \Big[V_{\vec{k}\vec{k}'}(t)\, c_{\vec{k}'}^\dagger\, c_{\vec{k}}\, b_g^\dagger\, b_* + \text{H.c.} \Big] + \sum_{\vec{k},\vec{q}} \Big[V_{\vec{k}\vec{q}}(t)\, c_{\vec{k}}\, c_{\vec{q}}^\dagger\, b_g^\dagger\, b_* + \text{H.c.} \Big] ,
\end{aligned} \tag{2.83}$$

where we have introduced the abbreviations

$$\varepsilon_g = \varepsilon_{0g} , \quad \varepsilon_* = \varepsilon_{1*} , \quad \varepsilon_- = \varepsilon_{0-} + \varepsilon_{1-} . \tag{2.84}$$

Note that by construction no term in (2.83) contains the operator f_+ or its adjoint since the positive ion $N_2^+(^2\Pi_u)$ is not involved in the transitions the Hamiltonian is supposed to model (see Eqs. (1.1), (1.2) and (1.3)). Furthermore, the physical meaning of the various terms in (2.83) is particularly transparent. Consider for instance the last term describing the indirect Auger de-excitation reaction (1.2). Here a metastable molecule and an electron from the surface are annihilated while a ground state molecule and an Auger electron are created.

Inspecting the structure of the resonant tunneling terms in (2.83) we can now fix the energies of the auxiliary boson states ω_0 and ω_1. In particular, the hybridization term describing the surface electron capture reaction,

$$\sum_{\vec{k}} \Big[V_{\vec{k}}(t)\, c_{\vec{k}}^\dagger\, b_0^\dagger\, b_*^\dagger\, f_- + \text{H.c.} \Big] , \tag{2.85}$$

involves the tunneling of a band electron $\vec{k}$ into the projectile's ground state level at the energy $\varepsilon_0 = \varepsilon_{0-} + \varepsilon_{1-} - \varepsilon_{1*} - \omega_0$. Since this transition forms the $N_2^-(^2\Pi_g)$-state

(see Eq. (1.1)), the energy of the projectile level capturing the electron should, however, be $\varepsilon_0 = \varepsilon_{0-}$. Consequently, we choose

$$\omega_0 = \varepsilon_{1-} - \varepsilon_{1*} \,. \tag{2.86}$$

An equivalent treatment can also be applied to the hybridization term associated with the resonant electron emission,

$$\sum_{\vec{q}} \left[V_{\vec{q}}(t)\, c^\dagger_{\vec{q}}\, b_1^\dagger\, b_g^\dagger\, f_- + \text{H.c.} \right] . \tag{2.87}$$

This expression describes the tunneling of an electron from the excited projectile level at the energy $\varepsilon_1 = \varepsilon_{1-} + \varepsilon_{0-} - \varepsilon_{0g} - \omega_1$ into a projectile continuum state $\vec{q}$. Since here the electron is emitted from the negative ion state $\mathrm{N}_2^-(^2\Pi_g)$ (see Eq. (1.1)), the excited level's energy should, however, amount to $\varepsilon_1 = \varepsilon_{1-}$. Hence, we choose

$$\omega_1 = \varepsilon_{0-} - \varepsilon_{0g} \,. \tag{2.88}$$

With the proper parametrization the auxiliary boson states $b^{(\dagger)}_{0/1}$, thus, account for the additional energy that is picked up or released by the passive projectile electrons in the course of the resonant de-excitation reaction (1.1).

In total, together with the constraint (2.82) and the bosonic energies (2.86) and (2.88) the Hamiltonian (2.83) is capable of describing the two-step resonant de-excitation reaction (1.1) as well as the Auger de-excitation channels (1.2) and (1.3) and their mutual interactions. Moreover, since the pseudo-particle operators f_- and $b_{*/g}$ comply to standard commutation and anti-commutation relations, it is possible to conduct a non-equilibrium diagrammatic expansion of the interaction terms involved in (2.83). However, while the Hamiltonian itself conserves the pseudo-particle number Q, the quantum-kinetic equations resulting from a diagrammatic treatment may contain terms which violate the constraint (2.82). Therefore, the projection onto the physical subspace $Q = 1$ needs to be carried out explicitly in the course of our quantum-kinetic calculation. For this purpose we will employ the Langreth-Nordlander projection technique[76] in Sec. 3.3.

2.6 Surface Transmission Functions

The last component of our effective model discussed in this chapter are the surface transmission functions which allow us to extract the amount of experimentally observable secondary electrons from our theory.

The surface reactions considered in this work release secondary electrons either into internally excited states of the solid surface or into continuum states of the projectile (see Sec. 1.2). In order to observe these electrons in an experiment, two conditions must hold. Firstly, the electron's wave vector must point outside the surface as otherwise the electron will travel into the interior of the solid and remain inaccessible to common diagnostic tools. Secondly, the electron must be energetic enough to breach through the surface barrier. For internally excited electrons transmission through the surface edge is handled by means of the transmission coefficient T_{k_z} appearing in the associated wave function[81,98] (see Eq. 2.3). Thus, to an extent determined by the transmission coefficient T_{k_z} these electrons can always

escape the surface as long as their vertical energy is positive. On the other hand, for electrons emitted into projectile continuum states we need to explicitly consider the effect of their image potential V_i (see Eq. (2.14)). The latter is not included in the wave functions (2.37) and can trap emitted electrons close to the surface. For an electron to escape the attractive image force the sum of its vertical kinetic energy and the image potential at the location of emission must be larger than zero. The latter can be approximated by the position of the projectile's center of mass $\vec{r}_p(t)$ in the moment of emission[82].

The aforementioned effects need to be incorporated into a calculation of the secondary electron emission coefficient. This can be done by introducing the surface transmission functions

$$\mathcal{T}_{\vec{k}}(t) = \Theta(k_z)\,\Theta(\varepsilon_{k_z})\,, \tag{2.89a}$$

$$\mathcal{T}_{\vec{q}}(t) = \Theta(q_z)\,\Theta\Big(\varepsilon_{q_z} + V_i\big(z_p(t)\big)\Big)\,, \tag{2.89b}$$

acting on internally excited electrons $\vec{k}$ and electrons in projectile continuum states $\vec{q}$, respectively. Note that for the latter the term surface transmission function is actually somewhat misleading since the electron is already emitted outside of the surface. Nevertheless, the term has been established in these situations as well[82] although the transmission is not through the surface itself but through the image potential in front of it.

In the quantum-kinetic calculations of chapter 3 the transmission functions (2.89) will be used to cut off the interaction matrix elements when considering electrons that have escaped the surface. Moreover, as pointed out in Sec. 2.2.3, the surface transmission function $\mathcal{T}_{\vec{q}}$ also needs to be incorporated into the natural decay rate Γ_n of the nitrogen shape resonance $N_2^-(^2\Pi_g)$. In particular, the fraction of the natural decay rate $\widetilde{\Gamma}_n$ that only pertains to emitted electrons capable of escaping the surface can be calculated from the integral

$$\widetilde{\Gamma}_n(t) = \frac{1}{\pi}\int_{-\infty}^{\infty}\mathrm{d}\varepsilon_{\vec{q}}^{\infty}\int_0^{\pi}\mathrm{d}\vartheta_{\vec{q}}\;\mathcal{T}_{\vec{q}}(t)\;\varrho_n(\varepsilon_{\vec{q}}^{\infty})\,. \tag{2.90}$$

Here $\vartheta_{\vec{q}} = \arccos(q_z/|\vec{q}|)$ and ϱ_n denotes the full decay rate's energy spectrum (see Eq. (2.42)). Employing (2.89b) we can carry out the $\vartheta_{\vec{q}}$-integration in (2.90) and obtain

$$\widetilde{\Gamma}_n(t) = \int_0^{\infty}\mathrm{d}\varepsilon_{\vec{q}}^{\infty}\;\tilde{\varrho}_n(\varepsilon_{\vec{q}}^{\infty}, t)\,, \tag{2.91}$$

where the spectral decay rate $\tilde{\varrho}_n(\varepsilon_{\vec{q}}^{\infty}, t)$ is given by

$$\tilde{\varrho}_n(\varepsilon_{\vec{q}}^{\infty}, t) = \frac{1}{\pi}\Theta\Big(\varepsilon_{\vec{q}}^{\infty} + V_i\big(z_p(t)\big)\Big)\arccos\left(\sqrt{\frac{-V_i\big(z_p(t)\big)}{\varepsilon_{\vec{q}}^{\infty}}}\right)\varrho_n(\varepsilon_{\vec{q}}^{\infty})\,. \tag{2.92}$$

The final energy integral (2.91) then needs to be calculated numerically. As we see, the rate $\widetilde{\Gamma}_n$ varies in time due to the inclusion of the transmission function (2.89b).

Finally, we stress that while in the past surface transmission functions have sometimes been used to fit numerical results to experimental measurements[44], this is not needed in our case. Here the surface transmission functions (2.89) are part of the physical structure of our effective model and do not involve any free parameter.

Chapter 3

Quantum Kinetics

In this chapter we will present quantum-kinetic descriptions of the surface reactions that were introduced in Sec. 1.2. Building upon the Hamiltonians derived in Secs. 2.4 and 2.5 we will analyze the isolated channels as well as their mutual interaction. For every particular case our goal is to obtain equations which directly relate our model's parameters (most importantly the matrix elements) to the transient occupation of the individual states within the system. The matrix elements are, however, not concretized at any point within this chapter and, thus, our calculations possess a universal character.

In the following we will first investigate the isolated electron capture and surface-induced electron emission subreactions of the resonant de-excitation channel (1.1) by means of the Green function formulation due to Keldysh (see Sec. 3.1). Subsequently, in Sec. 3.2 we will utilize the same approach to analyze the Auger de-excitation reactions (1.2) and (1.3). Afterwards, we will study the interplay of resonant and Auger de-excitation using the Kadanoff-Baym formulation in Sec. 3.3. The latter section will also embrace our treatment of the natural decay subreaction of (1.1). Finally, in Sec. 3.4 we will again employ the Keldysh formulation in order to examine the interaction of Auger and resonant neutralization due to (1.4) and (1.5).

3.1 Resonant Electron Capture and Release

Here we consider the dynamics of a single time-dependent fermion level $\varepsilon_p(t)$ which is resonantly coupled to a continuum of states $\vec{\xi}$. The associated Hamiltonian reads

$$\hat{H}(t) = \sum_{\vec{\xi}} \varepsilon_{\vec{\xi}}(t)\, c^\dagger_{\vec{\xi}} c_{\vec{\xi}} + \varepsilon_p(t)\, c^\dagger_p c_p + \sum_{\vec{\xi}} \left[V_{\vec{\xi}}(t)\, c^\dagger_{\vec{\xi}} c_p + \text{H.c.} \right], \tag{3.1}$$

where $V_{\vec{\xi}}$ denotes the tunneling matrix element. From the derivation of the overall Hamiltonian in Sec. 2.4 we know that upon choosing a proper parametrization the system (3.1) can be used to describe the electron capture and surface-induced electron emission subreactions of the resonant de-excitation channel (1.1). The particular link between the above Hamiltonian and these surface reactions will be established later on in this section[1]. First, however, we consider the general dynamics of (3.1).

[1] Note that the model (3.1) could also be used to study the resonant neutralization reaction (1.5). Even so, this will not be the subject of the current section since the neutralization channels (1.4) and (1.5) will be analyzed in detail in Sec. 3.4.

In terms of its structure the Hamiltonian (3.1) represents the time-dependent Newns-Anderson model without Coulomb interactions on the projectile (see for instance Ref. [143]). It was originally introduced in the description of magnetic impurities in metals[5] and has since been employed exhaustively in various contexts. As a standard problem of many particle physics it can be treated exactly using the Keldysh formulation of the non-equilibrium Green function technique[12]. Here the self-energy solely consists of a trivial first-order diagram possessing only non-diagonal components. The resulting advanced and retarded parts are given by

$$\Sigma^{A/R}_{\vec{\xi}p}(t_1,t_2) = \frac{i}{\hbar} V_{\vec{\xi}}(t_1)\,\delta(t_1-t_2) = -\left[\Sigma^{A/R}_{p\vec{\xi}}(t_1,t_2)\right]^* , \tag{3.2}$$

while the Keldysh component vanishes identically,

$$\Sigma^{K}_{\vec{\xi}p}(t_1,t_2) = 0 = \Sigma^{K}_{p\vec{\xi}}(t_1,t_2) . \tag{3.3}$$

Since the non-interacting part of the Hamiltonian (3.1) is consistent with the general form (1.32), the unperturbed Green functions are given by Eqs. (1.33) and (1.34). As a result, we can calculate the Keldysh component of the full Green function from Eq. (1.36) which upon insertion of (3.3) simplifies to

$$G^K_{\alpha\beta}(t,t') = -i\sum_\gamma \left[1-2n_\gamma(-\infty)\right] G^R_{\alpha\gamma}(t,-\infty)\, G^A_{\gamma\beta}(-\infty,t') . \tag{3.4}$$

Here and in the following α, β and γ can take any of the values p or $\vec{\xi}$. Combining (1.31) and (3.4) we can then calculate the occupation of an arbitrary state of the system α from

$$n_\alpha(t) = \sum_\beta n_\beta(-\infty)\left|G^R_{\alpha\beta}(t,-\infty)\right|^2 . \tag{3.5}$$

Note that in order to obtain (3.5), we have used the relation

$$\sum_\gamma G^R_{\alpha\gamma}(t,-\infty)\, G^A_{\gamma\alpha}(-\infty,t) = 1 , \tag{3.6}$$

which can for instance be derived from (3.4) and the definition of $G^{++}_{\alpha\beta}$ given by (1.18a) (see also Refs. [12, 95]). Inspecting the particular cases $\alpha = p$ and $\alpha = \vec{\xi}$ in (3.5) we obtain

$$n_p(t) = n_p(-\infty)\left|G^R_{pp}(t,-\infty)\right|^2 + \sum_{\vec{\xi}} n_{\vec{\xi}}(-\infty)\left|G^R_{p\vec{\xi}}(t,-\infty)\right|^2 , \tag{3.7a}$$

$$n_{\vec{\xi}}(t) = n_{\vec{\xi}}(-\infty)\left|G^R_{\vec{\xi}\vec{\xi}}(t,-\infty)\right|^2 + n_p(-\infty)\left|G^R_{\vec{\xi}p}(t,-\infty)\right|^2 . \tag{3.7b}$$

In order to calculate $n_p(t)$ and $n_{\vec{\xi}}(t)$ we, thus, need to calculate the four different retarded Green functions appearing in (3.7a) and (3.7b). The respective Dyson equations can be constructed from the general form (1.28a) and its adjoint variant. Employing the compact notation (1.29) they read

$$G^R_{pp}(t,t') = G^{R(0)}_{pp}(t,t') + \left\{G^{R(0)}_{pp} * \Sigma^R_{p\vec{\xi}} * G^{R(0)}_{\vec{\xi}\vec{\xi}} * \Sigma^R_{\vec{\xi}p} * G^R_{pp}\right\}(t,t') , \tag{3.8a}$$

$$G^R_{p\vec{\xi}}(t,t') = \left\{G^R_{pp} * \Sigma^R_{p\vec{\xi}} * G^{R(0)}_{\vec{\xi}\vec{\xi}}\right\}(t,t') , \tag{3.8b}$$

$$G^R_{\vec{\xi}\vec{\xi}}(t,t') = G^{R(0)}_{\vec{\xi}\vec{\xi}}(t,t') + \left\{G^{R(0)}_{\vec{\xi}\vec{\xi}} * \Sigma^R_{\vec{\xi}p} * G^R_{pp} * \Sigma^R_{p\vec{\xi}} * G^{R(0)}_{\vec{\xi}\vec{\xi}}\right\}(t,t') , \tag{3.8c}$$

$$G^R_{\vec{\xi}p}(t,t') = \left\{G^{R(0)}_{\vec{\xi}\vec{\xi}} * \Sigma^R_{\vec{\xi}p} * G^R_{pp}\right\}(t,t') . \tag{3.8d}$$

As we see, knowledge of the diagonal propagator G^R_{pp} is sufficient since the remaining Green functions are given in terms of integrals involving unperturbed propagators, self-energy components and G^R_{pp}. The latter's Dyson equation (3.8a) can be solved iteratively and yields

$$G^R_{pp}(t,t') = G^{R(0)}_{pp}(t,t')\,\sigma[\Delta](t,t')\,, \tag{3.9}$$

where $\sigma[\Delta]$ operates on a complex function $\Delta(t_1,t_2)$ and defines the infinite series

$$\sigma[\Delta](t,t') = \sum_{\nu=0}^{\infty} \sigma^{(\nu)}[\Delta](t,t')\,, \tag{3.10}$$

with

$$\sigma^{(\nu)}[\Delta](t,t') = (-1)^{\nu} \int_{t'}^{t} \mathrm{d}t_1 \int_{t'}^{t_1} \mathrm{d}t_2 \int_{t'}^{t_2} \mathrm{d}t_3 \ldots \int_{t'}^{t_{2\nu-1}} \mathrm{d}t_{2\nu} \prod_{i=1}^{\nu} \Delta(t_{2i-1},t_{2i})\,. \tag{3.11}$$

The Δ-function appearing as the argument of the σ-series in (3.9) emerges from the self-energy and reads

$$\Delta(t_1,t_2) = \frac{1}{\hbar^2} \sum_{\vec{\xi}} V^*_{\vec{\xi}}(t_1)\, V_{\vec{\xi}}(t_2)\, e^{-\frac{i}{\hbar}\int_{t_2}^{t_1} \mathrm{d}t_3 \left[\varepsilon_{\vec{\xi}}(t_3) - \varepsilon_p(t_3)\right]}\,. \tag{3.12}$$

The infinite series (3.10) will play a central role in all of the quantum-kinetic calculations of this chapter and is discussed in detail in Appendix C. In the latter we also derive three different integral identities involving combinations of σ- and Δ-terms that will be used at various points within this chapter. Furthermore, we demonstrate how the σ-series can be approximated by the exponential expression

$$\sigma[\Delta](t,t') \approx e^{-\int_{t'}^{t} \mathrm{d}t_1 \int_{t'}^{t_1} \mathrm{d}t_2\, \Delta(t_1,t_2)}\,, \tag{3.13}$$

which holds in cases where $\Delta(t_1,t_2)$ is strongly peaked along the time diagonal $t_1 = t_2$. Note that (3.13) is also known as semi-classical approximation and constitutes the basis of the numerical results that will be presented in Chapters 4 and 5. Its validity for the particular situations studied in this work will be demonstrated explicitly in Sec. 4.2.3. Here, however, we will not employ the approximate form (3.13) until the end of this section.

After inserting the exact expression for G^R_{pp} (see Eq. (3.9)) into the Dyson equations (3.8b), (3.8c) and (3.8d) we can now calculate the remaining retarded propagators. Substituting the resulting Green functions in (3.7a) and (3.7b) we can then evaluate the occupancies $n_p(t)$ and $n_{\vec{\xi}}(t)$.

Up to now we have not concretized the projectile level ε_p and treated the $\vec{\xi}$-states as a general continuum without any connection to the surface reactions studied in this work. This link will be established in the following as we investigate the expressions (3.7a) and (3.7b) for two special situations which are of physical relevance. In particular, we consider the cases (rc) meaning resonant capture and (rr) meaning resonant release which are defined by

$$(rc): \quad \varepsilon_p(t) = \varepsilon_{0-}(t)\,, \quad n_p(-\infty) = 0\,, \quad n_{\vec{\xi}}(-\infty) = 1 \;\; \forall\, \vec{\xi} \in B_r\,, \tag{3.14a}$$

$$(rr): \quad \varepsilon_p(t) = \varepsilon_{1-}(t)\,, \quad n_p(-\infty) = 1\,, \quad n_{\vec{\xi}}(-\infty) = 0 \;\; \forall\, \vec{\xi} \in B_r\,. \tag{3.14b}$$

Here B_r denotes the relevant portion of the continuum embracing only those $\vec{\xi}$-states that become resonant or almost resonant to the projectile level $\varepsilon_p(t)$ at some point during the dynamical evolution of the system. Note that continuum states which are clearly non-resonant to the projectile level can be neglected as they are unable to cause significant contributions to the tunneling reaction due to their strong violation of energy conservation.

As mentioned before, the cases (rc) and (rr) describe two distinct physically relevant situations. Case (rc), on the one hand, represents the empty ground state level of $N_2(^3\Sigma_u^+)$ in front of a completely filled continuum from which it can resonantly capture an electron to form the $N_2^-(^2\Pi_g)$-state. Consequently, the case (rc) can be used to study the first step of the resonant de-excitation reaction (1.1). Case (rr), on the other hand, describes the occupied excited level of $N_2^-(^2\Pi_g)$ interacting with an empty continuum into which it can resonantly release its electron. Here the continuum resembles the free projectile states and, consequently, case (rr) corresponds to the second step of the resonant de-excitation channel (1.1). As we know, this subreaction splits up into a natural and a surface-induced transition. However, since our effective model only provides us with a matrix element for the latter, the case (rr) does only describe the surface-induced electron emission subreaction of (1.1). In addition, (rr) does also apply to the tunneling of an electron from the excited molecular level into an empty portion of a surface's band structure. This type of reaction is, however, not studied in this work. In order to stay consistent with the notation established in Chapter 2, we, thus, introduce the substitutions $\vec{\xi} \to \vec{k}$ and $\vec{\xi} \to \vec{q}$ in the cases (rc) and (rr), respectively. Moreover, we will identify the localized level p with the ground state and excited molecular level as indicated in (3.14).

Employing the initial conditions of case (rc) in (3.7a) we then find

$$n_0^{(rc)}(t) = \int_{-\infty}^{t} \mathrm{d}t_1 \int_{-\infty}^{t} \mathrm{d}t_2 \, \Delta_{rc}(t_1, t_2)\, \sigma[\Delta](t, t_1)\, \sigma[\Delta^*](t, t_2) \,. \tag{3.15}$$

Here the term Δ_{rc} is equal to Δ as defined in (3.12) but with the $\vec{k}$-sum[2] restricted to the initially occupied states only,

$$\Delta_{rc}(t_1, t_2) = \frac{1}{\hbar^2} \sum_{\vec{k}} n_{\vec{k}}(-\infty)\, V_{\vec{k}}^*(t_1)\, V_{\vec{k}}(t_2)\, e^{-\frac{i}{\hbar}\int_{t_2}^{t_1} \mathrm{d}t_3 \left[\varepsilon_{\vec{k}}(t_3) - \varepsilon_{0-}(t_3)\right]} \,. \tag{3.16}$$

Since for the case (rc) we previously assumed that the projectile level stays well inside the initially occupied portion of the surface's band structure, initially unoccupied states do strongly violate energy conservation and can, thus, not contribute to the tunneling. Hence, we can safely replace Δ by Δ_{rc} in the σ-terms of (3.15). Employing the integral identity (C.18) we then can simplify (3.15) to

$$n_0^{(rc)}(t) = 1 - \sigma[\Delta_{rc}](t, -\infty)\, \sigma[\Delta_{rc}^*](t, -\infty) \,. \tag{3.17}$$

Note that the occupation of the continuum states $n_{\vec{k}}(t)$ is not of interest in the case (rc) since these states only act as a reservoir supplying electrons to the projectile level.

[2] Remember that we replaced $\vec{\xi}$ with $\vec{k}$ for the case (rc).

We now proceed with the case (rr). Here we assumed that the projectile level only becomes (near-)resonant with initially unoccupied continuum states. Consequently, we can restrict the $\vec{q}$-sum[3] in (3.12) to initially unoccupied states. Moreover, we can neglect the second term of (3.7a) due to its energy off-resonance as well as the first term of (3.7b) which only applies to initially occupied $\vec{q}$-states. As a result, we obtain

$$n_1^{(rr)}(t) = \sigma[\Delta_{rr}](t,-\infty)\,\sigma[\Delta_{rr}^*](t,-\infty)\;, \tag{3.18a}$$

$$n_{\vec{q}}^{(rr)}(t) = \int_{-\infty}^{t}\mathrm{d}t_1\int_{-\infty}^{t}\mathrm{d}t_2\;\Delta_{rr}^{\vec{q}}(t_1,t_2)\,\sigma[\Delta_{rr}^*](t_1,-\infty)\,\sigma[\Delta_{rr}](t_2,-\infty)\;, \tag{3.18b}$$

where (3.18b) only holds for initially unoccupied $\vec{q}$-states. Here the term $\Delta_{rr}^{\vec{q}}$ represents Δ as defined in 3.12 but without the $\vec{q}$-sum,

$$\Delta_{rr}^{\vec{q}}(t_1,t_2) = \frac{1}{\hbar^2}V_{\vec{q}}^*(t_1)\,V_{\vec{q}}(t_2)\,e^{-\frac{i}{\hbar}\int_{t_2}^{t_1}\mathrm{d}t_3\left[\varepsilon_{\vec{q}}(t_3)-\varepsilon_{1-}(t_3)\right]}\;, \tag{3.19}$$

and Δ_{rr} is given by

$$\Delta_{rr}(t_1,t_2) = \sum_{\vec{q}}\left[1-n_{\vec{q}}(-\infty)\right]\Delta_{rr}^{\vec{q}}(t_1,t_2)\;. \tag{3.20}$$

The spectrum of emitted electrons (3.18b) is quite involved and cannot be simplified analytically. Clearly, the shape of the spectrum is determined by the $\Delta_{rr}^{\vec{q}}$-function as it is the only component carrying a $\vec{q}$ dependence. The σ-factors, on the other hand, are proportional to the occupation of the excited level (see Eq. (3.18a)) and, hence, act in a renormalizing way accounting for the transient projectile occupation. Simply neglecting these terms is, therefore, only acceptable when Δ_{rr} is small and the excited molecular level stays almost completely occupied during the process. In cases where initially unoccupied continuum states are degenerate to ε_{1-} the tunneling will, however, most likely be very efficient unless the matrix element is very small. In such a situation the renormalizing effect of the σ-terms must not be neglected.

We now move on to the total number of electrons $n^{(rr)}(t)$ that have tunneled into the continuum of $\vec{q}$-states at a time t. This quantity can be obtained by summing (3.18b) over all initially unoccupied $\vec{q}$-states. Employing (3.20) and the integral identity (C.15) we find

$$n^{(rr)}(t) = \sum_{\vec{q}}\left[1-n_{\vec{q}}(-\infty)\right]n_{\vec{q}}^{(rr)}(t) = 1-\sigma[\Delta_{rr}](t,-\infty)\,\sigma[\Delta_{rr}^*](t,-\infty)\;. \tag{3.21}$$

Comparing this expression to the occupation of the projectile level (3.18a) we find

$$n_1^{(rr)}(t) + n^{(rr)}(t) = 1\;\forall t\;. \tag{3.22}$$

Hence, the overall number of particles in the projectile level and the initially unoccupied continuum states is conserved.

The result (3.21) does, however, not represent the amount of experimentally observable electrons since, as explained in Sec. 2.6, the surface's attractive image potential can trap electrons emitted at low energies or small distances from the

[3]Remember that we replaced $\vec{\xi}$ with $\vec{q}$ for the case (rr).

surface edge. To account for this effect, we need to include the surface transmission function $\mathcal{T}_{\vec{q}}(t)$ (see Eq. (2.89b)) in $\Delta^{\vec{q}}_{rr}$. This can be done by introducing the function

$$\widetilde{\Delta}^{\vec{q}}_{rr}(t_1,t_2) = \mathcal{T}_{\vec{q}}(t_1)\,\mathcal{T}_{\vec{q}}(t_2)\,\Delta^{\vec{q}}_{rr}(t_1,t_2)\;, \tag{3.23}$$

which replaces $\Delta^{\vec{q}}_{rr}$ when the number of escaped electrons is to be calculated. We admit that the particular structure of (3.23) might make the impression of double counting the transmission effect. Remember, however, that $\Delta^{\vec{q}}_{rr}$ includes two matrix element factors at different times (see Eq. (3.19)). Consequently, the transmission functions cut down the individual matrix elements when the transmission condition is violated.

The spectrum of escaped electrons $\tilde{n}^{(rr)}_{\vec{q}}(t)$ can now be obtained by replacing $\Delta^{\vec{q}}_{rr}$ with $\widetilde{\Delta}^{\vec{q}}_{rr}$ in (3.18b),

$$\tilde{n}^{(rr)}_{\vec{q}}(t) = \int_{-\infty}^{t}\mathrm{d}t_1 \int_{-\infty}^{t}\mathrm{d}t_2\;\widetilde{\Delta}^{\vec{q}}_{rr}(t_1,t_2)\,\sigma[\Delta^{*}_{rr}](t_1,-\infty)\,\sigma[\Delta_{rr}](t_2,-\infty)\;. \tag{3.24}$$

The total number of escaped electrons $\tilde{n}^{(rr)}(t)$ is then found by summing (3.24) over all initially unoccupied $\vec{q}$-states which yields

$$\tilde{n}^{(rr)}(t) = \int_{-\infty}^{t}\mathrm{d}t_1 \int_{-\infty}^{t}\mathrm{d}t_2\;\widetilde{\Delta}_{rr}(t_1,t_2)\,\sigma[\Delta^{*}_{rr}](t_1,-\infty)\,\sigma[\Delta_{rr}](t_2,-\infty)\;, \tag{3.25}$$

with

$$\widetilde{\Delta}_{rr}(t_1,t_2) = \sum_{\vec{q}}\big[1-n_{\vec{q}}(-\infty)\big]\,\widetilde{\Delta}^{\vec{q}}_{rr}(t_1,t_2)\;. \tag{3.26}$$

The associated secondary electron emission coefficient $\gamma_e^{(rr)}$ follows from (3.25) upon setting $t=\infty$. Note, however, that this emission coefficient does not hold for the two-step resonant de-excitation of $N_2(^3\Sigma_u^+)$ since in the calculations of the present section the two subreactions of (1.1), corresponding to the cases (rc) and (rr), were treated separately.

Finally, we stress that up to this point we have not used any approximations beyond the restriction to (near-)resonant states. The latter constitutes an excellent approximation due to the strong effect of energy conservation and, hence, all of the results presented so far within this section can be considered exact. Unfortunately, the equations we derived here are highly complex and cannot be evaluated easily due to the involvement of the infinite σ-series. As pointed out earlier, the latter can, however, be approximated by the exponential representation (3.13) when the function it operates on is peaked about equal times. In Sec. 4.2.3 it will be demonstrated that this is the case for the situations considered in this work. Therefore, we can use (3.13) to replace any of the σ-terms in our previous results. We stress that the usage of (3.13) is highly advantageous, since the infinite σ-series is not very convenient to handle in a numerical treatment although theoretically it allows for an explicit calculation up to arbitrary order in the Δ-terms. The approximate representation (3.13), on the other hand, can be calculated rather easily.

The incorporation of (3.13) in the results of this section is straightforward. The projectile occupancies for the cases (rc) and (rr) (see Eqs. (3.17) and (3.18a)), for instance, turn into the approximate expressions

$$n_0^{(rc)}(t) \approx 1 - e^{-\int_{-\infty}^{t}\mathrm{d}t_1\int_{-\infty}^{t}\mathrm{d}t_2\,\Delta_{rc}(t_1,t_2)}\;, \tag{3.27a}$$

$$n_1^{(rr)}(t) \approx e^{-\int_{-\infty}^{t}\mathrm{d}t_1\int_{-\infty}^{t}\mathrm{d}t_2\,\Delta_{rr}(t_1,t_2)}\;. \tag{3.27b}$$

The derived equations for other quantities like $n_{\vec{q}}^{(rr)}$, $\tilde{n}_{\vec{q}}^{(rr)}$ and $\tilde{n}^{(rr)}$ (see Eqs. (3.18b), (3.24) and (3.25)) can be approximated in an analogous way.

3.2 Direct and Indirect Auger De-Excitation

In this section we investigate the interplay of the Auger de-excitation channels (1.2) and (1.3). As mentioned earlier, the direct transition (1.3) is actually spin-blocked for the $N_2(^3\Sigma_u^+)$-state. It might, however, play an important role for other metastable states of the nitrogen molecule or different projectiles. Therefore, we will include this process in our quantum-kinetic analysis.

An appropriate Hamiltonian for the description of the two Auger reactions within the limits of our effective model was derived in Sec. 2.4. Adding up the relevant terms and concretizing the projectile energies it reads

$$\begin{aligned}\hat{H}(t) = &\sum_{\vec{k}} \varepsilon_{\vec{k}}\, c_{\vec{k}}^\dagger\, c_{\vec{k}} + \sum_{\vec{q}} \varepsilon_{\vec{q}}(t)\, c_{\vec{q}}^\dagger\, c_{\vec{q}} + \varepsilon_{0g}(t)\, c_0^\dagger\, c_0 + \varepsilon_{1*}(t)\, c_1^\dagger\, c_1 \\ &+ \sum_{\vec{k},\vec{k}'} \left[V_{\vec{k}\vec{k}'}(t)\, c_0^\dagger\, c_1\, c_{\vec{k}'}^\dagger\, c_{\vec{k}} + \text{H.c.} \right] + \sum_{\vec{k},\vec{q}} \left[V_{\vec{k}\vec{q}}(t)\, c_0^\dagger\, c_{\vec{k}}\, c_{\vec{q}}^\dagger\, c_1 + \text{H.c.} \right],\end{aligned} \tag{3.28}$$

where, as before, 0 and 1 represent the ground state and excited level of our molecular two-level system, $\vec{q}$ labels molecular continuum states and $\vec{k}^{(\prime)}$ refers to states within the solid surface. Moreover, $V_{\vec{k}\vec{k}'}$ and $V_{\vec{k}\vec{q}}$ denote the matrix elements of direct and indirect Auger de-excitation, respectively. Note that in the direct Auger transition term of (3.28) a surface electron residing in an occupied state $\vec{k}$ is excited into a previously empty state of the surface $\vec{k}'$. For the sake of clearness we will stick with this notation for the rest of this work. Hence, from now on $\vec{k}'$ always refers to an internally excited state of the surface. Furthermore, since in the reactions (1.2) and (1.3) the molecule initially is in its metastable state $N_2(^3\Sigma_u^+)$, our molecular two-level system exhibits the initial occupations $n_0(-\infty) = 0$ and $n_1(-\infty) = 1$. The molecular continuum states $\vec{q}$, on the other hand, are completely empty.

In the following we will present a quantum-kinetic analysis of the system (3.28) based on the Keldysh formulation. Since the non-interacting part of the Hamiltonian (3.28) exhibits the general form (1.32), the unperturbed Green functions are again given by (1.33) and (1.34). In order to calculate the full Green functions of the system, we now need expressions for the self-energies which, in line with the work of Makoshi[86], we derive from a diagrammatic expansion up to second order in the Auger matrix elements. This neglects diagrammatic couplings between the two Auger channels which is, however, justified because in general the associated matrix elements are rather small.

We start our investigations with the projectile states. The second-order self-energy diagrams for the ground state level and the excited level are shown in Fig. 3.1. Mathematically they evaluate to

$$\Sigma_{00}^A(t_1,t_2) = \Theta(t_2-t_1)\Sigma_{00}^K(t_1,t_2)\,, \tag{3.29a}$$

$$\Sigma_{00}^R(t_1,t_2) = -\Theta(t_1-t_2)\Sigma_{00}^K(t_1,t_2)\,, \tag{3.29b}$$

$$\Sigma_{00}^K(t_1,t_2) = \Sigma_{00}^{(dad)}(t_1,t_2) + \Sigma_{00}^{(iad)}(t_1,t_2)\,, \tag{3.29c}$$

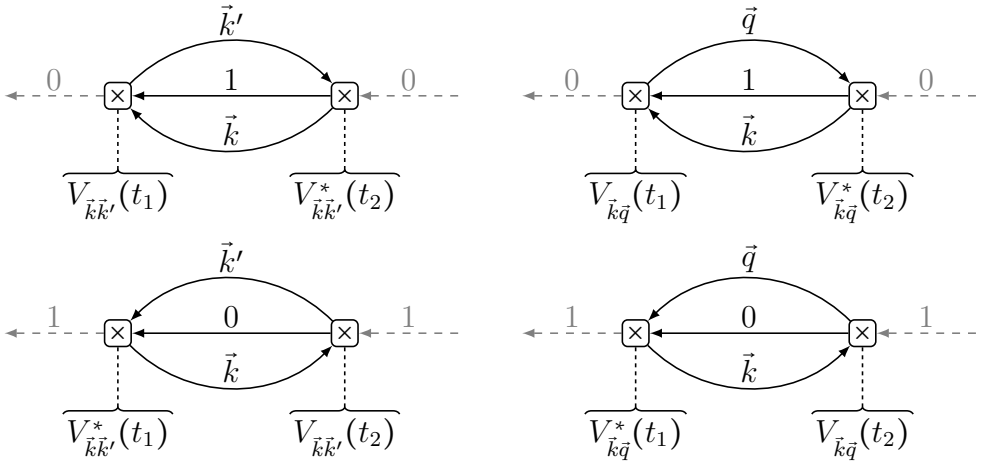

Figure 3.1: Second-order self-energy diagrams of the molecular ground state level (upper two diagrams) and the excited level (lower two diagrams). In both rows of this figure the left diagram is due to the direct de-excitation channel (1.3) while the right one pertains to the indirect reaction (1.2). Note that the gray dashed lines merely represent the diagram's connectors and do not belong to the actual self-energies.

and

$$\Sigma^A_{11}(t_1,t_2) = -\Theta(t_2-t_1)\Sigma^K_{11}(t_1,t_2)\,, \tag{3.30a}$$

$$\Sigma^R_{11}(t_1,t_2) = \Theta(t_1-t_2)\Sigma^K_{11}(t_1,t_2)\,, \tag{3.30b}$$

$$\Sigma^K_{11}(t_1,t_2) = \Sigma^{(dad)}_{11}(t_1,t_2) + \Sigma^{(iad)}_{11}(t_1,t_2)\,. \tag{3.30c}$$

Note that here and in the following the labels *dad* and *iad* are used to discriminate between the direct and indirect Auger de-excitation channels. Consequently, the terms $\Sigma^{(dad)}_{00/11}$ and $\Sigma^{(iad)}_{00/11}$ denote the components of the Keldysh self-energies $\Sigma^K_{00/11}$ due to the direct and indirect reaction, respectively. Their explicit form reads

$$\begin{aligned}\Sigma^{(dad)}_{00}(t_1,t_2) = \frac{i}{\hbar^2}\sum_{\vec{k},\vec{k}'} n_{\vec{k}}(-\infty)\big[1-n_{\vec{k}'}(-\infty)\big]V_{\vec{k}\vec{k}'}(t_1)V^*_{\vec{k}\vec{k}'}(t_2) \\ \times\, e^{-\frac{i}{\hbar}\int_{t_2}^{t_1}\mathrm{d}t_3\,[\varepsilon_{1*}(t_3)+\varepsilon_{\vec{k}}-\varepsilon_{\vec{k}'}(t_3)]}\,,\end{aligned} \tag{3.31a}$$

$$\begin{aligned}\Sigma^{(iad)}_{00}(t_1,t_2) = \frac{i}{\hbar^2}\sum_{\vec{k},\vec{q}} n_{\vec{k}}(-\infty)\big[1-n_{\vec{q}}(-\infty)\big]V_{\vec{k}\vec{q}}(t_1)V^*_{\vec{k}\vec{q}}(t_2) \\ \times\, e^{-\frac{i}{\hbar}\int_{t_2}^{t_1}\mathrm{d}t_3\,[\varepsilon_{1*}(t_3)+\varepsilon_{\vec{k}}-\varepsilon_{\vec{q}}(t_3)]}\,,\end{aligned} \tag{3.31b}$$

and

$$\Sigma^{(dad/iad)}_{11}(t_1,t_2) = \Big[\Sigma^{(dad/iad)}_{00}(t_1,t_2)\Big]^* e^{-\frac{i}{\hbar}\int_{t_2}^{t_1}\mathrm{d}t_3\,[\varepsilon_{0g}(t_3)+\varepsilon_{1*}(t_3)]}\,. \tag{3.32}$$

We now utilize the self-energies (3.29b) and (3.30b) to calculate the retarded propagators G^R_{00} and G^R_{11}. The corresponding Dyson equations can be constructed from (1.28a) and, similar to the previous section, allow for an iterative solution. A straightforward calculation yields

$$G^R_{00}(t,t') = G^{R(0)}_{00}(t,t')\,\sigma[\Delta_{dad+iad}](t,t')\,, \tag{3.33a}$$

$$G^R_{11}(t,t') = G^{R(0)}_{11}(t,t')\,\sigma[\Delta^*_{dad+iad}](t,t')\,, \tag{3.33b}$$

where σ represents the familiar infinite series of nested double integrals (see Appendix C). Here σ operates on a function $\Delta_{dad+iad}$ which itself is the sum of two complex functions given by

$$\Delta_{dad+iad}(t_1,t_2) = \Delta_{dad}(t_1,t_2) + \Delta_{iad}(t_1,t_2)\,, \tag{3.34}$$

with

$$\Delta_{dad/iad}(t_1,t_2) = -i\Sigma_{00}^{(dad/iad)}(t_1,t_2)\, e^{\frac{i}{\hbar}\int_{t_2}^{t_1} \mathrm{d}t_3\, \varepsilon_{0g}(t_3)}\,. \tag{3.35}$$

Note that the advanced propagators of the projectile levels can be obtained from the expressions (3.33) by means of (1.27),

$$G_{00}^{A}(t,t') = G_{00}^{A(0)}(t,t')\,\sigma[\Delta^*_{dad+iad}](t',t)\,, \tag{3.36a}$$

$$G_{11}^{A}(t,t') = G_{11}^{A(0)}(t,t')\,\sigma[\Delta_{dad+iad}](t',t)\,. \tag{3.36b}$$

We now calculate the transient occupancy of the projectile levels by combining (1.31) and (1.36). Employing the Keldysh self-energies (3.29c) and (3.30c) as well as the retarded and advanced propagators (3.33) and (3.36) we obtain

$$\begin{aligned} n_0^{(dad+iad)}(t) = {} & \frac{1}{2} - \frac{1}{2}\sigma[\Delta_{dad+iad}](t,-\infty)\,\sigma[\Delta^*_{dad+iad}](t,-\infty) \\ & + \frac{1}{2}\int_{-\infty}^{t}\mathrm{d}t_1 \int_{-\infty}^{t}\mathrm{d}t_2\, \Delta_{dad+iad}(t_1,t_2) \\ & \times \sigma[\Delta_{dad+iad}](t,t_1)\,\sigma[\Delta^*_{dad+iad}](t,t_2)\,, \end{aligned} \tag{3.37a}$$

$$\begin{aligned} n_1^{(dad+iad)}(t) = {} & \frac{1}{2} + \frac{1}{2}\sigma[\Delta_{dad+iad}](t,-\infty)\,\sigma[\Delta_{dad+iad}]^*(t,-\infty) \\ & - \frac{1}{2}\int_{-\infty}^{t}\mathrm{d}t_1 \int_{-\infty}^{t}\mathrm{d}t_2\, \Delta^*_{dad+iad}(t_1,t_2) \\ & \times \sigma[\Delta^*_{dad+iad}](t,t_1)\,\sigma[\Delta_{dad+iad}](t,t_2)\,. \end{aligned} \tag{3.37b}$$

Here the superscripts $(dad+iad)$ indicate that the occupation numbers are due to both the direct and the indirect Auger de-excitation channel. Employing the integral identity (C.18) and its complex conjugate the expressions (3.37) simplify to

$$n_0^{(dad+iad)}(t) = 1 - \sigma[\Delta_{dad+iad}](t,-\infty)\,\sigma[\Delta^*_{dad+iad}](t,-\infty)\,, \tag{3.38a}$$

$$n_1^{(dad+iad)}(t) = \sigma[\Delta_{dad+iad}](t,-\infty)\,\sigma[\Delta^*_{dad+iad}](t,-\infty)\,. \tag{3.38b}$$

Consequently, the total occupation of the two-level system remains constant since

$$n_0^{(dad+iad)}(t) + n_1^{(dad+iad)}(t) = 1\ \forall t\,. \tag{3.39}$$

We now turn to the electrons excited into initially empty states within the solid surface $\vec{k}'$ and electrons released into the continuum of free projectile states $\vec{q}$. The former are generated by the direct Auger de-excitation channel whereas the latter are the outcome of the indirect de-excitation reaction. The second-order self-energy diagrams for $\Sigma_{\vec{k}'\vec{k}'}$ and $\Sigma_{\vec{q}\vec{q}}$ can be obtained from the upper row of Fig. 3.1 by interchanging the labels 0 and $\vec{k}'$ in the left diagram and 0 and $\vec{q}$ in the right diagram, respectively. Note that the resulting self-energies also possess non-diagonal components which are, however, canceled in an iterative treatment of the Dyson

equations. Following along the lines of our previous calculation for the projectile's ground state level we obtain the occupation of the $\vec{k}'$- and $\vec{q}$-states in the form

$$n_{\vec{k}'}^{(dad+iad)}(t) = 1 - \left[1 - n_{\vec{k}'}(-\infty)\right] \sigma\left[\Delta_{dad}^{\vec{k}'}\right](t,-\infty) \left(\sigma\left[\Delta_{dad}^{\vec{k}'}\right](t,-\infty)\right)^* , \tag{3.40a}$$

$$n_{\vec{q}}^{(dad+iad)}(t) = 1 - \left[1 - n_{\vec{q}}(-\infty)\right] \sigma\left[\Delta_{iad}^{\vec{q}}\right](t,-\infty) \left(\sigma\left[\Delta_{iad}^{\vec{q}}\right](t,-\infty)\right)^* . \tag{3.40b}$$

Here $\Delta_{dad}^{\vec{k}'}$ and $\Delta_{iad}^{\vec{q}}$ are given by

$$\begin{aligned} \Delta_{dad}^{\vec{k}'}(t_1,t_2) = \frac{1}{\hbar^2} \sum_{\vec{k}} n_{\vec{k}}(-\infty)\, V_{\vec{k}\vec{k}'}(t_1)\, V_{\vec{k}\vec{k}'}^*(t_2) \\ \times e^{-\frac{i}{\hbar}\int_{t_2}^{t_1} \mathrm{d}t_3 \left[\varepsilon_{1*}(t_3) + \varepsilon_{\vec{k}} - \varepsilon_{0g}(t_3) - \varepsilon_{\vec{k}'}(t_3)\right]} , \end{aligned} \tag{3.41a}$$

$$\begin{aligned} \Delta_{iad}^{\vec{q}}(t_1,t_2) = \frac{1}{\hbar^2} \sum_{\vec{k}} n_{\vec{k}}(-\infty)\, V_{\vec{k}\vec{q}}(t_1)\, V_{\vec{k}\vec{q}}^*(t_2) \\ \times e^{-\frac{i}{\hbar}\int_{t_2}^{t_1} \mathrm{d}t_3 \left[\varepsilon_{1*}(t_3) + \varepsilon_{\vec{k}} - \varepsilon_{0g}(t_3) - \varepsilon_{\vec{q}}(t_3)\right]} , \end{aligned} \tag{3.41b}$$

which after comparison with (3.35) leads to

$$\sum_{\vec{k}'} \left[1 - n_{\vec{k}'}(-\infty)\right] \Delta_{dad}^{\vec{k}'}(t_1,t_2) = \Delta_{dad}(t_1,t_2) , \tag{3.42a}$$

$$\sum_{\vec{q}} \left[1 - n_{\vec{q}}(-\infty)\right] \Delta_{iad}^{\vec{q}}(t_1,t_2) = \Delta_{iad}(t_1,t_2) . \tag{3.42b}$$

Unfortunately, Eqs. (3.40) are not very useful, because they cannot easily be summed over $\vec{k}'$ and $\vec{q}$. This is, however, required in order to calculate the total number of Auger electrons. Moreover, the individual occupancies (3.40a) and (3.40b) are isolated that means they neglect the destruction of the metastable state by the respective other de-excitation channel. To make this more clear one may imagine a situation where the direct de-excitation reaction is only efficient at small distances from the surface while the indirect Auger channel is so effective that the metastable projectile is completely de-excited already at very large projectile-surface separations. In such a case the direct channel cannot operate at all since the metastable state is already destroyed entirely before it gets close enough to the surface. This behavior is, however, not reflected by Eq. (3.40a) as the latter only involves terms containing the direct matrix element $V_{\vec{k}\vec{k}'}$ but no contributions due to the indirect de-excitation channel.

Because of these obstacles we adopt the approach of Makoshi[86,87] and expand the general expression for the Keldysh components $G^K_{\vec{k}'\vec{k}'}$ and $G^K_{\vec{q}\vec{q}}$ (see Eq. (1.36)) up to first order in the self-energies. To make up for this approximation we replace the unperturbed Green function of the excited projectile level with the full propagator in the self-energies of the $\vec{k}'$- and $\vec{q}$-states. One may think of this propagator dressing as a way of accounting for lifetime effects of the excited projectile level[86]. Note, however, that the very same effect could also be achieved by employing the full propagator of the molecular ground state level instead. The second-order self-energy diagrams resulting from the dressing of the excited level are shown in Fig. 3.2. The

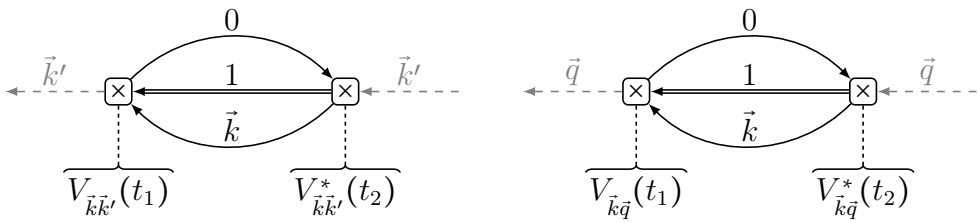

Figure 3.2: Second-order diagrammatic representation of the dressed self-energies $\Sigma_{\vec{k}'\vec{k}'}$ (left panel) and $\Sigma_{\vec{q}\vec{q}}$ (right panel). The full propagator of the excited level G_{11} is indicated by a double line.

Keldysh components of these diagrams evaluate to

$$\Sigma^K_{\vec{k}'\vec{k}'}(t_1,t_2) = \frac{1}{\hbar^2}\sum_{\vec{k}} V_{\vec{k}\vec{k}'}(t_1)\, V^*_{\vec{k}\vec{k}'}(t_2)\, G^{-+(0)}_{00}(t_2,t_1)\, G^{+-(0)}_{\vec{k}\vec{k}}(t_1,t_2)\, G^{+-}_{11}(t_1,t_2)\,, \tag{3.43a}$$

$$\Sigma^K_{\vec{q}\vec{q}}(t_1,t_2) = \frac{1}{\hbar^2}\sum_{\vec{k}} V_{\vec{k}\vec{q}}(t_1)\, V^*_{\vec{k}\vec{q}}(t_2)\, G^{-+(0)}_{00}(t_2,t_1)\, G^{+-(0)}_{\vec{k}\vec{k}}(t_1,t_2)\, G^{+-}_{11}(t_1,t_2)\,. \tag{3.43b}$$

In order to proceed we, thus, need to calculate the full Green function G^{+-}_{11}. For this purpose, we first rewrite the corresponding component of the matrix Dyson equation (see Sec. 1.3.2) into

$$G^{+-}_{11}(t,t') = \left\{G^{+-(0)}_{11} * \left[1 + \Sigma^A_{11} * G^A_{11}\right]\right\}(t,t') + \left\{G^{R(0)}_{11} * \Sigma^R_{11} * G^{+-}_{11}\right\}(t,t')\,, \tag{3.44}$$

where we have employed $\Sigma^{++}_{11}(t_1,t_2) = \Sigma^R_{11}(t_1,t_2)$ and $\Sigma^{--}_{11}(t_1,t_2) = -\Sigma^A_{11}(t_1,t_2)$ which follows directly from (3.30). Inserting the latter self-energy components and the full advanced Green function (3.36b) we can solve Eq. (3.44) iteratively and obtain

$$\begin{aligned} G^{+-}_{11}(t,t') = {} & G^{+-(0)}_{11}(t,t')\,\sigma[\Delta^*_{dad+iad}](t,-\infty) \\ & \times\left[1 - \int_{-\infty}^{t'}\mathrm{d}t_1 \int_{t_1}^{t'}\mathrm{d}t_2\, \sigma[\Delta_{dad+iad}](t',t_2)\,\Delta_{dad+iad}(t_2,t_1)\right]. \end{aligned} \tag{3.45}$$

After interchanging t_1 and t_2 in the integral term of (3.45) we can apply the identity (C.12) which results in

$$G^{+-}_{11}(t,t') = G^{+-(0)}_{11}(t,t')\,\sigma[\Delta^*_{dad+iad}](t,-\infty)\,\sigma[\Delta_{dad+iad}](t',-\infty)\,. \tag{3.46}$$

Employing the Green function (3.46) in the Keldysh self-energies (3.43a) and (3.43b) we then find

$$\Sigma^K_{\vec{k}'\vec{k}'}(t_1,t_2) = \frac{i}{\hbar^2}\sum_{\vec{k}} n_{\vec{k}}(-\infty)\,\mathcal{V}_{\vec{k}\vec{k}'}(t_1)\,\mathcal{V}^*_{\vec{k}\vec{k}'}(t_2)\, e^{-\frac{i}{\hbar}\int_{t_2}^{t_1}\mathrm{d}t_3\left[\varepsilon_{1*}(t_3)+\varepsilon_{\vec{k}}-\varepsilon_{0g}(t_3)\right]}\,, \tag{3.47a}$$

$$\Sigma^K_{\vec{q}\vec{q}}(t_1,t_2) = \frac{i}{\hbar^2}\sum_{\vec{k}} n_{\vec{k}}(-\infty)\,\mathcal{V}_{\vec{k}\vec{q}}(t_1)\,\mathcal{V}^*_{\vec{k}\vec{q}}(t_2)\, e^{-\frac{i}{\hbar}\int_{t_2}^{t_1}\mathrm{d}t_3\left[\varepsilon_{1*}(t_3)+\varepsilon_{\vec{k}}-\varepsilon_{0g}(t_3)\right]}\,, \tag{3.47b}$$

where $\mathcal{V}_{\vec{k}\vec{k}'}$ and $\mathcal{V}_{\vec{k}\vec{q}}$ denote the renormalized Auger matrix elements

$$\mathcal{V}_{\vec{k}\vec{k}'}(t) = V_{\vec{k}\vec{k}'}(t)\,\sigma[\Delta^*_{dad+iad}](t,-\infty)\,, \tag{3.48a}$$

$$\mathcal{V}_{\vec{k}\vec{q}}(t) = V_{\vec{k}\vec{q}}(t)\,\sigma[\Delta^*_{dad+iad}](t,-\infty)\,. \tag{3.48b}$$

As we see, here the individual matrix elements of direct and indirect Auger de-excitation are renormalized by the σ-series of $\Delta^{*}_{dad+iad}$ which is due to both Auger reaction channels. The inclusion of the σ-terms in renormalized matrix elements as proposed by Makoshi[86] does, however, not provide any further insight. In fact it might be even more advantageous to keep the σ-series out of the matrix elements which allows us to write the self-energies (3.47) in terms of $\Delta^{\vec{k}'}_{dad}$ and $\Delta^{\vec{q}}_{iad}$ (see Eqs. (3.41)),

$$\begin{aligned}\Sigma^{K}_{\vec{k}'\vec{k}'}(t_1,t_2) &= i\Delta^{\vec{k}'}_{dad}(t_1,t_2)\, e^{-\frac{i}{\hbar}\int_{t_2}^{t_1} \mathrm{d}t_3\, \varepsilon_{\vec{k}'}} \\ &\quad \times \sigma[\Delta^{*}_{dad+iad}](t_1,-\infty)\, \sigma[\Delta_{dad+iad}](t_2,-\infty)\;, \end{aligned} \tag{3.49a}$$

$$\begin{aligned}\Sigma^{K}_{\vec{q}\vec{q}}(t_1,t_2) &= i\Delta^{\vec{q}}_{iad}(t_1,t_2)\, e^{-\frac{i}{\hbar}\int_{t_2}^{t_1} \mathrm{d}t_3\, \varepsilon_{\vec{q}}} \\ &\quad \times \sigma[\Delta^{*}_{dad+iad}](t_1,-\infty)\, \sigma[\Delta_{dad+iad}](t_2,-\infty)\;. \end{aligned} \tag{3.49b}$$

We now proceed with the calculation of the occupation of $\vec{k}'$- and $\vec{q}$-states due to both Auger channels. Combining (1.31) and (1.36) we obtain

$$\begin{aligned} n^{(dad+iad)}_{\alpha}(t) &= \frac{1}{2}\Big[1-\sum_{\beta}\big[1-2n_{\alpha}(-\infty)\big]G^{R}_{\alpha\beta}(t,-\infty)\, G^{A}_{\beta\alpha}(-\infty,t)\Big] \\ &\quad -\frac{i}{2}\Big\{G^{R}_{\alpha\beta} * \Sigma^{K}_{\beta\gamma} * G^{A}_{\gamma\alpha}\Big\}(t,t)\;, \end{aligned} \tag{3.50}$$

where α stands for either $\vec{k}'$ or $\vec{q}$, β and γ run over all states of the system and, as before, the superscript $(dad+iad)$ indicates that the occupancy is due to both de-excitation channels. Note that the latter dependence is implicitly contained in $\Sigma^{K}_{\alpha\alpha}$ (see Eqs. (3.49)). We now expand (3.50) up to first order in the self-energy terms by inserting the once iterated advanced and retarded Dyson equations,

$$G^{A/R}_{\alpha\beta}(t,t') \approx G^{A/R(0)}_{\alpha\alpha}(t,t')\,\delta_{\alpha\beta} + \Big\{G^{A/R(0)}_{\alpha\alpha} * \Sigma^{A/R}_{\alpha\beta} * G^{A/R(0)}_{\beta\beta}\Big\}(t,t')\;. \tag{3.51}$$

After neglecting terms of higher than first order in the self-energies only diagonal terms survive. Upon employing[4]

$$\begin{aligned} \Sigma^{A}_{\alpha\alpha}(t_1,t_2) - \Sigma^{R}_{\alpha\alpha}(t_1,t_2) &= \underbrace{\Sigma^{++}_{\alpha\alpha}(t_1,t_2) + \Sigma^{--}_{\alpha\alpha}(t_1,t_2)}_{\Sigma^{K}_{\alpha\alpha}(t_1,t_2)} + 2\underbrace{\Sigma^{-+}_{\alpha\alpha}(t_1,t_2)}_{\sim n_0(-\infty)=0} \\ &= \Sigma^{K}_{\alpha\alpha}(t_1,t_2)\;, \end{aligned} \tag{3.52}$$

we, finally, arrive at[87]

$$\begin{aligned} n^{(dad+iad)}_{\alpha}(t) &\approx n_{\alpha}(-\infty) - i\big[1-n_{\alpha}(-\infty)\big] \\ &\quad \times \int_{-\infty}^{t}\mathrm{d}t_1 \int_{-\infty}^{t}\mathrm{d}t_2\, G^{R(0)}_{\alpha\alpha}(t,t_1)\, \Sigma^{K}_{\alpha\alpha}(t_1,t_2)\, G^{A(0)}_{\alpha\alpha}(t_2,t')\;. \end{aligned} \tag{3.53}$$

Concretizing (3.53) for $\alpha = \vec{k}'$ and $\alpha = \vec{q}$ by utilizing the self-energies (3.49) we then

[4] Remember that here α can only take the values $\vec{k}'$ or $\vec{q}$.

find

$$n_{\vec{k}'}^{(dad+iad)}(t) \approx n_{\vec{k}'}(-\infty) + \left[1 - n_{\vec{k}'}(-\infty)\right] \int_{-\infty}^{t} \mathrm{d}t_1 \int_{-\infty}^{t} \mathrm{d}t_2 \; \Delta_{dad}^{\vec{k}'}(t_1, t_2) \times \sigma[\Delta_{dad+iad}^{*}](t_1, -\infty)\, \sigma[\Delta_{dad+iad}](t_2, -\infty) \,, \tag{3.54a}$$

$$n_{\vec{q}}^{(dad+iad)}(t) \approx n_{\vec{q}}(-\infty) + \left[1 - n_{\vec{q}}(-\infty)\right] \int_{-\infty}^{t} \mathrm{d}t_1 \int_{-\infty}^{t} \mathrm{d}t_2 \; \Delta_{iad}^{\vec{q}}(t_1, t_2) \times \sigma[\Delta_{dad+iad}^{*}](t_1, -\infty)\, \sigma[\Delta_{dad+iad}](t_2, -\infty) \,. \tag{3.54b}$$

We stress that in contrast to (3.40a) and (3.40b), Eqs. (3.54a) and (3.54b) are not isolated since here $\Delta_{dad}^{\vec{k}'}$ and $\Delta_{iad}^{\vec{q}}$ are renormalized by σ-terms operating on $\Delta_{dad+iad}$ which is due to both reaction channels. Moreover, (3.54a) and (3.54b) can be used to calculate the total number of electrons ending up in $\vec{k}'$- and $\vec{q}$-states. For this purpose we sum these equations over all initially empty $\vec{k}'$- and $\vec{q}$-states, respectively,

$$n_{dad}^{(dad+iad)}(t) = \sum_{\vec{k}'} \left[1 - n_{\vec{k}'}(-\infty)\right] n_{\vec{k}'}^{(dad+iad)}(t) \,, \tag{3.55a}$$

$$n_{iad}^{(dad+iad)}(t) = \sum_{\vec{q}} \left[1 - n_{\vec{q}}(-\infty)\right] n_{\vec{q}}^{(dad+iad)}(t) \,. \tag{3.55b}$$

Note that in (3.55) the subscripts dad and iad denote the respective channel responsible for transferring electrons into $\vec{k}'$- or $\vec{q}$-states while the superscripts $(dad + iad)$ indicate that the renormalization effect of both channels is included. Making use of (3.42) and (3.54) we find

$$n_{dad}^{(dad+iad)}(t) = \int_{-\infty}^{t} \mathrm{d}t_1 \int_{-\infty}^{t} \mathrm{d}t_2 \; \Delta_{dad}(t_1, t_2) \times \sigma[\Delta_{dad+iad}^{*}](t_1, -\infty)\, \sigma[\Delta_{dad+iad}](t_2, -\infty) \,, \tag{3.56a}$$

$$n_{iad}^{(dad+iad)}(t) = \int_{-\infty}^{t} \mathrm{d}t_1 \int_{-\infty}^{t} \mathrm{d}t_2 \; \Delta_{iad}(t_1, t_2) \times \sigma[\Delta_{dad+iad}^{*}](t_1, -\infty)\, \sigma[\Delta_{dad+iad}](t_2, -\infty) \,. \tag{3.56b}$$

Considering the total number of Auger electrons due to both channels we can employ (C.15) to obtain

$$n^{(dad+iad)}(t) = n_{dad}^{(dad+iad)}(t) + n_{iad}^{(dad+iad)}(t) \tag{3.57a}$$

$$= 1 - \sigma[\Delta_{dad+iad}](t, -\infty)\, \sigma[\Delta_{dad+iad}^{*}](t, -\infty) \,. \tag{3.57b}$$

Comparing this result to (3.38a) we then find the relation

$$n^{(dad+iad)}(t) = n_0^{(dad+iad)}(t) \;\forall t \,. \tag{3.58}$$

Consequently, at any instant of time the amount of charge transferred into the projectile's ground state level equals the total number of electrons excited into $\vec{k}'$-states or released into $\vec{q}$-states. Hence, the probability of metastable de-excitation is equal to the probability of finding an electron in the $\vec{k}'$- and $\vec{q}$-states. Our approximate treatment of the latter states, thus, guarantees particle conservation.

In contrast to the total number of Auger electrons, the expressions for the individual occupancies (3.56a) and (3.56b) cannot be simplified further as long as both

de-excitation channels are active simultaneously. If, on the other hand, only one of the channels is open we can employ (C.15) to obtain

$$n_{dad}^{(dad)}(t) = 1 - \sigma[\Delta_{dad}](t,-\infty)\,\sigma[\Delta_{dad}^{*}](t,-\infty)\;, \tag{3.59a}$$

$$n_{iad}^{(iad)}(t) = 1 - \sigma[\Delta_{iad}](t,-\infty)\,\sigma[\Delta_{iad}^{*}](t,-\infty)\;. \tag{3.59b}$$

In either case the number of electrons ending up in $\vec{k}'$- and $\vec{q}$-states does not equal the number of electrons that can escape the surface, as was explained in Sec. 2.6. In order to strip out those Auger electrons that are trapped within the surface or in the image potential in front of it we, thus, need to employ the surface transmission functions $\mathcal{T}_{\vec{k}'}$ and $\mathcal{T}_{\vec{q}}$ (see Eqs. (2.89a) and (2.89b)), respectively. Following along the lines of Sec. 3.1 we introduce the functions

$$\widetilde{\Delta}_{dad}^{\vec{k}'}(t_1,t_2) = \mathcal{T}_{\vec{k}'}(t_1)\,\mathcal{T}_{\vec{k}'}(t_2)\,\Delta_{dad}^{\vec{k}'}(t_1,t_2)\;, \tag{3.60a}$$

$$\widetilde{\Delta}_{iad}^{\vec{q}}(t_1,t_2) = \mathcal{T}_{\vec{q}}(t_1)\,\mathcal{T}_{\vec{q}}(t_2)\,\Delta_{iad}^{\vec{q}}(t_1,t_2)\;. \tag{3.60b}$$

The distribution of escaped electrons over initially unoccupied $\vec{k}'$- and $\vec{q}$-states, $\tilde{n}_{\vec{k}'}$ and $\tilde{n}_{\vec{q}}$, can then be obtained by replacing $\Delta_{dad}^{\vec{k}'}$ and $\Delta_{iad}^{\vec{q}}$ with $\widetilde{\Delta}_{dad}^{\vec{k}'}$ and $\widetilde{\Delta}_{iad}^{\vec{q}}$ in (3.54a) and (3.54b),

$$\begin{aligned}\tilde{n}_{\vec{k}'}^{(dad+iad)}(t) \approx \int_{-\infty}^{t}\mathrm{d}t_1 \int_{-\infty}^{t}\mathrm{d}t_2\; \widetilde{\Delta}_{dad}^{\vec{k}'}(t_1,t_2) \\ \times \sigma[\Delta_{dad+iad}^{*}](t_1,-\infty)\,\sigma[\Delta_{dad+iad}](t_2,-\infty)\;,\end{aligned} \tag{3.61a}$$

$$\begin{aligned}\tilde{n}_{\vec{q}}^{(dad+iad)}(t) \approx \int_{-\infty}^{t}\mathrm{d}t_1 \int_{-\infty}^{t}\mathrm{d}t_2\; \widetilde{\Delta}_{iad}^{\vec{q}}(t_1,t_2) \\ \times \sigma[\Delta_{dad+iad}^{*}](t_1,-\infty)\,\sigma[\Delta_{dad+iad}](t_2,-\infty)\;.\end{aligned} \tag{3.61b}$$

The overall number of escaped electrons in $\vec{k}'$- and $\vec{q}$-states follows after summing (3.61a) and (3.61b) over all initially empty $\vec{k}'$- and $\vec{q}$-states, respectively,

$$\begin{aligned}\tilde{n}_{dad}^{(dad+iad)}(t) = \int_{-\infty}^{t}\mathrm{d}t_1 \int_{-\infty}^{t}\mathrm{d}t_2\; \widetilde{\Delta}_{dad}(t_1,t_2) \\ \times \sigma[\Delta_{dad+iad}^{*}](t_1,-\infty)\,\sigma[\Delta_{dad+iad}](t_2,-\infty)\;,\end{aligned} \tag{3.62a}$$

$$\begin{aligned}\tilde{n}_{iad}^{(dad+iad)}(t) = \int_{-\infty}^{t}\mathrm{d}t_1 \int_{-\infty}^{t}\mathrm{d}t_2\; \widetilde{\Delta}_{iad}(t_1,t_2) \\ \times \sigma[\Delta_{dad+iad}^{*}](t_1,-\infty)\,\sigma[\Delta_{dad+iad}](t_2,-\infty)\;.\end{aligned} \tag{3.62b}$$

Here we have introduced the quantities

$$\widetilde{\Delta}_{dad}(t_1,t_2) = \sum_{\vec{k}'}\big[1 - n_{\vec{k}'}(-\infty)\big]\,\widetilde{\Delta}_{dad}^{\vec{k}'}(t_1,t_2)\;, \tag{3.63a}$$

$$\widetilde{\Delta}_{iad}(t_1,t_2) = \sum_{\vec{q}}\big[1 - n_{\vec{q}}(-\infty)\big]\,\widetilde{\Delta}_{iad}^{\vec{q}}(t_1,t_2)\;. \tag{3.63b}$$

Finally, the secondary electron emission coefficient $\gamma_e^{(dad+iad)}$ due to both Auger de-excitation channels is given by the final overall number of escaped Auger electrons $\tilde{n}^{(dad+iad)}$ which follows from the addition of (3.62a) and (3.62b) at $t = \infty$,

$$\gamma_e^{(dad+iad)} = \tilde{n}^{(dad+iad)}(\infty) = \tilde{n}_{dad}^{(dad+iad)}(\infty) + \tilde{n}_{iad}^{(dad+iad)}(\infty)\;. \tag{3.64}$$

Note that due to their structure Eqs. (3.61a), (3.61b), (3.62a) and (3.62b) can not be simplified further analytically.

We stress that apart from our expansion of the Dyson equations of $G^K_{\vec{k}'\vec{k}'}$ and $G^K_{\vec{q}\vec{q}}$, which we made up for by introducing dressed self-energies, so far all of the results of this section are exact up to second order in the Auger matrix elements. However, as mentioned earlier, the infinite σ-series is difficult to handle in a numerical treatment. If, on the other hand, we assume that $\Delta_{dad}(t_1,t_2)$ and $\Delta_{iad}(t_1,t_2)$ are peaked about the time diagonal $t_1 = t_2$, we can approximate all of the σ-terms by means of (C.8). As a result, the projectile occupations (3.38) turn into

$$n_0^{(dad+iad)}(t) \approx 1 - e^{-\int_{-\infty}^{t} \mathrm{d}t_1 \int_{-\infty}^{t} \mathrm{d}t_2 \, \Delta_{dad+iad}(t_1,t_2)} \,, \tag{3.65a}$$

$$n_1^{(dad+iad)}(t) \approx e^{-\int_{-\infty}^{t} \mathrm{d}t_1 \int_{-\infty}^{t} \mathrm{d}t_2 \, \Delta_{dad+iad}(t_1,t_2)} \,. \tag{3.65b}$$

Similarly, the equation for the total number of Auger electrons (3.57b) becomes

$$n^{(dad+iad)}(t) \approx 1 - e^{-\int_{-\infty}^{t} \mathrm{d}t_1 \int_{-\infty}^{t} \mathrm{d}t_2 \, \Delta_{dad+iad}(t_1,t_2)} \,. \tag{3.66}$$

Moreover, for the total number of escaped electrons $\tilde{n}^{(dad+iad)}$ a particularly convenient approximation arises when we replace $\Delta_{dad+iad}$ with $\widetilde{\Delta}_{dad+iad}$ in the σ-terms of (3.62). We then can simplify the resulting equation by means of the integral identity (C.15) and obtain

$$\tilde{n}^{(dad+iad)}(t) = \tilde{n}^{(dad+iad)}_{dad}(t) + \tilde{n}^{(dad+iad)}_{iad}(t) \approx 1 - e^{-\int_{-\infty}^{t} \mathrm{d}t_1 \int_{-\infty}^{t} \mathrm{d}t_2 \, \widetilde{\Delta}_{dad+iad}(t_1,t_2)} \,, \tag{3.67}$$

which leads to

$$\gamma_e^{(dad+iad)} \approx 1 - e^{-\int_{-\infty}^{\infty} \mathrm{d}t_1 \int_{-\infty}^{\infty} \mathrm{d}t_2 \, \widetilde{\Delta}_{dad+iad}(t_1,t_2)} \,. \tag{3.68}$$

This kind of approximation does underestimate the lifetime effect of the metastable since in contrast to $\Delta_{dad+iad}$ the quantity $\widetilde{\Delta}_{dad+iad}$ is cropped by the surface transmission functions. Nevertheless, the lifetime effect is still included to some extent. Moreover, for the case of small de-excitation probabilities (3.67) constitutes an excellent approximation since here the σ-terms in (3.62) are close to unity already for $\Delta_{dad+iad}$.

Let us finally remark that although, as far as the logic of our approach is concerned, we closely followed Makoshi[86], our results have wider applicability. First of all, we did consider the interplay of direct and indirect Auger de-excitation while Makoshi was only concerned with the latter. Moreover, in contrast to him we are not restricted to a specific form of the matrix element and have not employed the wide-band approximation for the $\vec{k}'$- and $\vec{q}$-states which would lead to time-local self-energies. Finally, we are not limited to the approximate results following from the replacement of the σ-terms by (C.8) as in principle we can calculate corrections to these expressions using the higher order expansion coefficients of the σ-series.

3.3 Unification of Auger and Two-Step Resonant De-Excitation

Having analyzed the electron capture and surface-induced electron emission subreactions of the two-step resonant de-excitation channel (1.1) as well as the Auger

de-excitation channels (1.2) and (1.3) in Secs. 3.1 and 3.2, respectively, we will now investigate the interplay of these processes. As outlined in Sec. 2.5, this must be done in a slave-particle representation in order to account for the conditional coupling of the two steps of (1.1) and the intra-molecular Coulomb correlations introduced by the passive projectile electrons. The resulting Hamiltonian reads (see Eq. (2.83))

$$\begin{aligned}\hat{H}(t) = {} & \varepsilon_g(t)\, b_g^\dagger b_g + \varepsilon_*(t)\, b_*^\dagger b_* + \varepsilon_-(t)\, f_-^\dagger f_- \\ & + \sum_{\vec{k}} \varepsilon_{\vec{k}}\, c_{\vec{k}}^\dagger c_{\vec{k}} + \sum_{\vec{q}} \varepsilon_{\vec{q}}(t)\, c_{\vec{q}}^\dagger c_{\vec{q}} + \omega_0\, b_0^\dagger b_0 + \omega_1\, b_1^\dagger b_1 \\ & - \sum_{\vec{k}} \Big[V_{\vec{k}}(t)\, c_{\vec{k}}^\dagger\, b_0^\dagger\, b_*^\dagger\, f_- + \text{H.c.} \Big] + \sum_{\vec{q}} \Big[V_{\vec{q}}(t)\, c_{\vec{q}}^\dagger\, b_1^\dagger\, b_g^\dagger\, f_- + \text{H.c.} \Big] \\ & + \sum_{\vec{k},\vec{k}'} \Big[V_{\vec{k}\vec{k}'}(t)\, c_{\vec{k}'}^\dagger\, c_{\vec{k}}\, b_g^\dagger\, b_* + \text{H.c.} \Big] + \sum_{\vec{k},\vec{q}} \Big[V_{\vec{k}\vec{q}}(t)\, c_{\vec{k}}\, c_{\vec{q}}^\dagger\, b_g^\dagger\, b_* + \text{H.c.} \Big] ,\end{aligned} \tag{3.69}$$

and is supplemented by the constraint

$$Q = b_g^\dagger b_g + b_*^\dagger b_* + f_-^\dagger f_- + f_+^\dagger f_+ = 1 , \tag{3.70}$$

which needs to be enforced in the course of our calculation. Here the levels g, $*$ and $-$ represent the pseudo-particle states associated with the molecular ground state $N_2(^1\Sigma_g^+)$, the metastable molecule $N_2(^3\Sigma_u^+)$ and the negative ion $N_2^-(^2\Pi_g)$, respectively. The intra-molecular Coulomb correlations arising in these configurations are handled by means of the auxiliary bosons $b_{0/1}^{(\dagger)}$. Moreover, as before, $\vec{q}$ and $\vec{k}^{(\prime)}$ label molecular continuum states and states within the solid surface, respectively. In addition, $V_{\vec{k}}$ and $V_{\vec{q}}$ constitute the matrix elements of resonant electron capture and surface-induced resonant electron release whereas $V_{\vec{k}\vec{k}'}$ and $V_{\vec{k}\vec{q}}$ stand for the matrix elements of direct and indirect Auger de-excitation. Note that the effect of resonant electron emission due to the natural decay of $N_2^-(^2\Pi_g)$ will be manually incorporated into our description later on in this section.

We will now treat the system (3.69) by means of the non-equilibrium Green function technique. In contrast to the previous sections of this chapter, here we will employ the formulation due to Kadanoff and Baym instead of Keldysh's matrix notation. This allows us to compare our results to the previous works of Langreth et al.[3,76,120] who investigated systems similar to (3.69). In addition, we can make use of the powerful Langreth-Wilkins rules[77] (see Appendix B) which lead to the final quantum-kinetic equations in a more direct way.

We start our analysis with a consideration of the self-energy terms. Since the occupation of $\vec{k}'$- and $\vec{q}$-states[5] will be obtained from the projectile occupations by a logical argument at the end of our calculation, we merely have to focus on the self-energies associated with the three different pseudo-particle states g, $*$ and $-$. For the latter we truncate the diagrammatic expansion beyond the second order and employ the commonly used self-consistent non-crossing approximation[76]. The resulting diagrams for the fermionic self-energy Σ_{--} and the bosonic self-energies Π_{**} and Π_{gg} are shown in Figs. 3.3, 3.4 and 3.5, respectively. Mathematically they

[5] Remember that by convention we label initially unoccupied excited states within the surface with $\vec{k}'$.

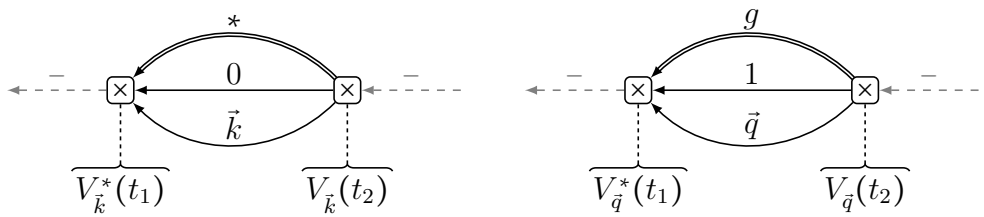

Figure 3.3: Second-order self-energy diagrams of the negative ion state in non-crossing approximation. Here the left diagram represents the contribution to Σ_{--} due to resonant electron capture while the right diagram pertains to the surface-induced resonant electron emission. As before, a double line indicates a full propagator.

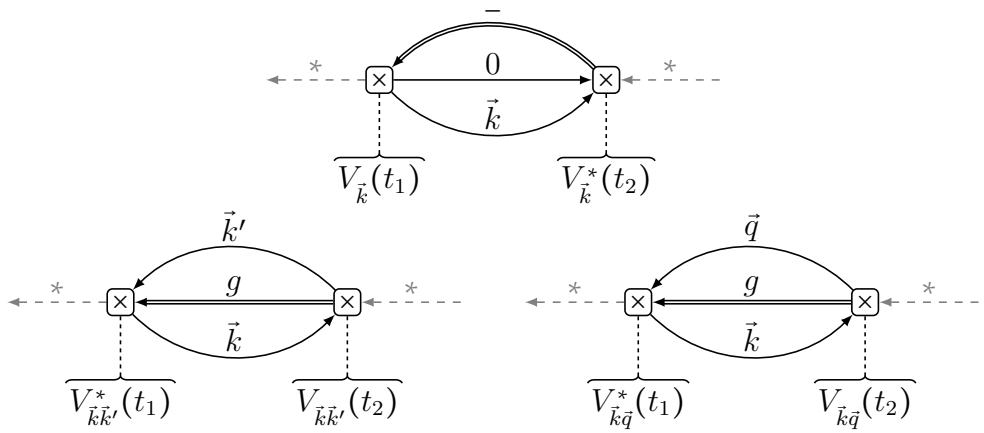

Figure 3.4: Second-order self-energy diagrams of the metastable state in non-crossing approximation. The upper diagram depicts the component of Σ_{**} due to resonant electron capture whereas the lower left and right diagrams constitute the direct and indirect Auger term, respectively. Here again a double line symbolizes a full propagator.

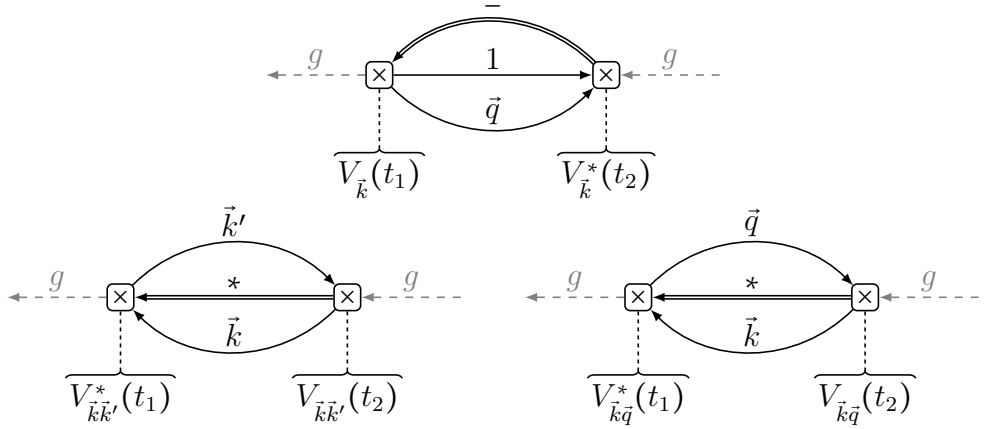

Figure 3.5: Second-order self-energy diagrams of the ground state in non-crossing approximation. Here the upper diagram pertains to the surface-induced resonant electron emission while the lower left and right diagrams embrace the contributions to Σ_{gg} due to direct and indirect Auger de-excitation, respectively. Like before, a double line stands for a full propagator.

evaluate to

$$\Sigma_{--}(t_1,t_2) = i\,\chi_{rc}(t_1,t_2)\,B_{**}(t_1,t_2) + i\,\chi_{rr}(t_1,t_2)\,B_{gg}(t_1,t_2)\;, \tag{3.71a}$$

$$\Pi_{**}(t_1,t_2) = -i\,\chi_{rc}(t_2,t_1)\,G_{--}(t_1,t_2) + \chi_{dad+iad}(t_1,t_2)\,B_{gg}(t_1,t_2)\;, \tag{3.71b}$$

$$\Pi_{gg}(t_1,t_2) = -i\,\chi_{rr}(t_2,t_1)\,G_{--}(t_1,t_2) + \chi_{dad+iad}(t_2,t_1)\,B_{**}(t_1,t_2)\;. \tag{3.71c}$$

Note that here we employed the subscript notation established in the previous sections of this chapter. Consequently, the terms χ_{rc}, χ_{rr} and $\chi_{dad+iad} = \chi_{dad} + \chi_{iad}$ pertain to the individual reactions of resonant electron capture, surface-induced resonant electron release, direct Auger de-excitation and indirect Auger de-excitation, respectively. The explicit form of these quantities reads

$$\chi_{rc}(t_1,t_2) = \frac{i}{\hbar^2}\sum_{\vec{k}} V^*_{\vec{k}}(t_1)\,V_{\vec{k}}(t_2)\,G^{(0)}_{\vec{k}\vec{k}}(t_1,t_2)\,B^{(0)}_{00}(t_1,t_2)\;, \tag{3.72a}$$

$$\chi_{rr}(t_1,t_2) = \frac{i}{\hbar^2}\sum_{\vec{q}} V^*_{\vec{q}}(t_1)\,V_{\vec{q}}(t_2)\,G^{(0)}_{\vec{q}\vec{q}}(t_1,t_2)\,B^{(0)}_{11}(t_1,t_2)\;, \tag{3.72b}$$

$$\chi_{dad}(t_1,t_2) = -\frac{1}{\hbar^2}\sum_{\vec{k},\vec{k}'} V^*_{\vec{k}\vec{k}'}(t_1)\,V_{\vec{k}\vec{k}'}(t_2)\,G^{(0)}_{\vec{k}\vec{k}}(t_2,t_1)\,G^{(0)}_{\vec{k}'\vec{k}'}(t_1,t_2)\;, \tag{3.72c}$$

$$\chi_{iad}(t_1,t_2) = -\frac{1}{\hbar^2}\sum_{\vec{k},\vec{q}} V^*_{\vec{k}\vec{q}}(t_1)\,V_{\vec{k}\vec{q}}(t_2)\,G^{(0)}_{\vec{k}\vec{k}}(t_2,t_1)\,G^{(0)}_{\vec{q}\vec{q}}(t_1,t_2)\;. \tag{3.72d}$$

As we see, the χ-terms contain unprojected propagators and, hence, possess a propagator character themselves. Moreover, since each of these terms represents an individual (sub)reaction, the resonant and Auger de-excitation channels are separated within the self-energies (3.71). A coupling of the reactions does, however, arise through the dressed propagators introduced by the non-crossing approximation.

We now investigate the effect of the self-energies (3.71) within the Dyson equations. Using the Langreth-Wilkins rules for analytic continuation (see Refs. [76, 77] and Appendix B) we obtain the Dyson equations for the lesser Green functions,

$$\begin{aligned}\left(i\frac{\partial}{\partial t} - \frac{\varepsilon_-(t)}{\hbar}\right) G^<_{--}(t,t') &= \int_{-\infty}^{t} \mathrm{d}t_1\; \Sigma^R_{--}(t,t_1)\,G^<_{--}(t_1,t') \\ &\quad + \int_{-\infty}^{t'} \mathrm{d}t_1\; \Sigma^<_{--}(t,t_1)\,G^A_{--}(t_1,t')\;,\end{aligned} \tag{3.73a}$$

$$\begin{aligned}\left(i\frac{\partial}{\partial t} - \frac{\varepsilon_{*/g}(t)}{\hbar}\right) B^<_{**/gg}(t,t') &= \int_{-\infty}^{t} \mathrm{d}t_1\; \Pi^R_{**/gg}(t,t_1)\,B^<_{**/gg}(t_1,t') \\ &\quad + \int_{-\infty}^{t'} \mathrm{d}t_1\; \Pi^<_{**/gg}(t,t_1)\,B^A_{**/gg}(t_1,t')\;,\end{aligned} \tag{3.73b}$$

and those for the retarded propagators,

$$\left(i\frac{\partial}{\partial t} - \frac{\varepsilon_-(t)}{\hbar}\right) G^R_{--}(t,t') = \delta(t-t') + \int_{t'}^{t} \mathrm{d}t_1\; \Sigma^R_{--}(t,t_1)\,G^R_{--}(t_1,t')\;, \tag{3.74a}$$

$$\left(i\frac{\partial}{\partial t} - \frac{\varepsilon_{*/g}(t)}{\hbar}\right) B^R_{**/gg}(t,t') = \delta(t-t') + \int_{t'}^{t} \mathrm{d}t_1\; \Pi^R_{**/gg}(t,t_1)\,B^R_{**/gg}(t_1,t')\;. \tag{3.74b}$$

The projected self-energy terms appearing in these equations can again be derived by employing the Langreth-Wilkins rules from Appendix B. Making use of the explicit form of the self-energies (see Eqs. (3.71)) we find the lesser components

$$\Sigma^<_{--}(t_1,t_2) = \chi^<_{rc}(t_1,t_2)\, B^<_{**}(t_1,t_2) + \chi^<_{rr}(t_1,t_2)\, B^<_{gg}(t_1,t_2)\ , \tag{3.75a}$$

$$\Pi^<_{**}(t_1,t_2) = \chi^>_{rc}(t_2,t_1)\, G^<_{--}(t_1,t_2) + i\chi^<_{dad+iad}(t_1,t_2)\, B^<_{gg}(t_1,t_2)\ , \tag{3.75b}$$

$$\Pi^<_{gg}(t_1,t_2) = \chi^>_{rr}(t_2,t_1)\, G^<_{--}(t_1,t_2) + i\chi^>_{dad+iad}(t_2,t_1)\, B^<_{**}(t_1,t_2)\ . \tag{3.75c}$$

For the retarded self-energies the calculation is analogous and yields

$$\begin{aligned}\Sigma^R_{--}(t_1,t_2) = {}& \chi^>_{rc}(t_1,t_2)\, B^R_{**}(t_1,t_2) + \chi^R_{rc}(t_1,t_2)\, B^<_{**}(t_1,t_2) \\ & + \chi^>_{rr}(t_1,t_2)\, B^R_{gg}(t_1,t_2) + \chi^R_{rr}(t_1,t_2)\, B^<_{gg}(t_1,t_2)\ ,\end{aligned} \tag{3.76a}$$

$$\begin{aligned}\Pi^R_{**}(t_1,t_2) = {}& \chi^<_{rc}(t_2,t_1)\, G^R_{--}(t_1,t_2) + \chi^A_{rc}(t_2,t_1)\, G^<_{--}(t_1,t_2) \\ & + i\chi^>_{dad+iad}(t_1,t_2)\, B^R_{gg}(t_1,t_2) + i\chi^R_{dad+iad}(t_1,t_2)\, B^<_{gg}(t_1,t_2)\ ,\end{aligned} \tag{3.76b}$$

$$\begin{aligned}\Pi^R_{gg}(t_1,t_2) = {}& \chi^<_{rr}(t_2,t_1)\, G^R_{--}(t_1,t_2) + \chi^A_{rr}(t_2,t_1)\, G^<_{--}(t_1,t_2) \\ & + i\chi^<_{dad+iad}(t_2,t_1)\, B^R_{**}(t_1,t_2) + i\chi^A_{dad+iad}(t_2,t_1)\, B^<_{**}(t_1,t_2)\ .\end{aligned} \tag{3.76c}$$

Note that the Langreth-Wilkins rules offer some kind of freedom as to which components are used to construct the projected terms (see Appendix B). Here we have chosen those projection rules that generate only lesser and retarded full propagators. The set of Eqs. (3.73) and (3.74) is, thus, complete and can be solved without having to take the greater and advanced propagators of the levels $-$, $*$ and g into account. The latter can be calculated from the solutions of (3.73) and (3.74) by means of the definitions (1.40) and the symmetry relation (1.27). Moreover, we note that the components of (3.75) and (3.76) pertaining to the RCT channel are equivalent to the equations published by Langreth and Nordlander[76] but with two bosonic pseudo-particles instead of one and an additional energy shift caused by the auxiliary bosons.

We now turn our attention to the constraint (3.70). The set of Dyson equations (3.73) and (3.74) contains terms which violate the latter relation. Before physically meaningful information can be extracted, the Dyson equations, thus, have to be projected onto the physical subspace defined by (3.70). The procedure to achieve this is originally due to Langreth and Nordlander and has been outlined several times[3,76,139]. It is based on an inspection of the order of the Green functions in the conserved pseudo-particle number Q. In particular, the retarded functions G^R_{--}, B^R_{**} and B^R_{gg} are proportional to Q^0 while the lesser propagators $G^<_{--}$, $B^<_{**}$ and $B^<_{gg}$ are proportional to Q^1. Hence, we have to drop terms of higher order than Q^0 from the retarded self-energies (3.76) and terms of higher order than Q^1 from the lesser self-energies (3.75). We stress that this procedure is not an additional approximation but an exact projection enforced by the constraint (3.70) (see also Ref. [76]).

Before carrying out the projection, we first split off the Green functions' oscillating factors by means of the decompositions[120]

$$G^{</R/A}_{--}(t,t') = \widetilde{G}^{</R/A}_{--}(t,t')\, e^{-\frac{i}{\hbar}\int_{t'}^{t} \mathrm{d}t_1\, \varepsilon_-(t_1)}\ , \tag{3.77a}$$

$$B^{</R/A}_{**}(t,t') = \widetilde{B}^{</R/A}_{**}(t,t')\, e^{-\frac{i}{\hbar}\int_{t'}^{t} \mathrm{d}t_1\, \varepsilon_*(t_1)}\ , \tag{3.77b}$$

$$B^{</R/A}_{gg}(t,t') = \widetilde{B}^{</R/A}_{gg}(t,t')\, e^{-\frac{i}{\hbar}\int_{t'}^{t} \mathrm{d}t_1\, \varepsilon_g(t_1)}\ , \tag{3.77c}$$

and

$$\widetilde{G}^{R}_{--}(t,t') = -i\,\Theta(t-t')\,g_{--}(t,t')\,, \tag{3.78a}$$

$$\widetilde{G}^{A}_{--}(t,t') = i\,\Theta(t'-t)\,g_{--}(t,t')\,, \tag{3.78b}$$

$$\widetilde{B}^{R}_{**/gg}(t,t') = -i\,\Theta(t-t')\,b_{**/gg}(t,t')\,, \tag{3.78c}$$

$$\widetilde{B}^{A}_{**/gg}(t,t') = i\,\Theta(t'-t)\,b_{**/gg}(t,t')\,. \tag{3.78d}$$

Using the definition of the retarded and advanced Green functions (1.40) we then obtain the following relations[120]

$$g_{--}(t,t) = b_{**/gg}(t,t) = 1\,, \tag{3.79a}$$

$$g_{--}(t,t') = \big[g_{--}(t',t)\big]^{*}\,, \tag{3.79b}$$

$$b_{**/gg}(t,t') = \big[b_{**/gg}(t',t)\big]^{*}\,. \tag{3.79c}$$

Moreover, by evaluating the explicit form of the bigger and lesser components of the χ-terms according to the Langreth-Wilkins rules (see Appendix B) and comparing the results to the definitions of the Δ-functions (3.16), (3.20) and (3.35) we find the identities

$$\chi^{<}_{rc}(t,t') = \Delta_{rc}(t,t')\,e^{-\frac{i}{\hbar}\int_{t'}^{t}\mathrm{d}t_1\,[\varepsilon_{-}(t_1)-\varepsilon_{*}(t_1)]}\,, \tag{3.80a}$$

$$\chi^{>}_{rr}(t,t') = \Delta_{rr}(t,t')\,e^{-\frac{i}{\hbar}\int_{t'}^{t}\mathrm{d}t_1\,[\varepsilon_{-}(t_1)-\varepsilon_{g}(t_1)]}\,, \tag{3.80b}$$

$$\chi^{>}_{dad+iad}(t,t') = -i\Delta^{*}_{dad+iad}(t,t')\,e^{-\frac{i}{\hbar}\int_{t'}^{t}\mathrm{d}t_1\,[\varepsilon_{*}(t_1)-\varepsilon_{g}(t_1)]}\,. \tag{3.80c}$$

Furthermore, the terms $\chi^{>}_{rc} \sim \big[1-n_0(-\infty)\big]$ and $\chi^{<}_{rr} \sim n_1(-\infty)$ vanish identically due to the initial conditions $n_0(-\infty) = 1$ and $n_1(-\infty) = 0$. In addition, we can also neglect the lesser component of $\chi_{dad+iad}$ since this term involves initially empty $\vec{k}$-states and initially occupied $\vec{k}'$- and $\vec{q}$-states and, hence, does not represent the Auger de-excitation channels we consider.

We now employ the Langreth-Nordlander technique together with (3.80) and the decompositions (3.77) and (3.78) in order to project the Dyson equations (3.73) and (3.74). Within the latter equations the oscillating terms emerging from (3.77) are absorbed in the Δ-functions introduced in (3.80). For the lesser propagators we then obtain

$$\begin{aligned}\frac{\partial}{\partial t}\widetilde{G}^{<}_{--}(t,t') = &-\int_{-\infty}^{t}\mathrm{d}t_1\,\Delta_{rr}(t,t_1)\,b_{gg}(t,t_1)\,\widetilde{G}^{<}_{--}(t_1,t') \\ &+\int_{-\infty}^{t'}\mathrm{d}t_1\,\Delta_{rc}(t,t_1)\,\widetilde{B}^{<}_{**}(t,t_1)\,g_{--}(t_1,t')\,,\end{aligned} \tag{3.81a}$$

$$\begin{aligned}\frac{\partial}{\partial t}\widetilde{B}^{<}_{**}(t,t') = &-\int_{-\infty}^{t}\mathrm{d}t_1\,\Delta_{rc}(t_1,t)\,g_{--}(t,t_1)\,\widetilde{B}^{<}_{**}(t_1,t') \\ &-\int_{-\infty}^{t}\mathrm{d}t_1\,\Delta^{*}_{dad+iad}(t,t_1)\,b_{gg}(t,t_1)\,\widetilde{B}^{<}_{**}(t_1,t')\,,\end{aligned} \tag{3.81b}$$

$$\begin{aligned}\frac{\partial}{\partial t}\widetilde{B}^{<}_{gg}(t,t') = &\int_{-\infty}^{t'}\mathrm{d}t_1\,\Delta_{rr}(t_1,t)\,\widetilde{G}^{<}_{--}(t,t_1)\,b_{gg}(t_1,t') \\ &+\int_{-\infty}^{t'}\mathrm{d}t_1\,\Delta^{*}_{dad+iad}(t_1,t)\,\widetilde{B}^{<}_{**}(t,t_1)\,b_{gg}(t_1,t')\,.\end{aligned} \tag{3.81c}$$

The Dyson equations of the retarded Green functions (3.74) can be treated in an analogous way. In particular, for $t > t'$ we find

$$\frac{\partial}{\partial t} g_{--}(t,t') = -\int_{t'}^{t} \mathrm{d}t_1 \, \Delta_{rr}(t,t_1)\, b_{gg}(t,t_1)\, g_{--}(t_1,t') \,, \tag{3.82a}$$

$$\begin{aligned} \frac{\partial}{\partial t} b_{**}(t,t') = &-\int_{t'}^{t} \mathrm{d}t_1 \, \Delta_{rc}(t_1,t)\, g_{--}(t,t_1)\, b_{**}(t_1,t') \\ &-\int_{t'}^{t} \mathrm{d}t_1 \, \Delta^{*}_{dad+iad}(t,t_1)\, b_{gg}(t,t_1)\, b_{**}(t_1,t') \,, \end{aligned} \tag{3.82b}$$

$$\frac{\partial}{\partial t} b_{gg}(t,t') = 0 \,. \tag{3.82c}$$

The corresponding equations for $t < t'$ can be constructed from (3.82) and the relations (3.79b) and (3.79c). Moreover, the adjoint Dyson equations can be calculated in the same manner. For the lesser propagators for instance we obtain

$$\begin{aligned} \frac{\partial}{\partial t'} \widetilde{G}^{<}_{--}(t,t') = &-\int_{-\infty}^{t'} \mathrm{d}t_1 \, \widetilde{G}^{<}_{--}(t,t_1)\, \Delta_{rr}(t_1,t')\, b_{gg}(t_1,t') \\ &+\int_{-\infty}^{t} \mathrm{d}t_1 \, g_{--}(t,t_1)\, \Delta_{rc}(t_1,t')\, \widetilde{B}^{<}_{**}(t_1,t') \,, \end{aligned} \tag{3.83a}$$

$$\begin{aligned} \frac{\partial}{\partial t'} \widetilde{B}^{<}_{**}(t,t') = &-\int_{-\infty}^{t'} \mathrm{d}t_1 \, \widetilde{B}^{<}_{**}(t,t_1)\, \Delta_{rc}(t',t_1)\, g_{--}(t_1,t') \\ &-\int_{-\infty}^{t'} \mathrm{d}t_1 \, \widetilde{B}^{<}_{**}(t,t_1)\, b_{gg}(t_1,t')\, \Delta^{*}_{dad+iad}(t_1,t') \,, \end{aligned} \tag{3.83b}$$

$$\begin{aligned} \frac{\partial}{\partial t'} \widetilde{B}^{<}_{gg}(t,t') = &\int_{-\infty}^{t} \mathrm{d}t_1 \, b_{gg}(t,t_1)\, \Delta_{rr}(t',t_1)\, \widetilde{G}^{<}_{--}(t_1,t') \\ &+\int_{-\infty}^{t} \mathrm{d}t_1 \, b_{gg}(t,t_1)\, \widetilde{B}^{<}_{**}(t_1,t')\, \Delta^{*}_{dad+iad}(t',t_1) \,. \end{aligned} \tag{3.83c}$$

Equations (3.81), (3.82) and (3.83) constitute the final set of projected Dyson equations determining the dynamics of the system within the subspace $Q = 1$. The rate-equation-like structure of these equations is already evident. The Dyson equation of the lesser Green function of the negative ion, Eq. (3.81a), for instance, contains a production term proportional to Δ_{rc} and $\widetilde{B}^{<}_{**}$ and a loss term proportional to Δ_{rr} and $\widetilde{G}^{<}_{--}$. These terms obviously relate to the production and loss of negative ions due to the electron capture and surface-induced electron emission subreactions of (1.1).

Upon employing (3.81) and (3.83) we can now calculate the time evolution of the occupation of the different projectile states from[76]

$$\frac{\mathrm{d}n^{(rc+rr+dad+iad)}_{-}(t)}{\mathrm{d}t} = \left.\frac{\partial \widetilde{G}^{<}_{--}(t,t')}{\partial t}\right|_{t=t'} + \left.\frac{\partial \widetilde{G}^{<}_{--}(t,t')}{\partial t'}\right|_{t=t'} \,, \tag{3.84a}$$

$$\frac{\mathrm{d}n^{(rc+rr+dad+iad)}_{*}(t)}{\mathrm{d}t} = \left.\frac{\partial \widetilde{B}^{<}_{**}(t,t')}{\partial t}\right|_{t=t'} + \left.\frac{\partial \widetilde{B}^{<}_{**}(t,t')}{\partial t'}\right|_{t=t'} \,, \tag{3.84b}$$

$$\frac{\mathrm{d}n^{(rc+rr+dad+iad)}_{g}(t)}{\mathrm{d}t} = \left.\frac{\partial \widetilde{B}^{<}_{gg}(t,t')}{\partial t}\right|_{t=t'} + \left.\frac{\partial \widetilde{B}^{<}_{gg}(t,t')}{\partial t'}\right|_{t=t'} \,. \tag{3.84c}$$

Note that here, similar to the previous sections of this chapter, we added the superscripts $(rc+rr+dad+iad)$ to indicate that the occupancies are due to the combination of resonant capture and release, constituting the RCT de-excitation reaction, as well as direct and indirect Auger de-excitation. We stress that due to the coupled structure of the Dyson equations (3.81) and (3.83) each of the pseudo-particle occupations depends on all four (sub)reactions.

While being conceptually appealing, the final Dyson equations (3.81), (3.82) and (3.83) involve the strongly oscillating functions Δ_{rc}, Δ_{rr} and $\Delta^*_{dad+iad}$ which turn out to be highly problematic in a numerical treatment. If, however, these Δ-functions are sharply peaked along the time diagonal, we can apply a saddle-point approximation to the time integrals in the Dyson equations. We explicitly demonstrate this for the first integral term in (3.81a),

$$\int_{-\infty}^{t} \mathrm{d}t_1 \, \Delta_{rr}(t,t_1)\, b_{gg}(t,t_1)\, \widetilde{G}^{<}_{--}(t_1,t') \approx b_{gg}(t,t)\, \widetilde{G}^{<}_{--}(t,t') \int_{-\infty}^{t} \mathrm{d}t_1 \, \Delta_{rr}(t,t_1) \; . \tag{3.85}$$

Note that this is the same approximation that leads to the approximate exponential representation of the σ-series occurring in Secs. 3.1 and 3.2 (see also Appendix C). As mentioned earlier, the validity of this approach for the particular situations considered in the present work will be demonstrated in Sec. 4.2.3.

We now introduce the saddle-point approximation within the Dyson equations of the lesser propagators (3.81) and (3.83) and combine the latter in order to calculate the projectile occupancies from (3.84). Making use of (1.39) and (3.79a) we then obtain the set of rate equations

$$\frac{\mathrm{d}n_{-}^{(rc+rr+dad+iad)}(t)}{\mathrm{d}t} \approx -\Gamma_{rr}(t)\, n_{-}^{(rc+rr+dad+iad)}(t) + \Gamma_{rc}(t)\, n_{*}^{(rc+dad+iad)}(t) \; , \tag{3.86a}$$

$$\frac{\mathrm{d}n_{*}^{(rc+dad+iad)}(t)}{\mathrm{d}t} \approx -\big[\Gamma_{rc}(t) + \Gamma_{dad}(t) + \Gamma_{iad}(t)\big]\, n_{*}^{(rc+dad+iad)}(t) \; , \tag{3.86b}$$

$$\begin{aligned} \frac{\mathrm{d}n_{g}^{(rc+rr+dad+iad)}(t)}{\mathrm{d}t} \approx{}& \big[\Gamma_{dad}(t) + \Gamma_{iad}(t)\big]\, n_{*}^{(rc+dad+iad)}(t) \\ &+ \Gamma_{rr}(t)\, n_{-}^{(rc+rr+dad+iad)}(t) \; . \end{aligned} \tag{3.86c}$$

Here Γ_{rc} and Γ_{rr} denote the rates of electron capture and surface-induced electron emission due to the resonant de-excitation channel while Γ_{dad} and Γ_{iad} represent the rates of direct and indirect Auger de-excitation. The explicit form of these quantities reads

$$\Gamma_{rc}(t) = \int_{-\infty}^{t} \mathrm{d}t_1 \; 2\Re\big\{\Delta_{rc}(t,t_1)\big\} \; , \tag{3.87a}$$

$$\Gamma_{rr}(t) = \int_{-\infty}^{t} \mathrm{d}t_1 \; 2\Re\big\{\Delta_{rr}(t,t_1)\big\} \; , \tag{3.87b}$$

$$\Gamma_{dad}(t) = \int_{-\infty}^{t} \mathrm{d}t_1 \; 2\Re\big\{\Delta_{dad}(t,t_1)\big\} \; , \tag{3.87c}$$

$$\Gamma_{iad}(t) = \int_{-\infty}^{t} \mathrm{d}t_1 \; 2\Re\big\{\Delta_{iad}(t,t_1)\big\} \; . \tag{3.87d}$$

Note that in (3.86) we dropped the rr-superscript from the occupation of the metastable state since, as seen from (3.86b), the latter is determined solely by Γ_{rc},

Γ_{dad} and Γ_{iad}. Thus, the saddle-point approximation lifts the dependence of n_* on the surface-induced resonant electron release subreaction which was present in the original equations (3.84).

At this point we now manually incorporate the natural decay of $N_2^-(^2\Pi_g)$ by introducing a new rate $\bar{\Gamma}_{rr}$ which is formed by adding the surface-induced decay rate Γ_{rr} (see Eq. (3.87b)) and the natural decay rate Γ_n (see Sec. 2.2.3),

$$\bar{\Gamma}_{rr}(t) = \Gamma_{rr}(t) + \Gamma_n \ . \tag{3.88}$$

The rate $\bar{\Gamma}_{rr}$ then replaces Γ_{rr} in the rate equation system (3.86). We stress that this manual approach is only needed because we could not derive the matrix element of resonant electron release due to the natural decay of $N_2^-(^2\Pi_g)$ within the limits of our effective model.

In total, similar to the works of Langreth et al. in the context of neutralization of atomic ions[76,120], we have reduced the complicated set of Dyson equations (3.81), (3.82) and (3.83), describing the de-excitation of a metastable molecule via the simultaneous action of the RCT channel and the Auger reactions, to the easy-to-handle system of rate equations (3.86). The reaction rates (3.87) and (3.88) entering the rate equations are linked to quantum-kinetic quantities and, thus, related to our semi-empirical model.

We will now seek an analytic solution to the coupled rate equations (3.86). As a starting point we first take a step back and consider the isolated decay channels of resonant electron capture, resonant electron emission and Auger de-excitation. Singling out the individual reactions in (3.86) we obtain

$$\frac{\mathrm{d}n_*^{(rc)}(t)}{\mathrm{d}t} = -\Gamma_{rc}(t)\, n_*^{(rc)}(t) \ , \tag{3.89a}$$

$$\frac{\mathrm{d}n_-^{(rr)}(t)}{\mathrm{d}t} = -\bar{\Gamma}_{rr}(t)\, n_-^{(rr)}(t) \ , \tag{3.89b}$$

$$\frac{\mathrm{d}n_*^{(dad)}(t)}{\mathrm{d}t} = -\Gamma_{dad}(t)\, n_*^{(dad)}(t) \ , \tag{3.89c}$$

$$\frac{\mathrm{d}n_*^{(iad)}(t)}{\mathrm{d}t} = -\Gamma_{iad}(t)\, n_*^{(iad)}(t) \ , \tag{3.89d}$$

where, as before, the superscripts (rc), (rr), (dad) and (iad) identify the isolated resonant electron capture, resonant electron emission[6], direct Auger de-excitation and indirect Auger de-excitation, respectively. Since the channels are isolated, each of the decay equations (3.89) comes with an analogous equation for the species that is produced. For instance, accompanying (3.89a) there is the equation

$$\frac{\mathrm{d}n_-^{(rc)}(t)}{\mathrm{d}t} = \Gamma_{rc}(t)\, n_*^{(rc)}(t) \ . \tag{3.90}$$

The time derivatives of $n_*^{(rc)}$ and $n_-^{(rc)}$ do, however, only differ in sign. Hence, the occupation $n_-^{(rc)}$ is given through the initial conditions upon exploiting the conservation of particles[7]. As a result, the supplementary equations do not contain

[6] Note that the label rr now refers to resonant electron release due to both the surface-induced and the natural decay of $N_2^-(^2\Pi_g)$.

[7] Remember that this is only valid when the channels are isolated.

additional information and, hence, can be omitted. The system (3.89) itself can be solved straightforwardly using the initial conditions

$$n_*^{(rc)}(-\infty) = n_*^{(dad)}(-\infty) = n_*^{(iad)}(-\infty) = 1 \,. \tag{3.91}$$

The result is

$$n_*^{(rc)}(t) = e^{-\int_{-\infty}^{t} \mathrm{d}t_1\, \Gamma_{rc}(t_1)} \,, \tag{3.92a}$$

$$n_-^{(rr)}(t) = n_-^{(rr)}(t')\, e^{-\int_{t'}^{t} \mathrm{d}t_1\, \bar{\Gamma}_{rr}(t_1)} \,, \tag{3.92b}$$

$$n_*^{(dad)}(t) = e^{-\int_{-\infty}^{t} \mathrm{d}t_1\, \Gamma_{dad}(t_1)} \,, \tag{3.92c}$$

$$n_*^{(iad)}(t) = e^{-\int_{-\infty}^{t} \mathrm{d}t_1\, \Gamma_{iad}(t_1)} \,. \tag{3.92d}$$

Inserting the explicit form of the reaction rates (3.87) and comparing (3.92) to (3.27) and (3.65) while leveraging (3.39) we obtain the relations

$$n_*^{(rc)}(t) = 1 - n_0^{(rc)}(t) \,, \tag{3.93a}$$

$$n_*^{(dad)}(t) = n_1^{(dad)}(t) = 1 - n_0^{(dad)}(t) \,, \tag{3.93b}$$

$$n_*^{(iad)}(t) = n_1^{(iad)}(t) = 1 - n_0^{(iad)}(t) \,. \tag{3.93c}$$

These equations connect the occupancies of the pseudo-particle states with the occupation of our molecular two-level system for the isolated reaction channels.

We can now employ the isolated occupancies (3.92) to calculate the solution of the full coupled system of rate equations (3.86). We start with the occupation of the metastable state. Using the initial condition $n_*^{(rc+dad+iad)}(-\infty) = 1$, Eq. (3.86b) can be solved by separation of variables and yields

$$n_*^{(rc+dad+iad)}(t) = e^{-\int_{-\infty}^{t} \mathrm{d}t_1 [\Gamma_{rc}(t_1)+\Gamma_{dad}(t_1)+\Gamma_{iad}(t_1)]} = n_*^{(rc)}(t)\, n_*^{(dad)}(t)\, n_*^{(iad)}(t) \,. \tag{3.94}$$

Next we turn to the occupancy of the negative ion state. To solve (3.86a) we first multiply this equation by a factor $\exp\bigl(\int_{-\infty}^{t} \mathrm{d}t_2\, \bar{\Gamma}_{rr}(t_2)\bigr)$ and afterwards rearrange the terms to obtain

$$\frac{\mathrm{d}}{\mathrm{d}t}\left(n_-^{(rc+rr+dad+iad)}(t)\, e^{\int_{-\infty}^{t} \mathrm{d}t_2\, \bar{\Gamma}_{rr}(t_2)} \right) = \Gamma_{rc}(t)\, n_*^{(rc+dad+iad)}(t)\, e^{\int_{-\infty}^{t} \mathrm{d}t_2\, \bar{\Gamma}_{rr}(t_2)} \,. \tag{3.95}$$

Relabeling t as t_1 and integrating the equation from $t_1 = -\infty$ to $t_1 = t$ while minding the initial condition $n_-(-\infty) = 0$ yields after a further rearrangement

$$n_-^{(rc+rr+dad+iad)}(t) = \int_{-\infty}^{t} \mathrm{d}t_1\, \Gamma_{rc}(t_1)\, n_*^{(rc+dad+iad)}(t_1)\, e^{-\int_{t_1}^{t} \mathrm{d}t_2\, \bar{\Gamma}_{rr}(t_2)} \tag{3.96a}$$

$$= \int_{-\infty}^{t} \mathrm{d}t_1 \left[-\frac{\mathrm{d}n_*^{(rc)}(t_1)}{\mathrm{d}t_1} \right] n_*^{(dad)}(t_1)\, n_*^{(iad)}(t_1)\, \frac{n_-^{(rr)}(t)}{n_-^{(rr)}(t_1)} \,. \tag{3.96b}$$

Finally, the occupancy of the ground state n_g, that is the solution of Eq. (3.86c), is given through the particle conservation property of the full system (3.86),

$$n_g^{(rc+rr+dad+iad)}(t) = 1 - n_*^{(rc+dad+iad)}(t) - n_-^{(rc+rr+dad+iad)}(t) \,. \tag{3.97}$$

Note that the projectile occupancies (3.94), (3.96), and (3.97) emerging from the combined rate equation scheme (3.86) are determined completely by the occupancies $n_*^{(rc)}$, $n_-^{(rr)}$, $n_*^{(dad)}$ and $n_*^{(iad)}$ due to the isolated reaction channels (3.89). However, for the combined system a direct relation between the occupations of the pseudo-particle states and the molecular two-level system is only obvious for the metastable state. In particular, inspection of (3.94) reveals

$$n_*^{(rc+dad+iad)}(t) = 1 - n_0^{(rc)}\, n_0^{(dad)}\, n_0^{(iad)} = 1 - n_0^{(rc+dad+iad)}\,, \tag{3.98}$$

where $n_0^{(rc+dad+iad)}$ is the occupation of the molecular ground state level due to the combination of resonant electron capture and the Auger de-excitation channels. For the remaining pseudo-particle states we now have to employ an intuitive approach. For this purpose we first consider the molecular ground state. From the structure of the Hamiltonian (3.69) and the reactions (1.1), (1.2) and (1.3) it is obvious that $N_2(^1\Sigma_g^+)$ can only be generated through the removal of the electron from the excited level of the incident $N_2(^3\Sigma_u^+)$ molecule. This observation directly yields

$$n_g^{(rc+rr+dad+iad)}(t) = 1 - n_1^{(rc+rr+dad+iad)}(t)\,. \tag{3.99}$$

As we see, in contrast to the ground state level's occupation given through (3.98), the occupancy of the excited molecular level $n_1^{(rc+rr+dad+iad)}$ depends on all four (sub)reactions. This is due to the fact that the resonant emission from the excited level can only proceed after an electron has been resonantly captured into the ground state level. Combining (3.98) and (3.99) by means of the particle conservation property of the system we now also find

$$n_-^{(rc+rr+dad+iad)}(t) = n_0^{(rc+dad+iad)} + n_1^{(rc+rr+dad+iad)} - 1\,. \tag{3.100}$$

We stress that (3.98), (3.99) and (3.100) only hold true because the positive ion state $N_2^+(^2\Pi_u)$ never occurs in the course of the de-excitation reaction.

We now move on to the spectrum of electrons emitted into initially empty states of the surface $\vec{k}'$ and the projectile's continuum states $\vec{q}$. While the evolution of these states has not been considered explicitly in our quantum-kinetic calculation, their occupation can, nevertheless, be found using the solution of (3.86). From the reactions (1.1), (1.2) and (1.3) it is obvious that the probability for emitting an electron $n^{(rc+rr+dad+iad)}(t)$ is equal $n_g^{(rc+rr+dad+iad)}(t)$ since every ground state molecule must have resulted from the reaction chain and, hence, must be accompanied by an emitted electron. Consequently, the evolution of $n^{(rc+rr+dad+iad)}(t)$ is governed by Eq. (3.86c).

As before, we are particularly interested in electrons that are able to escape the surface since these contribute to the secondary electron emission coefficient. In order to restrict our analysis to these electrons, we now adopt a two-step strategy. First we introduce the spectral rates $\varrho_{rr}(\varepsilon_{\vec{q}}^{\infty}, t)$, $\varrho_{dad}(\varepsilon_{\vec{k}'}, t)$ and $\varrho_{iad}(\varepsilon_{\vec{q}}^{\infty}, t)$ via

$$\bar{\Gamma}_{rr}(t) = \int_0^{\infty} \mathrm{d}\varepsilon_{\vec{q}}^{\infty}\; \varrho_{rr}(\varepsilon_{\vec{q}}^{\infty}, t) + \int_{-\infty}^{\infty} \mathrm{d}\varepsilon_{\vec{q}}^{\infty}\; \varrho_n(\varepsilon_{\vec{q}}^{\infty})\,, \tag{3.101a}$$

$$\Gamma_{dad}(t) = \int_{B_{k'}} \mathrm{d}\varepsilon_{\vec{k}'}\; \varrho_{dad}(\varepsilon_{\vec{k}'}, t)\,, \tag{3.101b}$$

$$\Gamma_{iad}(t) = \int_0^{\infty} \mathrm{d}\varepsilon_{\vec{q}}^{\infty}\; \varrho_{iad}(\varepsilon_{\vec{q}}^{\infty}, t)\,, \tag{3.101c}$$

where ϱ_n is the spectrum of the natural decay rate Γ_n (see Eq. (2.42)) and $B_{k'}$ denotes the overall domain for the $\vec{k}'$-integration embracing all initially empty excited states within the solid. Note that the integral over ϱ_n formally runs from $-\infty$ to $+\infty$ due to the definition of the natural line shape as a Breit-Wigner distribution (see Sec. 2.2.3). In a second step we then incorporate the surface transmission functions $\mathcal{T}_{\vec{k}'}$ and $\mathcal{T}_{\vec{q}}$ (see Sec. 2.6) by letting $\varrho_{rr/n/dad/iad} \to \tilde{\varrho}_{rr/n/dad/iad}$ with

$$\tilde{\varrho}_{rr/iad}(\varepsilon_{\vec{q}}^{\infty}, t) = \int_0^{\pi} \mathrm{d}\vartheta_{\vec{q}} \int_0^{2\pi} \mathrm{d}\varphi_{\vec{q}}\, \mathcal{T}_{\vec{q}}(t)\, \frac{\mathrm{d}^2\, \varrho_{rr/iad}(\varepsilon_{\vec{q}}^{\infty}, t)}{\mathrm{d}\vartheta_{\vec{q}}\, \mathrm{d}\varphi_{\vec{q}}}\,, \tag{3.102a}$$

$$\tilde{\varrho}_{dad}(\varepsilon_{\vec{k}'}, t) = \int_0^{\pi} \mathrm{d}\vartheta_{\vec{k}'} \int_0^{2\pi} \mathrm{d}\varphi_{\vec{k}'}\, \mathcal{T}_{\vec{k}'}(t)\, \frac{\mathrm{d}^2\, \varrho_{dad}(\varepsilon_{\vec{k}'}, t)}{\mathrm{d}\vartheta_{\vec{k}'}\, \mathrm{d}\varphi_{\vec{k}'}}\,, \tag{3.102b}$$

and $\tilde{\varrho}_n$ as given by Eq. (2.92). We now insert the resulting spectral decomposition of the rates into Eq. (3.86c), identify $n_g^{(rc+rr+dad+iad)}$ with $\tilde{n}^{(rc+rr+dad+iad)}$, denoting the probability for emitting an electron which can escape from the surface, and obtain

$$\begin{aligned}\frac{\mathrm{d}\tilde{n}^{(rc+rr+dad+iad)}(t)}{\mathrm{d}t} &= \int_0^{\infty} \mathrm{d}\varepsilon_{\vec{q}}^{\infty}\, \left[\tilde{\varrho}_{rr}(\varepsilon_{\vec{q}}^{\infty}, t) + \tilde{\varrho}_n(\varepsilon_{\vec{q}}^{\infty}, t)\right] n_-^{(rc+rr+dad+iad)}(t) \\ &\quad + \int_0^{\infty} \mathrm{d}\varepsilon_{\vec{q}}^{\infty}\, \tilde{\varrho}_{iad}(\varepsilon_{\vec{q}}^{\infty}, t)\, n_*^{(rc+dad+iad)}(t) \\ &\quad + \int_{B_{k'}} \mathrm{d}\varepsilon_{\vec{k}'}\, \tilde{\varrho}_{dad}(\varepsilon_{\vec{k}'}, t)\, n_*^{(rc+dad+iad)}(t)\,.\end{aligned} \tag{3.103}$$

Integrating over the time argument with the initial condition $\tilde{n}^{(rc+rr+dad+iad)}(-\infty) = 0$ we then find the overall number of electrons emitted into $\vec{k}'$- or $\vec{q}$-states at time t,

$$\begin{aligned}\tilde{n}^{(rc+rr+dad+iad)}(t) &= \int_{-\infty}^{t} \mathrm{d}t_1 \int_0^{\infty} \mathrm{d}\varepsilon_{\vec{q}}^{\infty}\, \tilde{\varrho}_{iad}(\varepsilon_{\vec{q}}^{\infty}, t_1)\, n_*^{(rc+dad+iad)}(t_1) \\ &\quad + \int_{-\infty}^{t} \mathrm{d}t_1 \int_0^{\infty} \mathrm{d}\varepsilon_{\vec{q}}^{\infty}\, \left[\tilde{\varrho}_{rr}(\varepsilon_{\vec{q}}^{\infty}, t_1) + \tilde{\varrho}_n(\varepsilon_{\vec{q}}^{\infty}, t_1)\right] n_-^{(rc+rr+dad+iad)}(t_1) \\ &\quad + \int_{-\infty}^{t} \mathrm{d}t_1 \int_{B_{k'}} \mathrm{d}\varepsilon_{\vec{k}'}\, \tilde{\varrho}_{dad}(\varepsilon_{\vec{k}'}, t_1)\, n_*^{(rc+dad+iad)}(t_1)\,.\end{aligned} \tag{3.104}$$

By letting $t \to \infty$ Eq. (3.104) can now be used to calculate the secondary electron emission coefficient $\gamma_e^{(rc+rr+dad+iad)}$ due to resonant and Auger de-excitation,

$$\gamma_e^{(rc+rr+dad+iad)} = \tilde{n}(\infty)\,. \tag{3.105}$$

Furthermore, the individual distributions of electrons over $\vec{k}'$- and $\vec{q}$-states can be derived from (3.104) by stripping out the energy integrals,

$$\tilde{n}_{\varepsilon_{\vec{q}}^{\infty}}^{(rc+rr+dad+iad)}(t) = \frac{\mathrm{d}\tilde{n}^{(rc+rr+dad+iad)}(t)}{\mathrm{d}\varepsilon_{\vec{q}}^{\infty}} \tag{3.106a}$$

$$\begin{aligned}&= \int_{-\infty}^{t} \mathrm{d}t_1 \left[\tilde{\varrho}_{rr}(\varepsilon_{\vec{q}}^{\infty}, t_1) + \tilde{\varrho}_n(\varepsilon_{\vec{q}}^{\infty}, t_1)\right] n_-^{(rc+rr+dad+iad)}(t_1) \\ &\quad + \int_{-\infty}^{t} \mathrm{d}t_1\, \tilde{\varrho}_{iad}(\varepsilon_{\vec{q}}^{\infty}, t_1)\, n_*^{(rc+dad+iad)}(t_1)\,,\end{aligned} \tag{3.106b}$$

$$\tilde{n}_{\varepsilon_{\vec{k}'}}^{(rc+dad+iad)}(t) = \frac{\mathrm{d}\tilde{n}^{(rc+rr+dad+iad)}(t)}{\mathrm{d}\varepsilon_{\vec{k}'}} \tag{3.106c}$$

$$= \int_{-\infty}^{t} \mathrm{d}t_1\, \tilde{\varrho}_{dad}(\varepsilon_{\vec{k}'}, t_1)\, n_*^{(rc+dad+iad)}(t_1)\,. \tag{3.106d}$$

Note that here $\tilde{n}_{\varepsilon_{\vec{k}'}}^{(rc+dad+iad)}$ does not depend on the electron emission subreaction of the resonant channel.

The occupations of the projectile pseudo-particle states (3.94), (3.96), (3.97), the total number of escaped electrons (3.104) and their spectra (3.106) are the main results of this section. The occupancies fully characterize the temporal evolution of the de-excitation of a metastable projectile when the RCT reaction and the Auger channels are active simultaneously. The required input ingredients, embracing the occupancies arising from the isolated processes $n_*^{(rc)}$, $n_-^{(rr)}$, $n_*^{(dad)}$ and $n_*^{(iad)}$ as well as the surface-transmitted spectral rates $\tilde{\varrho}_{rr}$, $\tilde{\varrho}_{dad}$ and $\tilde{\varrho}_{iad}$, can be obtained from the quantum-kinetic calculation and, thus, from our semi-empirical model. In addition, we also showed how the natural decay of the negative ion can be consistently integrated into our description by means of its decay rate Γ_n and the associated spectrum $\tilde{\varrho}_n$.

Finally, we note that, as we showed in Ref. [88], the rate equation system (3.86) can also be derived without the analysis presented in this section by following an intuitive approach. First of all, the general architecture of (3.86) can as well be postulated from the start by simply inspecting the structure of the reactions (1.1), (1.2) and (1.3). Moreover, the explicit form of the involved reaction rates (3.87) can be determined by considering the derivatives of the isolated semi-classical projectile occupations derived in Secs. 3.1 and 3.2. For the indirect Auger de-excitation channel, for instance, differentiation of (3.65a) leads to

$$\frac{\mathrm{d}\overbrace{\left(1-n_0^{(iad)}(t)\right)}^{n_*^{(iad)}(t)}}{\mathrm{d}t} = -\underbrace{\int_{-\infty}^{t}\mathrm{d}t_1\, 2\Re\left\{\Delta_{iad}(t,t_1)\right\}}_{\Gamma_{iad}(t)}\overbrace{\left(1-n_0^{(iad)}(t)\right)}^{n_*^{(iad)}(t)}. \tag{3.107}$$

This equation is identical to the isolated rate equation (3.89d) and yields the rate of indirect Auger de-excitation Γ_{iad} (see Eq. (3.87d)). The remaining rates occurring in (3.86) could be obtained in a similar manner. These findings a posteriori justify our pseudo-particle approach and underline the correctness of our analysis.

3.4 Auger and Resonant Neutralization

After our extensive investigation of the de-excitation channels in the previous sections of this chapter we will now turn to the reactions of Auger and resonant neutralization, (1.4) and (1.5). The corresponding Hamiltonian can be constructed by adding up the relevant terms from Sec. 2.4. After concretizing the projectile level's energy it reads

$$\begin{aligned}\hat{H}(t) = &\sum_{\vec{k}}\varepsilon_{\vec{k}}\, c_{\vec{k}}^{\dagger}\, c_{\vec{k}} + \varepsilon_{0g}(t)\, c_0^{\dagger}\, c_0 + \sum_{\vec{k}}\left[V_{\vec{k}}(t)\, c_{\vec{k}}^{\dagger}\, c_0 + \text{H.c.}\right]\\ &+ \sum_{\vec{k}_1,\vec{k}_2,\vec{k}'}\left[V_{\vec{k}_1\vec{k}_2\vec{k}'}(t)\, c_0^{\dagger}\, c_{\vec{k}_1}\, c_{\vec{k}'}^{\dagger}\, c_{\vec{k}_2} + \text{H.c.}\right],\end{aligned} \tag{3.108}$$

where 0 represents the projectile's initially empty ground state level and $\vec{k}^{(\prime)}$, $\vec{k}_1$ and $\vec{k}_2$ label states inside the solid surface. Moreover, $V_{\vec{k}}$ and $V_{\vec{k}_1\vec{k}_2\vec{k}'}$ denote the

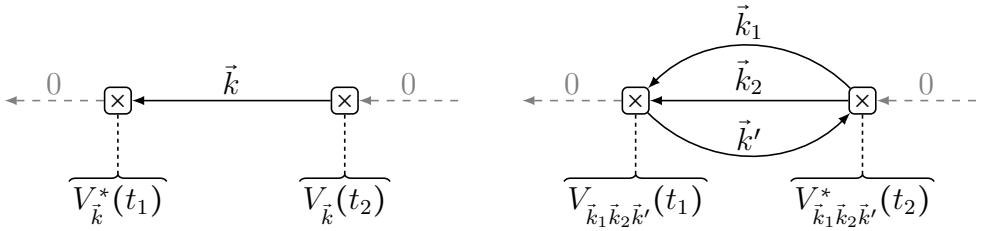

Figure 3.6: Diagrammatic representation of the self-energy Σ_{00} up to second order. The left diagram shows the component due to resonant neutralization which for the isolated resonant channel represents the exact self-energy. The right diagram, on the other hand, depicts the second-order self-energy term due to the Auger neutralization channel.

matrix elements of resonant and Auger neutralization, respectively. For the latter $\vec{k}_1$ and $\vec{k}_2$ represent initially occupied states within the surface while, as before, $\vec{k}'$ refers to an internally excited and initially empty state of the solid.

We will now study the dynamics of (3.108) using the non-equilibrium Green function technique. For this purpose we will once more employ the formulation due to Keldysh since, as we will see, the emitted electrons can be treated by the same renormalization procedure that was employed in our analysis of the Auger de-excitation channels in Sec. 3.2.

Similar to Sec. 3.2 we again start our investigations with the projectile self-energies. The resonant neutralization process was already described in Sec. 3.1 on the basis of an exact first-order non-diagonal self-energy. In order to couple the two neutralization reactions, it is, however, more convenient to work with a second-order diagonal self-energy for the resonant channel. Note that this is merely a different representation which is still exact. In addition, we perform an expansion of the Auger self-energy up to second order in $V_{\vec{k}_1\vec{k}_2\vec{k}'}$. Figure 3.6 shows the resulting self-energy diagrams for the ground state level. The advanced, retarded and Keldysh components of Σ_{00} evaluate to

$$\Sigma^A_{00}(t_1,t_2) = \Theta(t_2-t_1)\Big[\Sigma^{(an)}_{00}(t_1,t_2) + \Sigma^{(rn)}_{00}(t_1,t_2)\Big]\,, \tag{3.109a}$$

$$\Sigma^R_{00}(t_1,t_2) = -\Theta(t_1-t_2)\Big[\Sigma^{(an)}_{00}(t_1,t_2) + \Sigma^{(rn)}_{00}(t_1,t_2)\Big]\,, \tag{3.109b}$$

$$\Sigma^K_{00}(t_1,t_2) = \Sigma^{(an)}_{00}(t_1,t_2) + \widetilde{\Sigma}^{(rn)}_{00}(t_1,t_2)\,, \tag{3.109c}$$

where the terms $\Sigma^{(an)}_{00}$, $\Sigma^{(rn)}_{00}$ and $\widetilde{\Sigma}^{(rn)}_{00}$ are given by

$$\begin{aligned}\Sigma^{(an)}_{00}(t_1,t_2) = 2\frac{i}{\hbar^2}\sum_{\vec{k}_1\vec{k}_2\vec{k}'} & n_{\vec{k}_1}(-\infty)\, n_{\vec{k}_2}(-\infty)\big[1-n_{\vec{k}'}(-\infty)\big] \\ & \times V_{\vec{k}_1\vec{k}_2\vec{k}'}(t_1)\, V^*_{\vec{k}_1\vec{k}_2\vec{k}'}(t_2)\, e^{-\frac{i}{\hbar}(\varepsilon_{\vec{k}_1}+\varepsilon_{\vec{k}_2}-\varepsilon_{\vec{k}'})(t_1-t_2)}\,,\end{aligned} \tag{3.110a}$$

$$\Sigma^{(rn)}_{00}(t_1,t_2) = \frac{i}{\hbar^2}\sum_{\vec{k}} V^*_{\vec{k}}(t_1)\, V_{\vec{k}}(t_2)\, e^{-\frac{i}{\hbar}\varepsilon_k(t_1-t_2)}\,, \tag{3.110b}$$

$$\widetilde{\Sigma}^{(rn)}_{00}(t_1,t_2) = -\frac{i}{\hbar^2}\sum_{\vec{k}}\big[1-2n_{\vec{k}}(-\infty)\big]\, V^*_{\vec{k}}(t_1)\, V_{\vec{k}}(t_2)\, e^{-\frac{i}{\hbar}\varepsilon_k(t_1-t_2)}\,. \tag{3.110c}$$

Here we leveraged the fact that the non-interacting part of the Hamiltonian (3.108) exhibits the general form (1.32). Consequently, the unperturbed Green functions of

the system are given by (1.33) and (1.34). Furthermore, in Eqs. (3.109) and (3.110) the superscripts (an) and (rn) identify contributions due to Auger and resonant neutralization, respectively. Note that the Auger component $\Sigma_{00}^{(an)}$ actually contains an additional term proportional to $\left[1-n_{\vec{k}_1}(-\infty)\right]\left[1-n_{\vec{k}_2}(-\infty)\right]n_{\vec{k}'}(-\infty)$. This contribution can, however, be neglected since it would only be meaningful for an initially occupied projectile level which is not the situation considered here. Moreover, we manually introduced a factor 2 in (3.110a) in order to account for the arbitrary spin of the Auger electron which is not handled in our otherwise spinless description.

We now proceed with the calculation of the retarded and advanced Green functions G_{00}^R and G_{00}^A. The associated Dyson equations (see (1.28a)) can again be solved iteratively and yield

$$G_{00}^R(t,t') = G_{00}^{R(0)}(t,t')\,\sigma[\Delta_{an+rn}](t,t')\,, \tag{3.111a}$$

$$G_{00}^A(t,t') = G_{00}^{A(0)}(t,t')\,\sigma[\Delta_{an+rn}^*](t',t)\,. \tag{3.111b}$$

Here σ represents the well-known infinite series (C.1) and Δ_{an+rn} is the sum of two complex functions,

$$\Delta_{an+rn}(t_1,t_2) = \Delta_{an}(t_1,t_2) + \Delta_{rn}(t_1,t_2)\,, \tag{3.112}$$

with

$$\Delta_{an/rn}(t_1,t_2) = -i\Sigma_{00}^{(an/rn)}(t_1,t_2)\,e^{\frac{i}{\hbar}\int_{t_2}^{t_1}\mathrm{d}t_3\,\varepsilon_{0g}(t_3)}\,. \tag{3.113}$$

Note that, as indicated by their subscripts, the functions Δ_{an} and Δ_{rn} are due to the Auger and the resonant reaction, respectively. Moreover, the function Δ_{rn} is equal to Δ as defined in (3.12) with $\vec{\xi}$ and ε_p replaced by $\vec{k}$ and ε_{0g}. Similar to Sec. 3.1, we can restrict the $\vec{k}$-summation, implicitly contained in the (rn)-component of (3.113), to initially occupied surface states provided that the projectile level $\varepsilon_{0g}(t)$ does not get (near-)resonant to initially empty $\vec{k}$-states. As a result, Δ_{rn} is identical to Δ_{rc} as given by (3.16) if in the latter equation ε_{0-} is replaced by ε_{0g}.

We now employ the Green functions (3.111) and the Keldysh self-energy (3.109c) to calculate the transient occupation of the projectile level from the combination of (1.31) and (1.36). After a short rearrangement we find

$$\begin{aligned} n_0^{(an+rn)}(t) = \frac{1}{2}\Bigg[&1 - \sigma[\Delta_{an+rn}](t,-\infty)\,\sigma[\Delta_{an+rn}^*](t,-\infty) \\ &+ \int_{-\infty}^{t}\mathrm{d}t_1\int_{-\infty}^{t}\mathrm{d}t_2\;\Delta_{an+rn}(t_1,t_2)\,\sigma[\Delta_{an+rn}](t,t_1)\,\sigma[\Delta_{an+rn}^*](t,t_2)\Bigg]\,, \end{aligned} \tag{3.114}$$

where the superscript $(an+rn)$ indicates that the occupancy is due to both the Auger and the resonant neutralization channel. Making use of (C.18) we then, finally, obtain

$$n_0^{(an+rn)}(t) = 1 - \sigma[\Delta_{an+rn}](t,-\infty)\,\sigma[\Delta_{an+rn}^*](t,-\infty)\,. \tag{3.115}$$

Having analyzed the dynamics of the projectile level we now turn to the Auger electron states $\vec{k}'$ representing previously empty excited states of the surface. Similar to the Auger de-excitation reactions (see Sec. 3.2) here again a treatment of these states analogous to the projectile level is unrewarding as the resulting expression for

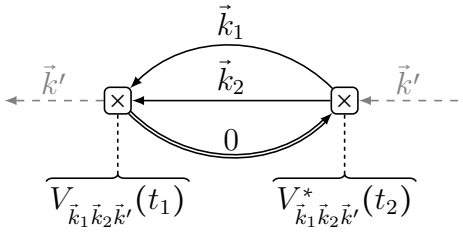

Figure 3.7: Dressed second-order self-energy of the excited surface states $\vec{k}'$. The full propagator of the projectile level is indicated by a double line.

the occupation number is not very convenient to sum over the continuum of final states. Consequently, we again employ Makoshi's approach[86] of renormalizing the Auger electrons' self-energy and expanding the associated Dyson equation.

The dressed self-energy of the excited surface electrons is depicted in Fig. 3.7. Here we only need to consider the diagonal component due to our later expansion of the Dyson equation. The associated Keldysh part evaluates to

$$\begin{aligned}\Sigma^K_{\vec{k}'\vec{k}'}(t_1,t_2) = \frac{2}{\hbar^2}\sum_{\vec{k}_1,\vec{k}_2} & V_{\vec{k}_1\vec{k}_2\vec{k}'}(t_1)\, V^*_{\vec{k}_1\vec{k}_2\vec{k}'}(t_2) \\ & \times G^{+-(0)}_{\vec{k}_1\vec{k}_1}(t_1,t_2)\, G^{+-(0)}_{\vec{k}_2\vec{k}_2}(t_1,t_2)\, G^{-+}_{00}(t_2,t_1)\,,\end{aligned} \tag{3.116}$$

where, similar to (3.110a), we manually inserted a factor 2 to incorporate the Auger electron's arbitrary spin. In order to evaluate (3.116), we need to calculate the full projectile propagator G^{-+}_{00}. The corresponding Dyson equation (see Sec. 1.3.2) can be rewritten into

$$\begin{aligned}G^{-+}_{00}(t,t') = G^{-+(0)}_{00}(t,t') &+ \left\{G^{-+(0)}_{00} * \Sigma^A_{00} * G^A_{00}\right\}(t,t') \\ &+ \left\{G^{R(0)}_{00} * \Sigma^R_{00} * G^R_{00}\right\}(t,t')\,,\end{aligned} \tag{3.117}$$

where we used

$$\Sigma^{-+}_{00}(t_1,t_2) \sim G^{+-(0)}_{\vec{k}'\vec{k}'}(t_1,t_2) \sim n_{\vec{k}'}(-\infty)\,, \tag{3.118}$$

which implies that Σ^{-+}_{00} can be neglected because the resulting terms would conflict with energy conservation for the processes we consider. Equation (3.117) can then be solved iteratively and yields

$$\begin{aligned}G^{-+}_{00}(t,t') = G^{-+(0)}_{00}(t,t')\,\sigma[\Delta_{an+rn}](t,-\infty) \\ \times\left[1 - \int_{-\infty}^{t'}\mathrm{d}t_1 \int_{-\infty}^{t_1}\mathrm{d}t_2\, \sigma[\Delta^*_{an+rn}](t',t_1)\,\Delta^*_{an+rn}(t_1,t_2)\right].\end{aligned} \tag{3.119}$$

Utilizing the complex conjugate of (C.12) this equation simplifies to

$$G^{-+}_{00}(t,t') = G^{-+(0)}_{00}(t,t')\,\sigma[\Delta_{an+rn}](t,-\infty)\,\sigma[\Delta^*_{an+rn}](t,-\infty)\,. \tag{3.120}$$

Hence, the Keldysh self-energy (3.116) becomes

$$\begin{aligned}\Sigma^K_{\vec{k}'\vec{k}'}(t_1,t_2) = 2\frac{i}{\hbar^2}\sum_{\vec{k}_1,\vec{k}_2} & n_{\vec{k}_1}(-\infty)\, n_{\vec{k}_2}(-\infty)\, V_{\vec{k}_1\vec{k}_2\vec{k}'}(t_1)\, V^*_{\vec{k}_1\vec{k}_2\vec{k}'}(t_2) \\ & \times \sigma[\Delta_{an+rn}](t_2,-\infty)\,\sigma[\Delta^*_{an+rn}](t_1,-\infty) \\ & \times e^{-\frac{i}{\hbar}\int_{t_2}^{t_1}\mathrm{d}t_3\left[\varepsilon_{k_1}+\varepsilon_{k_2}-\varepsilon_{0g}(t_3)\right]}\,.\end{aligned} \tag{3.121}$$

Note that here the σ-factors could again be used to form renormalized matrix elements. This does, however, not provide any further insights. Moreover, since $\Sigma^{-+}_{\vec{k}'\vec{k}'}$ can be neglected, we again have

$$\Sigma^{A}_{\vec{k}'\vec{k}'}(t_1,t_2) - \Sigma^{R}_{\vec{k}'\vec{k}'}(t_1,t_2) = \Sigma^{K}_{\vec{k}'\vec{k}'}(t_1,t_2)\,. \tag{3.122}$$

Thus, the expansion of (1.36) is analogous to the Auger de-excitation case (see Sec. 3.2). Focusing on the initially unoccupied $\vec{k}'$-states we, consequently, obtain

$$n^{(an+rn)}_{\vec{k}'}(t) \approx -i\int_{-\infty}^{t}\mathrm{d}t_1\int_{-\infty}^{t}\mathrm{d}t_2\, G^{R(0)}_{\vec{k}'\vec{k}'}(t,t_1)\,\Sigma^{K}_{\vec{k}'\vec{k}'}(t_1,t_2)\,G^{A(0)}_{\vec{k}'\vec{k}'}(t_2,t')\,. \tag{3.123}$$

After inserting the unperturbed Green functions and $\Sigma^{K}_{\vec{k}'\vec{k}'}$ from (3.121) we then find

$$\begin{aligned} n^{(an+rn)}_{\vec{k}'}(t) \approx \int_{-\infty}^{t}\mathrm{d}t_1\int_{-\infty}^{t}\mathrm{d}t_2\, \Delta^{\vec{k}'}_{an}(t_1,t_2) \\ \times\sigma[\Delta^{*}_{an+rn}](t_1,-\infty)\,\sigma[\Delta_{an+rn}](t_2,-\infty)\,, \end{aligned} \tag{3.124}$$

with

$$\Delta^{\vec{k}'}_{an}(t_1,t_2) = \frac{-i\Sigma^{K}_{\vec{k}'\vec{k}'}(t_1,t_2)\,e^{\frac{i}{\hbar}\varepsilon_{\vec{k}'}(t_1-t_2)}}{\sigma[\Delta^{*}_{an+rn}](t_1,-\infty)\,\sigma[\Delta_{an+rn}](t_2,-\infty)}\,, \tag{3.125}$$

and

$$\sum_{\vec{k}'}\big[1-n_{\vec{k}'}(-\infty)\big]\,\Delta^{\vec{k}'}_{an}(t_1,t_2) = \Delta_{an}(t_1,t_2)\,. \tag{3.126}$$

As we see from (3.124), the shape of the Auger electron spectrum is determined by $\Delta^{\vec{k}'}_{an}$ whereas Δ_{an+rn} only acts in a renormalizing way. This manifests the fact that only the Auger channel can generate secondary electrons while the resonant channel merely has an indirect effect on the electron yield by destroying the initial positive ion. The total number of electrons excited into initially empty surface states $\vec{k}'$ is given by

$$n^{(an+rn)}(t) = \sum_{\vec{k}'}\big[1-n_{\vec{k}'}(-\infty)\big]\,n^{(an+rn)}_{\vec{k}'}(t) \tag{3.127a}$$

$$\begin{aligned} = \int_{-\infty}^{t}\mathrm{d}t_1\int_{-\infty}^{t}\mathrm{d}t_2\,\Delta_{an}(t_1,t_2) \\ \times\sigma[\Delta^{*}_{an+rn}](t_1,-\infty)\,\sigma[\Delta_{an+rn}](t_2,-\infty)\,. \end{aligned} \tag{3.127b}$$

Note that if the resonant channel was absent, we could simplify (3.127b) by means of (C.15),

$$n^{(an)}(t) = 1-\sigma[\Delta_{an}](t,-\infty)\,\sigma[\Delta^{*}_{an}](t,-\infty)\,. \tag{3.128}$$

When both channels are operating at the same time, this is, however, not possible.

In order to calculate the number of secondary electrons that can escape the surface we now incorporate the surface transmission function $\mathcal{T}_{\vec{k}'}$ (see Eq. (2.89a)) by introducing a new function $\widetilde{\Delta}^{\vec{k}'}_{an}$ defined as

$$\widetilde{\Delta}^{\vec{k}'}_{an}(t_1,t_2) = \mathcal{T}_{\vec{k}'}(t_1)\,\mathcal{T}_{\vec{k}'}(t_2)\,\Delta^{\vec{k}'}_{an}(t_1,t_2)\,. \tag{3.129}$$

Upon replacing $\Delta^{\vec{k}'}_{an}$ with $\widetilde{\Delta}^{\vec{k}'}_{an}$ in (3.124) we then obtain the spectrum of escaped electrons $\tilde{n}^{(an+rn)}_{\vec{k}'}$ in the form

$$\begin{aligned} \tilde{n}^{(an+rn)}_{\vec{k}'}(t) = \int_{-\infty}^{t}\mathrm{d}t_1\int_{-\infty}^{t}\mathrm{d}t_2\,\widetilde{\Delta}^{\vec{k}'}_{an}(t_1,t_2) \\ \times\sigma[\Delta^{*}_{an+rn}](t_1,-\infty)\,\sigma[\Delta_{an+rn}](t_2,-\infty)\,. \end{aligned} \tag{3.130}$$

The total number of escaped electrons $\tilde{n}^{(an+rn)}$ can now be calculated by summing (3.130) over all initially empty $\vec{k}'$-states. The result reads

$$\begin{aligned}\tilde{n}^{(an+rn)}(t) = &\int_{-\infty}^{t} \mathrm{d}t_1 \int_{-\infty}^{t} \mathrm{d}t_2 \, \widetilde{\Delta}_{an}(t_1,t_2) \\ &\times \sigma[\Delta^*_{an+rn}](t_1,-\infty)\, \sigma[\Delta_{an+rn}](t_2,-\infty) \,,\end{aligned} \tag{3.131}$$

where, in accordance with (3.126),

$$\widetilde{\Delta}_{an}(t_1,t_2) = \sum_{\vec{k}'} \left[1 - n_{\vec{k}'}(-\infty)\right] \widetilde{\Delta}^{\vec{k}'}_{an}(t_1,t_2) \,. \tag{3.132}$$

The secondary electron emission coefficient $\gamma_e^{(an+rn)}$ due to Auger and resonant neutralization then follows from (3.131) by setting $t = \infty$,

$$\gamma_e^{(an+rn)} = \tilde{n}^{(an+rn)}(\infty) \,. \tag{3.133}$$

Note that due to their structure Eqs. (3.130) and (3.131) cannot be simplified further by analytical means.

Finally, we stress that all of the results presented so far in this section can be considered exact up to second order in the interaction matrix elements. The only approximation we employed was the expansion of the Keldysh Dyson equation for the Auger electrons which was, however, made up for by introducing a dressed self-energy. Unfortunately, as before, the equations emerging from our calculation are highly complex and cannot be evaluated easily due to the presence of the infinite σ-series. Therefore, we will again assume that the Δ-functions introduced in this section are strongly peaked about the time diagonal which allows us to employ the approximate representation (C.8). The latter is particularly easy to calculate and will significantly increase the performance in a numerical treatment.

Switching to (C.8) in our previous results is straightforward. The projectile occupation (3.115) for instance turns into

$$n_0^{(an+rn)}(t) \approx 1 - e^{-\int_{-\infty}^{t} \mathrm{d}t_1 \int_{-\infty}^{t} \mathrm{d}t_2 \, \Delta_{an+rn}(t_1,t_2)} \,. \tag{3.134}$$

Moreover, based on the assumption that $\widetilde{\Delta}^{\vec{k}'}_{an+rn}$ is strongly peaked for equal times we can also find a slight simplification of the equation describing the spectrum of escaped electrons, (3.130). In particular, we split the time integral in (3.130) into two identical additive components and afterwards perform a saddle-point approximation by setting $t_1 = t_2$ in the σ-terms of the first addend and $t_2 = t_1$ in the σ-terms of the second addend. Upon employing (3.115) this generates the symmetrical approximation

$$\begin{aligned}\tilde{n}^{(an+rn)}_{\vec{k}'}(t) \approx &\frac{1}{2} \int_{-\infty}^{t} \mathrm{d}t_1 \int_{-\infty}^{t} \mathrm{d}t_2 \, \widetilde{\Delta}^{\vec{k}'}_{an}(t_1,t_2) \overbrace{\sigma[\Delta^*_{an+rn}](t_2,-\infty)\, \sigma[\Delta_{an+rn}](t_2,-\infty)}^{1-n_0^{(an+rn)}(t_2)} \\ &+ \frac{1}{2} \int_{-\infty}^{t} \mathrm{d}t_1 \int_{-\infty}^{t} \mathrm{d}t_2 \, \widetilde{\Delta}^{\vec{k}'}_{an}(t_1,t_2) \underbrace{\sigma[\Delta^*_{an+rn}](t_1,-\infty)\, \sigma[\Delta_{an+rn}](t_1,-\infty)}_{1-n_0^{(an+rn)}(t_1)}\end{aligned} \tag{3.135a}$$

$$= \int_{-\infty}^{t} \mathrm{d}t_1 \int_{-\infty}^{t} \mathrm{d}t_2 \, \Re\{\widetilde{\Delta}^{\vec{k}'}_{an}(t_1,t_2)\} \left[1 - n_0^{(an+rn)}(t_2)\right] , \tag{3.135b}$$

which assures that the occupancy stays real. The advantage of (3.135b) over (3.130) is that the integrand is real valued from the start which simplifies a numerical treatment because it reduces the amount of data that has to be calculated and stored. Note that the saddle-point approximation leading to (3.135a) is the same one that is used in the derivation of the approximate exponential representation of the σ-series in Appendix C.

Finally, if the Auger neutralization is rather weak and the resonant channel is blocked completely, we can calculate the number of escaped electrons from the truncated approximate form

$$\tilde{n}^{(an)}(t) \approx 1 - \sigma\big[\widetilde{\Delta}^{*}_{an}\big](t,-\infty)\,\sigma\big[\widetilde{\Delta}_{an}\big](t,-\infty)\;, \tag{3.136}$$

which emerges after replacing $\Delta^{(*)}_{an}$ with $\widetilde{\Delta}^{(*)}_{an}$ in the σ-terms of (3.131) and employing (C.15) (see also Sec. 3.2). Setting $t = \infty$ and introducing the approximate representation of the σ-series (C.8) in (3.136) we find the secondary electron emission coefficient $\gamma_e^{(an)}$ due to Auger neutralization in the form

$$\gamma_e^{(an)} \approx 1 - e^{-\int_{-\infty}^{\infty}\mathrm{d}t_1\int_{-\infty}^{\infty}\mathrm{d}t_2\,\widetilde{\Delta}_{an}(t_1,t_2)}\;. \tag{3.137}$$

Chapter 4

De-Excitation of Metastable Nitrogen

Building upon the quantum-kinetic calculations of Chapter 3 we will now specifically consider the de-excitation of metastable $N_2(^3\Sigma_u^+)$ molecules due to the resonant de-excitation channel (1.1) and the indirect Auger de-excitation reaction (1.2). From the analysis presented in Secs. 3.1, 3.2 and 3.3 we know that the transient occupancies of projectile and surface states due to these reactions are given in terms of time integrals of various Δ-functions (Δ_{rc}, Δ_{rr}, Δ_{iad}, ...). Each of these functions describes a particular surface (sub)reaction and involves a double product of the associated matrix element at two different times. In the following we will first concretize these matrix elements in the context of our effective model and present suitable approximations for their efficient calculation in Sec. 4.1. The latter section also embraces an analysis of the particular structure of the Δ-functions and their time integrals for an exemplary case. In Sec. 4.2 we will then present numerical results for the isolated de-excitation reactions as well as the combined two-channel scheme. Note that, as mentioned earlier, the direct Auger de-excitation process (1.3) will not be investigated here since it is spin-blocked for the particular case of $N_2(^3\Sigma_u^+)$.

4.1 Matrix Elements and Δ-Functions

4.1.1 Indirect Auger De-Excitation

As we saw in Sec. 2.4, the indirect Auger de-excitation reaction (1.2) is driven by the electron-electron interaction term $\hat{H}_{ee}$. The latter, according to (2.61) and (2.72), involves Coulomb and image interactions between an electron on the projectile and another one in the surface. Clearly the Coulomb interaction is the dominating term here and in order not to overly complicate our analysis we, therefore, neglect the image interactions in $\hat{H}_{ee}$ (see also Ref. [58]). Switching to the position space representation the associated matrix element $V_{\vec{k}\vec{q}}$, thus, reads

$$\begin{aligned} V_{\vec{k}\vec{q}}(t) = \int \mathrm{d}\vec{r} \int \mathrm{d}\vec{r}\,' \left[\Psi_{0m}^{(N_2)}\big(\vec{r}_\varphi(t)\big)\right]^* \Psi_{\vec{k}}(\vec{r}) \\ \times V_C\big(|\vec{r}-\vec{r}\,'|\big)\left[\Psi_{\vec{q}_\varphi}^{(N_2)}\big(\vec{r}\,'_\varphi(t)\big)\right]^* \Psi_{1m}^{(N_2)}\big(\vec{r}\,'_\varphi(t)\big)\,. \end{aligned} \tag{4.1}$$

Here the interaction potential $V_C = V_C^1$ is the statically screened repulsive Coulomb potential (2.60). Moreover, $\Psi_{0m}^{(N_2)}$ and $\Psi_{1m}^{(N_2)}$ denote the wave functions of the nitro-

gen molecule's ground state hole and excited electron, respectively, both of which exhibit the same magnetic quantum number $m = \pm 1$ (see Eq. (2.32) and Sec. 2.2.3). Furthermore, the wave functions $\Psi^{(N_2)}_{\vec{q}_\varphi}$ and $\Psi_{\vec{k}}$ pertain to a projectile continuum state (see Eq. (2.37)) and a bound electron within the solid surface (see Eq. (2.2)), respectively.

Obviously, the molecular wave functions $\Psi^{(N_2)}_{0m}$, $\Psi^{(N_2)}_{1m}$ and $\Psi^{(N_2)}_{\vec{q}_\varphi}$ are defined with respect to the projectile reference frame. The latter possesses an orientation and is centered about the molecule's center of mass $\vec{r}_p(t)$ which moves with respect to the surface (see (2.49)). Consequently, in (4.1) the molecular wave functions need to be taken at the positions $\vec{r}^{\,(\prime)}_\varphi$ which mark the vectors $\vec{r}^{\,(\prime)}$ as seen from the molecular reference frame. Since, as explained in Sec. 2.3, we assume the molecule to move with a fixed orientation and to have its axis aligned perpendicular to the laboratory's y-axis, the vectors $\vec{r}^{\,(\prime)}_\varphi$ and $\vec{r}^{\,(\prime)}$ are interrelated by

$$\vec{r}^{\,(\prime)}_\varphi(t) = \Omega_\varphi \left[\vec{r}^{\,(\prime)} - \vec{r}_p(t) \right] , \tag{4.2}$$

where Ω_φ is the standard rotation matrix

$$\Omega_\varphi = \begin{pmatrix} \sin\varphi & 0 & -\cos\varphi \\ 0 & 1 & 0 \\ \cos\varphi & 0 & \sin\varphi \end{pmatrix} , \tag{4.3}$$

and φ denotes the angle between the molecular axis and the surface (see Fig. 2.5). In addition, the wave vectors of projectile continuum states are defined with respect to the molecular reference frame, too. Hence, in (4.1) we have to employ the wave vector $\vec{q}_\varphi$ which equals $\vec{q}$ as seen from the molecule's reference frame,

$$\vec{q}_\varphi = \Omega_\varphi \, \vec{q} \, . \tag{4.4}$$

Due to the complexity of the nitrogen wave functions, especially $\Psi^{(N_2)}_{\vec{q}_\varphi}$ (see Eq. (2.37)), the matrix element (4.1) cannot be simplified analytically. Moreover, a numerical computation of $V_{\vec{k}\vec{q}}$ by means of standard Monte Carlo techniques, although being straightforward, is rather costly from a performance point of view[1]. Therefore, we seek for physically motivated approximations to the matrix element which allow for an efficient calculation.

For this purpose we first utilize the particular form of the wave functions (see Secs. 2.1 and 2.2.3). Since the wave functions of bound molecular electrons $\Psi^{(N_2)}_{0m/1m}$ are localized on the molecule and, furthermore, the wave functions of electrons inside the surface and in projectile continuum states, $\Psi_{\vec{k}}$ and $\Psi^{(N_2)}_{\vec{q}_\varphi}$, are, in the mathematical sense, bounded throughout the entire integration domain, the main contribution to the matrix element (4.1) will arise from points close to the actual molecule position. Moreover, for the low kinetic energies we are interested in ($\varepsilon_{kin} \leq 1\,\mathrm{eV}$) the molecule's turning point lies far outside the surface ($z_0 \geq 4.35\,a_B$, see Fig. 2.6). We can, thus, safely restrict the $\vec{r}$-integration in (4.1) to $z \geq 0$ and, hence, neglect the overlap of the wave functions inside the solid.

[1] Remember that later the matrix element $V_{\vec{k}\vec{q}}$ has to be integrated over its multidimensional wave vector dependence in order to calculate the Δ-functions (see for instance Δ_{iad} defined in Eq. (3.35)). Therefore, a computation time of a few seconds for the matrix element itself already turns out to be incredibly expensive in view of the subsequent calculations.

By the same argument we also disregard any influence of the surface's static dielectric constant ε_r for the case of a dielectric surface. This is justified since the latter will only have a significant effect on Coulomb interactions within the surface which have, however, been neglected by requiring $z \geq 0$. Note that the dielectric constant might still have an effect in regions where z and z' are located on opposite sides of the surface edge. Due to the compactness of the projectile wave functions and the distant turning point we can, however, assume these areas to be of lesser importance to the matrix element.

In addition, we consider the Coulomb potential's static screening constant κ to be position-independent. When investigating the effect of screening for aluminum and tungsten surfaces in Sec. 4.2.1, this approximation will be made up for by employing the surface screening constant κ_s of the solid instead of the bare bulk value κ_b (see Table A.1). Note that for dielectric surfaces screening is suppressed by the energy gap and, hence, we can drop κ completely in these cases.

Employing the aforementioned facts and assumptions together with the transformation

$$\vec{r}^{\,(\prime)} = \Omega_\varphi^\dagger \, \vec{r}_{1(2)} + \vec{r}_p(t) \; , \tag{4.5}$$

the explicit form of the electronic wave functions (see Secs. 2.1 and 2.2.3) and the projectile trajectory (2.49) we then arrive at

$$V_{\vec{k}\vec{q}}(t) \approx N_L \, C_V \, e^{-\kappa_{k_z} z_p(t)} \, \bar{V}_{\vec{k}\vec{q}} \; , \tag{4.6}$$

with

$$C_V = \frac{e_0^2}{4\pi\varepsilon_0} \frac{1}{(2\pi)^{\frac{5}{2}} \, (\kappa_{\mathrm{N}_2})^2 \sqrt{N_0 \, N_1}} \; , \tag{4.7a}$$

$$\begin{aligned} \bar{V}_{\vec{k}\vec{q}} = T_{k_z} \left[N_{\bar{Z}}(q) \right]^2 \int \mathrm{d}\vec{r}_1 \int \mathrm{d}\vec{r}_2 \; \Theta\big(z_{1\varphi} + z_0\big) \, R_1 \, R_2 \, e^{im(\varphi_2 - \varphi_1)} \frac{e^{-\kappa|\vec{r}_1 - \vec{r}_2|}}{|\vec{r}_1 - \vec{r}_2|} \\ \times \left[e^{-|\vec{r}_{1+}|} + e^{-|\vec{r}_{1-}|} \right] \left[e^{-|\vec{r}_{2+}|} - e^{-|\vec{r}_{2-}|} \right] e^{i(k_x x_{1\varphi} + k_y y_{1\varphi})} \, e^{-\kappa_{k_z} z_{1\varphi}} \\ \times e^{-i\vec{q}_\varphi \cdot \vec{r}_2} \, C_{\bar{Z}}(\vec{q}_\varphi, \vec{r}_{2+}) \, C_{\bar{Z}}(\vec{q}_\varphi, \vec{r}_{2-}) \; , \end{aligned} \tag{4.7b}$$

where R_i and φ_i $(i = 1, 2)$ denote the lateral cylindrical coordinates associated with the vectors $\vec{r}_{1/2}$ and κ represents the surface's static screening constant. Moreover, we introduced the abbreviations

$$\bar{Z} = 2 \frac{Z_C}{Z_{\mathrm{eff}}} \; , \tag{4.8a}$$

$$\vec{r}_{1/2\pm} = \vec{r}_{1/2} \pm \frac{\varrho}{2} \vec{e}_z \; , \tag{4.8b}$$

$$\vec{r}_{1\varphi} = (x_{1\varphi}, y_{1\varphi}, z_{1\varphi}) = \Omega_\varphi^\dagger \, \vec{r}_1 \; , \tag{4.8c}$$

with ϱ labeling the bond length of the molecule. Note that in Eq. (4.7b) we silently switched to dimensionless atomic variables by letting

$$x_{\vec{r}} \to \frac{x_{\vec{r}}}{\kappa_{\mathrm{N}_2}} \; , \quad x_{\vec{k}} \to \kappa_{\mathrm{N}_2} \, x_{\vec{k}} \; , \quad x_t \to \frac{x_t}{\kappa_{\mathrm{N}_2} v} \; , \tag{4.9}$$

where $x_{\vec{r}}$ denotes any spatial variable (like $\vec{r}_1$ and $\vec{r}_p(t)$), $x_{\vec{k}}$ specifies a wave vector variable (like $\vec{k}$ and $\vec{q}_\varphi$) and x_t is shorthand for any time variable. Furthermore, in

the integrand of (4.7b) we replaced $\Theta\big(z_{1\varphi} + z_p(t)\big)$ by $\Theta(z_{1\varphi} + z_0)$ which, as numerical tests confirmed, is a good approximation for the distant turning point positions we are considering. In total, our approximate representation (4.6) of the matrix element (4.1) separates the time dependence from the spatial integral. As will become obvious later, this will greatly simplify the calculation of the system's occupancies since the time integrations can be carried out in separate.

In order to investigate the structure of the Δ-functions connected with the indirect Auger de-excitation channel and the effect of our approximate matrix element (4.6) in these quantities, we now consider the exemplary case of Δ_{iad}. Starting from (3.35) we insert (4.6) and convert the $\vec{k}$- and $\vec{q}$-sums into integrals according to (2.13) and (2.40) which yields

$$\begin{aligned}\Delta_{iad}(t_1,t_2) = \frac{|C_V|^2}{16\pi^3}\frac{(\kappa_{\mathrm{N}_2})^6}{\hbar^2}\int_{\mathrm{occ.}}\mathrm{d}\vec{k}\int_{\mathrm{unocc.}}\mathrm{d}\vec{q}\,\left|\bar{V}_{\vec{k}\vec{q}}\right|^2 e^{-\kappa_{k_z}\left[z_p(t_1)+z_p(t_2)\right]} \\ \times\, e^{-\frac{i}{a}\int_{t_2}^{t_1}\mathrm{d}t_3\left[\varepsilon_{1*}(t_3)+\varepsilon_{\vec{k}}-\varepsilon_{0g}(t_3)-\varepsilon_{\vec{q}}(t_3)\right]}\,,\end{aligned} \tag{4.10}$$

where the $(\kappa_{\mathrm{N}_2})^6$-prefactor is due to the rescaling (4.9) and a is given by

$$a = \hbar\kappa_{\mathrm{N}_2} v\,. \tag{4.11}$$

Note that in (4.10) the labels "occ."and "unocc." indicate that the integrals over $\vec{k}$- and $\vec{q}$-states exclusively involve initially occupied and unoccupied states, respectively. Moreover, in (4.10) we integrate over the $\vec{q}$-vector in the laboratory frame while $\bar{V}_{\vec{k}\vec{q}}$ still contains $\vec{q}$ as seen from the molecular reference frame (see Eq. (4.7b)).

Time integrals of Δ_{iad} can now be obtained from (4.10) in a straightforward manner. We will demonstrate this using the example of the double time integral

$$\mathcal{I}(t) = \frac{1}{(\kappa_{\mathrm{N}_2} v)^2}\int_{-\infty}^{t}\mathrm{d}t_1\int_{-\infty}^{t}\mathrm{d}t_2\,\Delta_{iad}(t_1,t_2)\,, \tag{4.12}$$

which is for instance needed to compute the projectile occupancies (3.66). Note that here the prefactor $(\kappa_{\mathrm{N}_2} v)^{-2}$ is again caused by the variable transformation (4.9). Inserting Δ_{iad} from (4.10) and interchanging the wave vector and time integrations we obtain

$$\begin{aligned}\mathcal{I}(t) = \frac{1}{(\kappa_{\mathrm{N}_2} v)^2}\frac{|C_V|^2}{16\pi^3}\frac{(\kappa_{\mathrm{N}_2})^6}{\hbar^2}\int_0^{\pi/2}\mathrm{d}\vartheta_{\vec{k}}\int_0^{2\pi}\mathrm{d}\varphi_{\vec{k}}\int_0^{\pi}\mathrm{d}\vartheta_{\vec{q}}\int_0^{2\pi}\mathrm{d}\varphi_{\vec{q}}\int_{\mathrm{occ.}}\mathrm{d}k\int_{\mathrm{unocc.}}\mathrm{d}q \\ \times\, k^2\,\sin(\vartheta_{\vec{k}})\,q^2\,\sin(\vartheta_{\vec{q}})\,e^{-2\kappa_{k_z} z_0}\,\left|\bar{V}_{\vec{k}\vec{q}}\right|^2\,\left|\Gamma_{\vec{k}\vec{q}}(t)\right|^2\,,\end{aligned} \tag{4.13}$$

where we switched to spherical wave vector coordinates and introduced the term

$$\Gamma_{\vec{k}\vec{q}}(t) = \int_{-\infty}^{t}\mathrm{d}t_1\,e^{-\kappa_{k_z}|t_1|}\,e^{-\frac{i}{a}\int_0^{t_1}\mathrm{d}t_2\left[\varepsilon_{1*}(t_2)+\varepsilon_{\vec{k}}-\varepsilon_{0g}(t_2)-\varepsilon_{\vec{q}}(t_2)\right]}\,. \tag{4.14}$$

In addition, we utilized the fact that within our effective model the initial occupation of $\vec{k}$- and $\vec{q}$-states follows from their energy and, hence, their radial components k and q.

Due to the approximate matrix element (4.6) the time and space integrations in (4.13) can be carried out separately which accounts for a significant performance boost in a numerical calculation. Actually, the time integral (4.14) is even solvable

analytically. The explicit solution does, however, involve very large numeric factors and is, thus, not suitable for numerical use. Therefore, it is most convenient to solve (4.14) by a standard one-dimensional integration routine. Furthermore, it is advantageous to tabulate the matrix element stub $\bar{V}_{\vec{k}\vec{q}}$ on a grid over the range of relevant wave vector coordinates[2]. Equation (4.13) can then be evaluated efficiently by means of a standard Monte Carlo integration procedure. For details of the numerical procedure we refer the reader to Appendix E.

Note that the remaining Δ-functions of the indirect Auger de-excitation channel, like for instance $\widetilde{\Delta}_{iad}$ (see Eq. (3.63b)), possess the same principal structure as Δ_{iad}. Consequently, they can be handled in an equal way. Moreover, single- or double-time integrals of the Δ-functions with different integration boundaries can be calculated in the same manner as (4.12). Since the procedure is obvious, this will, however, not be demonstrated here.

4.1.2 Two-Step Resonant De-Excitation

Here we will concretize the matrix elements and Δ-functions associated with the electron capture and surface-induced electron emission subreactions of the resonant de-excitation channel (1.1).

We start with the resonant electron capture. The associated matrix element $V_{\vec{k}}$ was given in (2.69). In position space representation it reads

$$V_{\vec{k}}(t) = \int \mathrm{d}\vec{r}\; \Psi^{*}_{\vec{k}}(\vec{r}) \Big[-V_C^{Z_{\mathrm{eff}}}\big(\vec{r}-\vec{r}_{p_1}(t)\big) - V_C^{Z_{\mathrm{eff}}}\big(\vec{r}-\vec{r}_{p_2}(t)\big) + V_i(z) \Big] \Psi_{0m}^{(\mathrm{N}_2)}\big(\vec{r}_{\varphi}(t)\big)\,, \quad (4.15)$$

where $\Psi_{\vec{k}}$ and $\Psi_{0m}^{(\mathrm{N}_2)}$ denote the wave functions of a bound surface electron (2.2) and the molecular ground state level (2.32), respectively. Due to the motion of the molecule the latter again has to be taken at the position $\vec{r}_{\varphi}$ given by (4.2). Furthermore, the interaction potential in (4.15) embraces the truncated classical image potential V_i defined in (2.14) as well as the attractive Coulomb potential $-V_C^{Z_{\mathrm{eff}}}$ associated with the molecular nuclei (see Eq. (2.60)). The latter account for an effective charge number $Z_{\mathrm{eff}} = 4$ (see Table A.3) and are located at the positions $\vec{r}_{p_{1/2}}$ which relate to the molecule's center of mass location $\vec{r}_p$ via

$$\vec{r}_{p_{1/2}}(t) = \vec{r}_p(t) \pm \frac{\vec{\varrho}}{2}\,. \quad (4.16)$$

Here $\vec{\varrho}$ denotes the inter-nuclear vector which was introduced in Fig. 2.5. Note that in contrast to the general matrix element given in (2.69), Eq. (4.15) does not involve interactions due to the image charges of the molecular cores since from the surface's point of view the nuclei charges are completely screened in the neutral initial state $\mathrm{N}_2(^3\Sigma_u^+)$.

Similar to the previous section an analytical simplification of the matrix element (4.15) seems to be impossible due to the complicated structure of the projectile wave function and the different interaction potentials. Consequently, we need to introduce further approximations to make a numerical calculation of the matrix element and derived quantities feasible.

[2]Since the effect of energy conservation is quite strong, one only has to tabulate $\bar{V}_{\vec{k}\vec{q}}$ for near-resonant energies $\varepsilon_{\vec{k}}$ and $\varepsilon_{\vec{q}}$.

In order to construct such approximations, we analyzed the components of the full matrix element (4.15) numerically. For this purpose we introduced a step approximation to the static dielectric constant within the Coulomb potential $V_C^{Z_{\text{eff}}}$,

$$\varepsilon_r(z) = \begin{cases} \varepsilon_r^b & \text{for } z \le 0 \,, \\ 1 & \text{for } z > 0 \,. \end{cases} \tag{4.17}$$

For dielectric materials corresponding values of the bulk dielectric constant ε_r^b are listed in Table A.2. For metallic surfaces, on the other hand, we formally set $\varepsilon_r^b = -\infty$ in order to neglect the perfectly screened Coulomb interaction inside the solid. Furthermore, as in Sec. 4.1.1, we drop the screening constant κ for dielectric surfaces and replace it by its surface value κ_s for metallic materials, respectively. Our numerical investigations then revealed that the Coulomb interactions $V_C^{Z_{\text{eff}}}$ clearly outweigh the image potential V_i. Moreover, we found that the matrix element can be neglected in the half space $z \le 0$ also for dielectric materials.

Making use of these findings we employ the coordinate transformation (4.5) and utilize the relation

$$\left|\vec{r} - \vec{r}_p(t) \pm \frac{\vec{\varrho}}{2}\right| = \left|\vec{r} - \vec{r}_p(t) \pm \frac{\varrho}{2}\,\Omega_\varphi^\dagger\,\vec{e}_z\right| = \left|\Omega_\varphi^\dagger\left[\vec{r}_\varphi \mp \frac{\varrho}{2}\,\vec{e}_z\right]\right| = \left|\vec{r}_\varphi \pm \frac{\varrho}{2}\,\vec{e}_z\right| \,. \tag{4.18}$$

As in Sec. 4.1.1, we then approximate $\Theta(z_{1\varphi} + z_p(t))$ by $\Theta(z_{1\varphi} + z_0)$ with $z_{1\varphi}$ defined in (4.8c) and obtain

$$V_{\vec{k}}(t) \approx N_L\, D_V\, e^{-\kappa_{k_z} z_p(t)}\, \bar{V}_{\vec{k}} \,, \tag{4.19}$$

where

$$D_V = \frac{m}{\sqrt{2\pi N_0 \kappa_{\text{N}_2}}} \frac{Z_{\text{eff}}\, e_0^2}{4\pi\varepsilon_0} \,, \tag{4.20a}$$

$$\begin{aligned} \bar{V}_{\vec{k}} = T_{k_z}^* \int \mathrm{d}\vec{r}_1\, \Theta(z_{1\varphi} - z_0)\, e^{-\kappa_{k_z} z_{1\varphi}}\, \frac{1}{\varepsilon_r(z_1)} \left[\frac{e^{-\kappa r_{1+}}}{r_{1+}} + \frac{e^{-\kappa r_{1-}}}{r_{1-}}\right] \left[e^{-r_{1+}} + e^{-r_{1-}}\right] \\ \times \left(x_1 + i m y_1\right) e^{-i(k_x x_{1\varphi} + k_y y_{1\varphi})} \,. \end{aligned} \tag{4.20b}$$

Note that here, as explained earlier, κ takes the value $\kappa = 0$ for a dielectric surface and $\kappa = \kappa_s$ for a metallic surface. Moreover, in (4.20b) we again used the atomic coordinate scaling (4.9) and introduced the shorthand notation

$$r_{1\pm} = \left|\vec{r}_1 \pm \frac{\varrho}{2}\,\vec{e}_{z_1}\right| \,. \tag{4.21}$$

Obviously, in the approximated matrix element (4.19) the time dependence is separated from the spatial integral which, as before, will immensely benefit the performance of a numerical calculation.

We now turn our attention to the function Δ_{rc} which is the only meaningful Δ-function associated with the resonant electron capture subreaction (see Sec. 3.1). In order to explicitly calculate this quantity, we insert the approximate matrix element (4.19) into (3.16). After converting the $\vec{k}$-sum into an integral by means of (2.13) we find

$$\Delta_{rc}(t_1, t_2) = \frac{D_V^2}{16\pi^3} \frac{\kappa_{\text{N}_2}^3}{\hbar^2} \int_{\text{occ.}} \mathrm{d}\vec{k}\, \left|\bar{V}_{\vec{k}}\right|^2 e^{-\kappa_{k_z}\left[z_p(t_1) + z_p(t_2)\right]}\, e^{-\frac{i}{a}\int_{t_2}^{t_1} \mathrm{d}t_3\, \left[\varepsilon_{\vec{k}}(t_3) - \varepsilon_{0^-}(t_3)\right]} \,, \tag{4.22}$$

where a is given by (4.11). In (4.22) the wave vector integral and the implicitly involved spatial integrations contained in the matrix element stub $\bar{V}_{\vec{k}}$ can be computed efficiently in a nested Monte Carlo integration scheme without additional tabulations. Moreover, the calculation of time integrals of Δ_{rc} is straightforward and follows our treatment of Δ_{iad} in Sec. 4.1.1. Similar to the latter section, our matrix element approximation (4.19) allows us to evaluate the involved space and time integrals independently. By employing a separate standard one-dimensional integration routine for the time integrals this results in a tremendous reduction in computation time during a numerical simulation.

We now turn to the surface-induced resonant electron emission. The associated tunneling matrix element $V_{\vec{q}}$ can be found in (2.68). Employing the position space representation it takes the form

$$V_{\vec{q}}(t) = \int \mathrm{d}\vec{r} \left[\Psi^{(\mathrm{N_2})}_{\vec{q}_\varphi}\big(\vec{r}_\varphi(t)\big)\right]^* \left[\Theta(-z)\, V_0 + V_i(z)\right] \Psi^{(\mathrm{N_2})}_{1m}\big(\vec{r}_\varphi(t)\big)\,, \tag{4.23}$$

where the bound and continuum molecular wave functions $\Psi^{(\mathrm{N_2})}_{1m}$ and $\Psi^{(\mathrm{N_2})}_{\vec{q}_\varphi}$ are given by (2.32) and (2.41), respectively. Note that here the latter represents a plane wave since the departing electron leaves a neutral molecule behind. As pointed out in Sec. 2.2.3, conceptually this corresponds to a two-center Coulomb wave with zero effective nucleus charge. Moreover, due to the motion and orientation of the molecule both wave functions in (4.23) have to be calculated in terms of the molecular coordinates $\vec{r}_\varphi$ (see Eq. (4.2)). For the same reason we also have to employ the emitted electron's wave vector $\vec{q}_\varphi$ instead of $\vec{q}$ (see Eq. (4.4)).

The interaction potential in (4.23) involves the constant bulk potential of the solid surface V_0 and the truncated classical image potential V_i (see Eq. (2.14)). Note that here again the nuclear charges do not generate image charges inside the surface since they are completely screened due to the bound molecular electrons. Consequently, the electron's self-image potential V_i constitutes the only relevant image interaction.

In order to analytically reduce the matrix element we now insert the explicit form of $\Psi^{(\mathrm{N_2})}_{\vec{q}_\varphi}$ from (2.41) and make use of

$$\vec{q}_\varphi\, \vec{r}_\varphi(t) = \big[\Omega_\varphi\, \vec{q}\big]\big[\Omega_\varphi\big(\vec{r} - \vec{r}_p(t)\big)\big] = \vec{q}\, \underbrace{\Omega_\varphi^\dagger\, \Omega_\varphi}_{1}\big(\vec{r} - \vec{r}_p(t)\big) = \vec{q}\,\big(\vec{r} - \vec{r}_p(t)\big)\,, \tag{4.24}$$

which allows us to rewrite (4.23) as

$$\begin{aligned} V_{\vec{q}}(t) = \frac{1}{(2\pi)^{\frac{3}{2}}} \int_{-\infty}^{\infty} \mathrm{d}z\; e^{-iq_z\left[z - z_p(t)\right]} \left[\Theta(-z)\, V_0 + V_i(z)\right] \\ \times \int_{-\infty}^{\infty} \mathrm{d}x \int_{-\infty}^{\infty} \mathrm{d}y\; \Psi^{(\mathrm{N_2})}_{1m}\big(\vec{r}_\varphi(t)\big)\, e^{-i(q_x x + q_y y)}\,. \end{aligned} \tag{4.25}$$

The x-y-integral in this equation is equal to 2π times the lateral Fourier transform of the projectile wave function $\Psi^{(\mathrm{N_2})}_{1m}$ of the rotated argument $\vec{r}_\varphi$. For the two principal molecule orientations $\varphi = 0$ (axis parallel to surface) and $\varphi = \frac{\pi}{2}$ (axis perpendicular to surface) this quantity can be calculated analytically (see Appendix D.4). Thus, formally we obtain

$$V^{\parallel/\perp}_{\vec{q}}(t) = \frac{1}{\sqrt{2\pi}} \int_{-\infty}^{\infty} \mathrm{d}z\; e^{-iq_z\left[z - z_p(t)\right]} \left[\Theta(-z)\, V_0 + V_i(z)\right] \Psi^{\parallel/\perp}_{1m}\big(q_x, q_y, z - z_p(t)\big)\,, \tag{4.26}$$

where we used $\parallel$ and $\perp$ to label the parallel and perpendicular molecule orientation, respectively. In addition, we introduced the abbreviations

$$\Psi^{\parallel}_{1m}(q_x,q_y,z) = \Psi^{(\mathrm{N}_2)}_{1m}(-z,q_y,q_x)\,, \quad \Psi^{\perp}_{1m}(q_x,q_y,z) = \Psi^{(\mathrm{N}_2)}_{1m}(q_x,q_y,z)\,, \tag{4.27}$$

which represent the lateral Fourier transforms of Ψ_{1m} for the two orientations. The explicit form of these expressions is given in Eqs. (D.52a) and (D.52b) using cylindrical coordinates. Hence, the matrix elements (4.26) represent a significant simplification over the original equation (4.23) since they only include a single one-dimensional spatial integral. The latter can be calculated very efficiently by a standard numerical integration routine.

Having analyzed the particular structure of the matrix element $V_{\vec{q}}$ we now turn to the Δ-functions of the surface-induced resonant electron emission subreaction. As an example we will consider $\widetilde{\Delta}_{rr}$ which involves the surface transmission function $\mathcal{T}_{\vec{q}}$. Starting from (3.26) we convert the $\vec{q}$-sum into an integral by means of (2.40) and obtain

$$\widetilde{\Delta}_{rr}(t_1,t_2) = \frac{\kappa^3_{\mathrm{N}_2}}{\hbar^2}\int_{\mathrm{unocc.}} \mathrm{d}\vec{q}\; \mathcal{T}_{\vec{q}}(t_1)\,\mathcal{T}_{\vec{q}}(t_2)\,V^*_{\vec{q}}(t_1)\,V_{\vec{q}}(t_2)\,e^{-\frac{i}{a}\left(\varepsilon^{\infty}_{\vec{q}}-\varepsilon^{\infty}_{1-}\right)(t_1-t_2)}\,, \tag{4.28}$$

with a defined in (4.11). Note that here the prefactor $\kappa^3_{\mathrm{N}_2}$ is again due to the scaling (4.9). Moreover, (4.28) only involves the unperturbed energies of the emitted electron and the excited molecular level, $\varepsilon^{\infty}_{\vec{q}}$ and $\varepsilon^{\infty}_{1-}$, since the associated classical image shifts cancel each other exactly (see Sec. 2.2.4). Numerically, Eq. (4.28) can be computed straightforwardly by combining a Monte Carlo procedure for the $\vec{k}$-integral with a standard one-dimensional integrator for $V_{\vec{q}}$ and its conjugate.

In order to calculate physical quantities, we now need to evaluate time integrals of the Δ-functions. For the particular case of $\widetilde{\Delta}_{rr}$ these integrals involve terms of the form

$$\Gamma_{\vec{q}}(t_a,t_b) = \frac{1}{\kappa_{\mathrm{N}_2} v}\int_{t_b}^{t_a}\mathrm{d}t_1\;\mathcal{T}_{\vec{q}}(t_1)\,V_{\vec{q}}(t_1)\,e^{\frac{i}{a}(\varepsilon^{\infty}_{\vec{q}}-\varepsilon^{\infty}_{1})t_1}\,, \tag{4.29}$$

where the prefactor $(\kappa_{\mathrm{N}_2} v)^{-1}$ is again a consequence of the coordinate transformation (4.9). Inserting the matrix elements (4.26) and the surface transmission function (2.89b), Eq. (4.29) turns into

$$\Gamma^{\parallel/\perp}_{\vec{q}}(t_a,t_b) = \frac{1}{\kappa_{\mathrm{N}_2} v}\frac{\Theta(q_z)}{(2\pi)^{\frac{3}{2}}\kappa_{\mathrm{N}_2}}\int_{-\infty}^{\infty}\mathrm{d}z\;\Psi^{\parallel/\perp}_{1m}\big(q_x,q_y,z\big)\,e^{-iq_z z}\,\mathcal{I}_{\vec{q}}(t_a,t_b,z)\,. \tag{4.30}$$

Here we shifted the time dependence into the interaction potential terms by transforming the z-integral and introduced the quantity

$$\begin{aligned}\mathcal{I}_{\vec{q}}(t_a,t_b,z) = \int_{t_b}^{t_a}\mathrm{d}t_1\;\Theta\Big(\varepsilon^{\infty}_{q_z}+V_i\big(z_p(t_1)\big)\Big)\,e^{\frac{i}{a}\left(\varepsilon^{\infty}_{\vec{q}}-\varepsilon^{\infty}_{1}\right)t_1}\\ \times\Big[\Theta\big(-z-z_p(t_1)\big)\,V_0+V_i\big(z+z_p(t_1)\big)\Big]\,.\end{aligned} \tag{4.31}$$

Using the explicit form of V_i (see Eq. (2.14)) this integral can be calculated analyt-

ically in a straightforward but rather tedious procedure. The result reads

$$\begin{aligned}\mathcal{I}_{\bar{q}}(t_a,t_b,z) = \frac{2V_0}{\alpha}\Bigg[&\Theta(\tau_2-\tau_1)\,\Theta(-t_b)\,e^{i\alpha\frac{\tau_1+\tau_2}{2}}\sin\left(\alpha\frac{\tau_2-\tau_1}{2}\right)\\ &+\Theta(t)\,\Theta(\tau_4-\tau_3)\,e^{i\alpha\frac{\tau_3+\tau_4}{2}}\sin\left(\alpha\frac{\tau_4-\tau_3}{2}\right)\Bigg]\\ &+Q_\varepsilon\frac{\kappa_{\mathrm{N}_2}e_0^2}{16\pi\varepsilon_0}\Bigg[\Theta(\tau_5-t_b)\,\Theta(-t_b)\,e^{i\alpha\bar{z}}\\ &\times\left\{\mathrm{Ei}\big(-i\alpha(\bar{z}-\tau_5)\big)+\frac{\pi}{2}\big(1+i\,\mathrm{sgn}(\alpha)\big)\right\}\\ &-\Theta(t_a)\,\Theta(t_a-\tau_6)\,e^{-i\alpha\bar{z}}\left\{\mathrm{Ei}\big(i\alpha(\bar{z}+t_a)\big)-\mathrm{Ei}\big(i\alpha(\bar{z}+\tau_6)\big)\right\}\Bigg],\end{aligned} \tag{4.32}$$

where Ei is the exponential integral and Q_ε is given by (2.16). Moreover, Eq. (4.32) involves a number of abbreviations which are summarized in the following

$$\begin{aligned}&\tau = z_c - z - z_0\,, && \tau_1 = \max(t_b,-\tau)\,, && \tau_2 = \min(0,t_{q_z},t_a)\,,\\ &\tau_3 = \max(t_b,t_{q_z},0)\,, && \tau_4 = \min(\tau,t_a)\,, && \tau_5 = \min(-\tau,-t_{q_z},0,t_a)\,,\\ &\tau_6 = \max(t_b,0,\tau,t_{q_z})\,, && \alpha = \frac{\varepsilon_{\bar{q}}^{\infty}-\varepsilon_1^{\infty}}{a}\,, && t_{q_z} = Q_\varepsilon\frac{\kappa_{\mathrm{N}_2}e_0^2}{16\pi\varepsilon_0}\frac{1}{\varepsilon_{q_z}} - z_0\,,\\ &\bar{z} = z + z_0\,.\end{aligned} \tag{4.33}$$

Note that (4.32) can be immediately adapted to the case of Δ_{rr} by setting $t_{q_z} = 0$ and dropping the $\Theta(q_z)$-term from (4.30). In addition, other Δ-functions associated with the surface-induced resonant electron emission, like for instance $\Delta_{rr}^{\bar{q}}$, may be treated in the same manner due to their equivalent structure.

4.2 Numerical Results

Utilizing the matrix elements and Δ-functions introduced in Sec. 4.1 we now present numerical results for the de-excitation of $\mathrm{N}_2(^3\Sigma_u^+)$ due to the isolated and combined reaction channels of indirect Auger de-excitation and two-step resonant de-excitation. All of our calculations build upon the simplified equations stemming from the saddle-point, or semi-classical, approximation to composite time integrals of the Δ-functions (see Chapter 3). The explicit validity of this approximation is demonstrated in Sec. 4.2.3.

In the following, we fix the molecule's turning point to the value given by Eq. (2.53) for 50 meV ($\approx 4.42\,a_B$) since, as seen from Fig. 2.6, z_0 varies only weakly within the considered energy range $\varepsilon_{\mathrm{kin}} \leq 1\,\mathrm{eV}$. In addition, we restrict our analysis to the special case $m = 1$ since, as our numerical investigations revealed, the initial magnetic quantum number $m = \pm 1$ seems to have no effect on our results. Moreover, we only consider the two principal molecule orientation $\varphi = 0$ (axis parallel to the surface) and $\varphi = \frac{\pi}{2}$ (axis perpendicular to the surface) as these are expected to produce the most fundamental results. Finally, for the most part we neglect the influence of Coulomb screening for metallic surfaces since the available screening constants are rather uncertain. The particular effect of screening will, however, be

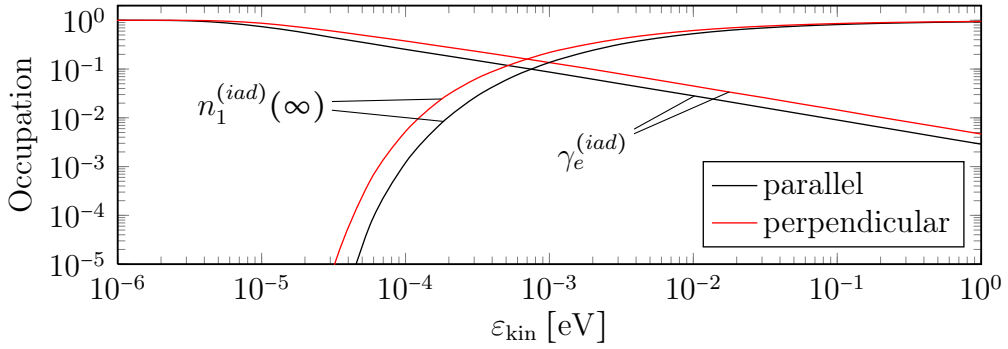

Figure 4.1: Secondary electron emission coefficient $\gamma_e^{(iad)}$ and final occupancy of the excited molecular level $n_1^{(iad)}(\infty)$ in parallel (black lines) and perpendicular (red lines) molecule orientation over the molecule's kinetic energy ε_{kin}. The curves were calculated for an aluminum surface without Coulomb screening using the formulas (3.65b) and (3.68), respectively.

analyzed at the end of Sec. 4.2.1. The explicit values of the screening constants and other material specific parameters used in our calculation are listed in Appendix A.

4.2.1 Indirect Auger De-Excitation

Here we consider the isolated indirect Auger de-excitation channel (1.2) and aim at calculating the transient and final occupancies of the two projectile levels as well as the final distribution of escaped electrons and their total amount which constitutes the secondary electron emission coefficient $\gamma_e^{(iad)}$. In particular, we focus on the case of metallic surfaces using the example of aluminum. Moreover, at the end of this section we will also present numerical results for a tungsten surface for a which a comparison to experimental measurements is possible. Due to their energetic structure (see Table A.1), both of these materials exclusively allow for the Auger de-excitation mechanism and suppress the resonant de-excitation channel almost entirely[3].

We start our analysis with an aluminum surface and consider the excited projectile level's final occupancy $n_1^{(iad)}(\infty)$ and the emission coefficient $\gamma_e^{(iad)}$ which represents those Auger electrons that can escape the surface. We calculate the former from the approximate expression (3.65b) while for the latter we employ the truncated approximate form (3.68). The resulting occupancies are shown in Fig. 4.1 over the kinetic energy of the incident molecule. Obviously, the de-excitation process gets more efficient for lower kinetic energies which is evident because lower kinetic energies correspond to smaller molecule velocities and, thus, to larger interaction times of the projectile-surface system. Furthermore, we see that the final occupancy of the excited projectile level, which represents the survival probability of the incident $N_2(^3\Sigma_u^+)$ molecule, saturates at unity for large kinetic energies. The emission coefficient, on the other hand, strives towards one for small projectile energies. Both of these effects are consequences of the exponential forms (3.65b) and (3.68) that

[3]Note that aluminum theoretically allows for the resonant channel. It is, however, strongly suppressed since for $N_2(^3\Sigma_u^+)$ the resonant projectile level capturing a surface electron in the first step of (1.1) lies very close to the bottom of the conduction band (see Tables A.1 and A.3). Here the extension of the solid's wave functions into the vacuum is very weak and, hence, the tunneling matrix element is particularly small.

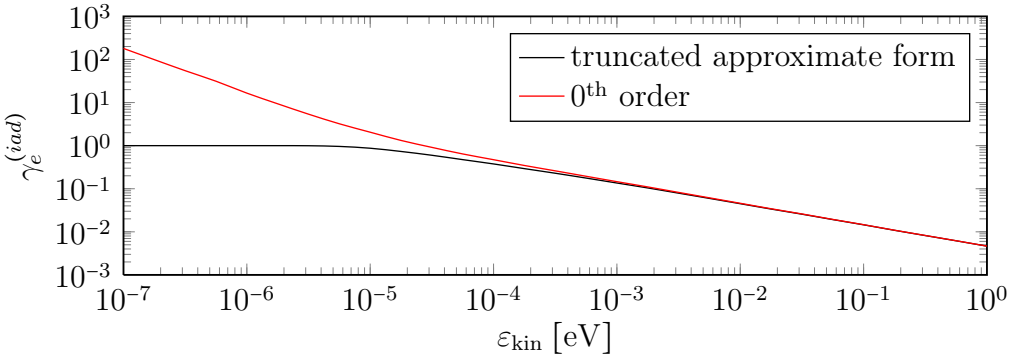

Figure 4.2: Comparison of the secondary electron emission coefficient $\gamma_e^{(iad)}$ computed from the truncated approximate form (3.68) (black line) and the zeroth order of (3.62b) (red line) which is obtained by dropping the σ-terms. The graphs were calculate for an aluminum surface without Coulomb screening and a nitrogen molecule in the perpendicular orientation.

were used to generate Fig. 4.1. If, on the contrary, we calculate $\gamma_e^{(iad)}$ by simply dropping the σ-terms from (3.62b), the emission coefficient diverges for $\varepsilon_{\mathrm{kin}} \to 0$ (see Fig. 4.2). This unphysical peculiarity is a consequence of the negligence of lifetime effects of the metastable which are encapsulated in the σ-terms. The approximate form (3.68), on the other hand, does account for the gradual de-excitation of the $N_2(^3\Sigma_u^+)$ molecule. Even though here the truncated σ-terms are underestimating the de-excitation probability, their approximate representation (see Eq. (C.8)) leads to exponential factors which damp the integrand in the divergent region and, thus, guarantee $\gamma_e^{(iad)} \to 1$ for $\varepsilon_{\mathrm{kin}} \to 0$. Figure 4.2 explicitly demonstrates this behavior.

Note that the region in which the zeroth-order result for $\gamma_e^{(iad)}$ exceeds unity corresponds to very low molecule velocities ($\varepsilon_{kin} \leq 10^{-5}\,\mathrm{eV}$). Moreover, for kinetic energies above approximately 0.1 meV the difference between the two curves in Fig. 4.2 is vanishingly small indicating that in this energy range the zeroth order of Eq. (3.62b) is sufficient. This fact is caused by the particular inefficiency of the Auger interaction and has an important implication. When considering the distribution of emitted electrons for thermal collision energies, it allows us to drop the σ-terms from (3.54b) and (3.61b). Consequently, the emission spectra can be determined solely in terms of the time integrated $\Delta_{iad}^{\vec{q}}$- and $\widetilde{\Delta}_{iad}^{\vec{q}}$-functions.

Going back to Fig. 4.1 we see that the de-excitation probability, which is given by $1 - n_1^{(iad)}(\infty)$, is higher in the parallel orientation while the amount of escaped electrons is larger in the perpendicular orientation. This seemingly contradictory result is a consequence of the different distributions of emitted electrons over $\vec{q}$-states in the two orientations. To make this more clear we calculate the final q_z-spectrum of the emitted electrons by integrating over the lateral wave vector dependence of (3.54b),

$$n_{q_z}^{(iad)}(\infty) = \int_{-\infty}^{\infty} \mathrm{d}q_x \int_{-\infty}^{\infty} \mathrm{d}q_y \; n_{\vec{q}}^{(iad)}(\infty) \,. \tag{4.34}$$

Focusing on the case of $\varepsilon_{\mathrm{kin}} = 50\,\mathrm{meV}$, which is about twice the thermal energy of a nitrogen molecule at room temperature, we can neglect the renormalizing σ-terms contained in $n_{\vec{q}}^{(iad)}$ (see Eq. (3.54b)) due to the previously given argument concerning the inefficiency of the Auger de-excitation process. The resulting lateral spectrum of the Auger electrons is shown in Fig. 4.3. As we see, for the parallel

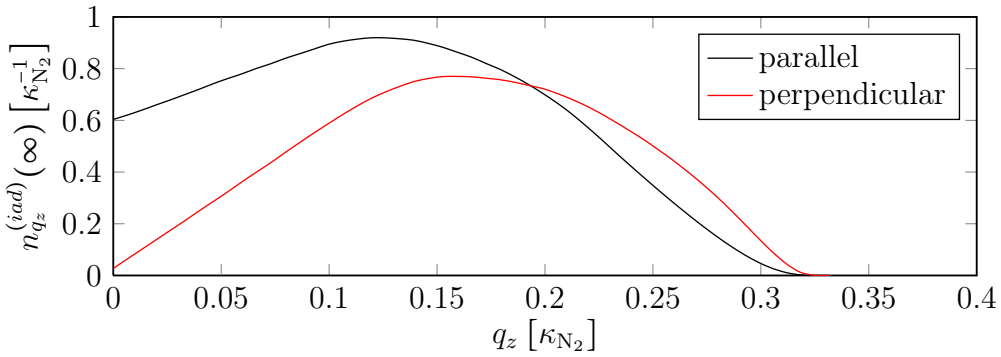

Figure 4.3: Distribution of emitted electrons over the z-component of $\vec{q}$ for an aluminum surface in parallel (black line) and perpendicular (red line) orientation. The curves were computed from (3.54b) by dropping the σ-terms and integrating over the lateral wave vector dependence. The effect of Coulomb screening was not included. Note that q_z is denoted in units of κ_{N_2} (see Eq. (2.34)) and only the region $q_z \geq 0$ is shown since wave vectors pointing in the negative z-direction traverse into the solid and, thus, cannot escape the surface.

case the electron has a significant probability to be emitted with a rather small vertical wave vector. For the perpendicular case, on the other hand, the spectrum almost vanishes at $q_z = 0$ and is concentrated at higher q_z-values around $0.15\,\kappa_{N_2}$. Since emitted electrons with a small q_z-component are very likely to get trapped in the image potential , large parts of the parallel spectrum are cut-off by the surface transmission function while the perpendicular spectrum is affected less strongly. Therefore, the emission coefficient is higher in the perpendicular orientation although the de-excitation probability is larger in the parallel orientation.

Next, we investigate the variation of the molecular occupancies $n_0^{(iad)}$ and $n_1^{(iad)}$ which can be obtained from (3.65a) and (3.65b), respectively. The arising occupation numbers are plotted in Fig. 4.4 for an aluminum surface at a kinetic energy of 50 meV. Obviously, the occupancy of the molecular levels changes significantly only in the range $|t| \leq 4$ which, taking the turning point into account, equals maximum distances of the molecule's center of mass from the surface of roughly $6.5\,a_B$. Thus, the indirect Auger de-excitation is only effective close to the projectile's turning point z_0. Moreover, the process is equally efficient in the incoming and outgoing branches of the trajectory which means that the projectile occupations depend only on $|t|$. Note that this behavior is neither evident nor expected from the double time integral structure of (3.65a) and (3.65b) and in part is a consequence of the particular inefficiency of the indirect Auger channel. In fact, for the case of a more effective de-excitation this symmetry would be broken by the exponentials in (3.65a) and (3.65b) which lead to a saturation of the molecular occupation numbers.

The final distribution of the escaped electrons over their unperturbed energy $\varepsilon_{\vec{q}}^{\infty}$ is also of interest. It can be obtained from (3.61b) by switching to spherical wave vector coordinates and integrating over the two angle components,

$$\tilde{n}_{\varepsilon_{\vec{q}}^{\infty}}^{(iad)}(\infty) = \frac{\kappa_{N_2}^3}{2}\left(\frac{2m_e}{\hbar^2\kappa_{N_2}^2}\right)^{\frac{3}{2}} \int_0^{\pi} \mathrm{d}\vartheta_{\vec{q}} \int_0^{2\pi} \mathrm{d}\varphi_{\vec{q}}\, \sqrt{\varepsilon_{\vec{q}}}\, \sin(\vartheta_{\vec{q}})\, \tilde{n}_{\vec{q}}^{(iad)}(\infty)\,. \tag{4.35}$$

Here we again consider a kinetic energy of $\varepsilon_{kin} = 50\,\mathrm{meV}$ which, as explained before, allows us to drop the σ-terms from $\tilde{n}_{\vec{q}}^{(iad)}$ (see Eq. (3.61b)). Figure 4.5 shows

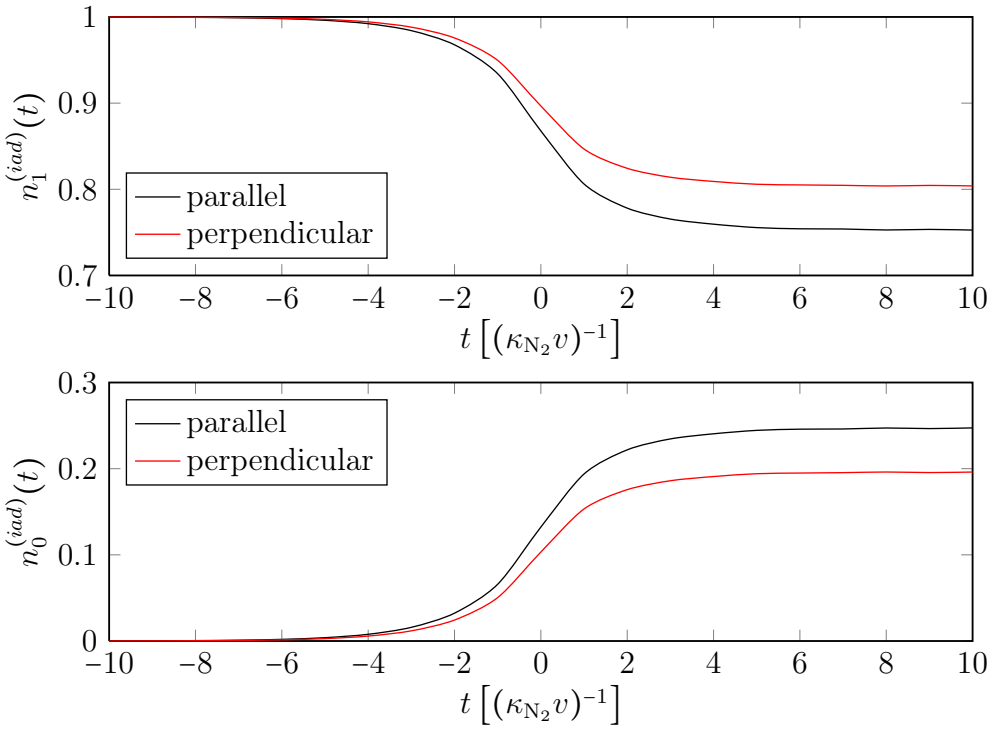

Figure 4.4: Time evolution of the occupancies of the excited molecular level (upper panel) and the ground state level (lower panel) for parallel (black lines) and perpendicular (red lines) molecule orientation on an aluminum surface. The kinetic energy of the incident molecule was fixed to 50 meV. Moreover, the curves were calculated from (3.65a) and (3.65b), respectively, while neglecting Coulomb screening effects. Note that here the time is measured in the atomic units of (4.9). Thus, a time difference of $\Delta t = 1$ corresponds to the motion of the molecule over a distance of $\Delta z = a_B/2$.

the resulting energy spectra for the two principal molecule orientations on an aluminum surface. Both graphs start at the origin, monotonously increase until approximately 4.8 eV and then drop off rapidly. The maximum observable energy resembles the classical cut-off energy $\varepsilon_{\vec{q}}^{max}$ which for a kinetic energy of 50 meV is given by

$$\varepsilon_{\vec{q}}^{max} = \varepsilon_{1*}^{\infty} - \varepsilon_{0g}^{\infty} + \varepsilon_F - V_i(z_0) \approx 5.74\,\text{eV} \ . \tag{4.36}$$

This implies that energy conservation is restored at the end of the collision, as it should be. Note that the spectrum shown in Fig. 4.5 is different from the one we published in Ref. [89]. The latter didn't include the influence of the image potential on the emitted electron's energy. This effect should, however, not be neglected since, as we see, it leads to a significant extension of the spectrum beyond the classical cut-off energy without the image potential which amounts to merely 3.43 eV.

Further inspection of Fig. 4.5 reveals that the low-energy part of the spectra is sharply cut off. This is caused by the surface transmission function $\mathcal{T}_{\vec{q}}$ contained in $\widetilde{\Delta}_{iad}^{\vec{q}}$ (see Eq. (3.60b)) which allows electrons to escape from the surface only when their perpendicular energy is large enough. Moreover, the spectrum takes on larger values for the perpendicular than for the parallel case, as was explained in connection with the q_z-spectrum of the emitted electron shown in Fig. 4.3.

Finally, integration of the energy spectra over $\varepsilon_{\vec{q}}^{\infty}$ yields the secondary electron emission coefficients listed in Table 4.1. Also shown here are the emission coefficients obtained from a surface-screened Coulomb potential. So far the results presented in

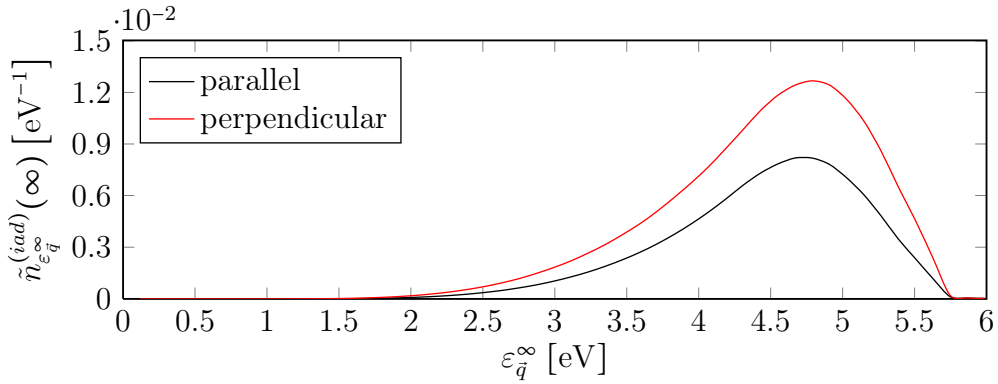

Figure 4.5: Final energy spectrum of the escaped electrons in parallel (black line) and perpendicular (red line) orientation. The kinetic energy of the incident molecule was fixed to 50 meV. Moreover, the graphs were calculated for an aluminum surface without Coulomb screening by means of (4.35) and (3.61b).

	unscreened	**surface screened**
parallel	$1.280 \cdot 10^{-2}$	$2.025 \cdot 10^{-3}$
perpendicular	$2.057 \cdot 10^{-2}$	$8.409 \cdot 10^{-3}$

Table 4.1: Secondary electron emission coefficient $\gamma_e^{(iad)}$ due to indirect Auger de-excitation of $N_2(^3\Sigma_u^+)$ on an aluminum surface in the two principal molecule orientations for a kinetic energy of 50 meV. The table shows the bare emission coefficients without Coulomb screening as well as those obtained by employing a statically screened Coulomb potential with the surface screening wave number κ_s listed in Table A.1.

this section were calculate without considering the static screening of the Coulomb potential which drives the Auger de-excitation of the molecule. In reality, however, the Coulomb interaction in the vicinity of a surface is screened due to the charge carriers of the solid. The strength of de-excitation should, thus, be affected by screening. In fact, the data in Table 4.1 indicates that upon using the surface screening constant κ_s (see Table A.1) the emission coefficients on aluminum are reduced by approximately 60% to 80%. However, the exact value of κ_s is rather uncertain[4]. Therefore, the previous results of this section were calculated without taking the screening into account.

We now apply our model to a different metallic surface, tungsten, and investigate the influence of the molecule's turning point on the de-excitation process. In order to do so, we calculate the final occupation of the excited projectile level for the two turning points $z_0 = 4.42\,a_B$ and $z_0 = 4\,a_B$. Note that the former value naturally arises from (2.53) for a kinetic energy of 50 meV while the latter one is artificial. The numerically obtained occupation numbers $n_1^{(iad)}(\infty)$ are shown in Fig. 4.6 over the projectile's kinetic energy. As we see, for the lowered turning point the de-excitation probability increases drastically at low energies leading to significantly reduced occupancies of the excited molecular level. At larger energies, on the other hand, the difference in the turning points shows almost no influence. Quantitatively,

[4]Here we converted between the bulk and the surface screening constant by using an empirical factor of 0.6 which was derived from the positron transmission and trapping experiments conducted by Neilson et al.[100] for various metallic films.

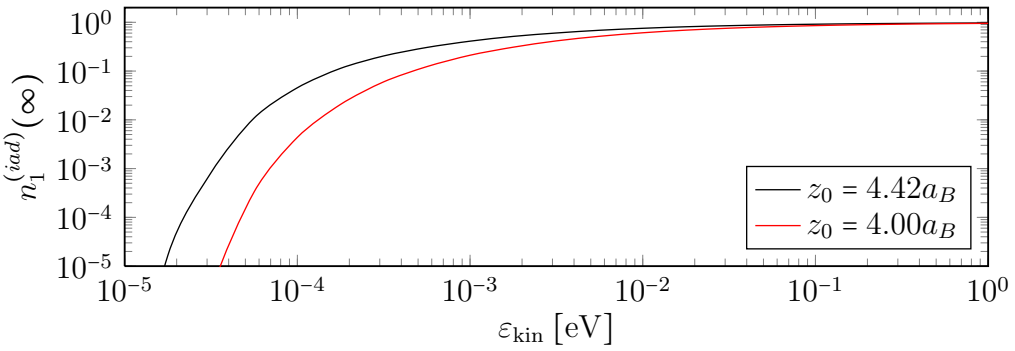

Figure 4.6: Comparison of the final occupancy of the excited molecular level $n_1^{(iad)}(\infty)$ for two different values of the turning point z_0. The curves were computed for a tungsten surface in the perpendicular orientation by means of (3.65b). The effect of screening was not included.

for energies below 0.1 meV, the occupancy of the excited molecular level for $z_0 = 4\,a_B$ is at least one order of magnitude smaller than the one obtained for $z_0 = 4.42\,a_B$. Note that this has, however, no influence on the number of escaped electrons (not shown in Fig. 4.6) because an electron emitted closer to the surface has a lower vertical energy and can, thus, no longer breach through the image potential, as we discussed before.

So far we have not compared our results to experimental measurements. In order to make contact with the experimental data obtained by Stracke et al.[127], we calculated the emission coefficient for tungsten using the turning point emerging from the surface potential (2.52) for 50 meV and the surface screening constant κ_s listed in Table A.1. We find the values $\gamma_e^{(iad)} \approx 1.533 \cdot 10^{-3}$ in the parallel and $\gamma_e^{(iad)} \approx 6.116 \cdot 10^{-3}$ in the perpendicular orientation both of which are rather close to the experimental estimate $\gamma_e^{(iad)} \approx 10^{-4} - 10^{-3}$ given by Stracke et al.[127]. Thus, despite of the crudeness of our effective model, which for instance neglects dangling bonds and surface states, and our simplistic treatment of screening near the surface, our approach seems to capture the essential physics even quantitatively. We attribute this to the rather large value of the molecule's turning point ($z_0 \approx 4.42\,a_B$) which partly immunizes the indirect Auger de-excitation against the details of the electronic structure in the immediate vicinity of the surface.

Finally, we note that, in contrast to Ref. [89], here we do not compare our results to the data of Lorente et al.[82]. In our opinion the latter work is rather intransparent, if not ambiguous, due to two reasons. Firstly, the authors claim to investigate the resonant de-excitation channel although the emission spectra published in Ref. [82] do not possess the corresponding structure with a strong peak at the resonance energy. In fact, the curves rather resemble Auger-like distributions since they monotonously rise until a cut-off energy is reached. Secondly, if Lorente et al.[82] did indeed include the indirect Auger channel in their calculation, they did, however, not account for the image shift of the emitted electron's energy. This can be seen from the fact that their spectra break down immediately at about 3.4 eV which resembles the classical cut-off energy (4.36) without the V_i-term. In total, the results published in Ref. [82] are not understood on our side and we, therefore, will not draw a comparison to the outcome of our calculations in this work.

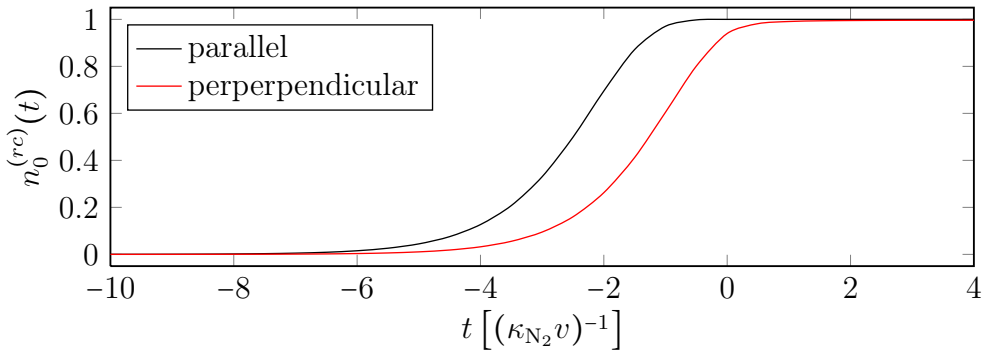

Figure 4.7: Time evolution of the occupation of the molecular ground state level $n_0^{(rc)}$ in front of an Al_2O_3 surface for parallel (black line) and perpendicular (red line) molecule orientation. The curves were calculated from (3.93a) and (3.92a) for a kinetic energy of 50 meV.

4.2.2 Two-Step Resonant De-Excitation

In this section we investigate the two-step resonant de-excitation channel (1.1). In order to study the isolated dynamics of this reaction, we require surface materials that suppress the indirect Auger de-excitation channel (1.2) due to their band structure. This is the case for a wide range of dielectric materials with sufficiently large energy gaps. In particular, we first consider an Al_2O_3 surface and projectile energy of 50 meV. For this setup we analyze the efficiency of the resonant electron capture and emission subreactions as well as the transient realization of the different molecular states and the spectrum of escaped electrons. Later we will calculate the electron emission coefficients of Al_2O_3, MgO, SiO_2 and diamond[5] for a wide range of kinetic energies.

All of the results presented in the course of this section were computed from the semi-classical equations of Sec. 3.3 while neglecting any contributions due to Auger de-excitation and employing the explicit and approximate form of the matrix elements and Δ-functions derived in Sec. 4.1.2. For details of our numerical scheme we refer the reader to Appendix E.

We start our analysis with the resonant electron capture into the ground state level which converts the incident $N_2(^3\Sigma_u^+)$ molecule into an $N_2^-(^2\Pi_g)$ ion. Since the indirect Auger de-excitation channel is blocked, we can employ (3.92a) to calculate the occupation of the metastable state $n_*^{(rc)}$. Note that the latter is only influenced by the first step of (1.1) and, therefore, does not depend on the resonant electron release subreaction. The occupancy of the lower projectile level $n_0^{(rc)}$ is then given through (3.93a) and, similar to the previous section, represents the de-excitation probability. Figure 4.7 shows the resulting time evolution of $n_0^{(rc)}$ for the case of an Al_2O_3 surface at a kinetic energy of 50 meV. We clearly see that the electron capture is very effective, since the molecular vacancy is completely filled within the incoming branch of the trajectory for both orientations. Moreover, the efficiency is higher in the parallel orientation where a complete filling of the ground state hole is realized at about $t = -1$, corresponding to a molecule-surface distance of approximately $4.92\,a_B$. In the perpendicular orientation, on the other hand, the

[5]Note that Diamond actually supports both de-excitation channels. However, as will be demonstrated in Sec. 4.2.3, the resonant channel strongly dominates over the Auger channel.

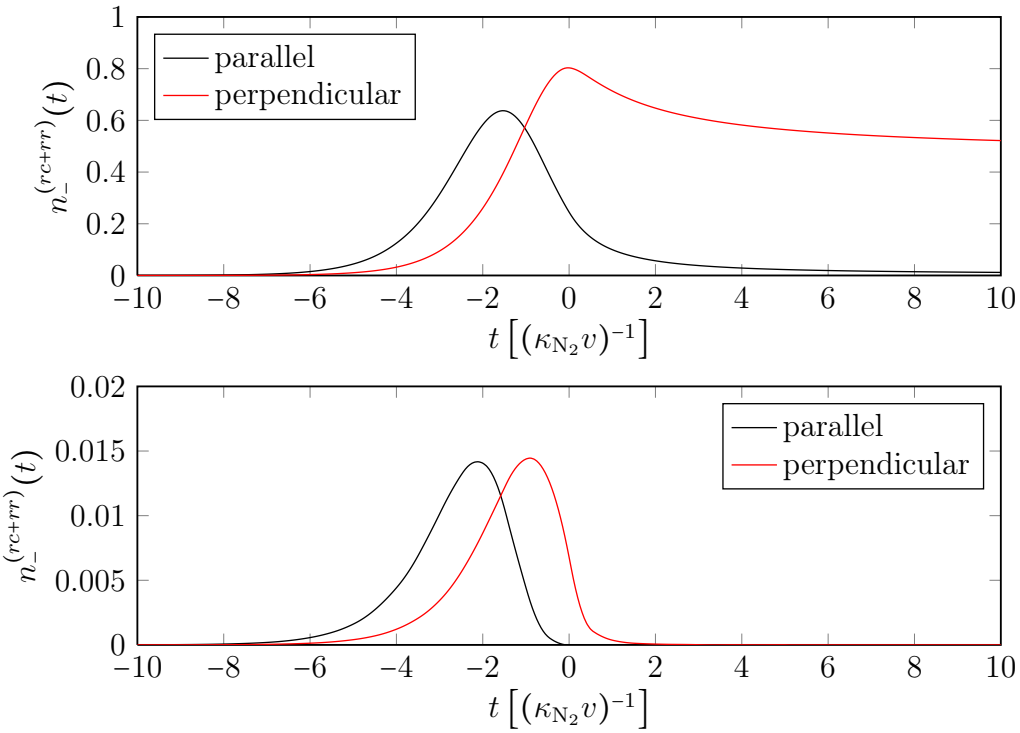

Figure 4.8: Fraction of negative ions versus time for the surface-induced decay process (upper panel) and the natural decay reaction (lower panel) in front of an Al_2O_3 surface at a molecular kinetic energy of 50 meV. The black lines represent the parallel orientation whereas the red lines denote the perpendicular orientation. The results were calculated from Eq. (3.96).

occupation only reaches unity at about $t = 1$ which represents the same distance from the surface but in the outgoing branch of the trajectory. Note that, in contrast to the indirect Auger de-excitation studied in the previous section (see Fig. 4.4), here the occupation of the projectile level is not symmetric with respect to t. This is caused by the effectiveness of the electron capture which in connection with the exponential structure of (3.92a) leads to a saturation of the occupancy.

Next, we focus on the decay of the negative ion which was generated through electron capture into the ground state level. As we know, this reaction can proceed in the subchannels of natural and surface-induced decay. To estimate the relative strength of these processes, we treat them separately and calculate the associated number of intermediate negative ions along the trajectory. From the respective amount of negative ions we will then be able to deduce the particular efficiency of the individual decay reactions. Figure 4.8 shows the time evolution of the fraction of negative ions $n_-^{(rc+rr)}$ as calculated from Eq. (3.96) for both processes in front of an Al_2O_3 surface at $\varepsilon_{kin} = 50$ meV. As we see, within the incoming branch the portion of negative ions first increases due to the previously demonstrated efficiency of electron capture into the ground state level and the finiteness of the decay rates. At some point, however, the decay process starts to outbalance the generating reaction, resulting in a decrease of the negative ion fraction. Apparently the negative ion share due to the surface-induced reaction levels out to a non-zero value at large collision times (see upper panel of Fig. 4.8). This can be explained by the fact that the corresponding matrix element (see Eq. (4.23)) is mainly driven by the image

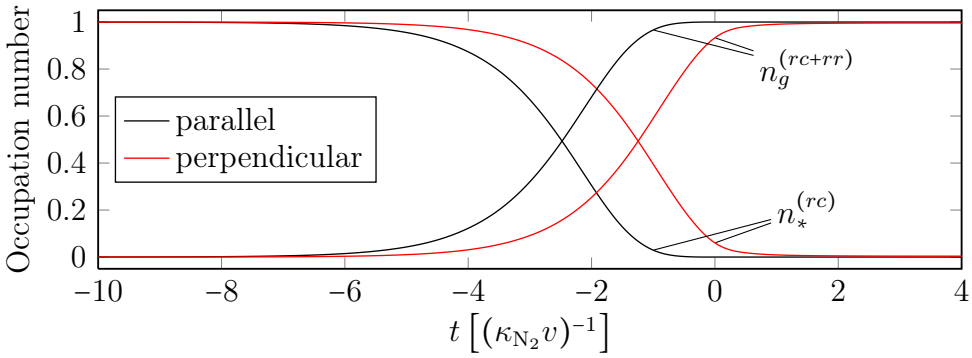

Figure 4.9: Time evolution of the molecular fractions $n_*^{(rc)}$ and $n_g^{(rc+rr)}$ pertaining to the metastable state and the ground state molecule, respectively. The figure shows data for the parallel (black lines) and perpendicular (red lines) orientation on an Al_2O_3 surface at a kinetic energy of 50 meV. The curves were obtained by employing Eqs. (3.92a) and (3.97), respectively, while only considering the natural decay channel.

potential which vanishes at large distances from the solid. For the natural decay, on the other hand, the decay rate is constant and, thus, the negative ion fraction eventually drops to zero (see lower panel of Fig. 4.8). Furthermore, we observe that the respective saturation level due to the surface-induced reaction is much lower for the parallel than for the perpendicular orientation. This is caused by the antisymmetry of the molecular wave function $\Psi_{1m}^{(N_2)}$ (see Eq. (2.31)) in the plane normal to the molecule's axis. In the parallel orientation this antisymmetry is broken by the surface which results in a significantly enlarged matrix element and, hence, in a higher rate of decay.

Inspecting Fig. 4.8 an important point to notice is that along the trajectory the amount of negative ions due to the surface-induced reaction is about two orders of magnitude higher than the amount of negative ions due to the natural decay channel. Consequently, the natural decay rate must be considerably larger than the surface-induced decay rate. We stress that in part this is caused by the distant turning point of the molecule. In fact, for a turning point closer to the surface an increased matrix element $V_{\tilde{q}}$ (see (4.23)) would arise which in turn would result in a higher rate of surface-induced decay. Since this is, however, not the case for the material combinations considered in this work we completely neglect the surface-induced decay channel in the following.

Focusing exclusively on the natural decay channel we now turn to the fraction of ground state molecules $n_g^{(rc+rr)}$. Note that the latter, in contrast to $n_*^{(rc)}$, is the result of the combined two-step resonant reaction. Its time evolution, therefore, has to be calculated from the solution of the coupled rate equation (3.97). The corresponding occupation for an Al_2O_3 surface and a kinetic energy of 50 meV is depicted in Fig. 4.9 together with the fraction of metastables $n_*^{(rc)}$. Obviously, with the decrease of $n_*^{(rc)}$ the number of ground state molecules $n_g^{(rc+rr)}$ almost immediately rises by the same amount. This effect is caused by the rather large rate of natural decay and the resulting small number of intermediate negative ions $n_-^{(rc+rr)}$ (see lower panel of Fig. 4.8).

We now move on to the energy distribution of the escaped electrons which can be calculated from Eq. (3.106b). Figure 4.10 shows the electronic spectrum at $t = \infty$, again for the case of Al_2O_3 and $\varepsilon_{kin} = 50$ meV, while neglecting the surface-induced

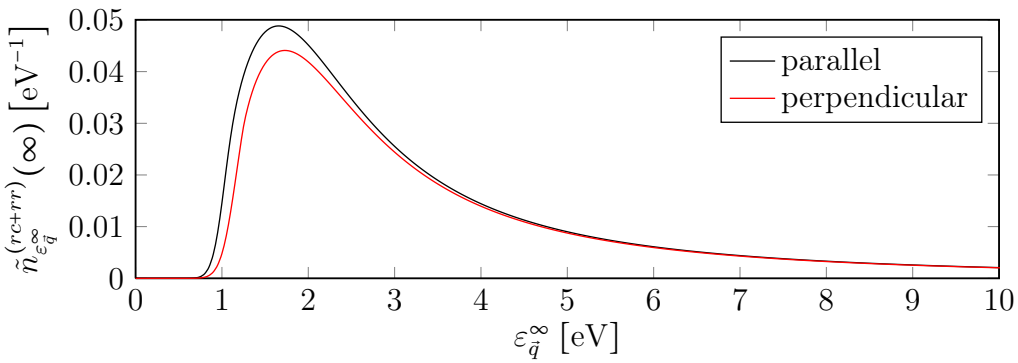

Figure 4.10: Final spectrum of escaped electrons for an Al_2O_3 surface calculated from Eq. (3.106b) in parallel (black line) and perpendicular (red line) orientation. The molecule's kinetic energy was fixed to 50 meV and only the natural decay process was taken into account.

decay channel. As we see, the spectrum exhibits a strong cut-off for energies below approximately 1 eV in both molecular orientations which is a direct consequence of the image potential. The latter traps low-energy electrons close to the surface and was incorporated into our calculation by means of the surface transmission function $\mathcal{T}_{\vec{q}}$ (see Eq. (2.89b)). Following the low-energy cut-off, the spectra show a strong peak at about 1.8 – 1.9 eV before they slowly fall off towards zero for larger energies. Examining the curves we further note that the spectrum is larger in the parallel orientation than in the perpendicular orientation. This can again be attributed to the trapping effect since, as seen from Fig. 4.9, in the perpendicular geometry the negative ion is generated and destroyed closer to the surface than in the parallel orientation. The image potential and, hence, the trapping effect are, thus, stronger in the perpendicular case which in turn reduces the amount of escaped electrons.

Finally, we calculate the secondary electron emission coefficient $\gamma_e^{(rc+rr)}$ for the particular cases of Al_2O_3, MgO, SiO_2 and diamond. As we assume (2.53) and the associated parameters to be valid for all of these materials, the turning point lies far outside the surface in each case. Consequently, we can neglect the surface-induced decay process over the much more efficient natural decay. Figure 4.11 depicts the resulting emission coefficients over the molecule's kinetic energy ε_{kin} as calculated from Eq. (3.105). Leaving MgO aside (for a discussion see below), the emission coefficients are on the order of 10^{-1} over the depicted range of kinetic energies. These rather large values of $\gamma_e^{(rc+rr)}$ can be attributed to the shape resonance $N_2^-(^2\Pi_g)$ which is not only efficiently formed in front of the surface but also quickly decays by releasing an electron. In contrast, atomic projectiles, for instance metastable argon which cannot form a negative ion, would lead to much smaller emission coefficients. Moreover, the size of the emission coefficients depicted in Fig. 4.11 agrees rather well with the values required for a convergent, self-consistent kinetic simulation of DBDs involving the resonant de-excitation channel[15]. Thus, in accordance with our initial motivation our effective microscopic model is indeed capable of providing input data for the kinetic modeling of gas discharges with sufficient accuracy.

Let us now analyze Fig. 4.11 in more detail. Apparently the emission coefficients increase with decreasing kinetic energy. This can be explained by the enlarged molecule-surface interaction time which leads to a more effective filling of the ground

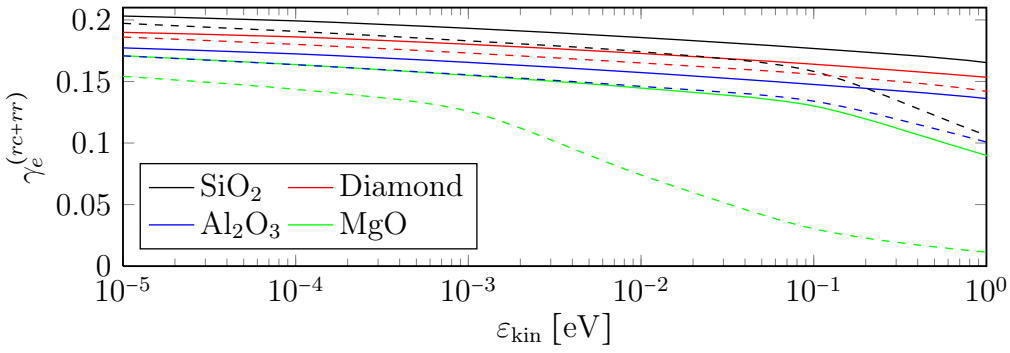

Figure 4.11: Secondary electron emission coefficient $\gamma_e^{(rc+rr)}$ for several dielectric surface materials plotted against the molecule's kinetic energy $\varepsilon_{\mathrm{kin}}$. The individual materials are encoded in different colors and in each case two curves are depicted. The solid one corresponds to the parallel molecule orientation whereas the dashed one identifies the perpendicular molecule orientation. All of the results were obtained from Eq. (3.105).

state hole. Apart from this obvious monotony property, the specific form of the particular graphs is, however, not easily understood. The reason for this is the complex dependence of the secondary electron emission coefficient on the surface's band structure and its static dielectric constant. For the materials we considered here a few general remarks can, nevertheless, be given.

First, we note that the value of $\gamma_e^{(rc+rr)}$ is sensitive to the efficiency of the electron capture into the molecular ground state level. A high efficiency results in negative ions getting produced at large distances from the surface. The subsequent electron emission will, thus, also take place at large distances because of the high natural decay rate of the ions. This is beneficial to the emission coefficient as the image potential trapping is less severe farther outside the surface. The efficiency of the electron capture in turn is determined by the alignment of the solid's valence band to the molecular hole level. Since the filling of the molecular vacancy is a resonant tunneling process, the vacancy level ε_{0^-} has to be degenerate to occupied states within the surface in order to allow for an efficient generation of negative ions. In addition, the electron capture is more productive if the degeneracy appears at higher energies within the valence band. This is due to the fact that at higher energies the wave functions of electrons within the solid have a larger extension outside the surface. Thus, their overlap with the molecular wave function is increased which directly influences the matrix element (4.15) and, hence, the efficiency of the electron capture. For the particular case of MgO both conditions, degeneracy and higher energies within the valence band, are violated since the molecular hole level ε_{0^-} shifts downwards out of the valence band at small distances (see Tabs. A.2 and A.3). As a result, MgO has the smallest emission coefficient of the materials under consideration.

In addition to the efficiency of electron capture the emission coefficient is also influenced by the surface material's dielectric constant ε_r^b. Here a larger value of ε_r^b seems to have an adverse effect on $\gamma_e^{(rc+rr)}$ since for the most part the emission coefficients for SiO_2 and diamond, both having lower dielectric constants, range above the emission coefficient of Al_2O_3 which possesses a higher dielectric constant (see Table A.2). This effect can probably be attributed to the amount of image potential trapping of slow electrons which is proportional to $(\varepsilon_r^b - 1)/(\varepsilon_r^b + 1)$. As

this factor increases with ε_r^b, the image potential and with it the effect of trapping is enlarged for materials with higher dielectric constants.

4.2.3 Combined Two-Channel De-Excitation

Having studied the isolated reactions of resonant and indirect Auger de-excitation we now turn to the combined two-channel de-excitation of $N_2(^3\Sigma_u^+)$. As mentioned earlier, diamond supports both de-excitation channels and will, therefore, be investigated in this section. However, as we will see, here the resonant channel clearly dominates over the Auger transition. In order to demonstrate the correct inclusion of both de-excitation reactions in our model we will, therefore, also discuss two artificial situations for an aluminum surface. Note that, in accordance with the findings of Sec. 4.2.2, we neglect the surface-induced decay channel in our analysis.

Similar to the previous section, the calculations discussed here build upon the semi-classical rate equations derived in Sec. 3.3 in which, this time, we only drop terms pertaining to the direct Auger de-excitation channel. The validity of the saddle-point approximation leading to these equations will be the first target of our investigations. As outlined in Sec. 3.3, approximations of the form (3.85), which were also used to derive the approximate exponential representation of the σ-series (C.8), are only acceptable if the involved Δ-function is sufficiently peaked on the time diagonal. In order to demonstrate the correctness of this assumption for the situations studied in this work, we calculate the functions $\Delta_{rc}(t_1, t_2)$ and $\Delta_{iad}(t_1, t_2)$, pertaining to the resonant electron capture subreaction of (1.1) and the indirect Auger de-excitation channel (1.2), respectively, along the anti-diagonal $t_1 = -t_2$. The results are shown in Fig. 4.12 for a diamond surface and a molecule in the perpendicular orientation at a kinetic energy of 50 meV. The plots represent profiles with respect to the time diagonal and were generated directly from the defining equations (4.22) and (4.10) while focusing only on those $\vec{k}$- and $\vec{q}$-states that allow for transitions in approximate agreement with energy conservation. Inspecting the results in Fig. 4.12 we see that for both functions the real part has its maximum on the time diagonal whereas the imaginary part vanishes on the diagonal itself but exhibits the largest value very close to it. Furthermore, when the distance from the time diagonal is enlarged, both functions decrease in an oscillating way. In particular, for Δ_{rc} the amplitude decreases to about 10% over a dimensionless time interval of $\Delta t \approx 0.05$. Via (4.9) this relates to a physical time span of

$$\Delta t_{\text{phys}} = \frac{a_B}{2v} \Delta t \approx 2.25\,\text{fs}\,, \tag{4.37}$$

and to a motion of the molecule along a distance of roughly $0.025\,a_B$. For Δ_{iad} the fall-off is even more drastic. Moreover, the behavior for shifted anti-diagonals and the parallel molecule orientation is very similar and, hence, not shown here.

Altogether, we can conclude that with respect to the macroscopic motion of the molecule the functions Δ_{rc} and Δ_{iad} are indeed sufficiently peaked on the time diagonal. Thus, the semi-classical approximation is valid in our case. We stress that this is a result of the particularly low kinetic energies considered in this work. For incident projectiles with higher kinetic energies the semi-classical approximation is, in general, not applicable.

Note that although we haven't shown results for Δ_{rr} here, we still assume the semi-classical approximation to be acceptable for this case as well because the matrix

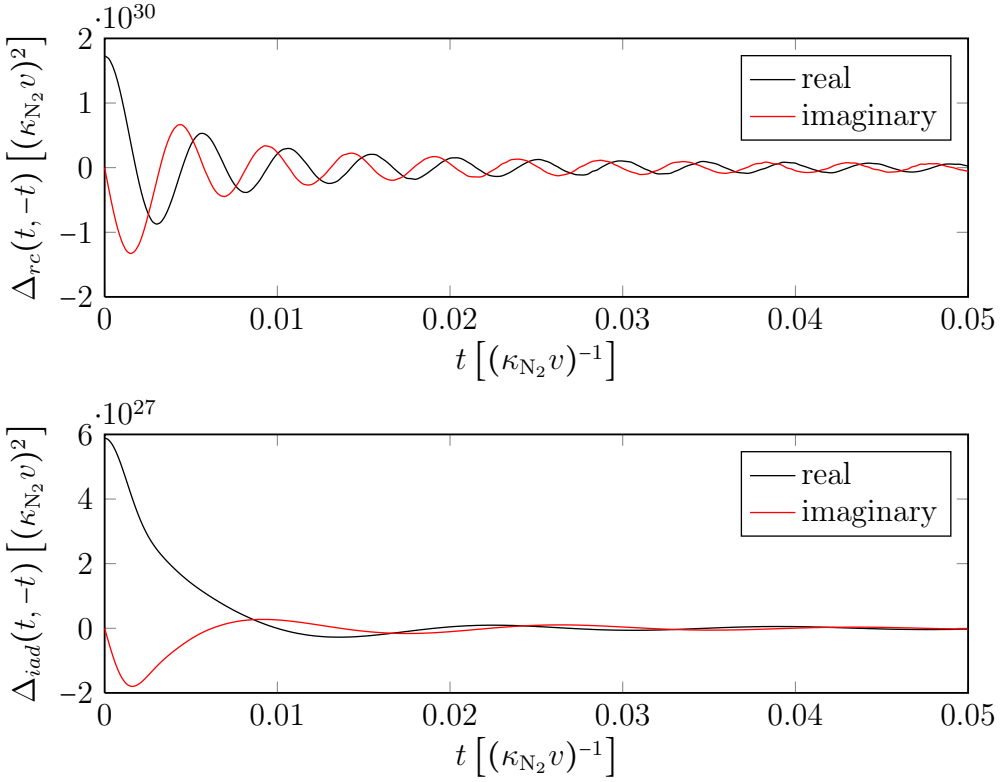

Figure 4.12: Variation of the real (black lines) and imaginary (red lines) part of $\Delta_{rc}(t_1, t_2)$ (upper panel) and $\Delta_{iad}(t_1, t_2)$ (lower panel) as calculated from (4.22) and (4.10) along the anti-diagonal $t_1 = -t_2 = t$. The results hold for a diamond surface and an $N_2(^3\Sigma_u^+)$ molecule with its axis aligned perpendicular to the surface at a kinetic energy of 50 meV. The behavior for negative time arguments t is omitted since the real (imaginary) part of both functions is symmetric (anti-symmetric) with respect to the time diagonal.

element structure and the energy scale are very similar. For the same reason the semi-classical approximation is also considered to hold true for the Δ-functions of the neutralization channels, Δ_{an} and Δ_{rn}.

We now move on to the occupancies of the molecular pseudo-particle states, that is, the probabilities with which the molecular configurations involved in the de-excitation process appear in the course of the two-channel scattering event. The time dependence of the occupancies $n_*^{(rc+iad)}$, $n_-^{(rc+rr+iad)}$ and $n_g^{(rc+rr+iad)}$ can be calculated from Eqs. (3.94), (3.96) and (3.97) where, in contrast to Sec. 4.2.2, we now retain the terms due to the indirect Auger de-excitation reaction. Figure 4.13 depicts the resulting occupation numbers for a diamond surface and $\varepsilon_{\rm kin} = 50$ meV in a semi-logarithmic plot. Inspection of the curves reveals that, similar to the isolated resonant reaction considered in the previous section, even close to the surface the occupancy of the negative ion state is rather low. Hence, the metastable molecule is almost immediately converted into its ground state. In Fig. 4.13 this fact is recognizable at the crossing point of the curves of $n_*^{(rc+iad)}$ and $n_g^{(rc+rr+iad)}$ which occurs at approximately half filling of both levels.

We stress that the low occupancy of the negative ion state is caused by the high efficiency of the natural decay channel and not by the Auger channel destroying the metastable molecule which constitutes the generating species of the negative ion. In fact, it is the other way around and in order to substantiate this claim, we now

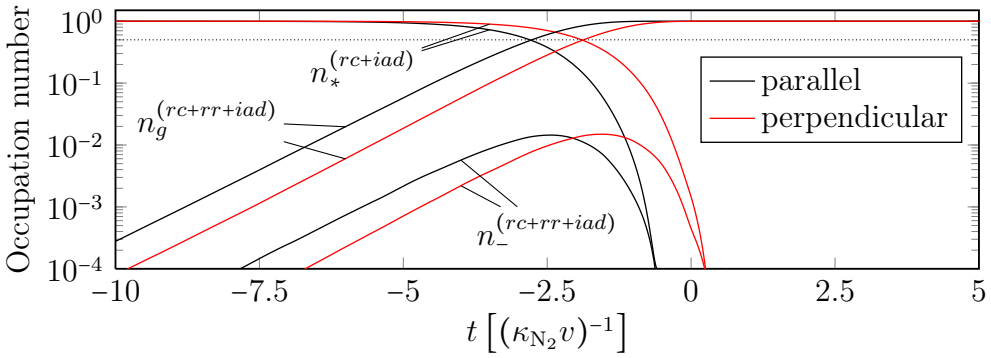

Figure 4.13: Transient occupation of the pseudo-particle levels of the ground state molecule $n_g^{(rc+rr+iad)}$, the metastable molecule $n_*^{(rc+iad)}$ and the negative ion $n_-^{(rc+rr+iad)}$ in parallel (black lines) and perpendicular (red lines) orientation for a diamond surface. The molecule's kinetic energy was fixed to 50 meV and the dotted line represents half filling of the respective level. The curves were calculated from Eqs. (3.94), (3.96) and (3.97), respectively.

investigate the relative efficiency of the two de-excitation channels by considering the respective reaction rates. Figure 4.14 shows the rates of resonant electron capture Γ_{rc} and indirect Auger de-excitation Γ_{iad} as calculated from Eqs. (3.87a) and (3.87d) for a diamond surface and a kinetic energy of 50 meV. For both channels the rates are highest at the molecule's turning point (approximately $4.42\,a_B$) which is the point of smallest molecule-surface separation and strongest molecule-surface interaction. Furthermore, when the distance from the surface is increased, the rates decrease exponentially. Quantitatively, the resonant reaction rate is about two orders of magnitude higher than the Auger rate. Consequently, the resonant channel captures surface electrons much more efficiently than the indirect Auger channel. In fact, the resonant channel is so effective in capturing electrons that it underruns the Auger reaction by destroying its starting point, the metastable state. As a result, in the combined two-channel system the Auger channel's performance is significantly diminished as compared to the isolated Auger reaction. This conclusion may be verified by considering the term within the rate equation scheme which is responsible for the production of ground state molecules due to indirect Auger de-excitation. It is given by (see Eqs. (3.86c) and (3.94))

$$\Gamma_{iad}(t)\, n_*^{(rc+iad)}(t) = \Gamma_{iad}(t)\, n_*^{(rc)}(t)\, n_*^{(iad)}(t)\,. \tag{4.38}$$

Here the factor $n_*^{(rc)}(t)$ is only present in the combined two-channel system but not for the isolated indirect Auger de-excitation. Based on numerical observations we note without explicit proof that the occupancies $n_*^{(rc)}(t)$ and $n_*^{(rc+iad)}(t)$ are almost identical. In combination with Fig. 4.13 we, thus, find that in the combined system the Auger channel's ground state production term (4.38) is strongly suppressed already in the incoming branch of the trajectory due to the efficiency of the resonant de-excitation mechanism.

Having discussed the occupancies of the projectile's pseudo-particle states, we now turn to the energy distribution of the observable secondary electrons. For the calculation of this quantity we employ (3.106b) while once more focusing on a diamond surface and a kinetic energy of 50 meV. Figure 4.15 depicts the resulting spectrum of escaped electrons at $t = \infty$ for the combined two-channel scheme as well

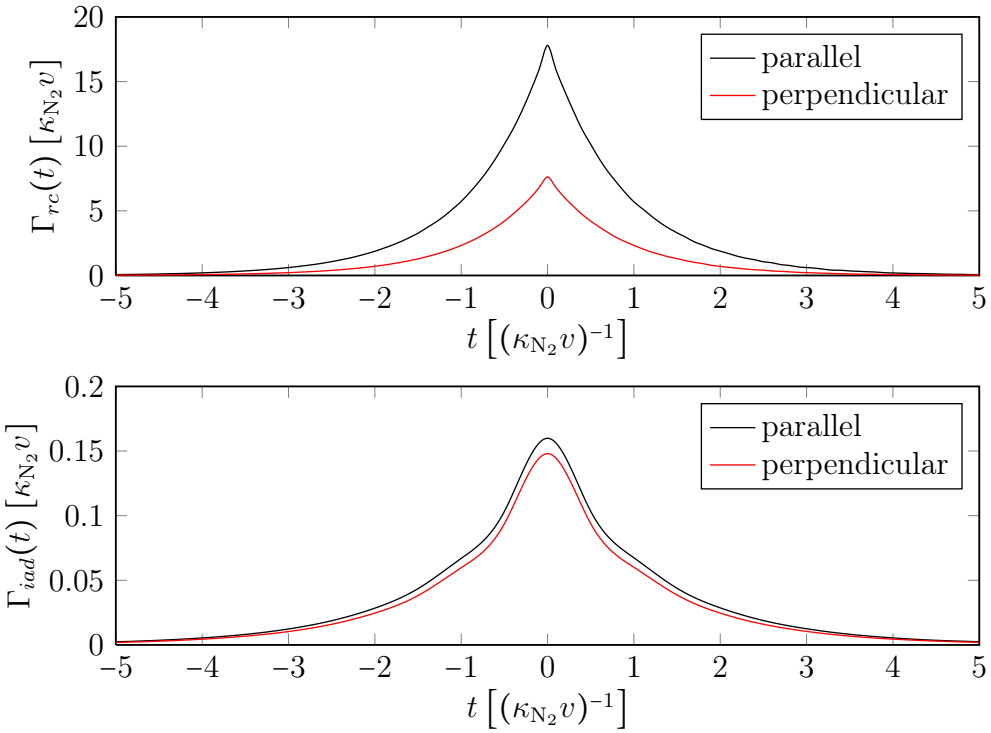

Figure 4.14: Variation of the rates of resonant electron capture Γ_{rc} (upper panel) and indirect Auger de-excitation Γ_{iad} (lower panel) for the parallel (black lines) and perpendicular (red lines) molecule orientation. The curves were calculated from (3.87a) and (3.87d) for a diamond surface at a projectile energy of 50 meV.

as for the isolated reaction channels. As we see, the isolated resonant spectra exhibit a strong peak at about 1.5 eV and slowly drop off for higher energies. The isolated Auger spectra, on the other hand, monotonously increase until approximately 2.8 eV and then strongly decline. The combined spectra, finally, are almost equal to the isolated resonant spectra and show a slight increase with respect to the latter curves in the range between 1.5 eV and 2.5 eV. Obviously this minor enlargement is due to the indirect Auger channel and supports our previous finding that the resonant transition dominates the Auger reaction. Note that, like before, the low-energy cut-off of all curves is due to the trapping of emitted electrons with small perpendicular energies in the image potential close to the surface.

We stress that the combined spectra shown in Fig. 4.15 are different from the simple addition of the isolated spectra. This behavior is caused by our unified treatment of the two de-excitation channels and would be even more pronounced for a projectile that is able to form a stable negative ion. Here the resonant electron emission would be almost completely blocked as the surface induced decay is always very weak. The resonant electron capture, however, would still be very efficient in destroying the initial species. Consequently, the spectrum of the emitted electron would resemble the Auger spectrum in shape but would be strongly decreased in magnitude.

Turning back to the situation depicted in Fig. 4.15 the secondary electron emission coefficients of the combined and isolated reaction channels are given by the area beneath the spectral curves and are summarized in Table 4.2. In accordance with our previous observations, the emission coefficients are not changed significantly by

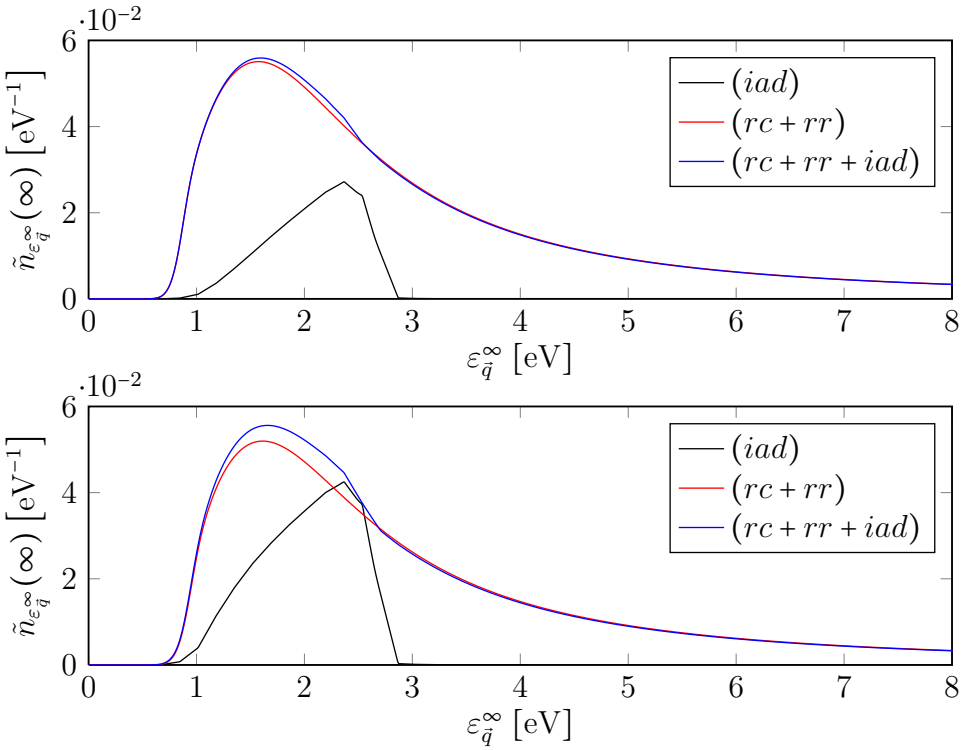

Figure 4.15: Energy spectrum of the escaped electrons in parallel (upper panel) and perpendicular (lower panel) orientation as calculated from (3.106b) for a diamond surface at a kinetic energy of 50 meV. In both panels the black line specifies the isolated spectrum of indirect Auger de-excitation (iad), the red line denotes the isolated spectrum due to the two-step resonant reaction $(rc+rr)$ and the blue line represents the combined two-channel spectrum $(rc+rr+iad)$. Note that the angularity of the Auger spectrum is a consequence of the tabulations performed in our numerical scheme and could be avoided by choosing a finer grid (see also Appendix E).

the inclusion of the Auger channel. A similar result was found by Stracke et al.[127] for $N_2(^3\Sigma_u^+)$ de-exciting on a tungsten surface. Their experimental measurements imply that only about 10% of the secondary electron emission coefficient is caused by the indirect Auger channel.

Finally, in order to demonstrate the correct inclusion of both de-excitation reactions in our model in a more impressive way, we now consider two artificial situations for an aluminum surface. As pointed out before, although theoretically the latter's band structure allows for both de-excitation channels, the resonant reaction is strongly suppressed since the molecular level capturing the surface electron is situated close to the bottom of the conduction band. In an attempt to generate a synthetic situation in which resonant and indirect Auger de-excitation are eye-to-eye competitors we, thus, manually shift the lower band edge downwards. Figure 4.16 shows the resulting spectra obtained from (3.106b) using the original value $V_0 = -16.5\,\text{eV}$ and the two artificial band edges $V_0 = -18.5\,\text{eV}$ and $V_0 = -24.5\,\text{eV}$ for a molecule in the perpendicular orientation and $\varepsilon_{\text{kin}} = 50\,\text{meV}$. As we see, in the combined spectrum of escaped electrons for the actual value, $V_0 = -16.5\,\text{eV}$, only the indirect Auger component is visible[6]. Furthermore, for a conduction band extending

[6]Note that for $V_0 = -16.5\,\text{eV}$ the combined spectrum depicted in Fig. 4.16 is identical to the one shown in Fig. 4.5 although the latter was calculated from (3.61b). This manifests the suppression

	parallel	perpendicular
$\gamma_e^{(iad)}$	0.02760	0.04921
$\gamma_e^{(rc+rr)}$	0.16685	0.15873
$\gamma_e^{(rc+rr+iad)}$	0.16754	0.16335

Table 4.2: Secondary electron emission coefficients for a diamond surface and a kinetic energy of 50 meV in parallel and perpendicular orientation. The table shows data for the isolated reactions of indirect Auger and two-step resonant de-excitation as well as for the combined two-channel de-excitation scheme.

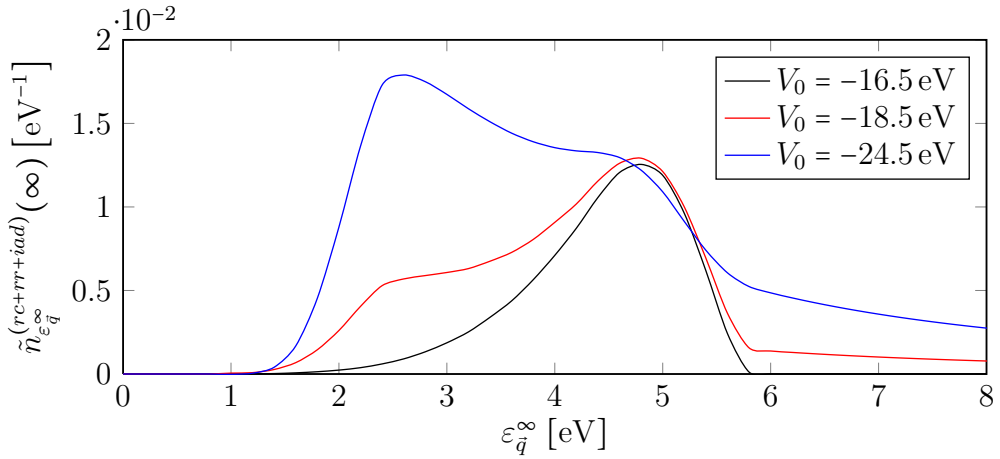

Figure 4.16: Two-channel energy spectrum of the escaped electrons in perpendicular orientation for an aluminum surface at three different depths of the conduction band V_0. Note that -16.5 eV is the original value of the band edge whereas -18.5 eV and -24.5 eV represent artificial cases. The curves were calculated from (3.106b) at a kinetic energy of 50 meV.

down to -18.5 eV the Auger channel still dominates the emission spectrum but we can already recognize a significant resonance peak at about 2.1 eV. Finally, when the lower band edge V_0 is shifted to -24.5 eV, this peak gets more prominent and starts to swallow the Auger contribution which is, however, still clearly visible.

In addition, we notice that while the resonant channel becomes more efficient as the conduction band gets deeper, the Auger component of the emission spectrum remains almost unaffected. Two understand this behavior one needs to consider the active parts of the band structure which can be estimated in terms of the classical energy conservation condition. For the indirect Auger channel the latter yields

$$\varepsilon_{1*}(t) + \varepsilon_{\vec{k}} \approx \varepsilon_{0g}(t) + \varepsilon_{\vec{q}}(t) \,, \tag{4.39}$$

which implies

$$\varepsilon_{\vec{k}} \approx \varepsilon^\infty_{0g} - \varepsilon^\infty_{1*} + \varepsilon^\infty_{\vec{q}} + V_i(z_p(t)) \,. \tag{4.40}$$

On the other hand, for the electron capture subreaction of the resonant de-excitation channel energy conservation requires

$$\varepsilon_{\vec{k}} \approx \varepsilon_{0-}(t) = \varepsilon^\infty_{0-} + V_i(z_p(t)) \,. \tag{4.41}$$

of the resonant channel and, in addition, proves the correctness of our treatment of the emitted electrons in Sec. 3.3.

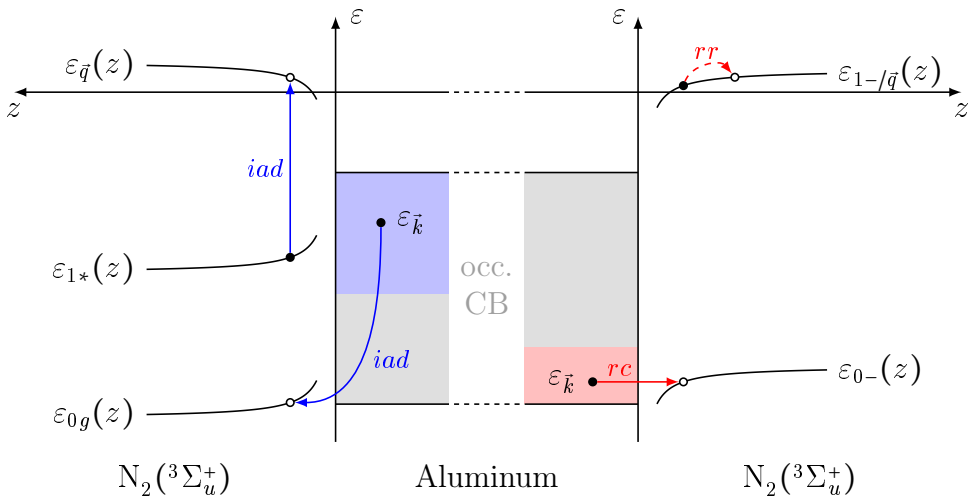

Figure 4.17: Band structure of aluminum together with the active zones for indirect Auger de-excitation (purple) and two-step resonant de-excitation (light red). The active areas were calculated from (4.40) and (4.41) using a maximum image shift of 2 eV and an additional near-resonance shift of ±1 eV. Note that only the occupied portion of the conduction band (occ. CB) is shown.

Upon inserting the particular unperturbed projectile energies and the maximum and minimum values of the image potential along the trajectory, Eqs. (4.40) and (4.41) can be used to calculate the range of energies $\varepsilon_{\vec{k}}$ (and $\varepsilon_{\vec{q}}^{\infty}$ for the Auger channel) that allow for a transition in agreement with energy conservation. For the band structure of aluminum the resulting active zones are shown in Fig. 4.17. As wee see, the Auger channel involves band states in the upper region of the conduction band's occupied portion whereas the resonant channel can only capture electrons close to the bottom of the band. Thus, when the band edge is shifted downwards the Auger channel is not affected since the associated active zone of the band structure as well as the energy of electrons therein remain fixed. The resonant channel, on the other hand, is strongly influenced by a variation of the conduction band depth since the latter directly determines the size of the band structure domain that allows for a resonant tunneling transition.

In total, our analysis of the lower band edge's influence (see Fig. 4.16) demonstrates that the interplay of resonant and indirect Auger de-excitation is captured correctly in our description.

Chapter 5

Neutralization of Positive Ions

In this chapter we will employ the results of our quantum-kinetic description presented in Sec. 3.4 to perform a numerical investigation of the neutralization of singly charged positive ions due to the Auger channel (1.4) and the resonant reaction (1.5). As mentioned earlier, we particularly investigate the neutralization of $He^+(^2S_{1/2})$, $Ar^+(^2P_{3/2})$ and $N_2^+(^2\Pi_u)$ on dielectric surfaces. Similar to Chapter 4 our analysis has to start with a concretization of the associated matrix elements and Δ-functions which will be done in Sec. 5.1. Building upon the explicit form of these expression and utilizing the semi-classical approximation we will then present numerical results concerning the isolated Auger and resonant neutralization reactions as well as the combined two-channel neutralization scheme in Sec. 5.2.

5.1 Matrix Elements and Δ-Functions

5.1.1 Auger Neutralization

From the derivation of the Hamiltonian in Sec. 2.4 we know that the matrix element of Auger neutralization $V_{\vec{k}_1\vec{k}_2\vec{k}'}$ involves the interaction term $\hat{H}_{ee}$ (see Eqs. (2.73) and (2.61)). In accordance with our treatment of the Auger de-excitation matrix element in Sec. 4.1.1, we reduce this term to the direct electron-electron Coulomb interaction $V_C = V_C^1$ (see Eq. (2.60)) which is the dominating contribution. Consequently, in position space representation $V_{\vec{k}_1\vec{k}_2\vec{k}'}$ has the form

$$V_{\vec{k}_1\vec{k}_2\vec{k}'}(t) = \int \mathrm{d}\vec{r} \int \mathrm{d}\vec{r}' \; \Psi_p^*\big(\vec{r}_\varphi(t)\big)\, \Psi_{\vec{k}_1}(\vec{r})\, V_C\big(|\vec{r}-\vec{r}'|\big)\, \Psi_{\vec{k}_2}(\vec{r}')\, \Psi_{\vec{k}'}^*(\vec{r}') \;, \tag{5.1}$$

where $\Psi_{\vec{k}_1}$, $\Psi_{\vec{k}_2}$ and $\Psi_{\vec{k}'}$ denote the wave functions of electrons within the surface (see Eq. (2.2)) and Ψ_p represents the wave function of the projectile's ground state hole. Note that, as explained in Sec. 4.1, within the matrix element the projectile wave function has to be taken at $\vec{r}_\varphi$ which was introduced in (4.2).

We will now show how the complicated matrix element (5.1) can be reduced to a one-dimensional integral. For this purpose we first insert the explicit form of the solid's wave functions (2.2) and express V_C by its inverse lateral Fourier transform (D.11). Equation (5.1) then turns into

$$\begin{aligned} V_{\vec{k}_1\vec{k}_2\vec{k}'}(t) = \frac{N_L^3}{2\pi} \int \mathrm{d}\vec{P} \int \mathrm{d}\vec{r} \int \mathrm{d}\vec{r}' \; \Psi_p^*\big(\vec{r}_\varphi(t)\big)\, \Psi_{k_{1z}}(z)\, \Psi_{k_{2z}}(z')\, \Psi_{k'_z}^*(z') \\ \times V_C\big(P, |z-z'|\big)\, e^{i\left[(k_{1x}+P_x)x+(k_{1y}+P_y)y-(P_x-k_{2x}+k'_x)x'-(P_y-k_{2y}+k'_y)y'\right]} \;, \end{aligned} \tag{5.2}$$

where $\vec{P} = (P_x, P_y)$. The x'- and y'-integrations in this equation can be carried out directly and yield

$$\int_{-\infty}^{\infty} \mathrm{d}x' \, e^{-i(P_x - k_{2x} + k'_x)x'} = 2\pi\,\delta\big(P_x - k_{2x} + k'_x\big) \,, \tag{5.3a}$$

$$\int_{-\infty}^{\infty} \mathrm{d}y' \, e^{-i(P_y - k_{2y} + k'_y)y'} = 2\pi\,\delta\big(P_y - k_{2y} + k'_y\big) \,. \tag{5.3b}$$

Furthermore, the x-y-integration in (5.2) represents the lateral Fourier transform of the conjugated projectile wave function Ψ_p^* of the rotated argument $\vec{r}_\varphi$. Restricting our analysis to the two principal projectile orientations we particularly obtain

$$\begin{aligned} &\frac{1}{2\pi} \int_{-\infty}^{\infty} \mathrm{d}x \int_{-\infty}^{\infty} \mathrm{d}y \; \Psi_p^*\big(z_p(t) - z, y, x\big)\, e^{i\left[(k_{1x}+P_x)x + (k_{1y}+P_y)y\right]} \\ &\qquad = \Psi_p\big(z_p(t) - z, k_{1y} + P_y, k_{1x} + P_x\big) \,, \end{aligned} \tag{5.4}$$

for the parallel case ($\varphi = 0$) and

$$\begin{aligned} &\frac{1}{2\pi} \int_{-\infty}^{\infty} \mathrm{d}x \int_{-\infty}^{\infty} \mathrm{d}y \; \Psi_p^*\big(x, y, z - z_p(t)\big)\, e^{i\left[(k_{1x}+P_x)x + (k_{1y}+P_y)y\right]} \\ &\qquad = \Psi_p\big(k_{1x} + P_x, k_{1y} + P_y, z - z_p(t)\big) \,, \end{aligned} \tag{5.5}$$

for the perpendicular situation ($\varphi = \frac{\pi}{2}$). Employing the explicit form of the ground state projectile wave functions of the ions $\mathrm{He}^+(^2S_{1/2})$, $\mathrm{Ar}^+(^2P_{3/2})$ and $\mathrm{N}_2^+(^2\Pi_u)$, introduced in Sec. 2.2, these Fourier integrals can be calculated analytically in an admittedly long-winded procedure (see Appendix D). In total, after relabeling the transforms (5.4) and (5.5) as $\Psi_p^{\parallel/\perp}\big(k_{1x} + P_x, k_{1y} + P_y, z - z_p(t)\big)$ Eq. (5.2) becomes

$$\begin{aligned} V^{\parallel/\perp}_{\vec{k}_1\vec{k}_2\vec{k}'}(t) = \frac{e_0^2}{4\pi\varepsilon_0} \frac{(2\pi)^2 N_L^3}{\sqrt{\kappa^2 + P^2}} \int_{-\infty}^{\infty} \mathrm{d}z \; \Psi_{k_{1z}}(z)\, \Omega_{k_{2z}k'_z}\big(\sqrt{\kappa^2 + P^2}, z\big) \\ \times \Psi_p^{\parallel/\perp}\big(k_{1x} + P_x, k_{1y} + P_y, z - z_p(t)\big) \,, \end{aligned} \tag{5.6}$$

with $P_x = k_{2x} - k'_x$, $P_y = k_{2y} - k'_y$ and κ denoting the static screening constant. Note that in this chapter the latter is only retained in our equations for the sake of universality and could actually be dropped since, as mentioned earlier, we are focusing on dielectric surfaces here. Furthermore, in (5.6) we introduced the quantity

$$\Omega_{k_{2z}k'_z}\big(\sqrt{\kappa^2 + P^2}, z\big) = \int_{-\infty}^{\infty} \mathrm{d}z' \; \frac{1}{\varepsilon_r(z, z')} \Psi_{k_{2z}}(z')\, \Psi^*_{k'_z}(z')\, e^{-\sqrt{\kappa^2+P^2}\,|z - z'|} \,. \tag{5.7}$$

Here ε_r denotes the static dielectric constant which due to the two-particle nature of the Auger matrix element, in general, depends on $\vec{r}$ and $\vec{r}\,'$. However, in order to simplify our analysis we employ a geometrical mean value approximation based on only the z-components of the position vectors,

$$\varepsilon_r(z, z') = \begin{cases} \varepsilon_r^b & \text{for } z \le 0 \text{ and } z' \le 0 \,, \\ 1 & \text{for } z \ge 0 \text{ and } z' \ge 0 \,, \\ \frac{\varepsilon_r^b + 1}{2} & \text{otherwise} \,. \end{cases} \tag{5.8}$$

This approach is particularly convenient as it merely involves piecewise constant combinations of the solid's bulk dielectric constant ε_r^b and the vacuum permittivity which will allow us to calculate the integral in (5.7) analytically. While (5.8)

of course represents a rather crude approximation, it, nevertheless, enables us to include the effect of the solid's dielectric constant which damps the Coulomb interaction, especially within the surface. A more sophisticated approximation might employ a continuous interpolation between the limiting values. This will, however, most certainly deny a analytical evaluation of (5.7) and is, therefore, not considered here.

We now proceed with the analytical calculation of $\Omega_{k_{2z}k'_z}$. Employing (2.3) we can express the vertical wave function term in (5.7) as

$$\Psi_{k_{2z}}(z')\,\Psi^*_{k'_z}(z') = \Theta(-z)\Phi^-_{k_{2z}k'_z}(z') + \Theta(z)\Phi^+_{k_{2z}k'_z}(z')\,, \tag{5.9}$$

with

$$\begin{aligned}\Phi^-_{k_{2z}k'_z}(z') &= \left[e^{ik_{2z}z'} + R_{k_{2z}}e^{-ik_{2z}z'}\right]\left[e^{-ik'_z z'} + R^*_{k'_z}e^{ik'_z z'}\right] \\ &= e^{ik_- z'} + R_{k_{2z}}e^{-ik_+ z'} + R^*_{k'_z}e^{ik_+ z'} + R_{k_{2z}}R^*_{k'_z}e^{-ik_- z'}\,,\end{aligned} \tag{5.10a}$$

$$\Phi^+_{k_{2z}k'_z}(z') = T_{k_{2z}}T^*_{k'_z}e^{i\bar{k}_- z'}\,, \tag{5.10b}$$

where we introduced the abbreviations

$$k_- = k_{2z} - k'_z\,, \tag{5.11a}$$

$$k_+ = k_{2z} + k'_z\,, \tag{5.11b}$$

$$\bar{k}_- = \bar{k}_{2z} - \left[\bar{k}'_z\right]^*\,. \tag{5.11c}$$

Note that $\bar{k}_{2z}$ and $\bar{k}'_z$ can be calculated from k_{2z} and k'_z by means of (2.5). Utilizing (5.9) together with (5.8) and the shorthand notation $\alpha = \sqrt{\kappa^2 + P^2}$ we now split up the integration domain in (5.7) and obtain

$$\begin{aligned}\Omega_{k_{2z}k'_z}(\alpha, z) = \Theta(-z)&\left[\frac{1}{\varepsilon^b_r}\,\Omega^{(1)}_{k_{2z}k'_z}(\alpha, z) + \frac{1}{\varepsilon^b_r}\,\Omega^{(2)}_{k_{2z}k'_z}(\alpha, z) + \frac{2}{\varepsilon^b_r + 1}\,\Omega^{(3)}_{k_{2z}k'_z}(\alpha, z)\right] \\ + \Theta(z)&\left[\frac{2}{\varepsilon^b_r + 1}\,\Omega^{(4)}_{k_{2z}k'_z}(\alpha, z) + \Omega^{(5)}_{k_{2z}k'_z}(\alpha, z) + \Omega^{(6)}_{k_{2z}k'_z}(\alpha, z)\right],\end{aligned} \tag{5.12}$$

which involves the terms

$$\Omega^{(1)}_{k_{2z}k'_z}(\alpha, z) = e^{-\alpha z}\int_{-\infty}^{z} \mathrm{d}z'\;\Phi^-_{k_{2z}k'_z}(z')\,e^{\alpha z'}\,, \tag{5.13a}$$

$$\Omega^{(2)}_{k_{2z}k'_z}(\alpha, z) = e^{\alpha z}\int_{z}^{0} \mathrm{d}z'\;\Phi^-_{k_{2z}k'_z}(z')\,e^{-\alpha z'}\,, \tag{5.13b}$$

$$\Omega^{(3)}_{k_{2z}k'_z}(\alpha, z) = e^{\alpha z}\int_{0}^{\infty} \mathrm{d}z'\;\Phi^+_{k_{2z}k'_z}(z')\,e^{-\alpha z'}\,, \tag{5.13c}$$

$$\Omega^{(4)}_{k_{2z}k'_z}(\alpha, z) = e^{-\alpha z}\int_{-\infty}^{0} \mathrm{d}z'\;\Phi^-_{k_{2z}k'_z}(z')\,e^{\alpha z'}\,, \tag{5.13d}$$

$$\Omega^{(5)}_{k_{2z}k'_z}(\alpha, z) = e^{-\alpha z}\int_{0}^{z} \mathrm{d}z'\;\Phi^+_{k_{2z}k'_z}(z')\,e^{\alpha z'}\,, \tag{5.13e}$$

$$\Omega^{(6)}_{k_{2z}k'_z}(\alpha, z) = e^{\alpha z}\int_{z}^{\infty} \mathrm{d}z'\;\Phi^+_{k_{2z}k'_z}(z')\,e^{-\alpha z'}\,. \tag{5.13f}$$

Assuming $\alpha = \sqrt{\kappa^2 + P^2} > 0$, all of these integrals are well behaved and can be calculated straightforwardly by means of the general rule

$$\int \mathrm{d}x\; e^{ikx}\,e^{\pm\alpha x} = \frac{e^{(\pm\alpha + ik)x}}{\pm\alpha + ik}\,. \tag{5.14}$$

Moreover, the case $\alpha = 0$ can be handled by considering the limit $\alpha \to 0^+$ in (5.14). In particular, we find

$$\Omega^{(1)}_{k_{2z}k'_z}(\alpha, z) = \frac{e^{ik_- z}}{\alpha + ik_-} + R_{k_{2z}} \frac{e^{-ik_+ z}}{\alpha - ik_+} + R^*_{k'_z} \frac{e^{ik_+ z}}{\alpha + ik_+} + R_{k_{2z}} R^*_{k'_z} \frac{e^{-ik_- z}}{\alpha - ik_-} , \tag{5.15a}$$

$$\begin{aligned} \Omega^{(2)}_{k_{2z}k'_z}(\alpha, z) = {} & \frac{e^{\alpha z} - e^{ik_- z}}{-\alpha + ik_-} + R_{k_{2z}} \frac{e^{\alpha z} - e^{-ik_+ z}}{-\alpha - ik_+} + R^*_{k'_z} \frac{e^{\alpha z} - e^{ik_+ z}}{-\alpha + ik_+} \\ & + R_{k_{2z}} R^*_{k'_z} \frac{e^{\alpha z} - e^{-ik_- z}}{-\alpha - ik_-} , \end{aligned} \tag{5.15b}$$

$$\Omega^{(3)}_{k_{2z}k'_z}(\alpha, z) = T_{k_{2z}} T^*_{k'_z} \frac{e^{\alpha z}}{\alpha - i\bar{k}_-} , \tag{5.15c}$$

$$\Omega^{(4)}_{k_{2z}k'_z}(\alpha, z) = \frac{e^{-\alpha z}}{\alpha + ik_-} + R_{k_{2z}} \frac{e^{-\alpha z}}{\alpha - ik_+} + R^*_{k'_z} \frac{e^{-\alpha z}}{\alpha + ik_+} + R_{k_{2z}} R^*_{k'_z} \frac{e^{-\alpha z}}{\alpha - ik_-} , \tag{5.15d}$$

$$\Omega^{(5)}_{k_{2z}k'_z}(\alpha, z) = T_{k_{2z}} T^*_{k'_z} \left[\frac{e^{i\bar{k}_- z}}{\alpha + i\bar{k}_-} - \frac{e^{-\alpha z}}{\alpha + i\bar{k}_-} \right] , \tag{5.15e}$$

$$\Omega^{(6)}_{k_{2z}k'_z}(\alpha, z) = T_{k_{2z}} T^*_{k'_z} \frac{e^{i\bar{k}_- z}}{\alpha - i\bar{k}_-} . \tag{5.15f}$$

Thus, upon employing (5.15) in (5.12) and inserting the resulting expression into (5.6) we, finally, achieved a reduction of the original matrix element (5.1) to a one-dimensional integral. We stress that this result could only be found by leveraging the particularly easy structure of the solid wave functions (2.2) and our approximation to the dielectric constant (5.8).

Similar to Sec. 4.1, we now employ the atomic variable transformation (4.9) where we replace κ_{N_2} with a placeholder κ_p which stands for κ_{He}, κ_{Ar} and κ_{N_2} for the ions $He^+(^2S_{1/2})$, $Ar^+(^2P_{3/2})$ and $N_2^+(^2\Pi_u)$, respectively (see Eqs. (2.27), (2.30) and (2.34)). The matrix element (5.6) then becomes

$$\begin{aligned} V^{\parallel/\perp}_{\vec{k}_1 \vec{k}_2 \vec{k}'}(t) = {} & \frac{e_0^2}{4\pi\varepsilon_0} \frac{(2\pi)^2 N_L^3}{\kappa_p^3 \sqrt{\kappa^2 + P^2}} \int_{-\infty}^{\infty} \mathrm{d}z \; \Psi_{k_{1z}}(z) \, \Omega_{k_{2z}k'_z}\Big(\sqrt{\kappa^2 + P^2}, z\Big) \\ & \times \Psi_p^{\parallel/\perp}\big(k_{1x} + P_x, k_{1y} + P_y, z - z_p(t)\big) . \end{aligned} \tag{5.16}$$

The final one-dimensional integral in (5.16) is dimensionless and can be calculated efficiently by a standard numerical integration routine.

We now turn to the Δ-functions associated with the Auger neutralization channel and consider $\widetilde{\Delta}_{an}$ as an exemplary case. Starting from (3.132) we employ the transformation (4.9) and convert the wave vector sums into integrals by means of (2.13). As a result, we obtain

$$\begin{aligned} \widetilde{\Delta}_{an}(t_1, t_2) = {} & \frac{2\kappa_p^9}{\hbar^2 (16\pi^3)^3 N_L^6} \int_{\text{occ.}} \mathrm{d}\vec{k}_1 \int_{\text{occ.}} \mathrm{d}\vec{k}_2 \int_{\text{unocc.}} \mathrm{d}\vec{k}' \; \mathcal{T}_{\vec{k}'}(t_1) \, \mathcal{T}_{\vec{k}'}(t_2) \\ & \times V_{\vec{k}_1 \vec{k}_2 \vec{k}'}(t_1) \, V^*_{\vec{k}_1 \vec{k}_2 \vec{k}'}(t_2) \, e^{-\frac{i}{a} \int_{t_2}^{t_1} \mathrm{d}t_3 \, [\varepsilon_{k_1} + \varepsilon_{k_2} - \varepsilon_{k'} - \varepsilon_{0g}(t_3)]} , \end{aligned} \tag{5.17}$$

with a as given by (4.11) but with the generic placeholder κ_p instead of κ_{N_2}. Note that the N_L^6-term contained in the prefactor of (5.17) is canceled by the N_L-factors of the matrix elements (see Eq. (5.16)). Thus, as before, the normalization of the solid's wave functions does not influence our results.

The direct numerical computation of (5.17) is extremely costly although each of the involved matrix elements only contains a single spacial integration. The reason for this is the large number of wave vector integration dimensions and the fast oscillation of the complex exponential throughout large areas of the integration domain. In order to reduce the numerical complexity we, therefore, approximate the product of the transmission function and the matrix element by an angular mean value[1],

$$\mathcal{T}_{\vec{k}'}(t)\, V_{\vec{k}_1\vec{k}_2\vec{k}'}(t) \approx \frac{V_{k_1k_2k'}(t)}{N_{\mathcal{T}_{\vec{k}'}}} \,, \tag{5.18}$$

with

$$V_{k_1k_2k'}(t) = \int \mathrm{d}\Omega_{\vec{k}_1} \int \mathrm{d}\Omega_{\vec{k}_2} \int \mathrm{d}\Omega_{\vec{k}'}\, \mathcal{T}_{\vec{k}'}(t)\, V_{\vec{k}_1\vec{k}_2\vec{k}'}(t) \,, \tag{5.19a}$$

$$N_{\mathcal{T}_{\vec{k}'}} = \int \mathrm{d}\Omega_{\vec{k}_1} \int \mathrm{d}\Omega_{\vec{k}_2} \int \mathrm{d}\Omega_{\vec{k}'}\, \mathcal{T}_{\vec{k}'}(t) \,. \tag{5.19b}$$

Here $\mathrm{d}\Omega_{\vec{k}_1}$, $\mathrm{d}\Omega_{\vec{k}_2}$ and $\mathrm{d}\Omega_{\vec{k}'}$ represent the differential solid angles of the three wave vectors and exhibit the general form

$$\mathrm{d}\Omega_{\vec{k}} = \mathrm{d}\vartheta_{\vec{k}}\, \mathrm{d}\varphi_{\vec{k}}\, \sin\!\left(\vartheta_{\vec{k}}\right) . \tag{5.20}$$

Moreover, the presence of the $\mathcal{T}_{\vec{k}'}$-factor in (5.19b) is caused by the fact that the transmission function restricts the angle $\vartheta_{\vec{k}'}$ and, thus, shrinks the integration domain. Employing the explicit form of $\mathcal{T}_{\vec{k}'}$ (see Eq. (2.89a)) we can evaluate (5.19b) analytically. The result reads

$$\begin{aligned} N_{\mathcal{T}_{\vec{k}'}} &= \int_0^{\pi/2} \mathrm{d}\vartheta_{\vec{k}_1} \int_0^{2\pi} \mathrm{d}\varphi_{\vec{k}_1} \int_0^{\pi/2} \mathrm{d}\vartheta_{\vec{k}_2} \int_0^{2\pi} \mathrm{d}\varphi_{\vec{k}_2}\, \sin\!\left(\vartheta_{\vec{k}_1}\right) \sin\!\left(\vartheta_{\vec{k}_2}\right) \\ &\quad \times \int_0^{\vartheta^{max}} \mathrm{d}\vartheta_{\vec{k}'} \int_0^{2\pi} \mathrm{d}\varphi_{\vec{k}'}\, \sin(\vartheta_{\vec{k}'}) \qquad (5.21a) \\ &= (2\pi)^3 \left(1 - \cos(\vartheta^{max})\right) , \qquad (5.21b) \end{aligned}$$

where ϑ^{max} amounts to

$$\vartheta^{max} = \Theta(\varepsilon_{\vec{k}'}) \arccos\left(\Theta(-V_0) \sqrt{\frac{-V_0}{\varepsilon_{\vec{k}'} - V_0}} \right) , \tag{5.22}$$

which is found by converting the Θ-functions contained in $\mathcal{T}_{\vec{k}'}$ into a condition for $\vartheta_{\vec{k}'}$. Substituting (5.21b) back into (5.18) we then obtain

$$\mathcal{T}_{\vec{k}'}(t)\, V_{\vec{k}_1\vec{k}_2\vec{k}'}(t) \approx \frac{V_{k_1k_2k'}(t)}{(2\pi)^3 \left(1 - \cos(\vartheta^{max})\right)} \,. \tag{5.23}$$

After inserting the approximate representation (5.23) into (5.17) we now can carry out the angle integrations and, finally, find

$$\begin{aligned} \widetilde{\Delta}_{an}(t_1, t_2) \approx \frac{2\kappa_p^9}{\hbar^2 (16\pi^3)^3 N_L^6 (2\pi)^3} \int_{\text{occ.}} \mathrm{d}k_1 \int_{\text{occ.}} \mathrm{d}k_2 \int_{\text{unocc.}} \mathrm{d}k' \, \frac{k_1^2\, k_2^2\, k'^2}{1 - \cos(\vartheta^{max})} \\ \times V_{k_1k_2k'}(t_1)\, V^*_{k_1k_2k'}(t_2)\, e^{-\frac{i}{a}\int_{t_2}^{t_1} \mathrm{d}t_3\, (\varepsilon_{\vec{k}_1} + \varepsilon_{\vec{k}_2} - \varepsilon_{\vec{k}'} - \varepsilon_{0g}(t_3))} \,, \end{aligned} \tag{5.24}$$

[1] Note that in our notation the full and the angle-integrated matrix element differ only in the vector arrows of the subscripts. Thus, the reader may not confuse $V_{\vec{k}_1\vec{k}_2\vec{k}'}$ and $V_{k_1k_2k'}$.

where we utilized the fact that within our effective model the occupied and unoccupied regions of the solid's band structure are determined solely by the energy and, thus, by the radial components of the wave vectors.

As we see, the original nine-dimensional wave vector integral of (5.17) has been approximated by a three-dimensional radial integral which, obviously, represents a tremendous simplification. The quality of this approximation can, however, not be analyzed because a calculation of the full integral (5.17) is clearly out of reach to us in terms of computing time. Even so, we assume the angle averaging (5.23) to produce acceptable results since it correctly retains the radial wave vector dependence of the matrix element which, probably, is more important than the angle components.

Note that the remaining Δ-functions of the Auger neutralization can be approximated in the very same way. In fact, we can immediately generalize (5.24) to Δ_{an}. The latter differs from $\widetilde{\Delta}_{an}$ only in the absence of the surface transmission functions (see Eq. (3.113)) which exclusively enter (5.24) through the upper boundary of the $\vartheta_{\vec{k}'}$-integration. Consequently, we can simply set $\vartheta^{max} = \frac{\pi}{2}$ to revoke their effect which corresponds to a switch from $\widetilde{\Delta}_{an}$ to Δ_{an} in (5.24).

Moreover, using the angle-integrated matrix element (5.18) and the resulting approximate form (5.24) time integrals of the Δ-functions can be calculated straightforwardly. The double time integral of $\widetilde{\Delta}_{an}$ with equal upper boundaries for instance reads

$$\begin{aligned}\int_{-\infty}^{t}\mathrm{d}t_1\int_{-\infty}^{t}\mathrm{d}t_2\,\widetilde{\Delta}_{an}(t_1,t_2) = \frac{2\kappa_p^7}{\hbar^2(16\pi^3)^3N_L^6(2\pi)^3v^2}\int_{\text{occ.}}\mathrm{d}k_1\int_{\text{occ.}}\mathrm{d}k_2\int_{\text{unocc.}}\mathrm{d}k' \\ \times\frac{k_1^2\,k_2^2\,(k')^2}{1-\cos(\vartheta^{max})}\,\left|\Gamma_{k_1k_2k'}(t)\right|^2\ ,\end{aligned} \tag{5.25}$$

with

$$\Gamma_{k_1k_2k'}(t) = \int_{-\infty}^{t}\mathrm{d}t_1\;V_{k_1k_2k'}(t_1)\,e^{-\frac{i}{a}\int_0^{t_1}\mathrm{d}t_2\left[\varepsilon_{\vec{k}_1}+\varepsilon_{\vec{k}_2}-\varepsilon_{\vec{k}'}-\varepsilon_{0g}(t_2)\right]}\ . \tag{5.26}$$

Other time integrals of $\widetilde{\Delta}_{an}$ or different Δ-functions associated with the Auger neutralization channel may be calculated in a similar manner.

Finally, we note that in order to calculate expressions of the form (5.24) or (5.25) numerically, it is advantageous to tabulate $V_{k_1k_2k'}(t_1)$ over the three wave vector components and the time argument. The integrals can then be calculated efficiently using a Monte Carlo procedure for the radial wave vector components and a standard one-dimensional integrator for the time variables.

5.1.2 Resonant Neutralization

As we know, the resonant neutralization reaction (1.5) is equivalent to the electron capture subprocess of the resonant de-excitation channel (1.1) since both of them are driven by the same matrix element $V_{\vec{k}}$ (see Eq. (2.69)). In Sec. 4.1.2 we saw that the latter can be approximated by the time-separated expression (4.19) which allows for an efficient calculation. Moreover, as pointed out in Sec. 3.4, the quantity Δ_{rn}, which constitutes the only relevant Δ-function of the resonant neutralization channel, is equal to Δ_{rc} with ε_{0g} instead of ε_{0-}. Consequently, the explicit calculation of Δ_{rn} and its time integrals follows the procedure presented in Sec. 4.1.2 where we merely have to replace κ_{N_2} with κ_p and adjust the energy of the lower projectile level by setting $\varepsilon_{0-} = \varepsilon_{0g}$.

	$Ar^+(^2P_{3/2})$	$He^+(^2S_{1/2})$	$N_2^+(^2\Pi_u)$
Al_2O_3	rn	an	rn
CaO	an	an	an
Diamond	$an + rn$	$an + rn$	$an + rn$
MgO	rn	an	-
$SiO_2^{(upper)}$	-	an	-
$SiO_2^{(lower)}$	rn	-	rn

Table 5.1: Overview of the considered material combinations and the energetically supported neutralization channels for the case of low kinetic energies ($\varepsilon_{kin} \leq 1\,eV$). As before, *an* stands for the Auger neutralization channel (1.4) while *rn* identifies the resonant neutralization reaction (1.5). Note that for SiO_2 we consider the upper and lower valence band separately.

5.2 Numerical Results

Having concretized the matrix elements and Δ-functions in Sec. 5.1 we now present numerical results for the isolated Auger and resonant neutralization as well as their combination. In particular, we focus on the neutralization of $He^+(^2S_{1/2})$, $Ar^+(^2P_{3/2})$ and $N_2^+(^2\Pi_u)$ on the dielectric materials Al_2O_3, CaO, MgO, SiO_2 and diamond. Moreover, we will again focus on the case of low kinetic energies ($\varepsilon_{kin} \leq 1\,eV$) which has been put in second place by most of the previous studies in this field. As a side effect of the slow projectile motion we can employ the saddle-point approximation leading to the approximate exponential representation of the σ-series (C.8). The validity of this semi-classical approach was demonstrated for Δ_{rc} and Δ_{iad} in Sec. 4.2.3. As mentioned earlier, we, however, assume it to hold for the Δ-functions of the neutralization channels as well.

In our subsequent numerical investigations we will only consider the major projectile orientations, similar to our treatment of the de-excitation channels in Chapter 4. Consequently, for $N_2^+(^2\Pi_u)$ we will limit our investigations to the cases $\varphi = 0$ (axis parallel to the surface) and $\varphi = \frac{\pi}{2}$ (axis perpendicular to the surface). For the two atomic ions, on the other hand, we will restrict ourselves to the situation $\varphi = \frac{\pi}{2}$ which means that the z-axis of the projectile's reference frame aligns with the laboratory z-axis. Note that the latter choice does, however, only affect $Ar^+(^2P_{3/2})$ since the wave function of the ground state hole of $He^+(^2S_{1/2})$ is spherically symmetric (see Eq. (2.25)). Moreover, as in Sec. 4.2, we will only consider the initial magnetic quantum number $m = 1$ for the $N_2^+(^2\Pi_u)$ ion.

Before starting our numerical analysis, we now first identify the presence of the two neutralization channels for the previously mentioned material combinations. The operativeness of the reactions for a particular system follows from the band structure of the surface and the energy of the projectile's ground state level. Table 5.1 summarizes the energetically allowed neutralization channels for the considered materials and the case of low kinetic energies. All of the listed operative combinations will be explicitly investigated in the following. Note, however, that for low kinetic energies no reference measurements concerning these projectile-surface systems seem to be available. Therefore, we, unfortunately, are unable to benchmark the outcome of our calculations against experimental results.

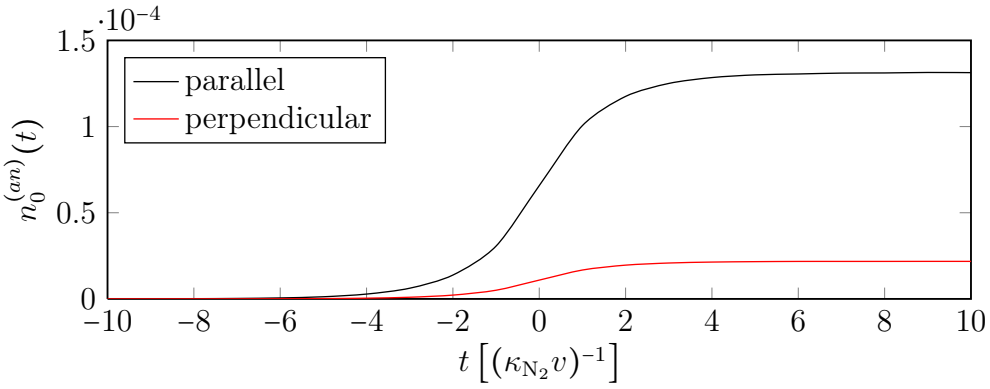

Figure 5.1: Time dependence of the occupation of the projectile level $n_0^{(an)}$ due to the Auger neutralization of $N_2^+(^2\Pi_u)$ on a CaO surface. Separate graphs are shown for the parallel (black line) and perpendicular (red line) orientation. The results were calculated from Eq. (3.134) at a kinetic energy of 50 meV.

5.2.1 Auger Neutralization

In this section we focus on the isolated Auger neutralization channel (1.4). We start our analysis with a consideration of the transient occupation of the initially empty projectile level $n_0^{(an)}(t)$ using the example of $N_2^+(^2\Pi_u)$ on a CaO surface. As seen from Table 5.1, this material combination blocks the resonant neutralization channel and exclusively supports Auger neutralization. Thus, we can calculate the variation of $n_0^{(an)}$ over time from (3.134) after dropping the components due to the resonant reaction. The resulting occupancy is depicted in Fig. 5.1 for a kinetic energy of 50 meV. As we see, the neutralization reaction is very weak in both of the principal molecule orientations. In particular, the occupation of the projectile level changes significantly only close to the turning point, in the range $|t| \leq 2$. Furthermore, in the outgoing branch of the trajectory the occupancy quickly saturates at about $1.3 \cdot 10^{-4}$ in the parallel and $0.2 \cdot 10^{-4}$ in the perpendicular orientation. Hence, the reaction is clearly more efficient in the parallel than in the perpendicular orientation which must be attributed to the symmetry of the matrix element (5.1). In addition, we notice that both curves are symmetric with respect to $t = 0$. Similar to the indirect Auger de-excitation reaction which was discussed in Sec. 4.2.1 (see Fig. 4.4), this is a consequence of the particular inefficiency of the Auger neutralization channel in the present situation. For the case of a more effective neutralization the exponential terms in (3.134) would break the symmetry and lead to a saturation of $n_0^{(an)}$ at unity.

We now move on to the spectrum of the internally excited Auger electrons and their transmission through the surface edge. Here we consider the case of a $He^+(^2S_{1/2})$ ion neutralizing on an Al_2O_3 surface. According to Table 5.1 this setup again suppresses resonant neutralization and exclusively allows for the Auger neutralization channel. Formally, the energy distribution of the internally excited electrons $n_{\varepsilon_{\bar{k}'}}^{(an)}$ and the escaped electrons $\tilde{n}_{\varepsilon_{\bar{k}'}}^{(an)}$ can be obtained by integrating over the angle dependence of (3.124) and (3.130), respectively. Since, as will become apparent, the Auger neutralization is rather inefficient for $He^+(^2S_{1/2})$ on Al_2O_3 as well, we can omit the σ-terms in these equations since they are a measure for the survival probability of the incident ion. Consequently, the quantities $n_{\varepsilon_{\bar{k}'}}^{(an)}$ and $\tilde{n}_{\varepsilon_{\bar{k}'}}^{(an)}$ are given by (5.25) upon adjusting ϑ^{max}, stripping out the k'-integration and converting

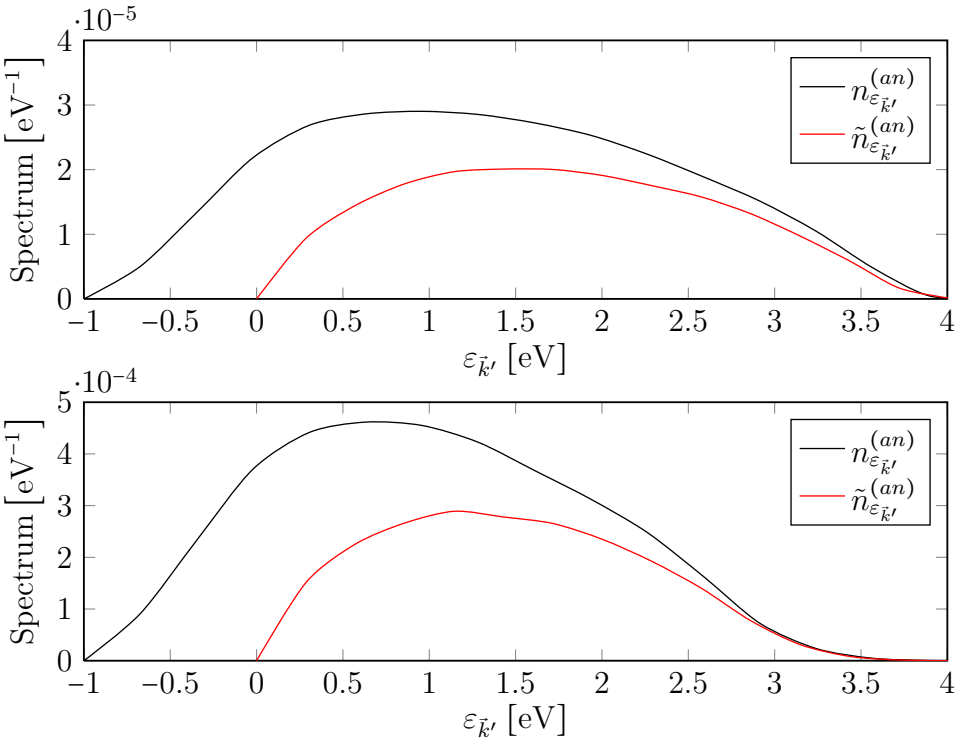

Figure 5.2: Final energy spectrum of the Auger electrons due to the neutralization of $He^+(^2S_{1/2})$ on Al_2O_3 at a kinetic energy of 50 meV. Here $n^{(an)}_{\varepsilon_{\vec{k}'}}$ and $\tilde{n}^{(an)}_{\varepsilon_{\vec{k}'}}$ refer to the internally excited electrons within the surface (black lines) and the electrons capable of escaping the surface (red lines), respectively. The upper panel shows the results obtained using the turning point $z_0 \approx 3.6\,a_B$ emerging from (2.53) with the parameters due to Bonini et al.[13] while in the lower panel we employed the turning point $z_0 = 1.2 \cdot 10^{-10}\,\mathrm{m} \approx 2.27\,a_B$ which was suggested by Modinos and Easa[96]. Note that the angularity of the curves is a consequence of our numerical tabulation scheme and could be removed by allowing for a larger computation time.

to an energy representation by means of

$$(k')^2\,\mathrm{d}k' = \frac{1}{2}\left(\frac{2m_e}{\hbar^2\kappa_p^2}\right)^{\frac{3}{2}}\sqrt{\varepsilon_{\vec{k}'} - V_0}\,\mathrm{d}\varepsilon_{\vec{k}'}\,. \tag{5.27}$$

Note that for the particular situation considered here the generic placeholder κ_p is equal to κ_{He} (see Eq. (2.27)) and $V_0 = -1\,\mathrm{eV}$ represents the lower band edge of the conduction band of Al_2O_3 (see Table A.2). Figure 5.2 shows the resulting spectra for $\varepsilon_{\mathrm{kin}} = 50\,\mathrm{meV}$ using the turning points $z_0 \approx 3.6\,a_B$ (upper panel) and $z_0 = 1.2 \cdot 10^{-10}\,\mathrm{m} \approx 2.27\,a_B$ (lower panel). The former emerges from (2.53) for the parameters of Bonini et al.[13] while the latter was proposed by Modinos and Easa[96]. Physically we would expect the lower turning point to result in a more efficient neutralization since here the overlap of projectile and solid wave functions is increased. Comparing the two panels in Fig 5.2 we see that this is indeed the case. In fact, the difference is dramatic since the spectrum comes out about one order of magnitude higher with the turning point of Modinos and Easa[96]. However, apart from the numeric values the spectra possess the same general shape. In both cases the distribution of internally excited electrons starts out at the bottom of the conduction band which, as mentioned before, amounts to $-1\,\mathrm{eV}$ for Al_2O_3

(see Table A.2). The curves then exhibit a broad maximum localized between 0 eV and 2 eV before they gradually fall off and eventually vanish at roughly 4 eV for the turning point due to Bonini et al.[13] and about 3.5eV for the z_0-value of Modinos and Easa[96]. Similar to the indirect Auger de-excitation process discussed in Sec. 4.2.1, the cut-off of the spectra can be estimated by considering the energy balance of the Auger transition which reads

$$\varepsilon_{\vec{k}_1} + \varepsilon_{\vec{k}_2} \approx \varepsilon_{\vec{k}'} + \varepsilon_{0g}(t) \; . \tag{5.28}$$

This directly leads to a maximum $\varepsilon_{\vec{k}'}$-energy of

$$\varepsilon_{\vec{k}'}^{max} \approx 2\varepsilon_U - \varepsilon_0^{\infty} - |V_i(z_0)| \; , \tag{5.29}$$

where ε_U marks the upper edge of the valence band. Employing the energetic parameters of Table A.2 and the truncated classical image potential (2.14) we obtain $\varepsilon_{\vec{k}'}^{max} \approx 3.66\,\text{eV}$ for the z_0-value due to Bonini et al.[13] and $\varepsilon_{\vec{k}'}^{max} \approx 2.76\,\text{eV}$ with the turning point of Modinos and Easa[96]. The discrepancy between these classical values and the observable breakdown energies of the spectra in Fig. 5.2 is due to the fact that energy conservation is not fulfilled completely in a non-equilibrium system. In particular, the engagement of three continuum states in the Auger neutralization reaction allows for a larger energy off-resonance as compared to the indirect Auger de-excitation process which only involves two continuum states that are each coupled to a localized projectile level (see also Fig. 4.5 and Eq. (4.36)). Nevertheless, the classical expression (5.29) can explain the difference in the cut-off energies of the two different turning points which results from the fact that for the narrowed z_0-value of Modinos and Easa[96] the image shift at the turning point $V_i(z_0)$ is increased.

In addition to the distribution of excited Auger electrons within the surface, Fig. 5.2 also shows the spectra of electrons that can escape the surface. The corresponding curves start out at $\varepsilon_{\vec{k}'} = 0$ and are obviously reduced with respect to the spectra of the internally excited electrons. At the high-energy end of the spectrum, however, the difference between the two distributions vanishes because here the effect of the surface transmission function is diminished.

The total amount of electrons that can breach through the surface barrier constitutes the secondary electron emission coefficient $\gamma_e^{(an)}$ and is given by the area beneath the spectra of escaped electrons. Table 5.2 lists the γ_e-values obtained from Fig. 5.2 together with the emission coefficients of other material combinations at $\varepsilon_{\text{kin}} = 50\,\text{meV}$. As seen from Table 5.1, all of these systems block the resonant neutralization channel and exclusively allow for Auger neutralization.

Inspecting the data in Table 5.2 a few remarks should be given. First of all, CaO possesses a negative electron affinity (see Table A.2) which means that all of the internally excited electrons can escape the surface. As a result, the emission coefficients for $N_2^+(^2\Pi_u)$ on CaO are equal to the final occupancies of the projectile level (see Fig. 5.1). Furthermore, the choice of the turning point of $He^+(^2S_{1/2})$ has a dramatic effect also for other materials than Al_2O_3. In particular, switching from the turning point due to Bonini et al.[13] to the one proposed by Modinos and Easa[96] results in a change of $\gamma_e^{(an)}$ by at least one order of magnitude. Thus, the turning point is crucial to the numeric value of the emission coefficient which was also found in connection with the indirect Auger de-excitation channel studied in Sec. 4.2.1.

Unfortunately, we have no means of determining the correct turning point of a $He^+(^2S_{1/2})$ ion. However, we assume the value of Modinos and Easa[96] to lie closer

Projectile	Surface Material	$\gamma_e^{(an)}$
$Ar^+(^2P_{3/2})$	CaO	$5.67 \cdot 10^{-6}$
$He^+(^2S_{1/2})$	Al_2O_3	$5.10 \cdot 10^{-5}$ (B) $6.23 \cdot 10^{-4}$ (M)
$He^+(^2S_{1/2})$	CaO	$1.06 \cdot 10^{-5}$ (B) $1.70 \cdot 10^{-4}$ (M)
$He^+(^2S_{1/2})$	MgO	$3.15 \cdot 10^{-4}$ (B) $3.97 \cdot 10^{-3}$ (M)
$He^+(^2S_{1/2})$	SiO_2	$6.10 \cdot 10^{-6}$ (B) $1.41 \cdot 10^{-4}$ (M)
$N_2^+(^2\Pi_u)$	CaO	$1.31 \cdot 10^{-4}$ ($\parallel$) $2.18 \cdot 10^{-5}$ ($\perp$)

Table 5.2: Secondary electron emission coefficients due to Auger neutralization of $Ar^+(^2P_{3/2})$, $He^+(^2S_{1/2})$ and $N_2^+(^2\Pi_u)$ on various dielectric surfaces at a kinetic energy of 50 meV. All of the listed material combinations block the resonant neutralization channel and exclusively support Auger neutralization (see also Table 5.1). Note that the symbols (B) and (M) indicate the turning point of $He^+(^2S_{1/2})$ due to Bonini et al.[13] and Modinos and Easa[96], respectively. Moreover, as before, $\parallel$ and $\perp$ denote the parallel and perpendicular orientation of the projectile axis in case of an incident $N_2^+(^2\Pi_u)$ ion.

to the real z_0 since it was specifically suggested for the neutralization of $He^+(^2S_{1/2})$ whereas the Morse potential parameters of Bonini et al.[13] were obtained for an uncharged metastable helium atom. In any case, our effective model allows for the immediate inclusion of arbitrary turning point values since z_0 only enters our description as a constant parameter.

In total, all of the emission coefficients listed in Table 5.2 are rather small with values ranging between 10^{-6} and 10^{-3}. Thus, the Auger neutralization reaction in general seems to be rather inefficient, at least for the low-energy case studied here.

5.2.2 Resonant Neutralization

We now proceed with an investigation of the isolated resonant neutralization channel (1.5). Since the latter merely neutralizes the incident ion without generating secondary electrons, the only meaningful physical quantity is the occupation of the projectile's ground state level $n_0^{(rn)}$ which represents the neutralization probability. Focusing on the case of an $N_2^+(^2\Pi_u)$ ion on an Al_2O_3 surface, which according to Table 5.1 exclusively supports the resonant neutralization reaction, we can calculate $n_0^{(rn)}$ from (3.134) upon neglecting the Auger terms. The resulting time-dependent occupation is depicted in Fig. 5.3 for a kinetic energy of 50 meV. As we see, the resonant filling of the molecular ground state level is very efficient here. In fact, the process is almost exclusively effective in the incoming branch of the trajectory and causes a rapid saturation of the occupancy to approximately 1 for the parallel and roughly 0.89 for the perpendicular orientation. Thus, similar to the Auger neutralization reaction discussed in Sec. 5.2.1, the process is more effective in the parallel than in the perpendicular orientation. In contrast to the Auger neutralization reaction, however, the curves show a strong asymmetry which is caused

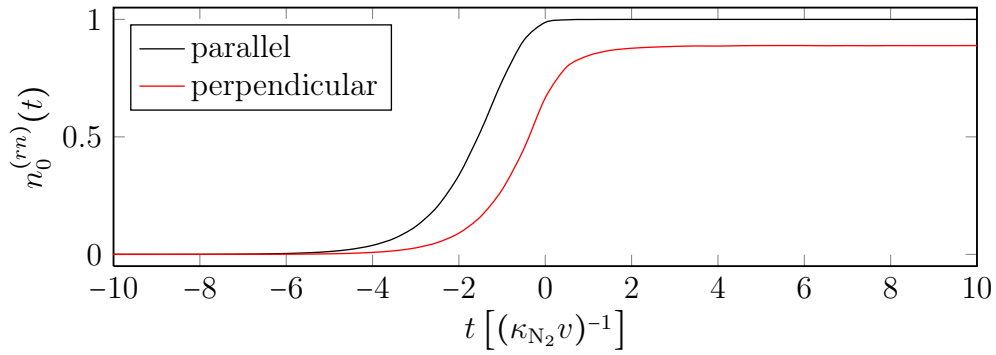

Figure 5.3: Time dependence of the occupation of the projectile level $n_0^{(rn)}(t)$ due to the resonant neutralization of $N_2^+(^2\Pi_u)$ on an Al_2O_3 surface. Separate graphs are shown for the parallel (black line) and perpendicular (red line) orientation. The results were calculated from Eq. (3.134) for a kinetic energy of 50 meV.

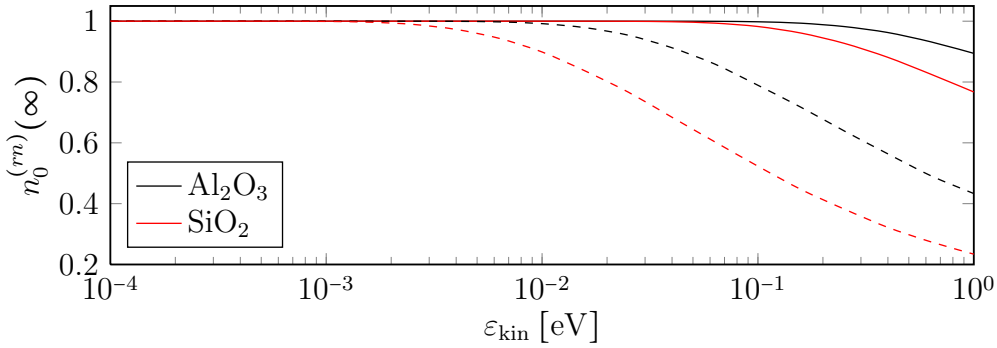

Figure 5.4: Kinetic energy dependence of the final occupation of the projectile's ground state level $n_0^{(rn)}(\infty)$ due to the resonant neutralization of $N_2^+(^2\Pi_u)$ on Al_2O_3 (black lines) and SiO_2 (red lines). The plot shows curves for the parallel (solid lines) as well as the perpendicular (dashed lines) molecule orientation. The results were calculated using Eq. (3.134).

by the particular efficiency of the tunneling reaction and the associated saturation of the occupation due to the exponential structure of (3.134).

In order to further investigate the effectiveness of the resonant neutralization reaction, we now analyze the dependence of the ground state level's final occupation $n_0^{(rn)}(\infty)$ on the kinetic energy of projectile. In addition to Al_2O_3, here we also consider SiO_2 which, for an $N_2^+(^2\Pi_u)$ ion, supports the resonant neutralization channel by way of its lower valence band while completely blocking Auger neutralization. Figure 5.4 depicts the resulting occupations, which represent the ion's overall neutralization probability, in the low-energy range between 10^{-4} eV and 1 eV. Obviously, for both materials the final occupancy is higher in the parallel than in the perpendicular orientation which we already recognized in connection with Fig. 5.3. Moreover, upon decreasing the projectile's kinetic energy the neutralization probabilities gradually rise and eventually reach one at the low-energy end of the plot. This behavior follows from the fact that the nitrogen molecule's turning point is practically constant in the depicted energy range (see Fig. 2.6). Thus, by lowering the kinetic energy the molecule-surface interaction time is increased which results in a more effective neutralization. Note that by an analogous argument we also explained the variation of the secondary electron emission coefficients due to the

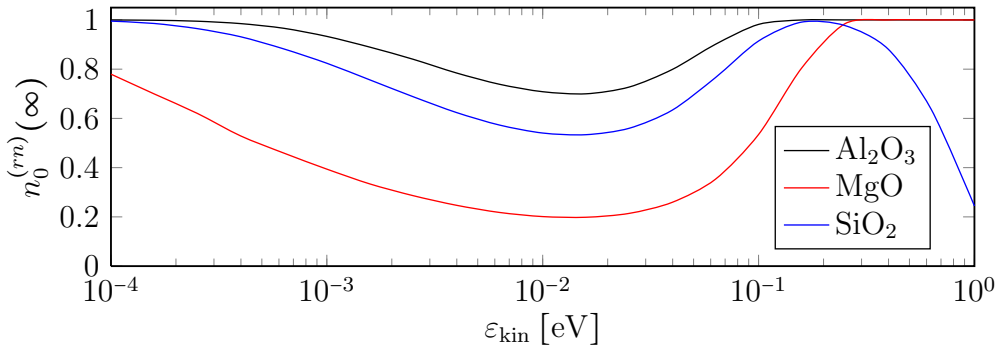

Figure 5.5: Kinetic energy dependence of the final occupation of the projectile's ground state level $n_0^{(rn)}(\infty)$ due to the resonant neutralization of $Ar^+(^2P_{3/2})$ on Al_2O_3 (black line), MgO (red line) and SiO_2 (blue line). The curves were calculated from (3.134).

de-excitation of $N_2(^3\Sigma_u^+)$ in Sec. 4.2.

In addition to the previously discussed material combinations involving the $N_2^+(^2\Pi_u)$ ion, we can also investigate the isolated resonant neutralization channel for $Ar^+(^2P_{3/2})$ on Al_2O_3, MgO and SiO_2. Figure 5.5 shows the corresponding final occupancies of the projectile level, or overall neutralization probabilities, for the same kinetic energy range we used in Fig. 5.4. As we see, the values range between 0.2 and 1 for the different surface materials and kinetic energies. In addition, the curves in Fig. 5.5 show a couple of interesting properties.

Let us first take a look at the graphs for Al_2O_3 and MgO. Here the neutralization probability shows a minimum at approximately 0.002 eV and gradually rises when the kinetic energy is reduced or enlarged. This behavior is caused by two effects working in opposite directions. On the one hand, with a reduction of the kinetic energy the turning point of the $Ar^+(^2P_{3/2})$ ion moves farther outside the surface (see Fig. 2.6). Hence, the overlap of projectile and solid wave functions is reduced which negatively affects the neutralization efficiency. At the same time, however, the projectile-surface interaction time is increased since the ion moves at a slower speed. This, on the other hand, benefits the neutralization process. Consequently, the effects of the turning point and the interaction time oppositely affect the efficiency of the neutralization reaction. The particular behavior of the curves for Al_2O_3 and MgO in Fig. 5.5 suggests that at lower energies the increase of the interaction time outweighs while at higher energies the decrease of the turning point predominates. In between, the two effects destructively interfere leading to the formation of the observed minima of the neutralization probabilities.

For SiO_2 the behavior is similar to the Al_2O_3 and MgO curves up to a kinetic energy of about 0.2 eV. For higher energies, however, the neutralization probability breaks down again. This is caused by the particular band structure of SiO_2 which possesses two valence bands. The upper one ranges between −8.9 eV and −11.6 eV while the lower one is situated between −14.7 eV and −20 eV (see Table A.2). The ground state level of argon lies at −15.755 eV when the ion is infinitely far away (see Table A.3) and shifts upwards as the projectile approaches the surface. Thus, for the low-energy case considered here the neutralizing resonant electron capture is only possible from the lower valence band. At the high energy end of Fig. 5.5 the projectile level does, however, begin to shift upwards out of the lower valence band into the inter-band gap. Consequently, the neutralization probability breaks

	$n_0^{(an)}(\infty)$	$\gamma_e^{(an)}$
$\mathbf{He^+(^2S_{1/2})}$	$9.37 \cdot 10^{-4}$ (B)	$8.41 \cdot 10^{-4}$ (B)
	$1.74 \cdot 10^{-2}$ (M)	$1.51 \cdot 10^{-2}$ (M)
$\mathbf{Ar^+(^2P_{3/2})}$	$2.97 \cdot 10^{-5}$	$2.19 \cdot 10^{-5}$
$\mathbf{N_2^+(^2\Pi_u)}$	$1.09 \cdot 10^{-4}$ ($\parallel$)	$8.91 \cdot 10^{-5}$ ($\parallel$)
	$9.94 \cdot 10^{-5}$ ($\perp$)	$8.12 \cdot 10^{-5}$ ($\perp$)

Table 5.3: Final projectile occupations $n_0^{(an)}(\infty)$ and secondary electron emission coefficients $\gamma_e^{(an)}$ due to the isolated Auger neutralization of $He^+(^2S_{1/2})$, $Ar^+(^2P_{3/2})$ and $N_2^+(^2\Pi_u)$ on a diamond surface. The values were calculated from Eqs. (3.134) and (3.137), respectively, for a kinetic energy of 50 meV. As before, the symbols (B) and (M) indicate the usage of the turning point of $He^+(^2S_{1/2})$ due to Bonini et al.[13] and Modinos and Easa[96] while $\parallel$ and $\perp$ stand for the parallel and perpendicular orientation of the $N_2^+(^2\Pi_u)$ ion.

down. Note that for even higher kinetic energies the ground state level might reach the upper valence band of SiO_2 which would lead to a recovery of the neutralization probability. This situation is, however, not considered here since, as pointed out earlier, this work deals with the low-energy case.

Altogether, we find that for the considered material combinations and kinetic energies the isolated resonant neutralization channel is very effective. Moreover, the calculated neutralization probabilities sensitively display the electronic structure of the projectile-surface system which underlines the correct description of the resonant channel within our effective model.

5.2.3 Combined Two-Channel Neutralization

Having investigated the isolated reactions of Auger and resonant neutralization we now turn to their combination. As seen from Table 5.1, the only surface material under consideration that supports both neutralization channels is diamond which was not included in the analysis of Secs. 5.2.1 and 5.2.2. Consequently, in order to investigate the particular strength of the individual neutralization channels for a diamond surface, we first consider the isolated reactions.

Table 5.3 summarizes the final occupancies of the projectile level $n_0^{(an)}(\infty)$ and the secondary electron emission coefficients $\gamma_e^{(an)}$ due to the isolated Auger neutralization of $He^+(^2S_{1/2})$, $Ar^+(^2P_{3/2})$ and $N_2^+(^2\Pi_u)$ on a diamond surface. The data was calculated for a kinetic energy of 50 meV and indicates that, similar to the material combinations studied in Sec. 5.2.1, here again the Auger channel is rather inefficient. In particular, the values of $n_0^{(an)}(\infty)$ and $\gamma_e^{(an)}$ range between 10^{-5} and 10^{-2}. Note that in each case the emission coefficient is slightly smaller than the final occupation of the projectile level, which constitutes the overall neutralization probability. This is caused by the positive electron affinity of diamond (see Table A.2) and the associated lossy transmission of Auger electrons through the surface barrier. Moreover, the highest neutralization probability emerges for $He^+(^2S_{1/2})$ with the turning point due to Modinos and Easa[96] and amounts to $1.74 \cdot 10^{-2}$.

We now proceed with the isolated resonant neutralization of the three ionic species on a diamond surface. The corresponding final occupation of the projec-

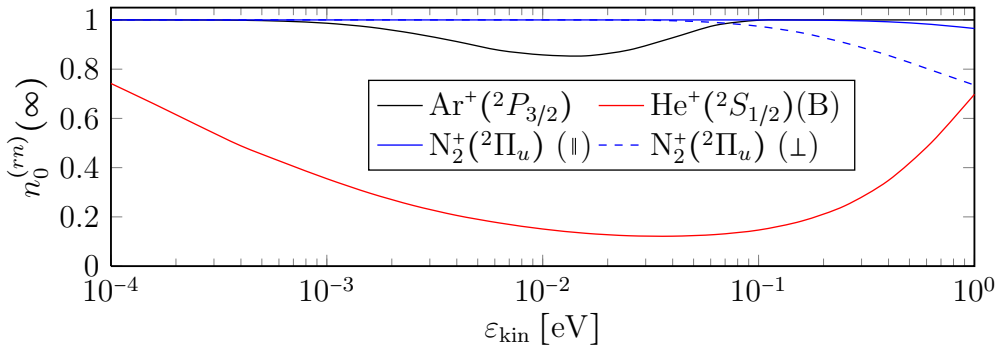

Figure 5.6: Kinetic energy dependence of the final occupation of the projectile's ground state level $n_0^{(rn)}(\infty)$ due to the isolated resonant neutralization of $\mathrm{He}^+(^2S_{1/2})$, $\mathrm{Ar}^+(^2P_{3/2})$ and $\mathrm{N}_2^+(^2\Pi_u)$ on a diamond surface. The curves were calculated from (3.134). Note that for $\mathrm{He}^+(^2S_{1/2})$ only the turning point due to Bonini et al.[13] (B) was considered since the z_0-value proposed by Modinos and Easa[96] only applies to $\varepsilon_{\mathrm{kin}} = 50\,\mathrm{meV}$. Moreover, as before, ∥ and ⊥ indicate the parallel and perpendicular orientation of the $\mathrm{N}_2^+(^2\Pi_u)$ ion.

tile's ground state level, the overall neutralization probability, is depicted in Fig. 5.6 over the kinetic energy of the incident ion. Obviously the resonant neutralization channel is very efficient here. In particular, for $\mathrm{N}_2^+(^2\Pi_u)$ and $\mathrm{Ar}^+(^2P_{3/2})$ the neutralization probability lies between 0.7 and 1 in the depicted energy range. Furthermore, for $\mathrm{He}^+(^2S_{1/2})$ with the turning point due to Bonini et al.[13] the value of $n_0^{(rn)}(\infty)$ ranges between 0.1 and 0.7. The turning point of Modinos and Easa[96] was suggested for $\mathrm{He}^+(^2S_{1/2})$ at a kinetic energy of 50 meV and is, therefore, not included in Fig. 5.6. The associated neutralization probability for 50 meV can, nevertheless, be calculated and amounts to approximately 0.99.

In total, the neutralization probabilities due to the resonant reaction clearly outbalance the neutralization probabilities due to the Auger reaction. Hence, when both channels are operative at the same time, the resonant reaction will suppress the efficiency of the Auger channel even more. In fact, for parameter regions where the resonant neutralization probability is close to unity (for instance for $\mathrm{N}_2^+(^2\Pi_u)$ at $\varepsilon_{\mathrm{kin}} \leq 0.1\,\mathrm{eV}$) the resonant channel will destroy the incident positive ion almost completely before the Auger process can become operative. When, on the other hand, the probability of resonant neutralization is significantly less then one, like for instance for $\mathrm{He}^+(^2S_{1/2})$ with the turning point of Bonini et al.[13] in the energy range between 0.01 eV and 0.1 eV, the electron yield resulting from the Auger channel is only slightly reduced.

In order to demonstrate this fact, we calculate the final spectrum of the escaped electrons $\tilde{n}_{\varepsilon_{\vec{k}'}}^{(an+rn)}$ for the combined two-channel neutralization scheme. Formally, this quantity can be obtained by integrating over the angular wave vector coordinates of (3.135b) and switching to an energy representation by means of (5.27). To simplify this procedure we utilize the angular mean value approximation of the matrix element (5.23). The final time integral can then be efficiently evaluated by tabulating the transient occupation of the projectile's ground state level due to both neutralization channels which is obtained from (3.134). Figure 5.7 shows the resulting spectrum together with the isolated Auger neutralization spectrum, calculated along the lines of Sec. 5.2.1 for the same parameter set. As we see, the combined two-channel spectrum exhibits lower values than the isolated Auger neutralization

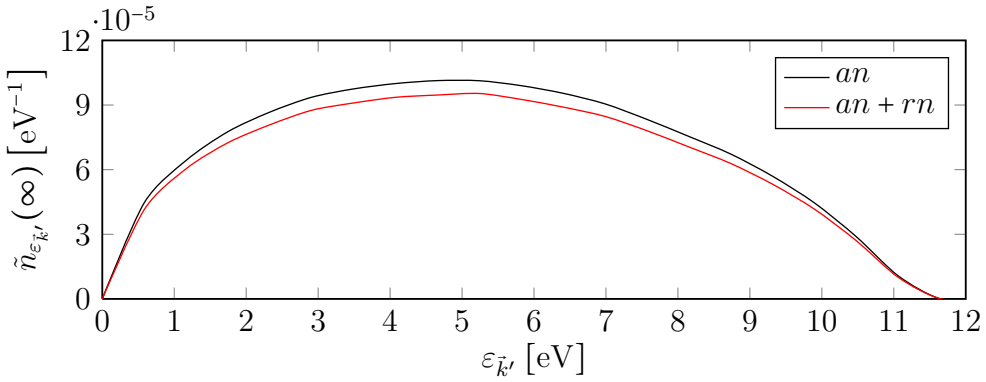

Figure 5.7: Final energy spectrum of the escaped Auger electrons due to the isolated Auger neutralization (an, black line) and the two channel neutralization ($an + rn$, red line) of $He^+(^2S_{1/2})$ on a diamond surface. The results were obtained for a kinetic energy of 50 meV with the turning point due to Bonini et al.[13]. Note that the angularity of the curves is a consequence of our numerical tabulation scheme and could be removed by allowing for a larger computation time.

spectrum. The secondary electron emission coefficient, given by the area beneath the curves, amounts to $8.41 \cdot 10^{-4}$ for the isolated Auger channel and $7.76 \cdot 10^{-4}$ for the two-channel scheme. Hence, the inclusion of the resonant channel with an isolated neutralization probability of about 0.13 (see Figure 5.6) results in a reduction of the secondary electron emission coefficient due to Auger neutralization by roughly 8%. From this result we see that in case of a very efficient resonant neutralization ($n_0^{(rn)}(\infty) \approx 1$) the Auger electron yield would get cut down completely.

Altogether, we conclude that the Auger neutralization channel can only generate meaningful amounts of secondary electrons when the resonant neutralization channel is either blocked energetically or exhibits a particularly low neutralization probability.

Chapter 6

Conclusion

In this work we presented a theoretical description of electron release due to the combination of resonant and Auger reactions in the collision of atomic and molecular projectiles with metallic and especially dielectric surfaces. In particular, we focused on the interaction of two-step resonant and Auger de-excitation of metastable molecules using the example of $N_2(^3\Sigma_u^+)$. In addition, we also regarded the interplay of resonant and Auger neutralization of singly charged positive ions where we explicitly considered the cases of $He^+(^2S_{1/2})$, $Ar^+(^2P_{3/2})$ and $N_2^+(^2\Pi_u)$.

In order to study these processes, we constructed a semi-empirical effective model of the projectile-surface system which is characterized by only a small number of material parameters. This was achieved by restricting our analysis to only those projectile orbitals that actively participate in the considered surface reactions. As a result, the projectile was reduced to a two- and one-level representation for the de-excitation and neutralization processes, respectively. Moreover, the energy bands of the surface were described by an interaction-free electron gas inside a square potential well. For both the projectile and the surface the many-particle details of the system are encapsulated in the effective parameters of our model the most important of which are the ionization energies of the active projectile levels and the edges of the involved energy bands within the surface. We stress that all of our model's parameters can be fixed by either theoretical calculations or experimental measurements. Thus, our description contains no free parameter.

Following the ideas of Gadzuk[30] we derived a Hamiltonian describing the dynamics of the active electrons within the system. The Hamiltonian embraces the individual subreactions of the two-step resonant de-excitation, the Auger de-excitation channels as well as the processes of resonant and Auger neutralization. In order to combine the two steps of the resonant de-excitation reaction and to account for Coulomb correlations due to the omitted passive electrons on the projectile, we subsequently employed a set of projection operators and two auxiliary boson levels. As a result, all of the considered de-excitation channels could be cast into a single Hamiltonian which, with the help of pseudo-particle operators, was made amenable to diagrammatic techniques.

Building upon our effective model we then conducted a quantum-kinetic simulation of the different reaction channels by utilizing the non-equilibrium Green function technique. For every particular situation we retained the full non-locality of the self-energy expressions and derived results that can be considered exact within the respective perturbation order. Only at the end of each calculation we employed

a saddle-point, or semi-classical, approximation to obtain equations that allow for a numerical evaluation.

In particular, we treated the isolated subreactions of the resonant de-excitation channel using the Keldysh formulation and an exact diagrammatic representation of the self-energy. Exploiting the strong effect of energy conservation we obtained virtually exact expressions for the occupancies of the bound and continuum projectile levels. The results involved an infinite series of nested double integrals, designated as the (infinite) σ-series, which emerged from an iterative solution of the Dyson equation. Variants of this series operating on different complex functions appeared at multiple points within this work. As we showed, all of them can be approximated by a compact semi-classical representation.

Furthermore, the isolated Auger de-excitation channels were also studied by means of the Keldysh formulation. As suggested by Makoshi[86], we employed a second-order approximation of the self-energy which was extended by a dressed projectile propagator. The latter was needed to make up for a first-order expansion of the Dyson equations of the Auger electrons. While our general approach followed the ideas of Makoshi[86], our analysis went beyond his work in multiple aspects. For one thing, we studied the interplay of direct and indirect Auger de-excitation whereas Makoshi[86] was only concerned with the latter. Moreover, in contrast to him, we did neither restrict our investigations to a phenomenological matrix element nor employ the wide-band approximation. In addition, our final representation of the occupancies in terms of the infinite σ-series theoretically allows us to calculate higher order correction terms to the simplified semi-classical results.

The combination of the resonant and Auger de-excitation channels was then analyzed within the scope of our pseudo-particle Hamiltonian while employing the self-consistent non-crossing approximation for the self-energies. Utilizing the Kadanoff-Baym formulation of the non-equilibrium Green function method and the Langreth-Nordlander projection technique[76] we derived a set of integro-differential quantum-kinetic equations for the various pseudo-particle propagators. By means of the semi-classical approximation this set was then reduced to a flexible and easy-to-use system of rate equations describing the occupations of the different projectile states occurring in the course of the de-excitation reaction.

Finally, for the neutralization channels we employed the Keldysh formulation together with a second-order representation of the Auger self-energy and an exact diagonal form of the resonant tunneling self-energy. Similar to the Auger de-excitation reactions, the secondary electrons were handled by introducing a dressed self-energy and expanding the associated Dyson equation up to first order. As a result, we obtained the occupancies of the projectile level and the Auger electron states in terms of the σ-series.

Following our quantum-kinetic calculation we concretized the transition matrix elements within the framework of our effective model. While our approximation to the wave functions might appear crude, it allows us to retain the full single particle quantum number dependence of the matrix elements which is usually dropped in favor of a phenomenological approximation[14,86]. However, even for our simplistic wave functions the final equations were so complex that they could only be evaluated efficiently by a combination of tabulation, interpolation and Monte Carlo techniques. In applying the latter we then were able to calculate explicit numerical results for the individual surface reactions and their combination.

In particular, for the de-excitation of $N_2(^3\Sigma_u^+)$ our numerical analysis revealed that on aluminum and tungsten the isolated indirect Auger de-excitation channel is rather weak. Specifically, for $\varepsilon_{\text{kin}} = 50\,\text{meV}$ and a tungsten surface we calculated a secondary electron emission coefficient $\gamma_e^{(iad)}$ of $1.533 \cdot 10^{-3}$ in the parallel and $6.116 \cdot 10^{-3}$ in the perpendicular molecule orientation. Both of these values agree well with the experimental estimate of Stracke et al.[127].

Moreover, for the isolated two-step resonant de-excitation of $N_2(^3\Sigma_u^+)$ we presented numerical results for various dielectric surface materials. Using Al_2O_3, in particular, we found that the spectrum of the emitted electrons exhibits the expected resonance structure with a strong peak at about $1.8 - 1.9\,\text{eV}$. In addition, concerning the decay of the temporary negative ion our results indicated that the surface-induced process can be neglected for our situation since it is about two orders of magnitude weaker than the natural decay. Focusing exclusively on the latter reaction we then calculated the emission coefficient $\gamma_e^{(rc+rr)}$ for Al_2O_3, MgO, SiO_2 and diamond, obtaining values between 0.02 and 0.2 for collision energies ranging from $10^{-5}\,\text{eV}$ to $1\,\text{eV}$. For thermal energies the $\gamma_e^{(rc+rr)}$-figures we found are on the order of 10^{-1} and, hence, coincide with the values deduced from kinetic simulations of dielectric barrier discharges taking this particular secondary electron emission process into account.

Regarding the combination of two-step resonant and indirect Auger de-excitation of $N_2(^3\Sigma_u^+)$ we subsequently considered the particular case of a diamond surface and explicitly demonstrated the validity of the semi-classical approximation for a kinetic energy of 50 meV. Using the same energy we also calculated the rates of electron capture due to the two reactions and found that the resonant tunneling channel clearly dominates the indirect Auger transition. As a result, the combined emission spectrum was almost identical to the resonant spectrum and only showed a slight increase due to the Auger reaction. The latter, thus, merely contributed a few percent to the overall secondary electron emission coefficient $\gamma_e^{(rc+rr+iad)}$ which was on the order of 10^{-1}. Finally, the correct inclusion of both channels in our theory was demonstrated by investigating two artificial situations for an aluminum surface in which we manually modified the lower conduction band edge in order to control the efficiency of the resonant reaction.

After our extensive investigation of the de-excitation channels we then turned to the neutralization reactions. Considering $He^+(^2S_{1/2})$, $Ar^+(^2P_{3/2})$ and $N_2^+(^2\Pi_u)$ our numerical results indicated that the isolated Auger neutralization channel is rather weak for all of the considered dielectric surface materials. In particular, at a kinetic energy of 50 meV typical values of the emission coefficient $\gamma_e^{(an)}$ ranged from $5.67 \cdot 10^{-6}$ for $Ar^+(^2P_{3/2})$ on CaO to $3.97 \cdot 10^{-3}$ for $He^+(^2S_{1/2})$ on MgO with the turning point of Modinos and Easa[96]. Here, and also in the rest of our results, we found the value of the turning point to have a critical impact on the emission coefficient.

In contrast to the Auger neutralization channel, for the resonant neutralization reaction we observed a particularly high efficiency. Here the associated neutralization probability exhibited values from 0.1 to 1 for $Ar^+(^2P_{3/2})$ and $N_2^+(^2\Pi_u)$ on Al_2O_3, MgO and SiO_2 at kinetic energies between $10^{-4}\,\text{eV}$ and $1\,\text{eV}$.

Focusing on the neutralization of $He^+(^2S_{1/2})$, $Ar^+(^2P_{3/2})$ and $N_2^+(^2\Pi_u)$ on a diamond surface we then found that for the considered low-energy range the resonant reaction clearly outbalances the Auger channel in terms of the isolated neutraliza-

tion probabilities. As a result, the efficiency of the Auger channel is reduced even more in the combined two-channel neutralization scheme which was validated for the particular case of $He^+(^2S_{1/2})$ at $\varepsilon_{kin} = 50\,meV$ with the turning point due to Bonini et al.[13]. Here we observed that the inclusion of the resonant neutralization channel with an overall isolated neutralization probability of 0.13 led to a reduction of the Auger electron yield by roughly 8%. Hence, in case of a very efficient resonant neutralization the Auger reaction would probably get suppressed completely. Therefore, we concluded that the Auger neutralization channel can only generate significant numbers of secondary electrons when the resonant neutralization channel is either blocked or possesses a particularly low neutralization probability.

In total, our numerical results imply that, despite its simplicity, our effective microscopic description seems to capture the essential physics of secondary electron emission due to the considered surface reactions quite well. We stress that the effective nature of our model and the associated small parameter space constitute an invaluable asset. In particular, our model can immediately be applied to arbitrary metallic and dielectric surfaces as long as the associated electronic parameters, most importantly the energetic boundaries of the band structure, are known. Moreover, with minor modifications of the matrix elements our model can also be used to study different projectiles. In our description of the Auger neutralization for instance the projectile only entered the matrix element via the Fourier transform of its ground state level's wave function which can be exchanged rather easily. This flexibility is highly advantageous especially in view of the application of our model to charge-transferring processes at plasma walls where a great variety of different projectile-surface material combinations arises.

Another advantage of our semi-empirical approach is that it separates the many-body theoretical description of the non-interacting projectile and target systems from the quantum-kinetic treatment of the scattering process. The former is encapsulated in the effective parameters of the Hamiltonian while the latter is performed by Green functions. This is particularly helpful in cases where the surface scattering event is studied primarily due to its connection to the physics of quantum-impurities.

Finally, we note that while not being all-embracing, our model can easily be extended to account for further effects due to the particular flexibility of the non-equilibrium Green function technique. The latter, for instance, would allow for a convenient inclusion of molecular vibrations in our description. In addition, our approach could also quickly be adapted to other surface reactions, like for instance Auger de-excitation and neutralization involving electrons from surface states of the solid. The latter are bound close to the vacuum level by the image potential and might play an important role for charged surfaces inside a plasma. Generalizing our description to these transitions merely requires an adaption of the matrix elements which is achieved rather conveniently. These facts underline the enormous versatility of our model and its particular value for the calculation of secondary electron emission coefficients, especially in the context of bounded low-temperature gas discharges.

Appendix A

Material Parameters

Here we list the explicit values of the various material parameters used in our numerical calculations. In addition, the following tables also provide an overview of the size of our model's parameter space.

	V_0 [eV]	ε_F [eV]	z_i [a_B]	κ_b [10^{10}m]
Al	-16.5[82]	-4.25[82]	2.95[61]	2.0475[16]
W	-10.9[43]	-4.5[43]	3.0[61]	1.7659[7]

Table A.1: Electronic parameters of solid aluminum and tungsten. In the above table V_0 represents the lower edge of the conduction band, ε_F denotes the Fermi energy, z_i specifies the position of the image plane and κ_b is the bulk Thomas-Fermi screening wave number. The latter relates to the surface screening wave number κ_s via $\kappa_s = 0.6\,\kappa_b$, where the factor 0.6 is empirical[16,100].

	ε_α [eV]	ε_g [eV]	$\Delta\varepsilon_V$ [eV]	ε_r^b
Al_2O_3	1.0[142]	8.7[19]	11.8[19]	9.0[112]
CaO	-0.86[126]	7.0[126]	3.5[130]	11.1[57]
Diamond	0.52[114]	5.48[113]	21.0[113]	5.66[11]
MgO	0.925[71]	7.6[128]	8.5[128]	9.83[28]
SiO_2(lower)	0.9[116]	13.8[20]	5.3[20]	3.9[112]
SiO_2(upper)	0.9[116]	8.0[20]	2.7[20]	3.9[112]

Table A.2: Electronic parameters for the dielectric materials considered in this work: electron affinity ε_α, energy gap ε_g, valence band width $\Delta\varepsilon_V$ and static bulk dielectric constant ε_r^b. The electron affinity of diamond and MgO is calculated from a mean value due to lack of consistent data. Note that for SiO_2 there exists a lower and an upper valence band which have been listed as two separate materials. Due to energetic restrictions, the surface processes considered in this work only involve one of these valence bands at the same time.

	He	**Ar**	**N_2**
$\varepsilon_{0g}^{\infty}$ **[eV]**	-24.55637[73]	-15.755[62]	-17.25[66]
$\varepsilon_{1*}^{\infty}$ **[eV]**	-	-	-9.67[66]
$\varepsilon_{0-}^{\infty}$ **[eV]**	-	-	-14.49[53]
$\varepsilon_{1-}^{\infty}$ **[eV]**	-	-	1.18[53]
Z_{eff}	1.7	6.75	4
M_p **[u]**	4.003[97]	39.962[97]	28.013[133]

Table A.3: Material parameters of the projectile substances considered in this work: unperturbed ionization energies of two projectile levels in the ground state ($\varepsilon_{0g}^{\infty}$), the metastable state ($\varepsilon_{1*}^{\infty}$) and the negative ion ($\varepsilon_{0/1-}^{\infty}$), effective nucleus charge number for the active orbitals Z_{eff} and total projectile mass M_p in atomic mass units ($u = 1.6605389 \cdot 10^{-27}$ kg). Note that for He and Ar only the ionization energy $\varepsilon_{0g}^{\infty}$ is listed since we did merely consider the neutralization of the respective positive ions. Moreover, the effective charge numbers of these projectile species were obtained by means of Slater's rules[123]. For N_2, on the other hand, Z_{eff} was determined by fitting the hydrogen-like wave functions (2.19) to the Roothaan-Hartree-Fock calculations of Clementi and Roetti[21]. Besides, for the nitrogen molecule, in addition to the above parameters, we also used the ground state bond length $\varrho = 2.067360389\, a_B$[121], the natural lifetime of the negative ion $\tau_n = 1.6$ fs[24] and the effective nucleus charge number $Z_C = \frac{1}{2}$[135] for electrons emitted from the neutral molecule.

	d **[eV]**	a **[1/a_B]**	z_e **[a_B]**	**Surface**
He	0.06[13]	0.55[13]	5.2[13]	sodium[13]
Ar	0.06[106]	$0.43 \cdot \nu_B$[106]	$4.5 \,/\, \nu_B$[106]	tungsten[106]
N_2	0.738[68]	$6.4 \cdot \nu_B$[68]	$2.45 \,/\, \nu_B$[68]	metallic[68]

Table A.4: Projectile specific material parameters d, a and z_e of the Morse potential (2.52) and the respective surface materials they were determined for. Here ν_B is a unit conversion factor and amounts to $a_B \,/\, 10^{-10}$ m.

Appendix B

Langreth-Wilkins Rules

The Langreth-Wilkins rules represent a generic type of algebraic rules for the analytic continuation of contour propagator combinations onto the real axis. They were first introduced in a work by Langreth and Wilkins[77] and have since been used and reviewed by a number of authors (see for instance Refs. [48, 75]). The explicit form of the rules sensitively depends on the initial definition of the Green functions. For the latter, unfortunately, there is no common agreement about the usage of i-factors. Moreover, rules published in former works sometimes contained typographic errors (see for instance Ref. [76]). Therefore, in the following we list the explicit form of the Langreth-Wilkins rules used in this work. Details of the derivation are left out as the rules follow directly from the definition of the lesser, bigger, retarded and advanced components of boson and fermion propagators (see Eqs. (1.38) and (1.40)) and the contour deformation described in Ref. [48]. Moreover, we only give rules for propagator pairs since combinations of three or more propagators can be projected by successive application of the pair projection rules.

We begin with the analytic continuation of propagator products. In the following F and B denote fermion and boson propagators, respectively. For the projection of a boson-like fermion-antifermion pair,

$$B(t,t') = F_1(t,t')\,F_2(t',t)\,, \tag{B.1}$$

we find

$$B^{>}(t,t') = i\,F_1^{>}(t,t')\,F_2^{<}(t',t)\,, \tag{B.2a}$$
$$B^{<}(t,t') = i\,F_1^{<}(t,t')\,F_2^{>}(t',t)\,, \tag{B.2b}$$
$$B^{R}(t,t') = -i\Big[F_1^{>}(t,t')\,F_2^{A}(t',t) + F_1^{R}(t,t')\,F_2^{>}(t',t)\Big] \tag{B.2c}$$
$$= \;\; i\Big[F_1^{<}(t,t')\,F_2^{A}(t',t) + F_1^{R}(t,t')\,F_2^{<}(t',t)\Big]\,, \tag{B.2d}$$
$$B^{A}(t,t') = -i\Big[F_1^{>}(t,t')\,F_2^{R}(t',t) + F_1^{A}(t,t')\,F_2^{>}(t',t)\Big] \tag{B.2e}$$
$$= \;\; i\Big[F_1^{<}(t,t')\,F_2^{R}(t',t) + F_1^{A}(t,t')\,F_2^{<}(t',t)\Big]\,. \tag{B.2f}$$

Furthermore, a fermion-like fermion-boson pair,

$$F(t,t') = F_1(t,t')\,B_1(t,t')\,, \tag{B.3}$$

can be projected by

$$F^{>}(t,t') = -i\, F_1^{>}(t,t')\, B_1^{>}(t,t') \,, \tag{B.4a}$$
$$F^{<}(t,t') = -i\, F_1^{<}(t,t')\, B_1^{<}(t,t') \,, \tag{B.4b}$$
$$F^{R}(t,t') = -i\Big[F_1^{R}(t,t')\, B_1^{>}(t,t') - F_1^{<}(t,t')\, B_1^{R}(t,t')\Big] \tag{B.4c}$$
$$= -i\Big[F_1^{R}(t,t')\, B_1^{<}(t,t') + F_1^{>}(t,t')\, B_1^{R}(t,t')\Big] \,, \tag{B.4d}$$
$$F^{A}(t,t') = -i\Big[F_1^{A}(t,t')\, B_1^{>}(t,t') - F_1^{<}(t,t')\, B_1^{A}(t,t')\Big] \tag{B.4e}$$
$$= -i\Big[F_1^{A}(t,t')\, B_1^{<}(t,t') + F_1^{>}(t,t')\, B_1^{A}(t,t')\Big] \,. \tag{B.4f}$$

Moreover, for a boson-like boson-boson pair,

$$B(t,t') = B_1(t,t')\, B_2(t,t') \,, \tag{B.5}$$

the following rules hold

$$B^{>}(t,t') = -i\, B_1^{>}(t,t')\, B_2^{>}(t,t') \,, \tag{B.6a}$$
$$B^{<}(t,t') = -i\, B_1^{<}(t,t')\, B_2^{<}(t,t') \,, \tag{B.6b}$$
$$B^{R}(t,t') = -i\Big[B_1^{R}(t,t')\, B_2^{>}(t,t') + B_1^{<}(t,t')\, B_2^{R}(t,t')\Big] \,, \tag{B.6c}$$
$$B^{A}(t,t') = -i\Big[B_1^{A}(t,t')\, B_2^{>}(t,t') + B_1^{<}(t,t')\, B_2^{A}(t,t')\Big] \,. \tag{B.6d}$$

Finally, to project a boson-like boson-antiboson pair,

$$B(t,t') = B_1(t,t')\, B_2(t',t) \,, \tag{B.7}$$

one may use

$$B^{>}(t,t') = -i\, B_1^{>}(t,t')\, B_2^{<}(t',t) \,, \tag{B.8a}$$
$$B^{<}(t,t') = -i\, B_1^{<}(t,t')\, B_2^{>}(t',t) \,, \tag{B.8b}$$
$$B^{R}(t,t') = -i\Big[B_1^{<}(t,t')\, B_2^{A}(t',t) + B_1^{R}(t,t')\, B_2^{<}(t',t)\Big] \tag{B.8c}$$
$$= -i\Big[B_1^{>}(t,t')\, B_2^{A}(t',t) + B_1^{R}(t,t')\, B_2^{>}(t',t)\Big] \,, \tag{B.8d}$$
$$B^{A}(t,t') = -i\Big[B_1^{<}(t,t')\, B_2^{R}(t',t) + B_1^{A}(t,t')\, B_2^{<}(t',t)\Big] \tag{B.8e}$$
$$= -i\Big[B_1^{>}(t,t')\, B_2^{R}(t',t) + B_1^{A}(t,t')\, B_2^{>}(t',t)\Big] \,. \tag{B.8f}$$

In addition, for the analytic continuation of the Dyson equations we also need to project terms of the form

$$C(t,t') = \int_{\mathcal{C}} \mathrm{d}t_1\, C_1(t,t_1)\, C_2(t_1,t') \,, \tag{B.9}$$

where all of C, C_1 and C_2 are either fermion-like or boson-like. This can be accomplished by the rules

$$C^<(t,t') = \int_{-\infty}^{\infty} \mathrm{d}t_1 \left[C_1^R(t,t_1)\, C_2^<(t_1,t') + C_1^<(t,t_1)\, C_2^A(t_1,t') \right], \tag{B.10a}$$

$$C^>(t,t') = \int_{-\infty}^{\infty} \mathrm{d}t_1 \left[C_1^R(t,t_1)\, C_2^>(t_1,t') + C_1^>(t,t_1)\, C_2^A(t_1,t') \right], \tag{B.10b}$$

$$C^R(t,t') = \int_{-\infty}^{\infty} \mathrm{d}t_1 \; C_1^R(t,t_1)\, C_2^R(t_1,t') \;, \tag{B.10c}$$

$$C^A(t,t') = \int_{-\infty}^{\infty} \mathrm{d}t_1 \; C_1^A(t,t_1)\, C_2^A(t_1,t') \;. \tag{B.10d}$$

Appendix C

The Infinite σ-Series

In this part of the appendix we investigate the properties of the infinite σ-series which is defined by

$$\sigma[\Delta](t,t') = \sum_{\nu=0}^{\infty} \sigma^{(\nu)}[\Delta](t,t') \,, \tag{C.1}$$

with

$$\sigma^{(\nu)}[\Delta](t,t') = (-1)^{\nu} \int_{t'}^{t} \mathrm{d}t_1 \int_{t'}^{t_1} \mathrm{d}t_2 \int_{t'}^{t_2} \mathrm{d}t_3 \ldots \int_{t'}^{t_{2\nu-1}} \mathrm{d}t_{2\nu} \prod_{i=1}^{\nu} \Delta(t_{2i-1}, t_{2i}) \,. \tag{C.2}$$

Here $\Delta(t_i, t_j)$ is an arbitrary complex-valued function of two real arguments and obeys the relation

$$\Delta(t_i, t_j) = \left[\Delta(t_j, t_i)\right]^* \,. \tag{C.3}$$

Nested double integral series of the form (C.1) occurred at multiple points within the quantum-kinetic calculations of Chapter 3 and involved various Δ-functions emerging from the respective self-energy. While in these contexts the infinite series (C.1) is an exact expression, it is almost useless for numerical calculations as an evaluation of series terms beyond the first order usually involves unreasonable computational efforts. Because of this, it is useful to switch to a differential representation. To do so we inspect the definition of the series coefficients $\sigma^{(\nu)}$ (see Eq. (C.2)). Taking the derivative of (C.2) with respect to t while treating t' as constant we obtain the recursion relation

$$\left.\frac{\mathrm{d}\big(\sigma^{(\nu)}[\Delta](t,t')\big)}{\mathrm{d}t}\right|_{t'=\text{const.}} = -\int_{t'}^{t} \mathrm{d}t_1 \, \Delta(t,t_1)\, \sigma^{(\nu-1)}[\Delta](t_1,t') \,, \quad \nu \geq 1 \,. \tag{C.4}$$

Utilizing (C.4) we then find that the infinite series (C.1) is equivalent to the ordinary integro-differential equation

$$\left.\frac{\mathrm{d}\big(\sigma[\Delta](t,t')\big)}{\mathrm{d}t}\right|_{t'=\text{const.}} = -\int_{t'}^{t} \mathrm{d}t_1 \, \Delta(t,t_1)\, \sigma[\Delta](t_1,t') \,, \tag{C.5}$$

with the initial condition $\sigma[\Delta](t',t') = 1$. Moreover, interchanging the roles of t and t' we also find the alternative equation

$$\left.\frac{\mathrm{d}\big(\sigma[\Delta](t,t')\big)}{\mathrm{d}t'}\right|_{t=\text{const.}} = \int_{t'}^{t} \mathrm{d}t_1 \, \sigma[\Delta](t,t_1)\, \Delta(t_1,t') \,, \tag{C.6}$$

which is supplemented by the same initial condition.

While the differential forms (C.5) and (C.6) are by far easier to calculate than the infinite series (C.1), the computational effort is still enormous when $\Delta(t_i, t_j)$ oscillates rapidly in its time arguments which, unfortunately, is the case in our situation. Equations (C.5) and (C.6) can, however, be solved approximately when $\Delta(t_i, t_j)$ is strongly peaked on the time diagonal $t_i = t_j$. In this case we can apply a saddle-point approximation and drag the σ-term out of the integral in (C.5) which leads to

$$\left.\frac{\mathrm{d}\big(\sigma[\Delta](t,t')\big)}{\mathrm{d}t}\right|_{t'=\text{const.}} \approx -\sigma[\Delta](t,t') \int_{t'}^{t} \mathrm{d}t_1\, \Delta(t,t_1)\,. \tag{C.7}$$

This equation can be solved immediately by separation of variables and yields

$$\sigma[\Delta](t,t') \approx e^{-\int_{t'}^{t}\,\mathrm{d}t_1 \int_{t'}^{t_1}\mathrm{d}t_2\,\Delta(t_1,t_2)}\,. \tag{C.8}$$

The alternative differential equation (C.6) does of course produce the same approximate solution. As we showed in Sec. 4.2.3, the Δ-functions appearing in our analysis are indeed strongly peaked on the time diagonal for the low-energy case considered in this work. Hence, the exponential representation (C.8) is a reasonable approximation to the infinite series (C.1) and, therefore, was applied in all of our numerical calculations.

The approximate form (C.8) can also be obtained by means of an exponential resummation[85] of the series (C.1). For this purpose we introduce the virtual expansion parameter $\lambda = 1$ which denotes the order of a term in Δ and require that $\sigma[\Delta]$ be equal to the exponential of a new quantity $\bar{\sigma}[\Delta]$. Expanding $\sigma[\Delta]$ and $\bar{\sigma}[\Delta]$ in λ we then obtain

$$\sigma[\Delta](t,t') = \sum_{\nu=0}^{\infty} \lambda^\nu \sigma^{(\nu)}[\Delta](t,t') \overset{!}{=} e^{\bar{\sigma}[\Delta](t,t')} = e^{\sum_{\nu=0}^{\infty}\lambda^\nu \bar{\sigma}^{(\nu)}[\Delta](t,t')}\,. \tag{C.9}$$

The components $\bar{\sigma}^{(\nu)}[\Delta]$ can now be calculated by expanding the exponential on the right-hand side of (C.9) and comparing the different orders of λ on both sides of the equation. Up to third order the resulting terms read[89]

$$\bar{\sigma}^{(0)}[\Delta](t,t') = 0\,, \tag{C.10a}$$

$$\bar{\sigma}^{(1)}[\Delta](t,t') = \sigma^{(1)}[\Delta](t,t')\,, \tag{C.10b}$$

$$\bar{\sigma}^{(2)}[\Delta](t,t') = \sigma^{(2)}[\Delta](t,t') - \frac{1}{2}\big(\sigma^{(1)}[\Delta](t,t')\big)^2\,, \tag{C.10c}$$

$$\begin{aligned}\bar{\sigma}^{(3)}[\Delta](t,t') = {}& \sigma^{(3)}[\Delta](t,t') - \sigma^{(2)}[\Delta](t,t')\,\sigma^{(1)}[\Delta](t,t') \\ & + \frac{1}{3}\big(\sigma^{(1)}[\Delta](t,t')\big)^3\,.\end{aligned} \tag{C.10d}$$

Upon retaining only the lowest-order non-vanishing term $\bar{\sigma}^{(1)}[\Delta]$ we then essentially obtain (C.8). In fact, Eq. (C.8) implies that for a time-diagonal Δ-function

$$\bar{\sigma}^{(\nu)}[\Delta](t,t') \approx 0\,, \quad \nu > 1\,. \tag{C.11}$$

We stress that the exponential resummation does not have a strong motivation on its own as we could have chosen any other resummation form as well. It is, however, strongly supported by the exponential form of the approximate solution (C.8).

In the works of Makoshi et al.[87,95] the infinite series (C.1) is represented by an opaque double-time-ordering operator acting on the approximate solution (C.8). The details of the time ordering are, however, not laid out and the time-ordering operator is lifted without further explanation. Our previously presented analysis explicitly justifies the truncation of Makoshi's time-ordering operator a posteriori.

We close our analysis of the σ-series by deriving three important integral identities which were employed at various points within the calculations of Chapter 3. We stress that the following equations hold for the complete infinite series (C.1) and do not involve any approximation.

Integral Identity I

For $\sigma[\Delta](t,t')$ and $\Delta(t_i,t_j)$ as defined in (C.1), (C.2) and (C.3) the following identity holds

$$\int_{t'}^{t} \mathrm{d}t_1 \int_{t'}^{t_1} \mathrm{d}t_2 \; \sigma[\Delta](t,t_1)\,\Delta(t_1,t_2) = 1 - \sigma(t,t') \; . \tag{C.12}$$

Proof: We treat t as constant and label the left- and right-hand side of (C.12) as $\zeta_L(t,t')$ and $\zeta_R(t,t')$, respectively. Obviously, both sides of the equation possess one and the same initial condition since

$$\zeta_L(t,t) = 0 = \zeta_R(t,t) \; . \tag{C.13}$$

Furthermore, the derivatives of $\zeta_L(t,t')$ and $\zeta_R(t,t')$ with respect to t' evaluate to

$$\left.\frac{\mathrm{d}\zeta_L(t,t')}{\mathrm{d}t'}\right|_{t=\text{const.}} = -\int_{t'}^{t} \mathrm{d}t_1 \; \sigma[\Delta](t,t_1)\,\Delta(t_1,t') = \left.\frac{\mathrm{d}\zeta_R(t,t')}{\mathrm{d}t'}\right|_{t=\text{const.}} , \tag{C.14}$$

where the equality on the right-hand side represents (C.6). Consequently, ζ_L and ζ_R obey one and the same ordinary differential equation (C.14) with one and the same initial condition (C.13). By virtue of the uniqueness of the solution of (C.14) the functions ζ_L and ζ_R must, thus, be equal.

Integral Identity II

Under the preconditions of the first integral identity we postulate the following equality

$$\int_{t'}^{t} \mathrm{d}t_1 \int_{t'}^{t} \mathrm{d}t_2 \; \Delta(t_1,t_2)\,\sigma[\Delta](t_2,t')\,\sigma[\Delta^*](t_1,t') = 1 - \sigma[\Delta](t,t')\,\sigma[\Delta^*](t,t') \; . \tag{C.15}$$

Proof: As we demonstrated in Ref. [88], the identity (C.15) can be proven along the same lines as the first integral identity (C.12). Here, however, we employ a more direct approach. Treating t' as constant we again label the left- and right-hand side of (C.15) as $\zeta_L(t,t')$ and $\zeta_R(t,t')$ and calculate the derivative of $\zeta_R(t,t')$ with respect to t',

$$\begin{aligned} \left.\frac{\mathrm{d}\zeta_R(t,t')}{\mathrm{d}t}\right|_{t'=\text{const.}} &= \sigma[\Delta^*](t,t') \int_{t'}^{t} \mathrm{d}t_2 \; \Delta(t,t_2)\,\sigma[\Delta](t_2,t') \\ &\quad + \sigma[\Delta](t,t') \int_{t'}^{t} \mathrm{d}t_2 \; \Delta^*(t,t_2)\,\sigma[\Delta^*](t_2,t') \; . \end{aligned} \tag{C.16}$$

In (C.16) we now relabel t as t_1 and integrate the equation from $t_1 = t'$ to $t_1 = t$. Employing $\zeta_R(t',t') = 0$ we then obtain

$$\begin{aligned}\zeta_R(t,t') &= \int_{t'}^{t} \mathrm{d}t_1 \int_{t'}^{t_1} \mathrm{d}t_2\, \Delta(t_1,t_2)\, \sigma[\Delta](t_2,t')\, \sigma[\Delta^*](t_1,t') \\ &\quad + \int_{t'}^{t} \mathrm{d}t_1 \int_{t'}^{t_1} \mathrm{d}t_2\, \Delta^*(t_1,t_2)\, \sigma[\Delta](t_1,t')\, \sigma[\Delta^*](t_2,t') \qquad \text{(C.17a)} \\ &= \int_{t'}^{t} \mathrm{d}t_1 \int_{t'}^{t} \mathrm{d}t_2\, \Delta(t_1,t_2)\, \sigma[\Delta](t_2,t')\, \sigma[\Delta^*](t_1,t') = \zeta_L(t,t')\,, \qquad \text{(C.17b)}\end{aligned}$$

where the second equality follows after exchanging t_1 and t_2 within the second term of (C.17a) and exploiting (C.3). Thus, we have explicitly proven the equality of $\zeta_L(t,t')$ and $\zeta_R(t,t')$.

Integral Identity III

Starting from the premises of the former two integral identities the following equality holds

$$\int_{t'}^{t} \mathrm{d}t_1 \int_{t'}^{t} \mathrm{d}t_2\, \Delta(t_1,t_2)\, \sigma[\Delta](t,t_1)\, \sigma[\Delta^*](t,t_2) = 1 - \sigma[\Delta](t,t')\, \sigma[\Delta^*](t,t')\,. \quad \text{(C.18)}$$

Proof: As before, we label the left- and right-hand side of Eq. (C.18) as $\zeta_L(t,t')$ and $\zeta_R(t,t')$, respectively. Splitting up the integration domain in the ζ_L-term we then find

$$\begin{aligned}\zeta_L(t,t') &= \int_{t_2}^{t} \mathrm{d}t_1 \int_{t'}^{t} \mathrm{d}t_2\, \Delta(t_1,t_2)\, \sigma[\Delta](t,t_1)\, \sigma[\Delta^*](t,t_2) \\ &\quad + \int_{t'}^{t} \mathrm{d}t_1 \int_{t_1}^{t} \mathrm{d}t_2\, \Delta(t_1,t_2)\, \sigma[\Delta](t,t_1)\, \sigma[\Delta^*](t,t_2) \qquad \text{(C.19a)} \\ &= 2\Re\Bigg\{ \int_{t'}^{t} \mathrm{d}t_2 \underbrace{\int_{t_2}^{t} \mathrm{d}t_1\, \sigma[\Delta](t,t_1)\, \Delta(t_1,t_2)}_{\frac{\mathrm{d}(\sigma[\Delta](t,t_2))}{\mathrm{d}t_2}\Big|_{t=\text{const.}} \text{ (see Eq. (C.6))}} \sigma[\Delta^*](t,t_2) \Bigg\}\,, \qquad \text{(C.19b)}\end{aligned}$$

where the second equality follows after interchanging t_1 and t_2 within the second term of (C.19a) and leveraging (C.3). We now apply integration by parts to (C.19b) and utilize $\sigma[\Delta](t',t') = \sigma[\Delta^*](t',t') = 1$ which yields

$$\begin{aligned}\zeta_L(t,t') &= 2\big\{1 - \sigma[\Delta](t,t')\, \sigma[\Delta^*](t,t')\big\} \\ &\quad - 2\Re\Bigg\{ \int_{t'}^{t} \mathrm{d}t_2\, \sigma[\Delta](t,t_2) \frac{\mathrm{d}\big(\sigma[\Delta^*](t,t_2)\big)}{\mathrm{d}t_2}\Big|_{t=\text{const.}} \Bigg\}\,. \qquad \text{(C.20)}\end{aligned}$$

Finally, adding up (C.19b) and (C.20) the integral terms cancel and we obtain

$$\begin{aligned}\zeta_L(t,t') &= \Re\big\{1 - \sigma[\Delta](t,t')\, \sigma[\Delta^*](t,t')\big\} \\ &= 1 - \sigma[\Delta](t,t')\, \sigma[\Delta^*](t,t') = \zeta_R(t,t')\,, \qquad \text{(C.21)}\end{aligned}$$

which proves the identity of ζ_L and ζ_R.

Appendix D

Lateral Fourier Transforms

In the following we derive the explicit form of the lateral Fourier transforms of the Coulomb potential and the projectile wave functions. As we saw, these quantities are needed in the calculation of the matrix elements $V_{\vec{q}}$ and $V_{\vec{k}_1\vec{k}_2\vec{k}'}$ pertaining to the reactions of surface-induced resonant electron emission and Auger neutralization, respectively (see Secs. 4.1.2 and 5.1.1). Employing symmetrical prefactors a one-dimensional function $f(x)$ and its Fourier transform $f(p)$ are related by

$$f(p) = \frac{1}{\sqrt{2\pi}} \int_{-\infty}^{\infty} \mathrm{d}x \; f(x)\, e^{-ipx} \,, \tag{D.1a}$$

$$f(x) = \frac{1}{\sqrt{2\pi}} \int_{-\infty}^{\infty} \mathrm{d}p \; f(p)\, e^{ipx} \,. \tag{D.1b}$$

Consequently, the lateral Fourier transform of a three-dimensional function $f(x, y, z)$ is given by the two-dimensional integral

$$f(P_x, P_y, z) = \frac{1}{2\pi} \int_{-\infty}^{\infty} \mathrm{d}x \int_{-\infty}^{\infty} \mathrm{d}y \; f(x, y, z)\, e^{-i\vec{P}\cdot\vec{R}} \,, \tag{D.2}$$

with $\vec{P} = (P_x, P_y)$ and $\vec{R} = (x, y)$. In accordance with (D.2) the inverse lateral Fourier transform of a function $f(P_x, P_y, z)$ is given by

$$f(x, y, z) = \frac{1}{2\pi} \int_{-\infty}^{\infty} \mathrm{d}P_x \int_{-\infty}^{\infty} \mathrm{d}P_y \; f(P_x, P_y, z)\, e^{i\vec{P}\cdot\vec{R}} \,. \tag{D.3}$$

The integrals in (D.2) and (D.3) are most conveniently calculated in cylindrical coordinates,

$$\begin{aligned} R &= \sqrt{x^2 + y^2} \,, \qquad \varphi = \arctan\left(\frac{y}{x}\right) \,, \\ P &= \sqrt{P_x^2 + P_y^2} \,, \quad \varphi_{\vec{P}} = \arctan\left(\frac{P_y}{P_x}\right) \,. \end{aligned} \tag{D.4}$$

For the forward transform (D.2), in particular, this leads to

$$f(P, \varphi_{\vec{P}}, z) = \frac{1}{2\pi} \int_0^{\infty} \mathrm{d}R \int_0^{2\pi} \mathrm{d}\varphi \; R\, f(R, \varphi, z)\, e^{-iPR\cos(\varphi - \varphi_{\vec{P}})} \,. \tag{D.5}$$

Here a special case emerges when f is independent of φ. In this situation we can drop $\varphi_{\vec{P}}$ from the exponent in (D.5) because of the 2π periodicity of the integrand.

Consequently, the lateral transform becomes a function P and z only. The remaining angle integral can then be looked up (see Ref. [42, Eq. 3.715 18]) and we obtain

$$f(P,z) = \frac{1}{2\pi}\int_0^\infty \mathrm{d}R\, R\, f(R,z) \int_0^{2\pi} \mathrm{d}\varphi\, e^{-iPR\cos(\varphi)} \tag{D.6a}$$

$$= \frac{1}{\pi}\int_0^\infty \mathrm{d}R\, R\, f(R,z) \int_0^{\pi} \mathrm{d}\varphi\, \cos\big(PR\cos(\varphi)\big) \tag{D.6b}$$

$$= \int_0^\infty \mathrm{d}R\, R\, f(R,z)\, J_0(PR)\ , \tag{D.6c}$$

where J_0 is the zeroth-order Bessel function of the first kind.

Utilizing (D.5) and (D.6c) we will now explicitly calculate the lateral Fourier transforms of the Coulomb potential and the projectile wave functions.

D.1 Screened Coulomb Potential

Neglecting the position dependence of the dielectric constant the screened Coulomb potential $V_C = V_C^1$ is given by (see Eq. (2.60))

$$V_C(\vec{r}) = \frac{e_0^2}{4\pi\varepsilon_0\varepsilon_r}\frac{e^{-\kappa|\vec{r}|}}{|\vec{r}|} = \frac{e_0^2}{4\pi\varepsilon_0}\frac{e^{-\kappa\sqrt{R^2+z^2}}}{\sqrt{R^2+z^2}} = V_C(R,z)\ , \tag{D.7}$$

and obviously only depends on R and z. Hence, its lateral Fourier transform can be calculated from Eq. (D.6c). In particular, after employing the substitution

$$\xi = \frac{\sqrt{R^2+z^2}}{|z|}\ , \quad R = |z|\sqrt{\xi^2-1}\ , \quad \mathrm{d}R = |z|^2\,\frac{\xi}{R}\,\mathrm{d}\xi\ , \tag{D.8}$$

we arrive at

$$V_C(P,z) = \frac{e_0^2}{4\pi\varepsilon_0\varepsilon_r}\int_0^\infty \mathrm{d}R\, R\,\frac{e^{-\kappa\sqrt{R^2+z^2}}}{\sqrt{R^2+z^2}}\, J_0(PR) \tag{D.9a}$$

$$= |z|\,\frac{e_0^2}{4\pi\varepsilon_0\varepsilon_r}\int_1^\infty \mathrm{d}\xi\, e^{-\kappa|z|\xi}\, J_0\Big(P\,|z|\sqrt{\xi^2-1}\Big)\ . \tag{D.9b}$$

The value of this integral can be found in the literature (see Ref. [42, Eq. 6.616 2]) and, finally, leads to

$$V_C(P,z) = \frac{e_0^2}{4\pi\varepsilon_0\varepsilon_r}\frac{e^{-\sqrt{\kappa^2+P^2}\,|z|}}{\sqrt{\kappa^2+P^2}}\ . \tag{D.10}$$

Equation (D.10) can now be used to express the screened Coulomb potential (D.7) by the backward transform (see Eq. (D.3))

$$V_C(\vec{r}) = \frac{1}{2\pi}\frac{e_0^2}{4\pi\varepsilon_0\varepsilon_r}\int_{-\infty}^\infty \mathrm{d}P_x \int_{-\infty}^\infty \mathrm{d}P_y\, \frac{e^{-\sqrt{\kappa^2+P^2}\,|z|}}{\sqrt{\kappa^2+P^2}}\, e^{i\vec{P}\cdot\vec{R}}\ . \tag{D.11}$$

D.2 Helium Wave Function

The ground state helium wave function $\Psi_0^{(\mathrm{He})}$ (see Eq. (2.25)) is a function of $|\vec{r}|$ only. As a result, we can employ (D.6c) to calculate its lateral Fourier transform,

$$\Psi_0^{(\mathrm{He})}(P,z) = \frac{(\kappa_{\mathrm{He}})^{\frac{3}{2}}}{\sqrt{\pi}}\int_0^\infty \mathrm{d}R\, R\, e^{-\kappa_{\mathrm{He}}\sqrt{R^2+z^2}}\, J_0(PR)\ . \tag{D.12}$$

To evaluate this integral we need to employ integration by parts with $u(R)$ and $v'(R)$ chosen as

$$u(R) = e^{-\kappa_{\mathrm{He}}\sqrt{R^2+z^2}} , \tag{D.13a}$$

$$v'(R) = R\,J_0(PR) . \tag{D.13b}$$

The complementary terms $u'(R)$ and $v(R)$ can be calculated straightforwardly and read

$$u'(R) = -\kappa_{\mathrm{He}} \frac{R}{\sqrt{R^2+z^2}}\, e^{-\kappa_{\mathrm{He}}\sqrt{R^2+z^2}} , \tag{D.14a}$$

$$v(R) = \frac{R}{P} J_1(PR) , \tag{D.14b}$$

where we have used the general property (see for instance Ref. [1])

$$\frac{\mathrm{d}^k}{\mathrm{d}x^k}\big(x^n J_n(x)\big) = x^n J_{n-k}(x) , \quad k = 0, 1, 2, \dots . \tag{D.15}$$

Employing (D.13) and (D.14) together with the substitution (D.8) we obtain

$$\Psi_0^{(\mathrm{He})}(P,z) = \frac{(\kappa_{\mathrm{He}})^{\frac{5}{2}}}{\sqrt{\pi}P} \int_0^\infty \mathrm{d}R\, \frac{R^2}{\sqrt{R^2+z^2}}\, e^{-\kappa_{\mathrm{He}}\sqrt{R^2+z^2}}\, J_1(PR) \tag{D.16a}$$

$$= |z|^2 \frac{(\kappa_{\mathrm{He}})^{\frac{5}{2}}}{\sqrt{\pi}P} \int_1^\infty \mathrm{d}\xi\, \sqrt{\xi^2-1}\, e^{-\kappa_{\mathrm{He}}|z|\xi}\, J_1\Big(P|z|\sqrt{\xi-1}\Big) . \tag{D.16b}$$

The remaining integral can be looked up (see Ref. [42, Eq. 6.645 2]) and yields the final result

$$\Psi_0^{(\mathrm{He})}(P_\kappa, z_\kappa) = \frac{1}{\pi}\sqrt{\frac{2}{\kappa_{\mathrm{He}}}} \frac{|z_\kappa|^{\frac{3}{2}}}{(1+P_\kappa^2)^{\frac{3}{4}}} K_{\frac{3}{2}}\Big(|z_\kappa|\sqrt{1+P_\kappa^2}\Big) , \tag{D.17}$$

with $z_\kappa = z\,\kappa_{\mathrm{He}}$, $P_\kappa = P/\kappa_{\mathrm{He}}$ and K denoting the modified Bessel function of the second kind.

D.3 Argon Wave Function

The ground state wave function of argon, $\Psi_0^{(\mathrm{Ar})}$ (see Eq. (2.28)), depends on the azimuthal angle φ. Consequently, its lateral Fourier transform has to be calculated from the general form (D.5). Shifting the angle argument and exploiting the 2π periodicity of the integrand we obtain

$$\begin{aligned}\Psi_0^{(\mathrm{Ar})}(P, \varphi_{\vec{P}}, z) = \frac{1}{2\pi}\frac{2(\kappa_{\mathrm{Ar}})^{\frac{5}{2}}}{\sqrt{3\pi}} e^{-i\varphi_{\vec{P}}} \int_0^\infty \mathrm{d}R \int_0^{2\pi} \mathrm{d}\varphi\, e^{-i\varphi}\, e^{-iPR\cos(\varphi)} \\ \times R^2 \left(1 - \frac{\kappa_{\mathrm{Ar}}}{2}\sqrt{R^2+z^2}\right) e^{-\kappa_{\mathrm{Ar}}\sqrt{R^2+z^2}} .\end{aligned} \tag{D.18}$$

After partitioning the angular integration domain the φ integral can be found in the literature (see Ref. [42, Eq. 3.715 12]) and evaluates to

$$\int_0^{2\pi} \mathrm{d}\varphi\, e^{-i\varphi}\, e^{-iPR\cos(\varphi)} = -4i \int_0^{\pi/2} \mathrm{d}\varphi\, \cos(\varphi)\, \sin\big(PR\cos(\varphi)\big) \tag{D.19a}$$

$$= -i\,2\pi J_1(PR) . \tag{D.19b}$$

Substituting (D.19b) back into (D.18) we arrive at

$$\Psi_0^{(\mathrm{Ar})}(P,\varphi_{\vec{P}},z) = -i\,e^{-i\varphi_{\vec{P}}}\,\frac{2(\kappa_{\mathrm{Ar}})^{\frac{5}{2}}}{\sqrt{3\pi}}\left(\Psi_1(P,z) - \frac{\kappa_{\mathrm{Ar}}}{2}\Psi_2(P,z)\right), \tag{D.20}$$

with

$$\Psi_1(P,z) = \int_0^\infty \mathrm{d}R\; R^2\, e^{-\kappa_{\mathrm{Ar}}\sqrt{R^2+z^2}}\, J_1(PR)\,, \tag{D.21a}$$

$$\Psi_2(P,z) = \int_0^\infty \mathrm{d}R\; R^2\,\sqrt{R^2+z^2}\, e^{-\kappa_{\mathrm{Ar}}\sqrt{R^2+z^2}}\, J_1(PR)\,. \tag{D.21b}$$

We first consider the term Ψ_1. In order to evaluate (D.21a) we employ integration by parts with

$$u(R) = e^{-\kappa_{\mathrm{Ar}}\sqrt{R^2+z^2}}\,, \tag{D.22a}$$

$$v'(R) = R^2\, J_1(PR)\,, \tag{D.22b}$$

and

$$u'(R) = -\kappa_{\mathrm{Ar}}\frac{R}{\sqrt{R^2+z^2}}\, e^{-\kappa_{\mathrm{Ar}}\sqrt{R^2+z^2}}\,, \tag{D.23a}$$

$$v(R) = \frac{R^2}{P} J_2(PR)\,, \tag{D.23b}$$

where we again made use of (D.15). Utilizing (D.22), (D.23) and the substitution (D.8) we obtain

$$\Psi_1(P,z) = \frac{\kappa_{\mathrm{Ar}}}{P}\int_0^\infty \mathrm{d}R\;\frac{R^3}{\sqrt{R^2+z^2}}\, e^{-\kappa_{\mathrm{Ar}}\sqrt{R^2+z^2}}\, J_2(PR) \tag{D.24a}$$

$$= |z|^3\,\frac{\kappa_{\mathrm{Ar}}}{P}\int_1^\infty \mathrm{d}\xi\;(\xi^2-1)\, e^{-\kappa_{\mathrm{Ar}}|z|\xi}\, J_2\Big(P\,|z|\,\sqrt{\xi^2-1}\Big)\,. \tag{D.24b}$$

This integral can be looked up (see Ref. [42, Eq. 6.645 2]) and yields

$$\Psi_1(P_\kappa,z_\kappa) = \frac{1}{(\kappa_{\mathrm{Ar}})^3}\sqrt{\frac{2}{\pi}}\,\frac{P_\kappa}{(1+P_\kappa^2)^{\frac{5}{4}}}\,|z_\kappa|^{\frac{5}{2}}\, K_{\frac{5}{2}}\Big(|z_\kappa|\sqrt{1+P_\kappa^2}\Big)\,, \tag{D.25}$$

where we introduced the abbreviations

$$z_\kappa = z\kappa_{\mathrm{Ar}}\,, \quad P_\kappa = \frac{P}{\kappa_{\mathrm{Ar}}}\,. \tag{D.26}$$

We now proceed with the calculation of Ψ_2. For the evaluation of (D.21b) we employ integration by parts with $v(R)$ and $v'(R)$ as defined in (D.22b) and (D.23b) and

$$u(R) = \sqrt{R^2+z^2}\, e^{-\kappa_{\mathrm{Ar}}\sqrt{R^2+z^2}}\,, \tag{D.27a}$$

$$u'(R) = R\, e^{-\kappa_{\mathrm{Ar}}\sqrt{R^2+z^2}}\left(\frac{1}{\sqrt{R^2+z^2}} - \kappa_{\mathrm{Ar}}\right). \tag{D.27b}$$

Equation (D.21b) then turns into

$$\Psi_2(P,z) = -\frac{1}{P}\Big(\Psi_2^{(1)}(P,z) - \kappa_{\mathrm{Ar}}\Psi_2^{(2)}(P,z)\Big)\,, \tag{D.28}$$

with

$$\Psi_2^{(1)}(P,z) = \int_0^\infty \mathrm{d}R\, \frac{R^3}{\sqrt{R^2+z^2}}\, e^{-\kappa_{\mathrm{Ar}}\sqrt{R^2+z^2}}\, J_2(PR)\,, \tag{D.29a}$$

$$\Psi_2^{(2)}(P,z) = \int_0^\infty \mathrm{d}R\, R^3\, e^{-\kappa_{\mathrm{Ar}}\sqrt{R^2+z^2}}\, J_2(PR)\,. \tag{D.29b}$$

Comparing (D.29a) and (D.24a) we see the $\Psi_2^{(1)}$ is given by

$$\Psi_2^{(1)}(P_\kappa, z_\kappa) = P_\kappa\, \Psi_1(P_\kappa, z_\kappa)\,, \tag{D.30}$$

with P_κ and z_κ as defined in (D.26). For the calculation of $\Psi_2^{(2)}$, on the other hand, we once more need to integrate by parts, this time using

$$u(R) = e^{-\kappa_{\mathrm{Ar}}\sqrt{R^2+z^2}}\,, \tag{D.31a}$$

$$v'(R) = R^3\, J_2(PR)\,, \tag{D.31b}$$

and

$$u'(R) = -\kappa_{\mathrm{Ar}}\frac{R}{\sqrt{R^2+z^2}}\, e^{-\kappa_{\mathrm{Ar}}\sqrt{R^2+z^2}}\,, \tag{D.32a}$$

$$v(R) = \frac{R^3}{P} J_3(PR)\,, \tag{D.32b}$$

where we again leveraged (D.15). Employing the transformation (D.8) together with (D.31) and (D.32) we then obtain

$$\Psi_2^{(2)}(P,z) = \frac{\kappa_{\mathrm{Ar}}}{P}\int_0^\infty \mathrm{d}R\, \frac{R^4}{\sqrt{R^2+z^2}}\, e^{-\kappa_{\mathrm{Ar}}\sqrt{R^2+z^2}}\, J_3(PR) \tag{D.33a}$$

$$= |z|^4\, \frac{\kappa_{\mathrm{Ar}}}{P}\int_1^\infty \mathrm{d}\xi\, (\xi^2-1)^{\frac{3}{2}}\, e^{-\kappa_{\mathrm{Ar}}|z|\xi}\, J_3\Big(P\,|z|\sqrt{\xi^2-1}\Big)\,. \tag{D.33b}$$

The integral in (D.33b) can be found in the literature (see Ref. [42, Eq. 6.645 2]) and leads to

$$\Psi_2^{(2)}(P_\kappa, z_\kappa) = \frac{1}{(\kappa_{\mathrm{Ar}})^4}\sqrt{\frac{2}{\pi}}\,\frac{P_\kappa^2}{(1+P_\kappa^2)^{\frac{7}{4}}}\,|z_\kappa|^{\frac{7}{2}}\, K_{\frac{7}{2}}\Big(|z_\kappa|\sqrt{1+P_\kappa^2}\Big)\,, \tag{D.34}$$

with P_κ and z_κ given by (D.26).

We now, finally, can construct the overall lateral Fourier transform of $\Psi_{\mathrm{Ar}}^{(0)}(\vec{r})$ by combining (D.25), (D.30) and (D.34) according to (D.20) and (D.28). The result reads

$$\Psi_0^{(\mathrm{Ar})}(P_\kappa, \varphi_{\vec{P}}, z_\kappa) = -i\, e^{-i\varphi_{\vec{P}}}\,\frac{(\kappa_{\mathrm{Ar}})^{\frac{5}{2}}}{\sqrt{3\pi}}\left(3\,\Psi_1(P_\kappa, z_\kappa) - \frac{\kappa_{\mathrm{Ar}}}{P_\kappa}\Psi_2^{(2)}(P_\kappa, z_\kappa)\right) \tag{D.35a}$$

$$= -i\, e^{-i\varphi_{\vec{P}}}\,\frac{1}{\pi}\sqrt{\frac{2}{3\kappa_{\mathrm{Ar}}}}\,\frac{P_\kappa}{(1+P_\kappa^2)^{\frac{5}{4}}}\,|z_\kappa|^{\frac{5}{2}}\,\Psi(P_\kappa, z_\kappa)\,, \tag{D.35b}$$

with

$$\Psi(P_\kappa, z_\kappa) = 3K_{\frac{5}{2}}\Big(|z_\kappa|\sqrt{1+P_\kappa^2}\Big) - \frac{|z_\kappa|}{\sqrt{1+P_\kappa^2}}\, K_{\frac{7}{2}}\Big(|z_\kappa|\sqrt{1+P_\kappa^2}\Big)\,. \tag{D.36}$$

D.4 Molecular Nitrogen Wave Functions

For the lateral Fourier transform of the nitrogen wave functions we first consider the ground state level. Since in position space the associated wave function $\Psi_{0m}^{(\mathrm{N}_2)}(\vec{r})$ (see Eq. (2.33)) depends on R, φ and z, its lateral transform has to be calculated from Eq. (D.5). After shifting the φ-dependence we obtain

$$\begin{aligned}\Psi_{0m}^{(\mathrm{N}_2)}(P,\varphi_{\vec{P}},z) = -\frac{m}{2\pi}\frac{(\kappa_{\mathrm{N}_2})^{\frac{5}{2}}}{\sqrt{2\pi N_0}}\,e^{im\varphi_{\vec{P}}}\int_0^\infty \mathrm{d}R\int_0^{2\pi}\mathrm{d}\varphi\,e^{im\varphi}\,e^{-iPR\cos(\varphi)}\\ \times R^2\left(e^{-\kappa_{\mathrm{N}_2}\sqrt{R^2+\left(z+\frac{\varrho}{2}\right)^2}}+e^{-\kappa_{\mathrm{N}_2}\sqrt{R^2+\left(z-\frac{\varrho}{2}\right)^2}}\right).\end{aligned} \tag{D.37}$$

The value of the angular integral can be constructed from (D.19b) and, hence, we are left with

$$\Psi_{0m}^{(\mathrm{N}_2)}(P,\varphi_{\vec{P}},z) = im\,e^{im\varphi_{\vec{P}}}\frac{(\kappa_{\mathrm{N}_2})^{\frac{5}{2}}}{\sqrt{2\pi N_0}}\left(\Psi\left(P,z+\frac{\varrho}{2}\right)+\Psi\left(P,z-\frac{\varrho}{2}\right)\right), \tag{D.38}$$

where Ψ is defined by

$$\Psi(P,z) = \int_0^\infty \mathrm{d}R\,R^2\,e^{-\kappa_{\mathrm{N}_2}\sqrt{R^2+z^2}}\,J_1(PR)\,. \tag{D.39}$$

The integral in (D.39) is identical to (D.21a) with κ_{Ar} replaced by κ_{N_2}. Consequently, its value is given by (D.25) with the same substitution. The overall result, thus, reads

$$\begin{aligned}\Psi_{0m}^{(\mathrm{N}_2)}(P_\kappa,\varphi_{\vec{P}},z_\kappa) = im\,e^{im\varphi_{\vec{P}}}\frac{1}{\pi}\frac{1}{\sqrt{N_0\kappa_{\mathrm{N}_2}}}\frac{P_\kappa}{(1+P_\kappa^2)^{\frac{5}{4}}}\\ \times\left[\Phi\left(P_\kappa,\left|z_\kappa+\frac{\varrho_\kappa}{2}\right|\right)+\Phi\left(P_\kappa,\left|z_\kappa-\frac{\varrho_\kappa}{2}\right|\right)\right],\end{aligned} \tag{D.40}$$

with

$$\Phi(P_\kappa,z_\kappa) = |z_\kappa|^{\frac{5}{2}}\,K_{\frac{5}{2}}\left(|z_\kappa|\sqrt{1+P_\kappa^2}\right), \tag{D.41}$$

and

$$z_\kappa = z\kappa_{\mathrm{N}_2}\,,\qquad P_\kappa = \frac{P}{\kappa_{\mathrm{N}_2}}\,. \tag{D.42}$$

We now proceed with the lateral Fourier transform of the nitrogen ground state wave function of rotated arguments $\bar{\Psi}_{0m}^{(\mathrm{N}_2)}(\vec{r}) = \Psi_{0m}^{(\mathrm{N}_2)}(-z,y,x)$ which is needed when the molecular axis is aligned parallel to the surface. Starting from the general form (D.2) we oppositely shift the x dependence in the two exponential terms of the wave function and obtain

$$\begin{aligned}\bar{\Psi}_{0m}^{(\mathrm{N}_2)}(P_x,P_y,z) = -\cos\left(P_x\frac{\varrho}{2}\right)\frac{m}{\pi}\frac{(\kappa_{\mathrm{N}_2})^{\frac{5}{2}}}{\sqrt{2\pi N_0}}\\ \times\int_{-\infty}^\infty \mathrm{d}x\int_{-\infty}^\infty \mathrm{d}y\,(-z+imy)\,e^{-\kappa_{\mathrm{N}_2}\sqrt{x^2+y^2+z^2}}\,e^{-i\vec{P}\cdot\vec{R}}\,.\end{aligned} \tag{D.43}$$

After switching to cylindrical coordinates this equation turns into

$$\begin{aligned}\bar{\Psi}_{0m}^{(\mathrm{N}_2)}(P,\varphi_{\vec{P}},z) = -\cos\left(P\cos(\varphi_{\vec{P}})\frac{\varrho}{2}\right)\frac{m}{\pi}\frac{(\kappa_{\mathrm{N}_2})^{\frac{5}{2}}}{\sqrt{2\pi N_0}}\\ \times\left[im\bar{\Psi}_1(P,\varphi_{\vec{P}},z)-z\bar{\Psi}_2(P,\varphi_{\vec{P}},z)\right],\end{aligned} \tag{D.44}$$

with $\bar{\Psi}_1$ and $\bar{\Psi}_2$ given by

$$\bar{\Psi}_1(P,\varphi_{\vec{P}},z) = \int_0^\infty \mathrm{d}R \int_0^{2\pi} \mathrm{d}\varphi\, R^2\, \sin(\varphi)\, e^{-\kappa_{\mathrm{N}_2}\sqrt{R^2+z^2}}\, e^{-iPR\cos(\varphi-\varphi_{\vec{P}})}\,, \tag{D.45a}$$

$$\bar{\Psi}_2(P,\varphi_{\vec{P}},z) = \int_0^\infty \mathrm{d}R \int_0^{2\pi} \mathrm{d}\varphi\, R\, e^{-\kappa_{\mathrm{N}_2}\sqrt{R^2+z^2}}\, e^{-iPR\cos(\varphi-\varphi_{\vec{P}})}\,. \tag{D.45b}$$

We first focus on $\bar{\Psi}_1$. To evaluate (D.45a) we start with the angle integral which after partitioning the integration domain can be looked up (see Ref. [42, Eq. 3.715 12]),

$$\begin{aligned}\int_0^{2\pi} \mathrm{d}\varphi\, \sin(\varphi)\, e^{-iPR\cos(\varphi-\varphi_{\vec{P}})} &= -4i\sin(\varphi_{\vec{P}}) \\ &\quad\times \int_0^{\pi/2} \mathrm{d}\varphi\, \cos(\varphi)\, \sin\big(PR\cos(\varphi)\big) \qquad \text{(D.46a)}\\ &= -i\,2\pi\sin(\varphi_{\vec{P}})\, J_1(PR)\,. \qquad \text{(D.46b)}\end{aligned}$$

Consequently, (D.45a) reduces to

$$\bar{\Psi}_1(P,\varphi_{\vec{P}},z) = -i\,2\pi\sin(\varphi_{\vec{P}}) \int_0^\infty \mathrm{d}R\, R^2\, e^{-\kappa_{\mathrm{N}_2}\sqrt{R^2+z^2}}\, J_1(PR)\,, \tag{D.47}$$

where the remaining integral is again identical to (D.21a) with κ_{Ar} and κ_{N_2} interchanged. Hence, $\bar{\Psi}_1$ is given by (D.25) under the same replacement. In total we find

$$\begin{aligned}\bar{\Psi}_1(P_\kappa,\varphi_{\vec{P}},z_\kappa) &= -i\,\sin(\varphi_{\vec{P}})\frac{2\sqrt{2\pi}}{(\kappa_{\mathrm{N}_2})^3}\,\frac{P_\kappa}{(1+P_\kappa^2)^{\frac{5}{4}}} \\ &\quad\times |z_\kappa|^{\frac{5}{2}}\, K_{\frac{5}{2}}\Big(|z_\kappa|\sqrt{1+P_\kappa^2}\Big)\,,\end{aligned} \tag{D.48}$$

with z_κ and P_κ as defined in (D.42).

We now proceed with the calculation of $\bar{\Psi}_2$. The angle integration in (D.45b) can be carried out by means of (D.6) and leads to

$$\bar{\Psi}_2(P,\varphi_{\vec{P}},z) = 2\pi \int_0^\infty \mathrm{d}R\, R\, e^{-\kappa_{\mathrm{N}_2}\sqrt{R^2+z^2}}\, J_0(PR)\,. \tag{D.49}$$

The integral appearing in this equation is identical to the one in (D.12) with κ_{He} replaced by κ_{N_2}. The value of $\bar{\Psi}_2$ can, thus, be constructed from (D.17) by employing the same substitution and adjusting the prefactor. In particular, we obtain

$$\bar{\Psi}_2(P_\kappa,\varphi_{\vec{P}},z_\kappa) = \frac{2\sqrt{2\pi}}{(\kappa_{\mathrm{N}_2})^2}\,\frac{|z_\kappa|^{\frac{3}{2}}}{(1+P_\kappa^2)^{\frac{3}{4}}} K_{\frac{3}{2}}\Big(|z_\kappa|\sqrt{1+P_\kappa^2}\Big)\,, \tag{D.50}$$

where, as before, z_κ and P_κ are given by (D.42).

The overall lateral transform of $\bar{\Psi}_{0m}^{(\mathrm{N}_2)}(\vec{r}) = \Psi_{0m}^{(\mathrm{N}_2)}(-z,y,x)$ can now be constructed from (D.48) and (D.50) by means of (D.44). The final expression reads

$$\begin{aligned}\bar{\Psi}_{0m}^{(\mathrm{N}_2)}(P_\kappa,\varphi_{\vec{P}},z_\kappa) &= -\cos\left(P_\kappa\cos(\varphi_{\vec{P}})\,\frac{\varrho_\kappa}{2}\right)\frac{1}{\pi}\,\frac{2m}{\sqrt{N_0\kappa_{\mathrm{N}_2}}}\,\frac{|z_\kappa|^{\frac{3}{2}}}{(1+P_\kappa^2)^{\frac{3}{4}}} \\ &\quad\times\Bigg[m\sin(\varphi_{\vec{P}})\,\frac{P_\kappa}{\sqrt{1+P_\kappa^2}}\,|z_\kappa|\,K_{\frac{5}{2}}\Big(|z_\kappa|\sqrt{1+P_\kappa^2}\Big) \\ &\quad - z_\kappa\, K_{\frac{3}{2}}\Big(|z_\kappa|\sqrt{1+P_\kappa^2}\Big)\Bigg]\,.\end{aligned} \tag{D.51}$$

Our results for the ground state wave function, Eqs. (D.40) and (D.51), can now immediately be generalized to the excited level's wave function since the two only differ in the sign of the involved atomic wave functions and the normalization constant (see Eq. (2.31)). In particular, we find

$$\begin{aligned}\Psi_{1m}^{(\mathrm{N}_2)}(P_\kappa, \varphi_{\vec{P}}, z_\kappa) &= im\, e^{im\varphi_{\vec{P}}}\, \frac{1}{\pi}\, \frac{1}{\sqrt{N_1 \kappa_{\mathrm{N}_2}}}\, \frac{P_\kappa}{(1+P_\kappa^2)^{\frac{5}{4}}} \\ &\quad \times \left[\Phi\left(P_\kappa, \left|z_\kappa + \frac{\varrho_\kappa}{2}\right|\right) - \Phi\left(P_\kappa, \left|z_\kappa - \frac{\varrho_\kappa}{2}\right|\right)\right], \end{aligned} \tag{D.52a}$$

$$\begin{aligned}\bar{\Psi}_{1m}^{(\mathrm{N}_2)}(P_\kappa, \varphi_{\vec{P}}, z_\kappa) &= -i \sin\left(P_\kappa \cos(\varphi_{\vec{P}})\, \frac{\varrho_\kappa}{2}\right) \frac{1}{\pi}\, \frac{2m}{\sqrt{N_1 \kappa_{\mathrm{N}_2}}}\, \frac{|z_\kappa|^{\frac{3}{2}}}{(1+P_\kappa^2)^{\frac{3}{4}}} \\ &\quad \times \left[m \sin(\varphi_{\vec{P}})\, \frac{P_\kappa}{\sqrt{1+P_\kappa^2}}\, |z_\kappa|\, K_{\frac{5}{2}}\left(|z_\kappa| \sqrt{1+P_\kappa^2}\right)\right. \\ &\quad \left. - z_\kappa\, K_{\frac{3}{2}}\left(|z_\kappa| \sqrt{1+P_\kappa^2}\right)\right], \end{aligned} \tag{D.52b}$$

where Φ is given by (D.41) and, in accordance with our previous notation, $\bar{\Psi}_{1m}^{(\mathrm{N}_2)}$ denotes the excited level's wave function of rotated arguments which, in position space, is defined by $\bar{\Psi}_{1m}^{(\mathrm{N}_2)}(\vec{r}) = \Psi_{1m}^{(\mathrm{N}_2)}(-z, y, x)$.

Appendix E

Numerical Scheme

In order to cope with the numerical tasks of this work, an extensive[1] C program was developed. The application is capable of executing all of the previously described numerical calculations. Moreover, it is modular in the sense that different components of the numerical scheme can be enabled or disabled at compile time. The compilation process itself is automated by a set of makefiles[36]. In the following we give a short outline of the particular numerical techniques that were used in our analysis.

Most of our calculations were concerned with numerical integration. In particular, we had to deal with time integrals of the various Δ-functions, the wave vector integrations contained in the Δ-functions themselves and the spatial integrations within the different matrix elements. All of these integrals were treated by routines included in the GNU Scientific Library[37] (GSL). The latter includes industrial strength implementations of standard numerical algorithms which, in part, have been tested for more than a decade. In particular, we handled one and two-dimensional integrals by means of (nested) adaptive Gauss-Kronrod rules while for integrals with higher dimensionality we employed an adaptive Monte Carlo scheme based on the VEGAS algorithm[78].

Another important component of our numerical scheme is the tabulation and subsequent interpolation of intermediate results. Due to the multitude of integration dimensions and the nested structure of the integrals the final semi-classical equations of our theory could not be solved as a whole. Instead we often broke our calculations down into multiple steps by evaluating intermediate results on a grid, temporarily storing the discrete values and interpolating between them in subsequent calculation steps. This approach of course constitutes a trade-off since the gain in performance was accompanied by an increase in memory consumption. The performance boost did, however, outbalance the enhanced memory requirements.

The use of interpolation techniques obviously required us to choose sensible values for the grid spacings. A too dense grid wastes computing resources while an overly sparse grid will not allow for an accurate representation of the original quantity. Therefore, we always tested our interpolation against the original quantity using a significant number of sample points and parameter configurations. Similarly, we also sensitively controlled the overall extension of the tabulation grid in order not to introduce truncations in sensitive regions.

In particular, we tabulated $\bar{V}_{\vec{k}\vec{q}}$, the time-independent part of the separated ma-

[1] The overall codebase contains roughly 66,000 lines of code and comments.

trix element of indirect Auger de-excitation (see Eq. (4.7b)), over its six-dimensional wave vector dependence in spherical coordinates. Here we chose the $\vec{k}$-grid to stretch over the entire occupied region of the band structure's active portion. Moreover, for the $\vec{q}$-grid we introduced a maximum radial component which was chosen slightly higher than the approximate classical cut-off energy (4.36). As we saw in the energetic distribution of escaped Auger electrons, Fig. 4.5, this is justified since the spectrum falls off very rapidly beyond the classical cut-off. The subsequent wave vector integration contained in Δ_{iad} and similar functions was then carried out by means of Monte Carlo techniques while using sexalinear interpolation to obtain the intergrid-values of $\bar{V}_{\vec{k}\vec{q}}$.

Moreover, in order to speed up the calculation of the number of negative ions n_- due to the resonant and combined two-channel de-excitation (see Eq. (3.96)) we tabulated the molecular occupancies $n_0^{(rc)} = 1 - n_*^{(rc)}$ and $n_0^{(iad)} = 1 - n_*^{(iad)}$ over the collision time. Since these occupations saturated rather quickly in our situation (see Figs. 4.4 and 4.7), we cropped the tabulation at $|t| \leq 20$ (in the dimensionless units of (4.9)). The inter-grid values of $n_0^{(rc)}$ and $n_0^{(iad)}$ were then obtained using the cubic spline interpolation routines contained in the GSL. Note that along the same lines we also tabulated the time-dependent occupancy of the ground state projectile level $n_0^{(an+rn)}$ for the efficient calculation of the Auger neutralization spectrum from (3.135b).

Furthermore, in the context of the two-channel de-excitation we tabulated the spectral decay rate $\tilde{\varrho}_{iad}(\varepsilon_{\vec{q}}^{\infty}, t)$ (see Eq. (3.102a)) over $\varepsilon_{\vec{q}}^{\infty}$ and t in order to calculate the combined spectrum of escaped electrons (see Figs. 4.15 and4.16). Here the extension of the interpolation grid was chosen in accordance with the aforementioned argument of energy conservation. For the interpolation of $\tilde{\varrho}_{iad}$ we then employed a standard bilinear scheme.

Finally, we also tabulated the angular mean value of the Auger neutralization matrix element $V_{k_1k_2k'}(t)$ (see (5.19a)) over its wave vector and time dependence. Here again the extension of the tabulation grid was derived from the classical energy conservation. This time, however, the cut-off energy had to be chosen significantly larger than the classical value, as seen from the spectra in Fig. 5.2. The inter-grid values of $V_{k_1k_2k'}(t)$ were obtained using quater-linear interpolation.

In addition to the described tabulation techniques, we also limited the boundaries of some of the Δ-functions' time integrations in order to speed-up the calculation. This is motivated by the fact that extremely large or small times cannot contribute to these integrals because all of the matrix elements vanish far away from the surface. These regions can, however, involve rapid oscillations of the integrands, introduced by the energy exponentials, which can lead to numerically incorrect results.

Besides, all of the special functions involved in our numerical scheme (Γ-function, Bessel functions, ...) were calculated using routines from the GSL. The confluent hypergeometric function M, however, marks an exception from this rule. This function appears as part of the projectile continuum wave function $\Psi_{\vec{q}}^{(\mathrm{N_2})}$ in the matrix element of indirect Auger de-excitation (see Eqs. (2.37) and (4.1)). Within the matrix element $\Psi_{\vec{q}}^{(\mathrm{N_2})}$ is multiplied by a bound projectile wave function of the same argument which is strongly localized about the projectile position. Thus, it suffices to generate an accurate approximation of the hypergeometric function M close to the respective projectile position. In order to calculate M, we, therefore, directly employed its series expansion (see for instance Ref. [1]) with an empirically deter-

mined maximum expansion order. Note that for fixed $|\vec{q}|$ the associated expansion coefficients can be calculated in advance and don't need to be adapted for changing angular components of $\vec{q}$. This fact significantly boosts the performance of the $\bar{V}_{\vec{k}\vec{q}}$-tabulation when it is arranged to traverse along lines of equal $|\vec{q}|$.

Moreover, the precision settings involved in the numerical routines (order of Gauss-Kronrod rules, number of Monte Carlo samples, ...) were always chosen to obtain satisfactory correctness while maintaining acceptable computing time. This of course calls for a trade-off since it is impossible to have both simultaneously. However, all of the results published here have an error estimate of below one percent.

Finally, we stress that while the individual numerical operations involved in our calculation may not be very complex, their combination into such an extensive numerical scheme is what makes the process highly complicated.

List of Scientific Contributions

In the following we give an overview of the scientific contributions that were created in connection with the present work.

Publications

{6} J. Marbach, F. X. Bronold and H. Fehske. "Pseudoparticle Approach for Charge-Transferring Molecule-Surface Collisions". *Phys. Rev. B* **86** (2012), 115417. DOI: 10.1103/PhysRevB.86.115417

{5} F. X. Bronold, H. Fehske, R. L. Heinisch and J. Marbach. "Wall Charge and Potential from a Microscopic Point of View". *Contrib. Plasma Phys.* **1-8** (2012). DOI: 10.1002/ctpp.201200032

{4} J. Marbach, F. X. Bronold and H. Fehske. "Resonant Charge Transfer at Dielectric Surfaces". *Eur. Phys. J. D* **66** (2012), 1. DOI: 10.1140/epjd/e2012-30014-8

{3} J. Marbach, F. X. Bronold and H. Fehske. "Auger De-Excitation of Metastable Molecules at Metallic Surfaces". *Phys. Rev. B* **84** (2011), 085443. DOI: 10.1103/PhysRevB.84.085443

{2} F. X. Bronold, R. L. Heinisch, J. Marbach and H. Fehske. "Plasma Walls Beyond the Perfect Absorber Approximation for Electrons". *IEEE Trans. Plasma Science* **39** (2011), 644. DOI: 10.1109/TPS.2010.2094209

{1} B. Bruhn, B. May and J. Marbach. "Hopf-Bifurcations, Global Coupling and Hysteresis in DC-Driven Oxygen Discharges". *Contrib. Plasma Phys.* **51** (2011), 650. DOI: 10.1002/ctpp.201000083

Conference Contributions

{6} J. Marbach, F. X. Bronold and H. Fehske. "Secondary Electron Emission from Dielectric Surfaces due to De-Excitation of Impacting Metastable Nitrogen Molecules". *Poster for DPG Spring Meeting SAMOP*, Stuttgart (2012)

{5} J. Marbach, F. X. Bronold and H. Fehske. "Secondary Electron Emission due to Auger De-Excitation of Metastable Nitrogen Molecules at Metallic Surfaces". *Contribution to ICPIG* (2011). arXiv:1109.0845

{4} J. Marbach, F. X. Bronold and H. Fehske. "Secondary Electron Emission due to Auger De-Excitation of Metastable Nitrogen Molecules at Metallic Surfaces". *Poster for ICPIG*, Belfast (2011)

{3} J. Marbach, F. X. Bronold and H. Fehske. "Quantum-Kinetic Modeling of Auger De-Excitation of Metastable Molecules at Metallic Surfaces". *Poster for 2^{nd} Graduate Summer Institute "Complex Plasmas"*, Greifswald (2010)

{2} F. X. Bronold, H. Fehske, R. L. Heinisch and J. Marbach. "Quantum Kinetics of Electrons at Plasma Boundaries". *Poster for DPG Spring Meeting SKM*, Regensburg (2010)

{1} J. Marbach, F. X. Bronold and H. Fehske. "De-Excitation of Metastable Nitrogen Molecules on Surfaces – Quantum-Kinetic Modelling". *Poster for DPG Spring Meeting SAMOP*, Hannover (2010)

List of Figures

List of Tables

Bibliography

[1] M. Abramowitz and I. A. Stegun. *Handbook of Mathematical Functions: With Formulas, Graphs, and Mathematical Tables*. 9th ed. Dover Publications, 1965. ISBN: 978-0-486-61272-0.

[2] A. A. Abrikosov, L. P. Gorkov and I. E. Dzyaloshinski. *Quantum Field Theoretical Methods in Statistical Physics*. 1st ed. Dover Publications, 1975. ISBN: 978-0-486-63228-5.

[3] R. Aguado and D. C. Langreth. "Kondo Effect in Coupled Quantum Dots: A Noncrossing Approximation Study". *Phys. Rev. B* **67** (2003), 245307. DOI: 10.1103/PhysRevB.67.245307.

[4] A. T. Amos, B. L. Burrows and S. G. Davison. "Competition Between Auger and Resonant Charge Transfer in Surface Ion Neutralization". *Surf. Sci. Lett.* **277** (1992), L100. DOI: 10.1016/0167-2584(92)90141-Q.

[5] P. W. Anderson. "Localized Magnetic States in Metals". *Phys. Rev.* **124** (1961), 41. DOI: 10.1103/PhysRev.124.41.

[6] A. G. Aronov and V. L. Gurevich. "Response of a Pure Superconductor to a Slowly Varying Perturbation". *Sov. Phys. Solid State* **16** (1974), 1722. URL: http://www.osti.gov/energycitations/product.biblio.jsp?osti_id=7220644.

[7] N. W. Ashcroft and N. D. Mermin. *Solid State Physics*. 1st ed. Saunders College Publishing, 1976. ISBN: 978-0-03-049346-1.

[8] P. W. Atkins and R. S. Friedman. *Molecular Quantum Mechanics*. 5th ed. Oxford University Press, 2010. ISBN: 978-0-19-954142-3.

[9] G. Auday, P. Guillot and J. Galy. "Secondary Emission of Dielectrics Used in Plasma Display Panels". *J. Appl. Phys.* **88** (2000), 4871. DOI: 10.1063/1.1290461.

[10] K. H. Becker, K. H. Schoenbach and J. G. Eden. "Microplasmas and Applications". *J. Phys. D* **39** (2006), R55. DOI: 10.1088/0022-3727/39/3/R01.

[11] S. Bhagavantam and D. Narayana Rao. "Dielectric Constant of Diamond". *Nature* **161** (1948), 729. DOI: 10.1038/161729a0.

[12] A. Blandin, A. Nourtier and D. W. Hone. "Localized Time-Dependent Perturbations in Metals: Formalism and Simple Examples". *J. Physique* **37** (1976), 369. DOI: 10.1051/jphys:01976003704036900.

[13] N. Bonini, G. P. Brivio and M. I. Trioni. "Theory of Metastable Deexcitation Spectroscopy on Simple Metals". *Phys. Rev. B* **68** (2003), 035408. DOI: 10.1103/PhysRevB.68.035408.

[14] R. Brako and D. M. Newns. "Theory of Electronic Processes in Atom Scattering from Surfaces". *Rep. Prog. Phys.* **52** (1989), 655. DOI: 10.1088/0034-4885/52/6/001.

[15] R. Brandenburg et al. "Diffuse Barrier Discharges in Nitrogen with Small Admixtures of Oxygen: Discharge Mechanism and Transition to the Filamentary Regime". *J. Phys. D* **38** (2005), 2187. DOI: 10.1088/0022-3727/38/13/017.

[16] F. X. Bronold, H. Deutsch and H. Fehske. "Physisorption Kinetics of Electrons at Plasma Boundaries". *Eur. Phys. J. D* **54** (2009), 519. DOI: 10.1140/epjd/e2009-00213-7.

[17] G. Carmona and J. L. Cardoso. "Slave Boson Gas, a Toy". *Rev. Mex. Fis. Suppl.* **48** (2002), 254. URL: http://adsabs.harvard.edu/cgi-bin/nph-bib_query?bibcode=2002RMxFS..48a.254C.

[18] M. A. Cazalilla et al. "Theory of Auger Neutralization and Deexcitation of Slow Ions at Metal Surfaces". *Phys. Rev. B* **58** (1998), 13991. DOI: 10.1103/PhysRevB.58.13991.

[19] S. Ciraci and I. P. Batra. "Electronic Structure of α-Alumina and Its Defect States". *Phys. Rev. B* **28** (1983), 982. DOI: 10.1103/PhysRevB.28.982.

[20] S. Ciraci and S. Ellialtioğlu. "Surface Electronic Structure of Silicon Dioxide". *Phys. Rev. B* **25** (1982), 4019. DOI: 10.1103/PhysRevB.25.4019.

[21] E. Clementi and C. Roetti. "Roothaan-Hartree-Fock Atomic Wavefunctions: Basis Functions and Their Coefficients for Ground and Certain Excited States of Neutral and Ionized Atoms, $Z \leq 54$". *At. Nucl. Data Tables* **14** (1974), 177. DOI: 10.1016/S0092-640X(74)80016-1.

[22] P. Coleman. "New Approach to the Mixed-Valence Problem". *Phys. Rev. B* **29** (1984), 3035. DOI: 10.1103/PhysRevB.29.3035.

[23] P. Danielewicz. "Quantum Theory of Nonequilibrium Processes, I". *Ann. Phys. (N.Y.)* **152** (1984), 239. DOI: 10.1016/0003-4916(84)90092-7.

[24] A. Dreuw and L. S. Cederbaum. "Long-Lived High-Spin Sextet States of N_2^-". *Int. J. Mass Spectr.* **188** (1999), 199. DOI: 10.1016/S1387-3806(99)00039-1.

[25] F. B. Dunning, P. Nordlander and G. K. Walters. "Dynamics of Metastable-Atom Deexcitation at Metal Surfaces". *Phys. Rev. B* **44** (1991), 3246. DOI: 10.1103/PhysRevB.44.3246.

[26] C. M. Dutta and P. Nordlander. "Simple Master Equation for the Description of Charge Transfer in Atom-Surface Scattering". *Prog. Surf. Sci.* **67** (2001), 155. DOI: 10.1016/S0079-6816(01)00021-1.

[27] V. N. Fleurov and A. N. Kozlov. "Quantum Kinetic Equation for Electrons in Metals". *J. Phys. F* **8** (1978), 1899. DOI: 10.1088/0305-4608/8/9/013.

[28] J. Fontanella, C. Andeen and D. Schuele. "Low-Frequency Dielectric Constants of Alpha-Quartz, Sapphire, MgF_2, and MgO". *J. Appl. Phys.* **45** (1974), 2852. DOI: 10.1063/1.1663690.

[29] C. J. Foot. *Atomic Physics*. 1st ed. Oxford University Press, 2005. ISBN: 978-0-19-850695-9.

[30] J. W. Gadzuk. "Theory of Atom-Metal Interactions I. Alkali Atom Adsorption". *Surf. Sci.* **6** (1967), 133. DOI: 10.1016/0039-6028(67)90001-5.

[31] J. W. Gadzuk. "Theory of Atom-Metal Interactions II. One-Electron Transition Matrix Elements". *Surf. Sci.* **6** (1967), 159. DOI: 10.1016/0039-6028(67)90002-7.

[32] E. A. García, P. G. Bolcatto and E. C. Goldberg. "Model Calculation of the Charge Transfer in Low-Energy He^+ Scattering from Metallic Surfaces". *Phys. Rev. B* **52** (1995), 16924. DOI: 10.1103/PhysRevB.52.16924.

[33] E. A. García et al. "Interference Between Resonant and Auger Mechanisms for Charge-Exchange Processes near Surfaces". *Phys. Rev. B* **67** (2003), 205426. DOI: 10.1103/PhysRevB.67.205426.

[34] E. A. García et al. "Ion Fractions in the Scattering of Hydrogen on Different Reconstructed Silicon Surfaces". *Surf. Sci.* **600** (2006), 2195. DOI: 10.1016/j.susc.2006.03.008.

[35] S. Gasiorowicz. *Quantum Physics*. 3rd ed. Wiley, 2003. ISBN: 978-0-471-05700-0.

[36] *GNU Make*. URL: http://www.gnu.org/software/make/.

[37] *GNU Scientific Library*. URL: http://www.gnu.org/software/gsl/.

[38] E. C. Goldberg and F. Flores. "Charge Exchange in Many-Body Time-Dependent Processes". *Phys. Rev. B* **45** (1992), 8657. DOI: 10.1103/PhysRevB.45.8657.

[39] E. C. Goldberg et al. "New Model for Ion Neutralization at Surfaces". *Surf. Sci.* **440** (1999), L875. DOI: 10.1016/S0039-6028(99)00863-8.

[40] Y. B. Golubovskii et al. "Influence of Interaction Between Charged Particles and Dielectric Surface over a Homogeneous Barrier Discharge in Nitrogen". *J. Phys. D* **35** (2002), 751. DOI: 10.1088/0022-3727/35/8/306.

[41] H. Grabert and M. H. Devoret. *Single Charge Tunneling: Coulomb Blockade Phenomena in Nanostructures*. 1st ed. Plenum Press, 1992. ISBN: 978-0-306-44229-2.

[42] I. S. Gradshteyn et al. *Table of Integrals, Series, and Products*. 7th ed. Academic Press, 2007. ISBN: 978-0-12-373637-6.

[43] H. D. Hagstrum. "Auger Ejection of Electrons from Tungsten by Noble Gas Ions". *Phys. Rev.* **96** (1954), 325. DOI: 10.1103/PhysRev.96.325.

[44] H. D. Hagstrum. "Theory of Auger Ejection of Electrons from Metals by Ions". *Phys. Rev.* **96** (1954), 336. DOI: 10.1103/PhysRev.96.336.

[45] H. D. Hagstrum. "Theory of Auger Neutralization of Ions at the Surface of a Diamond-Type Semiconductor". *Phys. Rev.* **122** (1961), 83. DOI: 10.1103/PhysRev.122.83.

[46] H. Haken and H. C. Wolf. *Molecular Physics and Elements of Quantum Chemistry*. 2nd ed. Springer, 2004. ISBN: 978-3-540-40792-8.

[47] Y. Harada, S. Masuda and H. Ozaki. "Electron Spectroscopy Using Metastable Atoms as Probes for Solid Surfaces". *Chem. Rev.* **97** (1997), 1897. DOI: 10.1021/cr940315v.

[48] H. Haug and A.-P. Jauho. *Quantum Kinetics in Transport and Optics of Semiconductors*. 2nd ed. Springer, 2008. ISBN: 978-3-540-73561-8.

[49] W. Heiland. "The Interaction of Molecular Ions with Surfaces". In: *Low Energy Ion-Surface Interactions*. Ed. by J. W. Rabalais. 1st ed. Wiley, 1994, 313. ISBN: 978-0-471-93891-0.

[50] R. Hentschke et al. "Matrix Element and Transition Rate for Auger Neutralization of Low Energy Ions near Metal Surfaces". *Surf. Sci.* **173** (1986), 565. DOI: 10.1016/0039-6028(86)90210-4.

[51] A. C. Hewson. *The Kondo Problem to Heavy Fermions*. 1st ed. Cambridge University Press, 1997. ISBN: 978-0-521-59947-4.

[52] X. He and J. A. Yarmoff. "Correlated Electron Effects in Low Energy Sr^+ Ion Scattering". *Phys. Rev. Lett.* **105** (2010), 176806. DOI: 10.1103/PhysRevLett.105.176806.

[53] M. Honigmann, R. J. Buenker and H. P. Liebermann. "Complex Self-Consistent Field and Multireference Single- and Double-Excitation Configuration Interaction Calculations for the $^2\Pi_g$ Resonance State of N_2^-". *J. Chem. Phys.* **125** (2006), 234304. DOI: 10.1063/1.2403856.

[54] C. R. Hu. "New Set of Time-Dependent Ginzburg-Landau Equations for Dirty Superconductors near T_c". *Phys. Rev. B* **21** (1980), 2775. DOI: 10.1103/PhysRevB.21.2775.

[55] U. Imke, K. J. Snowdon and W. Heiland. "Resonant Transition Rates for Charge Transfer Between Diatomic Molecular Ions and Simple Metals". *Phys. Rev. B* **34** (1986), 48. DOI: 10.1103/PhysRevB.34.48.

[56] U. Imke, K. J. Snowdon and W. Heiland. "Theory of Charge Exchange in the Scattering of Molecular Ions from Simple Metals". *Phys. Rev. B* **34** (1986), 41. DOI: 10.1103/PhysRevB.34.41.

[57] J. L. Jacobson and E. R. Nixon. "Infrared Dielectric Response and Lattice Vibrations of Calcium and Strontium Oxides". *J. Phys. Chem. Solids* **29** (1968), 967. DOI: 10.1016/0022-3697(68)90233-3.

[58] R. K. Janev and N. N. Nedeljković. "Interaction of Atomic Particles with Solid Surfaces. V. Auger De-excitation of Metastable Atoms". *J. Phys. B* **14** (1981), 2995. DOI: 10.1088/0022-3700/14/16/027.

[59] R. K. Janev and N. N. Nedeljković. "Interaction of Atomic Particles with Solid Surfaces. VI. Auger Neutralisation of Positive Ions". *J. Phys. B* **18** (1985), 915. DOI: 10.1088/0022-3700/18/5/011.

[60] A. P. Jauho. "Quantum Electron-Phonon Transport Equations Revisited". *J. Phys. F* **13** (1983), L203. DOI: 10.1088/0305-4608/13/10/004.

[61] P. J. Jennings, R. O. Jones and M. Weinert. "Surface Barrier for Electrons in Metals". *Phys. Rev. B* **37** (1988), 6113. DOI: 10.1103/PhysRevB.37.6113.

[62] R. A. W. Johnstone and M. E. Rose. *Mass Spectrometry for Chemists and Biochemists*. 2nd ed. Cambridge University Press, 1996. ISBN: 978-0-521-42497-4.

[63] R. O. Jones, P. J. Jennings and O. Jepsen. "Surface Barrier in Metals: A New Model with Application to W(001)". *Phys. Rev. B* **29** (1984), 6474. DOI: 10.1103/PhysRevB.29.6474.

[64] B. B. Joulakian et al. "Dissociative Ionization of H_2^+ by Fast-Electron Impact: Use of a Two-Center Continuum Wave Function". *Phys. Rev. A* **54** (1996), 1473. DOI: 10.1103/PhysRevA.54.1473.

[65] L. P. Kadanoff and G. Baym. *Quantum Statistical Mechanics*. 2nd ed. Westview Press, 1994. ISBN: 978-0-201-41046-4.

[66] U. Kaldor. "General-Model-Space Perturbation Theory: Excitation and Ionization of N_2". *J. Chem. Phys.* **81** (1984), 2406. DOI: 10.1063/1.447942.

[67] L. N. Kantorovich et al. "The Prediction of Metastable Impact Electronic Spectra (MIES): Perfect and Defective MgO(001) Surfaces by State-of-the-Art Methods". *Surf. Sci.* **444** (2000), 31. DOI: 10.1016/S0039-6028(99)01049-3.

[68] G. Katz and R. Kosloff. "Temperature Dependence of Nitrogen Dissociation on Metal Surfaces". *J. Chem. Phys.* **103** (1995), 9475. DOI: 10.1063/1.470008.

[69] L. V. Keldysh. "Diagram Technique for Non-Equilibrium Processes". *Sov. Phys. JETP* **20** (1965), 1018.

[70] C. A. Keller, A. C. Lavery and B. H. Cooper. "Positive- and Negative-Ion Formation in Low-Energy O^+-Cu(001) Scattering". *Phys. Rev. B* **58** (1998), 10959. DOI: 10.1103/PhysRevB.58.10959.

[71] Y.-S. Kim et al. "Electron Emission Characteristics of MgO Thin Films Used for ac-PDPs:Part I. Secondary Electron Emission". *Electronic Materials Lett.* **4** (2008), 113. URL: http://eml.kim.or.kr/PublishedPaper/year_abstract.asp?idx=126.

[72] P. Kürpick and U. Thumm. "Basic Matrix Elements for Level Shifts and Widths of Hydrogenic Levels in Ion-Surface Interactions". *Phys. Rev. A* **54** (1996), 1487. DOI: 10.1103/PhysRevA.54.1487.

[73] C. S. Lam and Y. P. Varshni. "Ionization Energy of the Helium Atom in a Plasma". *Phys. Rev. A* **27** (1983), 418. DOI: 10.1103/PhysRevA.27.418.

[74] L. D. Landau, E. M. Lifshitz and L. P. Pitaevskii. *Course of Theoretical Physics Volume 9: Statistical Physics Part 2*. 3rd ed. Butterworth-Heinemann, 1980. ISBN: 978-0-7506-2636-1.

[75] D. C. Langreth. "Linear and Non-Linear Response Theory with Applications". In: *Linear and Nonlinear Electron Transport in Solids*. Ed. by J. T. Devreese and V. E. van Doren. 1st ed. Plenum Press, 1976. ISBN: 978-0-306-35717-6.

[76] D. C. Langreth and P. Nordlander. "Derivation of a Master Equation for Charge-Transfer Processes in Atom-Surface Collisions". *Phys. Rev. B* **43** (1991), 2541. DOI: 10.1103/PhysRevB.43.2541.

[77] D. C. Langreth and J. W. Wilkins. "Theory of Spin Resonance in Dilute Magnetic Alloys". *Phys. Rev. B* **6** (1972), 3189. DOI: 10.1103/PhysRevB.6.3189.

[78] G. P. Lepage. "A New Algorithm for Adaptive Multidimensional Integration". *J. Comp. Phys.* **27** (1978), 192. DOI: 10.1016/0021-9991(78)90004-9.

[79] M. A. Lieberman and A. J. Lichtenberg. *Principles of Plasma Discharges and Materials Processing*. 2nd ed. Wiley, 2005. ISBN: 978-0-471-72001-0.

[80] E. M. Lifshitz and L. P. Pitaevskii. *Course of Theoretical Physics Volume 10: Physical Kinetics*. 1st ed. Butterworth-Heinemann, 1981. ISBN: 978-0-7506-2635-4.

[81] N. Lorente, R. C. Monreal and M. Alducin. "Local Theory of Auger Neutralization for Slow and Compact Ions Interacting with Metal Surfaces". *Phys. Rev. A* **49** (1994), 4716. DOI: 10.1103/PhysRevA.49.4716.

[82] N. Lorente, D. Teillet-Billy and J. P. Gauyacq. "The $N_2^-(^2\Pi_g)$ Shape Resonance in Slow N_2^* Collisions with Metallic Surfaces". *Surf. Sci.* **432** (1999), 155. DOI: 10.1016/S0039-6028(99)00443-4.

[83] N. Lorente et al. "Auger Neutralization and De-Excitation of Helium at an Aluminium Surface: A Unified Treatment". *Surf. Sci.* **411** (1998), L888. DOI: 10.1016/S0039-6028(98)00407-5.

[84] L. A. MacColl. "Numerical Calculations of the Reflection of Electrons by Metals". *Phys. Rev.* **56** (1939), 699. DOI: 10.1103/PhysRev.56.699.

[85] G. D. Mahan. *Many-Particle Physics*. 3rd ed. Springer, 2000. ISBN: 978-0-306-46338-9.

[86] K. Makoshi. "Effect of Atom Motion on Metastable Deexcitation Spectroscopy". *Surf. Sci.* **254** (1991), 281. DOI: 10.1016/0039-6028(91)90660-K.

[87] K. Makoshi and H. Kaji. "Second Order Selfenergy and Rate Equation in Time-Dependent Auger Processes". *Prog. Theor. Phys. Suppl.* **106** (1991), 327. DOI: 10.1143/PTPS.106.327.

[88] J. Marbach, F. X. Bronold and H. Fehske. "Resonant Charge Transfer at Dielectric Surfaces". *Eur. Phys. J. D* **66** (2012), 1. DOI: 10.1140/epjd/e2012-30014-8.

[89] J. Marbach, F. X. Bronold and H. Fehske. "Auger De-Excitation of Metastable Molecules at Metallic Surfaces". *Phys. Rev. B* **84** (2011), 085443. DOI: 10.1103/PhysRevB.84.085443.

[90] J. B. Marston et al. "Many-Body Theory of Charge Transfer in Hyperthermal Atomic Scattering". *Phys. Rev. B* **48** (1993), 7809. DOI: 10.1103/PhysRevB.48.7809.

[91] F. Massines et al. "Physics and Chemistry in a Glow Dielectric Barrier Discharge at Atmospheric Pressure: Diagnostics and Modelling". *Surf. Coatings Technol.* **174** (2003), 8. DOI: 10.1016/S0257-8972(03)00540-1.

[92] F. Massines et al. "Recent Advances in the Understanding of Homogeneous Dielectric Barrier Discharges". *Eur. Phys. J. Appl. Phys.* **47** (2008), 22805. DOI: 10.1051/epjap/2009064.

[93] P. M. Mathews and K. Venkatesan. *A Textbook of Quantum Mechanics*. 37th ed. Tata McGraw-Hill, 2007. ISBN: 978-0-07-096510-2.

[94] J. Merino and J. B. Marston. "Room-Temperature Kondo Effect in Atom-Surface Scattering: Dynamical $1/N$ Approach". *Phys. Rev. B* **58** (1998), 6982. DOI: 10.1103/PhysRevB.58.6982.

[95] T. Mii and K. Makoshi. "An Interpolation Formula for Electron Transfer in Atom-Surface Collision and Its Validity". *Surf. Sci.* **363** (1996), 145. DOI: 10.1016/0039-6028(96)00124-0.

[96] A. Modinos and S. I. Easa. "On the Interpretation of Ion Neutralisation Spectra at Metal Surfaces". *Surf. Sci.* **185** (1987), 569. DOI: 10.1016/S0039-6028(87)80178-4.

[97] P. J. Mohr, B. N. Taylor and D. B. Newell. "CODATA Recommended Values of the Fundamental Physical Constants: 2006". *Rev. Mod. Phys.* **80** (2008), 633. DOI: 10.1103/RevModPhys.80.633.

[98] R. C. Monreal. "Electron Emission Spectra in Auger Processes near Metal Surfaces". *Surf. Sci.* **388** (1997), 231. DOI: 10.1016/S0039-6028(97)00404-4.

[99] W. C. Murphy and T. F. George. "Overlap Integrals for Atom-Metal Surface Interactions". *Int. J. Quantum Chem.* **28** (1985), 631. DOI: 10.1002/qua.560280509.

[100] D. Neilson, R. M. Nieminen and J. Szymański. "Emission of Thermal Positrons from Metal Surfaces". *Phys. Rev. B* **33** (1986), 1567. DOI: 10.1103/PhysRevB.33.1567.

[101] D. M. Newns et al. "Charge Transfer in Inelastic Ion and Atom-Surface Collisions". *Physica Scripta* **1983** (1983), 5. DOI: 10.1088/0031-8949/1983/T6/001.

[102] A. V. Onufriev and J. B. Marston. "Memory Loss and Auger Processes in a Many-Body Theory of Charge Transfer". *Phys. Rev. B* **53** (1996), 13340. DOI: 10.1103/PhysRevB.53.13340.

[103] D. R. Penn and P. Apell. "Theory of Spin-Polarized Metastable-Atom-Deexcitation Spectroscopy: Ni-He". *Phys. Rev. B* **41** (1990), 3303. DOI: 10.1103/PhysRevB.41.3303.

[104] R. T. Pepino and G. G. Kleiman. "A New Approach to Auger and Quasi-Resonant Processes in Ion-Surface Collisions". *Solid State Commun.* **124** (2002), 317. DOI: 10.1016/S0038-1098(02)00596-3.

[105] P. Pluvinage. "Nouvelle Famille de Solutions Approchées pour Certaines Équations de Schrödinger Non Séparables. Application à l'État Fondamental de l'Hélium". *J. Physique Rad.* **12** (1951), 789.

[106] E. Pollak and J. Tatchen. "Rainbow Scattering of Argon from 2H-W(100)". *Phys. Rev. B* **80** (2009), 115404. DOI: 10.1103/PhysRevB.80.115404.

[107] C. Punset, J. P. Boeuf and L. C. Pitchford. "Two-Dimensional Simulation of an Alternating Current Matrix Plasma Display Cell: Cross-Talk and Other Geometric Effects". *J. Appl. Phys.* **83** (1998), 1884. DOI: 10.1063/1.366913.

[108] J. W. Rabalais. *Low Energy Ion-Surface Interactions*. 1st ed. Wiley, 1994. ISBN: 978-0-471-93891-0.

[109] Y. P. Raizer. *Gas Discharge Physics*. 1st ed. Springer, 1991. ISBN: 978-3-540-19462-0.

[110] J. Rammer and H. Smith. "Quantum Field-Theoretical Methods in Transport Theory of Metals". *Rev. Mod. Phys.* **58** (1986), 323. DOI: 10.1103/RevModPhys.58.323.

[111] M. Remy. "Theory Concerning the Interaction of an Alkali Atom and a Metallic Surface". *J. Chem. Phys.* **53** (1970), 2487. DOI: 10.1063/1.1674351.

[112] J. Robertson. "High Dielectric Constant Gate Oxides for Metal Oxide Si Transistors". *Rep. Prog. Phys.* **69** (2006), 327. DOI: 10.1088/0034-4885/69/2/R02.

[113] J. Robertson, K. Xiong and S. J. Clark. "Band Structure of Functional Oxides by Screened Exchange and the Weighted Density Approximation". *Phys. Status Solidi B* **243** (2006), 2054. DOI: 10.1002/pssb.200666802.

[114] M. J. Rutter and J. Robertson. "Ab Initio Calculation of Electron Affinities of Diamond Surfaces". *Comp. Materials Sci.* **10** (1998), 330. DOI: 10.1016/S0927-0256(97)00104-3.

[115] L. A. Salmi. "Theory of Spin Polarization in the Metastable-He-Metal Interaction". *Phys. Rev. B* **46** (1992), 4180. DOI: 10.1103/PhysRevB.46.4180.

[116] E. Schreiber and H. J. Fitting. "Monte Carlo Simulation of Secondary Electron Emission from the Insulator SiO_2". *J. Electr. Spectr. Related Phenomena* **124** (2002), 25. DOI: 10.1016/S0368-2048(01)00368-1.

[117] F. Schwabl. *Advanced Quantum Mechanics*. 3rd ed. Springer, 2005. ISBN: 978-3-540-25901-5.

[118] F. Schwabl. *Quantum Mechanics*. 4th ed. Springer, 2007. ISBN: 978-3-540-73674-5.

[119] W. Sesselmann et al. "Interaction of Metastable Noble-Gas Atoms with Transition-Metal Surfaces: Resonance Ionization and Auger Neutralization". *Phys. Rev. B* **35** (1987), 1547. DOI: 10.1103/PhysRevB.35.1547.

[120] H. Shao, D. C. Langreth and P. Nordlander. "Many-Body Theory for Charge Transfer in Atom-Surface Collisions". *Phys. Rev. B* **49** (1994), 13929. DOI: 10.1103/PhysRevB.49.13929.

[121] R. J. Silbey, R. A. Alberty and M. G. Bawendi. *Physical Chemistry*. 4th ed. Wiley, 2005. ISBN: 978-0-471-21504-2.

[122] A. Sindona et al. "Many-Body Shake-Up in Auger Neutralization of Slow Ar^+ Ions at Al Surfaces". *Phys. Rev. A* **71** (2005), 052903. DOI: 10.1103/PhysRevA.71.052903.

[123] J. C. Slater. "Atomic Shielding Constants". *Phys. Rev.* **36** (1930), 57. DOI: 10.1103/PhysRev.36.57.

[124] K. J. Snowdon et al. "Auger and Resonant Neutralization of Low Energy Ions near Metal Surfaces". *Surf. Sci.* **173** (1986), 581. DOI: 10.1016/0039-6028(86)90211-6.

[125] K. J. Snowdon et al. "Comparison of Auger and Resonant Transition Rates in the Hydrogen-Metal Surface Interaction". *Nucl. Instrum. Methods Phys. Res. B* **23** (1987), 309. DOI: 10.1016/0168-583X(87)90383-1.

[126] A. M. Stoneham and M. J. L. Sangster. "Multiple Charge-States of Transition Metal Impurities". *Phil. Mag. B* **43** (1981), 609. URL: http://www.tandfonline.com/doi/abs/10.1080/01418638108222163.

[127] P. Stracke et al. "Formation of the Nitrogen Shape Resonance in N_2^+ and $N_2^*(A^3\Sigma_u^+)$ Collisions with Metallic Surfaces". *Surf. Sci.* **396** (1998), 212. DOI: 10.1016/S0039-6028(97)00670-5.

[128] M. Tobita and S. Ho. "Electronic Structure Calculation of MgO (001) Surface with Aggregated Oxygen Vacancies". *J. Chem. Theor. Comp.* **4** (2008), 1057. DOI: 10.1021/ct700303v.

[129] J. C. Tully. "Neutralization of Ions at Surfaces". *Phys. Rev. B* **16** (1977), 4324. DOI: 10.1103/PhysRevB.16.4324.

[130] H. Van Doveren and J. A. T. H. Verhoeven. "XPS Spectra of Ca, Sr, Ba and Their Oxides". *J. Electr. Spectr. Related Phenomena* **21** (1980), 265. DOI: 10.1016/0368-2048(80)85055-9.

[131] M. A. Vicente Alvarez, V. H. Ponce and E. C. Goldberg. "Auger, Resonant, and Plasmon-Assisted Charge-Transfer Processes in Atom-Surface Collisions". *Phys. Rev. B* **57** (1998), 14919. DOI: 10.1103/PhysRevB.57.14919.

[132] T. J. Vink et al. "Materials with a High Secondary-Electron Yield for Use in Plasma Displays". *Appl. Phys. Lett.* **80** (2002), 2216. DOI: 10.1063/1.1464229.

[133] J. M. Wallace and P. V. Hobbs. *Atmospheric Science: An Introductory Survey*. 2nd ed. Academic Press, 2006. ISBN: 978-0-12-732951-2.

[134] N. P. Wang et al. "Low-Energy Ion Neutralization at Surfaces: Resonant and Auger Processes". *Phys. Rev. A* **64** (2001), 012901. DOI: 10.1103/PhysRevA.64.012901.

[135] P. F. Weck et al. "Two-Center Continuum Approximation with Correct Boundary Conditions for Single-Electron Emission in $e^- + H_2$ Collisions". *Phys. Rev. A* **66** (2002), 012711. DOI: 10.1103/PhysRevA.66.012711.

[136] P. F. Weck et al. "Two-Effective Center Approximation for the Single Ionization of Molecular Hydrogen by Fast Electron Impact". *Phys. Rev. A* **63** (2001), 042709. DOI: 10.1103/PhysRevA.63.042709.

[137] C. T. Whelan et al. *New Directions in Atomic Physics*. 1st ed. Springer, 1999. ISBN: 978-0-306-46181-1.

[138] U. Wille. "Resonant Electron Transfer at Metal Surfaces: Theoretical Analysis of Scaling Properties and Universal Behavior". *Phys. Rev. B* **50** (1994), 1888. DOI: 10.1103/PhysRevB.50.1888.

[139] N. S. Wingreen and Y. Meir. "Anderson Model out of Equilibrium: Noncrossing-Approximation Approach to Transport Through a Quantum Dot". *Phys. Rev. B* **49** (1994), 11040. DOI: 10.1103/PhysRevB.49.11040.

[140] H. Winter. "Collisions of Atoms and Ions with Surfaces Under Grazing Incidence". *Phys. Rep.* **367** (2002), 387. DOI: 10.1016/S0370-1573(02)00010-8.

[141] H. Winter and J. Burgdörfer. *Slow Heavy-Particle Induced Electron Emission from Solid Surfaces*. 1st ed. Springer, 2007. ISBN: 978-3-540-70788-2.

[142] Y. C. Yeo, T. J. King and C. Hu. "Metal-Dielectric Band Alignment and Its Implications for Metal Gate Complementary Metal-Oxide-Semiconductor Technology". *J. Appl. Phys.* **92** (2002), 7266. DOI: 10.1063/1.1521517.

[143] A. Yoshimori and K. Makoshi. "Time-Dependent Newns-Anderson Model". *Prog. Surf. Sci.* **21** (1986), 251. DOI: 10.1016/0079-6816(86)90007-9.

[144] G. L. Yudin, S. Chelkowski and A. D. Bandrauk. "Coulomb Continuum Effects in Molecular Interference". *J. Phys. B* **39** (2006), L17. DOI: 10.1088/0953-4075/39/2/L01.

[145] R. Zimny et al. "Interplay of Resonant and Auger Processes in Proton Neutralization After Grazing Surface Scattering". *Surf. Sci.* **255** (1991), 135. DOI: 10.1016/0039-6028(91)90017-M.

Danksagung

Mein Dank gilt in erster Linie meinem Betreuer PD Dr. Franz Xaver Bronold der mir stets ein aufgeschlossener und kritischer Gesprächspartner war und mich in allen Phasen meiner Promotion sowohl fachlich als auch menschlich unterstützt hat. In gleichem Maße richtet sich mein Dank an Prof. Dr. Holger Fehske, der mein Promotionsvorhaben ermöglicht hat und sich oft für meine Interessen einsetzte. Des Weiteren bedanke ich mich bei Dr. Thomas Meyer und Jens Schleede für die Administration des Rechenclusters am Institut für Physik der Universität Greifswald. Ohne Letzteren wäre diese Arbeit nicht entstanden. Darüber hinaus danke ich dem Land Mecklenburg-Vorpommern für die finanzielle Förderung meiner Promotion im Rahmen eines Landesgraduiertenstipendiums.

Letztlich danke ich meiner Lebenspartnerin Ulrike Krampe, die mich in dieser schweren und arbeitsreichen Zeit stets unterstützt, aufgemuntert und ermutigt hat. Vergessen seien auch nicht meine lieben Eltern, Ute und Stephan Marbach, für deren Förderung und Rückhalt ich auf ewig dankbar bin. Die Finanzierung des Projektes "Johannes Marbach" ist für euch nun endgültig abgeschlossen.